Smart Fast charge of Lithium-ion battery

Rakesh Khatokar Amarnath

THÈSE

Pour obtenir le grade de

DOCTEUR DE L'UNIVERSITÉ GRENOBLE ALPES

École doctorale : I-MEP2 - Ingénierie - Matériaux, Mécanique, Environnement, Energétique, Procédés, Production
Spécialité : MEP : Mécanique des fluides Energétique, Procédés
Unité de recherche : Laboratoire d'Electrochimie et de Physico-Chimie des Matériaux et des Interfaces.

Charge rapide intelligente de batterie Lithium-ion

Smart Fast charge of Lithium-ion battery

Présentée par :

Rakesh KHATOKAR AMARNATH

Direction de thèse :

Pierre Xavier THIVEL MAITRE DE CONFERENCES, Université Grenoble Alpes	Directeur de thèse
Jean-Claude LEPRETRE PROFESSEUR DES UNIVERSITES, Université Grenoble Alpes	Co-encadrant de thèse

Rapporteurs :

Serge PELISSIER
DIRECTEUR DE RECHERCHE, Université Gustave Eiffel
Christophe FORGEZ
PROFESSEUR DES UNIVERSITES, Université de Technologie de Compiègne

Thèse soutenue à huis clos le **12 décembre 2022**, devant le jury composé de :

Pierre Xavier THIVEL MAITRE DE CONFERENCES HDR, Grenoble INP	Directeur de thèse
Serge PELISSIER DIRECTEUR DE RECHERCHE, Université Gustave Eiffel	Rapporteur
Christophe FORGEZ PROFESSEUR DES UNIVERSITES, Université de Technologie de Compiègne	Rapporteur
Pascal VENET PROFESSEUR DES UNIVERSITES, Université Lyon 1 - Claude Bernard	Examinateur
DELPHINE RIU PROFESSEUR DES UNIVERSITES, Grenoble INP	Présidente

Invités :

Jean Claude Lepretre
PROFESSEUR DES UNIVERSITES, UGA
Francis Roy
INGENIEUR DOCTEUR, Stellantis
Thomas PEUCHANT
INGENIEUR,Saft

Table of abbreviations and parameters

AC	Alternating Current
Al	Aluminium
BOL	Begining of Life
C	Graphite
CC	Constant Current
CI	Current Interrupt
CID	Current Interrupt Device
C-rate	Current rate relative to nominal capacity of battery
CP	Current Pulse
CV	Constant Voltage
DMC	Dimethyl Carbonate
DC	Direct Current
DT	Duty Cycle
EC	Ethylene Carbonate
EIS	Electrochemical Impedance Spectroscopy
EMC	Ethyl Methyl Carbonate
EMF	Electro-motive Force
EOL	End of Life
EV	Electric Vehicle
HEV	Hybrid Electric Vehicle
IBIS	Intelligent Battery Integrated System
ICA	Incremental Capacity Analysis

ICE	Internal Combustion Engine
ISA	International Seabed Authority
LAM	Loss of Active Material
LCO	Lithium Cobalt Oxide
LFP	Lithium Iron Phosphate
LLI	Loss of Lithium Inventory
LTO	Lithium Titanium Dioxide
M_N	Active mass of negative electrode
M_P	Active mass of Positive electrode
NE	Negative Electrode
Ni-Cd	Nickel Cadmium
NMC	Nickel Manganese Cobalt oxide
Ni-MH	Nickel Metal Hydride
OCV	Open Circuit Voltage
ODC	Ohmic Drop Compensation
OFS	Offset Parameter
OCP	Open Circuit Potential
PE	Positive Electrode
PHEV	Plug-in Hybrid Electric Vehicle
redox	Reduction - Oxidation
SEI	Solid Electrolyte Interphase
SoC	State of Charge
SoD	State of Discharge

SoH	State of Health
Ri	Internal Resistance
RPT	Reference Performance Test
T	Temperature
tc	Charge time
tr	Rest time
td	Discharge pulse time
VSCL	Voltage Step with Current Limit
VSTL	Voltage Step with Time Limit

Table des matières

Abstract 18

Introduction 20

Chapter 1. Li battery and application 24

1. Battery technology and application 25

1.1 Li-ion batteries 27

1.2 Terminologies 38

2. State of the art: Fast Charge 39

2.1 Constant current constant voltage technique 39

2.2 Multistage constant current technique 41

2.3 Constant current constant voltage with ohmic drop compensation technique 43

2.4 Current based pulse charging technique 46

2.5 Varying current technique 49

2.6 Sinusoidal current charging technique 49

2.7 Conclusion 50

3. State of the art: Ageing 50

3.1 Introduction 50

3.2 Calendar ageing 51

3.3 Cyclic ageing 52

3.4 Physio chemical analysis 56

3.5 State of Health estimation 60

3.6 Conclusion 62

Chapter 2. Experimental setup 63

1. Experimental set up and characterization 64

1.1 Introduction 64

1.2 Lithium battery 64

1.3 Battery test bench 66
2. Cell characterization 70
2.1 Precondition 70
2.2 Internal resistance estimation using current interrupt 72
2.3 Electrochemical impedance spectroscopy (EIS) 74
2.4 Incremental capacity analysis 76
2.5 Open circuit voltage (OCV) 77
3. Post-mortem analysis methodology 78
3.1 X-ray tomography 78
3.2 Electrochemical characterization with coin cell 79
Chapter 3. Current control technique 80
1. Introduction 81
2. Fast charging technique : constant current constant voltage protocol 81
2.1 Constant current constant voltage technique 81
2.2 Constant current constant voltage with Ohmic Drop Compensation 85
2.3 Comparison of CCCV with and without ODC in relation to target 90
3. Fast charge technique: Pulse charge method 93
3.1 Presentation of protocol: square current with rest pulse 93
3.2 Presentation of protocol: square current with discharge pulse 98
3.3 Presentation of protocol: Triangular current pulse 103
4. Discussion of current based protocol 107
5. Conclusion 112
Chapter 4. Voltage control technique 113
1. Introduction 114
2. Proposed techniques 115
2.1 Presentation of protocols 115
2.2 Results and Discussion 121

3. Comparison of protocols 127
3.1 Comparison between VSTL and VSCL 127
3.2 Comparison between VSCL and constant current with ODC 128
4. Conclusion 132
Chapter 5. Ageing study: Part-I 133
1. Introduction 134
2. Cyclic ageing 134
2.1 Current based protocols 137
2.2 Voltage based protocols 151
3. Reproducibility of results 159
3.1 Current based protocol 159
3.2 Voltage based protocol 161
4. Conclusion 163
Chapter 6. Ageing Study: Part-II 164
1. Introduction 165
2. X-ray Tomography of cells 165
3. Characterization of Aged electrodes 168
3.1 Coin cell construction 168
3.2 Characterization method 169
3.3 Charging protocol discussion 170
4. Conclusion 172
General Conclusion 173
References 177

List of Figures

Fig. 0.1 H-bridge architecture interconnecting the modules to form a battery pack under IBIS project from Stellantis 21
Fig. 1.1 Comparison of various battery technologies [7] 27
Fig. 1.2 Operating principle of Li-ion battery during charging (left) and discharging (right) . 29
Fig. 1.3 Typical discharge profiles of various positive electrode active material [11] 31
Fig. 1.4 Crystal structure (a) lithiated graphite (b) LTO and (c) Silicon during lithiation (d) charge-discharge profiles with voltage hysteresis for different materials[11]. 33
Fig. 1.5 Constant current constant voltage (CCCV) protocol (Blue: Current ; Red : Voltage) 40
Fig. 1.6 Charging time (minutes) and battery discharged capacity (% C) when different charging rates (from 0.1C to 1.5C) are used in the constant current step: the constant voltage step finishes in each case when battery capacity reaches the desirable value [1] 41
Fig. 1.7 Multistage Constant Current Constant Voltage (MSCCCV) technique 42
Fig. 1.8 Multistage fast charging strategy during constant current stage [33] 43
Fig. 1.9 Multistage fast charging strategy during constant voltage stage [34] 43
Fig. 1.10 CCCV technique with Ohmic Drop Compensation (ODC) technique [8] 45
Fig. 1.11 Total charging time for different compensation rate (α) for LTO/LFP battery at 6Crate (red) and 11 C-rate (blue) 46
Fig. 1.12 Waveforms of the voltage with and without the BRC technique. The CC stage of the original design is extended to the CC' stage with the BRC design [36] 46
Fig. 1.13 Current pulse charging technique 47
Fig. 1.14 Schematic of fast charging process of different pulse sequences. (A) Constant amplitude pulsed current interspersed with identical rest periods; (B) constant amplitude pulsed current interspersed with alternating constant amplitude discharge pulses; and (C) pulsed current consisting of a sequence of different amplitudes charge current density pulses [38] .. 48
Fig. 1.15 Degradation mechanism inside Li-ion battery [50] 51
Fig. 1.16 Factors affecting the calendar ageing [54] [55] 52
Fig. 1.17 Factors affecting the cyclic ageing [56] 53
Fig. 1.18 Effect of high temperature on ageing [57] 53
Fig. 1.19 Effect of low temperature on ageing [57] 54
Fig. 1.20 Effect of high current on ageing [58]. 54
Fig. 1.21 Effect of cycle number on ageing [59] 55

Fig. 1.22 X-Ray tomography of 6 C- high level ODC aged cell [60] 56
Fig. 1.23 Flow chart for disassembly of Li-ion cell and post-mortem analysis [61] 57
Fig. 1.24 Overview of inside components in a Li-ion battery and physio-chemical analysis methods [61] 58
Fig. 1.25 a)-k) simplified schematics of detected particles in different analysis methods. Electromagnetic radiation hv corresponds to visible light in (a), (f), (g), X-rays in (d), (e), (k) and to radio waves in (j). In (b), the emitted electrons can be distinguished between backscattered electrons, Auges electrons, and secondary electrons. H) IR in reflectance mode. 1) Principle of separation of the components in a mixture in chromatography. The circles and the lines represent the sample molecules and the stationary phase, respectively [61]. 58
Fig. 1.26 Post-mortem analysis methods [61] 59
Fig. 1.27 SoH estimation methods[63] 60
Fig. 2.1 (a) Biologic potentiostat with climatic chamber and (b) Biologic cycler for ageing study 66
Fig. 2.2 Schematic diagram of the high frequency pulse charger 67
Fig. 2.3 Voltage drop across 20mΩ shunt resistor measured using Keysight oscilloscope for 4A with 50% duty cycle (2C equivalent of power cell) at (a) 250mHz (b) 25Hz (c) 2.5kHz and (d) 10kHz respectively 69
Fig. 2.4 Voltage and current curves at 25°C for C/NMC power (top) and energy (bottom) cell during the reference charging, relax period and reference discharging process 71
Fig. 2.5 Average discharge capacity at 25°C for power (blue) and energy (red) cells with standard deviation during preconditioning 72
Fig. 2.6 Internal resistance in mohms at 25°C for power (blue) and energy (red) cells used in this study with respective standard deviation. 73
Fig. 2.7 Internal resistance in mohms for power (blue) and energy (red) cells at 25°C at different SoC 74
Fig. 2.8 AC impedance evolution at 50% SoC and at 25°C ambient temperature for new power (blue) and energy (red) cells 75
Fig. 2.9 Electrical equivalent circuit (EEC) model of the cell 76
Fig. 2.10 incremental capacity analysis for power cell (blue) and energy cell (red) 77
Fig. 2.11 OCV vs SoC characterization for power (blue) and energy (red) cells at 25°C for fresh cells 78

Fig. 3.1 Current in blue and cell voltage in red variation during charging using CCCV method at (a) 0.5C-rate for power cell (b)4C-rate for power (c) 0.5C-rate for energy cell and (d) 4C-rate for energy cell. 82
Fig. 3.2 SoC in blue and Δ Temperature in red variation during charging using CCCV method at (a) 0.5C-rate for power cell (b)4C-rate for power (c) 0.5C-rate for energy cell and (d) 4C-rate for energy cell. 83
Fig. 3.3 Time taken to charge 80% SoC from 0% SoC and Δ Temperature from 0.5C to 4C-rate for energy and power cells 85
Fig. 3.4 3C-rate CC CV with ohmic drop compensation for Energy cell at 25°C ambient temperature 86
Fig. 3.5 Current in blue and cell voltage in red variation during charging using CCCV method with ODC at (a) 0.5C-rate for power cell (b)3C-rate for power (c) 0.5C-rate for energy cell and (d) 3C-rate for energy cell. 87
Fig. 3.6 SoC in blue and Δ Temperature in red variation during charging using CCCV method with ODC at (a) 0.5C-rate for power cell (b)3C-rate for power (c) 0.5C-rate for energy cell and (d) 3C-rate for energy cell. 88
Fig. 3.7 Time taken to charge 80% SoC from 0% SoC and Δ Temperature from 0.5C to 3C-rate with ODC for energy and power cells 89
Fig. 3.8 (a)Voltage and (b) SoC comparison between CCCV with and without ODC at 3C-rate for energy cell 91
Fig. 3.9 Comparison of time taken to charge 80% SOC from 0% Soc at different C rates with ODC and without ODC for power and energy cell at 25°C ambient temperature. 92
Fig. 3.10 square Current pulse charging technique 94
Fig. 3.11 (a) voltage, (b) current, (c) SoC and Δ temperature curves for power cell charging at 2C peak current with tc = 2s, tr = 2s and a duty cycle of 50% at 25°C ambient temperature . 95
Fig. 3.12 Δ Temperature comparison for current pulse technique at 50% and 80% Duty cycle at different frequencies for energy and power cells 96
Fig. 3.13 Time taken to recharge 80% SOC from 0% SOC at 50% and 80% duty cycle for frequencies ranging from 0.25Hz to 2.5kHz for energy and power cell at 25°C ambient temperature 98
Fig. 3.14 Illustration of square current pulse with intermediate discharge pulses 99

Fig. 3.15 (a) voltage, (b) current, (c) SoC and Δ temperature curves for power cell charging at 2C and -0.1C-rate current pulse with tc = 2s, td = 2s and a duty cycle of 50% at 25°C ambient temperature 100
Fig. 3.16 Time taken to recharge 80% SOC from 0% SOC at 50% and 80% duty cycle for frequencies ranging from 250mHz to 250Hz for energy and power cell at 25°C ambient temperature 101
Fig. 3.17 Δ Temperature comparison for current with discharge pulse technique at 50% and 80% Duty cycle for frequencies ranging from 0.25Hz to 250Hz for energy and power cells 102
Fig. 3.18 Illustration of triangular current pulse 103
Fig. 3.19 voltage in red and current in blue for energy cell charging at 2C-rate triangular pulse with dI/dt =2.6A/s and a frequency of 250mHz at 25°C ambient temperature 104
Fig. 3.20 Snippet of voltage in red and current in blue at 20 minutes for energy cell charging at 2C triangular pulse with dI/dt =2.6A/s and a frequency of 250mHz at 25°C ambient temperature 105
Fig. 3.21 Comparison of time taken to charge 80% SOC from 0% Soc at different mean C rates with ODC and without ODC for energy (a) and power (b) cell at 25°C ambient temperature 107
Fig. 3.22 (a) Comparison of Voltage curves for Square in blue and Triangular in red. (b) Comparison of current curves for Square in blue and Triangular in red for Energy cell at 2C, 250mHz peak current and 50% DT 108
Fig. 3.23 (a)voltage (V) comparison between 1C CC-CV and 1C mean square current pulse without ODC at 500mHz for energy cell (b) Temperature (°C) and SoC (%) comparison between 1C CC-CV and 1C mean square current pulse without ODC at 500mHz and 50% DT for energy cell (c) voltage (V) comparison between 2C CC-CV and 2C mean square current pulse without ODC at 500mHz and 50% DT for energy cell (d) Temperature (°C) and SoC (%) comparison between 2C CC-CV and 2C mean square current pulse without ODC at 500mHz and 50% DT for energy cell 109
Fig. 4.1 Proposed voltage step with time limit (left) and voltage step with current limit (right) protocol 119
Fig. 4.2 Pulsed voltage steps for VSTL (left) and VSCL (right) protocols 121
Fig. 4.3 voltage, current, Δ Temperature and SoC curves for (a) Power cell and (b) Energy cell using voltage step with time as step limit at first iteration at 25°C ambient temperature 122

Fig. 4.4 voltage, current Δ Temperature and SoC curves for (a) Power cell and (b) Energy cell using voltage step with time as step limit at 25°C ambient temperature 124
Fig. 4.5 voltage, current Δ temperature and SoC curves for (a) Power cell and (b) Energy cell using voltage step with current as step limit at 25°C ambient temperature 126
Fig. 4.6 Voltage comparison for VSTL (Blue Curve) and VSCL (Red Curve) protocol for power cell (reference 1c) 127
Fig. 4.7 Comparison of voltage (a), current(b), Δ SoC (c) and Temperature(d) curves for power cell (reference 1c) using voltage step with current as step limit (blue) and 3C CC with ODC (red) at 25°C ambient temperature 129
Fig. 4.8 Comparison of voltage (a), current(b), Δ SoC (c) and Temperature(d) curves for energy cell (reference 2c) using voltage step with current as step limit (blue) and 3C CC with ODC (red) at 25°C ambient temperature 130
Fig. 5.1 Flow chart of experimental test procedure..... 136
Fig. 5.2 Cycle-life test; Comparison of evolution of (a) Δ SoC (%) during stage I (b) stage I time (c) ΔSoC (%) during stage II (d) stage II time (minutes) (e) SoH (%) (f) total charge time (minutes) for power cells cycled with 1C-rate CCCV (black; Reference: 1e), square current pulse (Red; Reference: 1f) with 1C-rate mean current and Triangular current pulse (blue; Reference: 1g) with 1C-rate mean current 140
Fig. 5.3 Cycle-life test; Comparison of evolution of (a) Δ SoC (%) during stage I (b) stage I time (c) Δ SoC (%) during stage II (d) stage II time (minutes) (e) SoH (%) (f) total charge time (minutes) for energy cells cycled with 1C-rate CCCV (black; Reference: 2e), square current pulse (Red; Reference: 2f) with 1C-rate mean current and Triangular current pulse (blue; Reference: 2g) with 1C-rate mean current 141
Fig. 5.4 Cycle-life test; Comparison of evolution of (a) Δ SoC (%) during stage I (b) stage I time (c) Δ SoC (%) during stage II (d) stage II time (minutes) (e) SoH (%) (f) total charge time (minutes) for energy cells cycled with 2C-rate CCCV (black; Reference: 2h), square current pulse (Red; Reference: 2i) with 2C-rate mean current and Triangular current pulse (blue; Reference: 2j) with 2C-rate mean current at 25C ambient temperature..... 142
Fig. 5.5 Comparison of evolution of current (left) and temperature elevation (right) during stage II for energy cells cycled with square current pulse (Reference: 2f) with 1C-rate mean current at 25C ambient temperature. 144
Fig. 5.6 Cycle-life test; Comparison of evolution of SoH (%) (left) and internal resistance vs SoH (right) for power cells cycled with 1C-rate CCCV (black; Reference: 1e), square current

pulse (Red; Reference: 1f) with 1C-rate mean current and triangular current pulse (blue; Reference: 1g) with 1C-rate mean current; 1C-rate CCCV (Navy blue; Reference: 2e), square current pulse (orange; Reference: 2f) with 1C-rate mean current and triangular current pulse (yellow; Reference: 2g) with 1C-rate mean current for energy cells; 2C-rate CCCV (purple; Reference: 2h), square current pulse (Green; Reference: 2i) with 1C-rate mean current and triangular current pulse (cyan; Reference: 2j) with 2C-rate mean current at 25°C ambient temperature 146
Fig. 5.7 ICA curves for power and energy cells cycled with 1C-rate and 2C-rate CCCV, Square CP and Triangular CP at 25°C ambient temperature. 148
Fig. 5.8 comparison of peak A height (left) and peak B height (right) 149
Fig. 5.9 Cycle-life test; Comparison of evolution of (a) Δ SoC (%) (left) total charge time (minutes) (right) for power cell cycled with VSCL (blue; Reference: 1k), 3C CC with ODC (red; Reference: 1l) at 25°C ambient temperature 153
Fig. 5.10 Cycle-life test; Comparison of evolution of (left) Δ SoC (%) (right) total charge time (minutes) for energy cell cycled with VSCL (blue; Reference: 2k), 3C CC with ODC (red; Reference: 2l) at 25°C ambient temperature 153
Fig. 5.11 Cycle-life test; Comparison of temperature elevation for power cell cycled with VSCL (blue; Reference: 1k), 3C CC with ODC (red; Reference: 1l) at 25°C ambient temperature 154
Fig. 5.12 Cycle-life test; Comparison of temperature elevation for energy cell cycled with VSCL (blue; Reference: 2k), 3C CC with ODC (red; Reference: 2l) at 25°C ambient temperature 155
Fig. 5.13 Cycle-life test; Comparison of evolution of SoH (%) (left) and internal resistance vs SoH (right) for power( )and energy ( )cells cycled with VSCL (blue; Reference: 1k;2k) and 3C CC with ODC (red; Reference: 1l;2l) at 25°C ambient temperature 156
Fig. 5.14 IC curves for power(top) and energy (bottom) cells cycled with VSCL (left; Reference: 1k;2k), and 3C CC with ODC (right; Reference: 1l;2l) at 25°C ambient temperature 157
Fig. 5.15 Comparison of A peak height (left) and B peak height (right) for power (bottom) and energy (top)cells cycled with VSCL 1C-rate CCCV (Reference: 1k;2k), and 3C CC with ODC (Reference: 1l;2l) at 25°C ambient temperature 158
Fig. 5.16 Average SoH for power cells cycled with 1C CCCV (black), square CP (red) and triangular CP (blue) with standard deviation during ageing at 25°C 160

Fig. 5.17 Average SoH for energy cells cycled with CCCV (black), square CP (red) and triangular CP (blue)with 1C-rate mean current (left) and 2C-rate mean current (right) with standard deviation during ageing at 25°C 161
Fig. 5.18 Average SoH for power cells cycled with VSCL (blue) and 3C CC with ODC (red) with standard deviation during ageing at 25°C 162
Fig. 5.19 Average SoH for energy cells cycled with VSCL (blue) and 3C CC with ODC (red) with standard deviation during ageing at 25°C 162
Fig. 6.1 longitudinal cross section of the fresh energy cell showing various parts. 166
Fig. 6.2 X-ray Tomography of energy cells cycled with various charging protocols alongside with fresh cell 167
Fig. 6.3 Various components in a coin cell [91] 168
Fig. 6.4 OCV model procedure for eneryg cell (a) OCP's of electrodes vs lithium content, (b) initialisation of OCP's to start at same position vs lithium content, (c) OCP's of electrode and full cell experimental OCV vs capacity (d) OCP's of electrode, full cell experimental OCV and fitted OCV vs capacity 170
Fig. 6.5 LAM evolution for negative electrode (left) and positive electrode (right) between the RPT's for energy cell cycled with various protocol during ageing 171

List of tables

Table 1 characteristics of several types of battery 26
Table 2 characteristics of positive electrode active materials [11] 30
Table 3 Characteristics of negative electrode active material [11] 32
Table 4 Summary of requirements for EV battery [21] 37
Table 5 Power optimised 18650C/NMC cell characteristics from Samsung 65
Table 6 Energy optimized 18650 C/NMC characteristics from LG Chem 65
Table 7 Overview of the characteristics of the cells 73
Table 8 Summary results of all the experiments on CC CV technique 92
Table 9 Summary of the parameters used to study the impact of square current with rest protocol 94
Table 10 Summary results of all the experiments on Square Current with rest pulse 97
Table 11 Summary of the parameters used to study the impact of square current with discharge pulse protocol 99

Table 12 Summary results of all the experiments on Square Current with discharge pulse .. 102
Table 13 Summary of the parameters used to study the impact of triangular current pulse protocol 104
Table 14 Summary results of all the experiments on current pulse with discharge technique 106
Table 15 comparison of charging time and Δ Temperature between Square and Triangular current based pulse charging 111
Table 16 Overview of the parameters used in the VSTL experiments 117
Table 17 Overview of the parameters used in the VSCL experiments 118
Table 18 summary results of voltage step with time as step limit at first iteration 122
Table 19 summary results of voltage step with time as step limit at 12^{th} iteration 124
Table 20 summary results of voltage step with current as step limit 126
Table 21 comparison of VSTL and VSCL protocols to charge Δ SoC of 80% from 10% SoC 128
Table 22 Comparison of VSCL and 3C CC with ODC protocols to charge Δ SoC of 80% from 10% SoC 131
Table 23 Overview of cell characteristics used in following section 137
Table 24 summary of experimental parameters used during cyclic ageing study for current based protocol 139
Table 25 summary of experimental parameters used during cyclic ageing study for voltage-based protocol 152
Table 26 summary of SoH of all the cycled cells. 163

Abstract

Recent technological advancements in the field of Li-ion battery technology has made it to become a promising solution in the transportation sector to shift from Internal combustion engine to Electric vehicle. This paradigm shift has drawn the interest of researchers globally to contribute greatly to improve the performance of Li-ion battery. In this regard, extensive research on fast charging of Li-ion batteries is under progress to reduce the charging time and improve the life span of the batteries in-order to compete neck to neck with Internal Combustion Engine (ICE).

In this work, fast charging protocols have been developed for two type of cell one dedicated to power application (2Ah, Samsung SDI), and one cell dedicated to energy application (2.6Ah, LG Chem).

In a first part, different charging protocols are tested in order to reach a charge of 80% of SOC in 20 minutes with a limiting temperature increase of 25°C. Current based protocols (classical Constant Current-Constant Voltage with or without ohmic drop compensation and pulse current methods) and voltage bases protocols (pulse voltage methods) have been developed and tested. In particular, a specific pulses voltage method (patented) lead to a reduce charging time of 15 minutes with an increase of 15°C.

In a second part, aging study have been performed to check the impact of the protocol on the degradation of the cell. It is shown that fast protocol doesn’t affect the aging of power cell type (550 cycles with SOH of 83%) but strongly affect the aging of energy cell (100 cycles with SOH of 80%) demonstrating the importance of the cell design for fast protocol use.

Les avancées technologiques récentes dans le domaine de la technologie des batteries Li-ion en ont fait une solution prometteuse dans le secteur des transports pour passer du moteur à combustion interne au véhicule électrique. Ce changement de paradigme a suscité l'intérêt des chercheurs du monde entier pour contribuer grandement à améliorer les performances des batteries Li-ion. À cet égard, des recherches approfondies sur la charge rapide des batteries Li-ion sont en cours pour réduire le temps de charge tout en assurant un faible vieillissement des batteries afin de rivaliser avec les moteurs thermiques. Dans ce travail, des protocoles de charge rapide ont été développés pour deux types de cellules, l'un dédié à des applications typées

puissance (2Ah, Samsung SDI), et l'autre dédié à des applications typées énergie (2.6Ah, LG Chem). Dans une première partie, différents protocoles de charge ont été développés en vue d'atteindre une recharge de 80% de la capacité de la batterie en 20 minutes avec une augmentation de température limitée à 25°C. Des protocoles basés sur le courant (méthodes classiques type "courant constant-tension constante" avec ou sans compensation de chute ohmique et méthodes en courant pulsé) et des protocoles basés sur la tension (méthodes en tension pulsée) ont été développés et testés. En particulier, une méthode spécifique de tension pulsée (brevetée) conduit à un temps de charge réduit de 15 minutes avec une augmentation de 15°C.

Dans une deuxième partie, des études de vieillissement ont été réalisées pour vérifier l'impact du protocole sur la dégradation de la cellule. Il a été démontré que le protocole rapide n'affecte pas le vieillissement des cellules typées puissance (550 cycles avec SOH de 83%) mais affecte fortement le vieillissement des cellules typée énergie (100 cycles avec SOH de 80%) démontrant l'importance de la conception de la cellule pour utilisation rapide du protocole

Introduction

Nowadays, the transportation sector is being flooded with electric vehicle (EV) due to stringent rules being applied on the Internal Combustion Engine (ICE) vehicle. The main goal behind this is to reduce CO_x and NO_x emissions from ICE, which are prime culprits for global warming. Due to this, the transportation sector is on a constant hunt for more energy efficient, robust and sustainable energy resources to power the vehicles. As a result, Li-ion battery has become more successful in meeting the expectation of most of the automakers since, they possess high energy density per volume and mass as compared to other secondary battery technologies existing in the market so far [1].

With the increase in sales of EV's, the automakers are on a constant look out for efficient recharging technique to reduce the overall charging time. Currently the longer charging time of 3 to 4 hours is discouraging. Therefore, lots of scientific efforts has been undertaken to reduce the charging time significantly. However, significant reduction of recharging time has led to poor performance by accelerating ageing. This is due to the fact that, lowering charging time involves higher current rates leading high temperatures contributing to rapid degradation [2]. This accelerated ageing of the Li-ion batteries has a counter effect on the sales of EV, since its range decreases and becomes a dead load in the EV. Hence the need of the hour is to reduce the charging time without compromising the performance and life span.

This thesis was carried out under the frame work on Intelligent Battery Integrated System (IBIS) ADEME project supervised by Stellantis group and other industrial partners such as SAFT, E2-CAD and Sherpa Engineering and labs academic partners as SATIE, GEEPS and LEPMI. The IBIS project aims to bring about a profound change in the way of designing electric powertrains. Technological innovation concerns the integration of inverter, charger and converter functions in the energy storage battery. To achieve this, the IBIS battery pack is divided into several modules. These modules are connected through a ***H-bridge*** as shown in Fig. 0.1. It uses 4 electronically controlled semiconductor switches namely S1, S2, S3 and S4. These switches comprise of MOSFET. The Vsupply is either a power source or a load made up of bidirectional DC-DC converter. The switches S1, S2, S3 and S4 are controlled in such a way that the module gets connected to pack or disconnects from the pack.

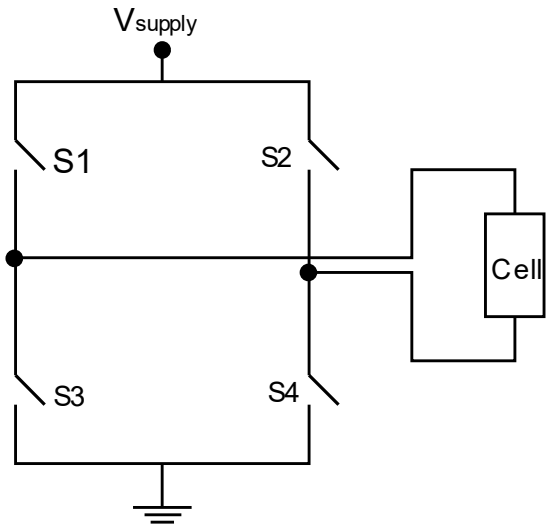

Fig. 0.1 H-bridge architecture interconnecting the modules to form a battery pack under IBIS project from Stellantis

In this configuration, it is possible to control the module voltages or current. Therefore, it is interesting to design a fast charging protocol utilizing voltage or current control strategy so as to be implement in the IBIS architecture.

Hence, in this work, we analyze the impact of shape of the current profiles and potential on the performance of the Li-ion battery. To begin with we introduce this work with extensive literature survey on the various types of fast charging techniques on the Li-ion battery to understand the influence of various parameters followed by characterization of the 18650 cells. Thereafter, considering the influence of the various parameters a fast recharging technique is proposed. The aim of the technique is to reduce the temperature increase at high current recharge and to reduce the overall charging time. Various charging techniques are applied on NMC based 18650 cells of energy and power type. Later, the proposed fast charging results are compared with standard Constant Current – Constant Voltage (CCCV) technique. Furthermore, the ageing tests are carried out to understand the different degradation mechanisms affecting the performance of the cell. Fortunately, there are some studies conducted in the same direction. It will be developed and explained slowly throughout this manuscript in the following way:

Chapter 1 proposes a short overview of the lithium-ion technologies and the materials composition inside battery cell such as the negative and positive electrode, separator, electrolyte and current collector. The principal of operation of lithium-ion battery is also presented.

Different methods of fast-charging protocols alongside with ageing mechanisms and methods to analyse are also described based on a bibliography study.

Chapter 2 describes the experimental setup for this study such the apparatus, materials and the test bench used. Battery cells characteristics that are used in this work are detailed in this chapter. Some methods to determine important parameters and ageing post-mortem procedures are also specified.

Chapter 3 and 4 give the main results obtained during the period of the thesis. Chapter 3 report the results of fast charging using current control methods in term of charging time and temperature elevation while Chapter 4 presents the results of voltage controlled fast charging technique.

Chapter 5 describes the results obtained from the ageing tests. Also, it compares the SoH of various charging protocols. And, finally Chapter 6 depicts the results of the post-mortem analysis of the battery ageing caused by the various fast charging protocol.

The main outcome of this work is filing of 2 patents in collaboration with Stellantis and TOTAL SAFT. The details of the filed patent are as follows:

Reference number : FR20220926	Authors: KHATOKAR AMARNATH, Rakesh ; ROY, Francis ; DOUET, Jean Bernard ; LAHLOU, Anas ; PEUCHANT, Thomas ; HERPE, David ; THIVEL, Pierre Xavier ; LEPRÊTRE, Jean Claude ; BULTEL, Yann
Title: SYSTEME DE CONTROLE DE CHARGE POUR BATTERIE DE TRACTION DE VEHICULE AUTOMOBILE, VEHICULE ET PROCEDE SUR LA BASE D'UN TEL SYSTEME	
Reference number : 2022DI03148	Authors: KHATOKAR AMARNATH, Rakesh ; ROY, Francis ; DOUET, Jean Bernard ; LAHLOU, Anas ; PEUCHANT, Thomas ; HERPE, David ; THIVEL, Pierre Xavier ; LEPRÊTRE, Jean Claude ; BULTEL, Yann
Title: Procédé de charge rapide impulsionnelle à paliers de tension d'amplitude régulée	

Communication:

Pulsed Current Based Fast Charging Methods for Li-Ion Battery
RK Amarnath, PX Thivel, JC Leprêtre, Y Bultel, F Roy, G Thorner; ECS Meeting Abstracts, 456, 2020

Chapter 1. Li battery and application

1. Battery technology and application

A battery is a device that converts stored chemical energy into electrical energy by electrochemical reaction called reduction-oxidation (redox) reaction. In consumer application we can find several types of battery technology based on the nature of material used in both the electrodes. Each technology has its own advantage and drawback based on the application to which it is used for. Batteries are divided into two categories. First being the primary battery or non-rechargeable battery. As the name indicates these batteries cannot be recharged once depleted. The second being the secondary battery or rechargeable battery that can be recharged once depleted. Table 1 depicts some characteristics of several battery technology.

After comparing closely, Li-ion battery is superior in many aspects with respect to others. The high energy density per unit mass and volume compared to other technologies, as shown in Fig. 1.1, makes it a viable solution for high energy demanding application such as portable electronics and transportation sector. In addition, Li-ion battery technology provides higher voltage as compared to nickel-based systems. However, the energy cost of Li-ion technology is comparatively higher due to the utilization of rare earth metals. Nevertheless, Li-ion batteries have gained significant popularity in the transportation sector as they require high energy density, safety, reliability, long cycle life and cost to weight ratio.

Li-ion batteries have performances such as high energy density, high power density and high discharge rate which makes them suitable for various applications including portable transportation vehicle (i.e. electric scooters etc...). Whereas, in individual electric transportation vehicle for example, the Li-ion battery seems to be dominating due to the required high specific energy. As they possess high energy density of approximately three to seven times higher when compared to other technologies which allows manufacturer to build electric vehicles capable of high performance in term of range, speed and acceleration.

The cost of Li-ion batteries is one of the vital issues for transportation applications. The high cost is mainly attributed to the materials which constitute the batteries; positive electrode material represents 40-50% of the overall battery cost, and negative about 20-30% [3].

Apart from safety issues of Li-ion batteries, one of the main setbacks of electric transportation vehicle is the recharging time of these battery packs. The charging procedures require suitable hardware supporting fast charging protocols and monitoring the battery cells to shorten the overall charging time of the vehicles. Nowadays, the charging process still takes a

long time and the problems need to be addressed quickly and thoroughly to cope with the consumers' demands as this type of vehicle starts flooding into the transportation market. Our study is pivoted towards this objective as base foundation.

Table 1 characteristics of several types of battery

Technology	Voltage (V)	Specific Energy density ($Wh.kg^{-1}$)	Volumetric Energy density ($Wh.L^{-1}$)	Advantage	Disadvantage
Lead acid	2	30-40	60-75	Cheaper, widely available	Limited life, heavy
Ni-Cd	1.2	20-60	20-150	Low temperature behavior, reliable	Toxic material, memory effect and high self-discharge rate
Ni-MH	1.2	50-80	90-300	Environment friendly and high energy density	High self-discharge and high internal resistance
Lithium ion with $Li(Ni,Co,Al)O_2$ based positive electrode	3.6	100-160	160-315	High specific energy and low self-discharge rate	Requires additional safety electronics, expensive
Lithium ion with $LiFePO_4$ based positive electrode	3.2	80-120	170-1400	Safe operation, voltage plateau between 20%<SoC<90%	Requires additional safety electronics, expensive
Lithium polymer	3.7	100-158	185-220	Thin profile, light weight and customizable sizes	Expensive and fragile
Potassium ion	3.9V [4]	120-145	280-400	Cheap and environment friendly	
Sodium ion	3.7 [5]	75-165	250-375 [6]	Cheap and environment friendly	Heavier than Lion battery
Lithium ion with $Li(Ni,Co,Mn)O_2$ based positive electrode	3.7	100-180	160-330	High specific energy and low self-discharge rate	Requires additional safety electronics, expensive

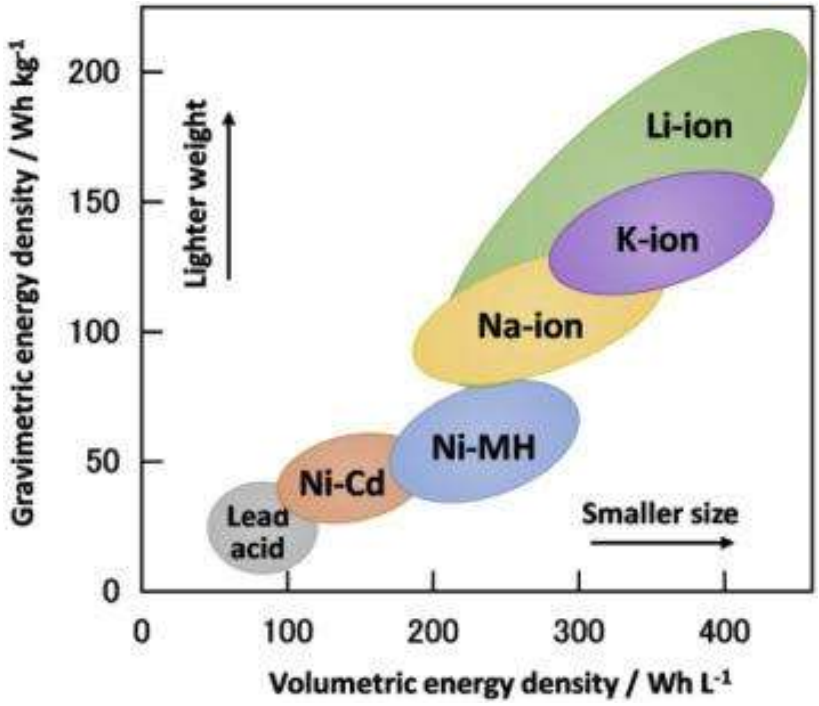

Fig. 1.1 Comparison of various battery technologies [7]

However, within Li-ion battery technology, there are many types of technologies that have been implemented. The main difference between each is the active materials used to construct their electrodes, but all in all the most common feature is the exchange of Li^+ ions. Another difference between them could be the size, shape, electrolyte and/or separator utilized. In this study only, Li-ion technology that are used is presented. Obviously, there are many other technologies gaining the ground these days.

1.1 Li-ion batteries

1.1.1. Construction

The fundamental building blocks of Lithium battery cell is very similar regardless of its chemistry. It consists of four main parts: Negative electrode, positive electrode, separator and electrolyte. Two electrodes positive and negative, each contains an active material and a current collector enabling the connection to the external electrical circuit. These active materials are directly involved in oxidation-reduction reaction which is the driving force of any battery.

These batteries therefore differ according to the material used for construction of active materials as highlighted in Table 1. The electrodes are immersed in an electrolyte made up of lithium salt dissolved in a solvent which allows ionic conduction, necessary for the redox reaction to take place. An example of organic liquid electrolyte is the lithium salt $LiPF_6$ dissolved in an organic solvent mixture i.e. ethylene and dimethyl-carbonate. The separator acts as an electrical insulation between the negative and positive electrode to prevent electron transfer internally at the same time allowing ionic transfer.

1.1.2. Principle of operation

In general, electrochemical cell can represented as [8]:

$$(-)\ [LixM_N]/[M_N]\ //\ electrolyte\ //\ [LixM_P]/[M_P]\ (+)$$

with,

M_P: active positive material, operating at high potential between +2.5 to +5V vs. Li^+/Li

M_N: active negative material, operating at low potential +0.1V to 1.1V vs. Li^+/Li

The operation of a battery cell consists of two redox half-reactions. There are two charge carriers: the Li^+ cations in the electrolyte and electrons in the active materials of both electrodes. These two types of charge carriers are called mobile species[9]. The main mobile species in a Li-ion battery is the Li^+ cation. When the half-reaction at either electrode takes place, this cation is inserted directly into or extracted from the structure of the active material of the electrodes. This insertion and extraction are called as intercalation and deintercalation respectively. The chemical half-reactions which take place at the active material of the negative electrode, M_N and at the active material of the positive electrode, M_P can be written as follows [10]:

At negative electrode:

$$M_N + x.Li^+ + x.\ e^- \underset{discharge}{\overset{charge}{\rightleftharpoons}} Li_xM_N \qquad (1)$$

At positive electrode:

$$Li_xM_P \underset{discharg}{\overset{charge}{\rightleftharpoons}} = M_p + x.Li^+ + x.\ e^- \qquad (2)$$

With x, the number of Li^+ cations inserted or deinserted during charging or discharging.

The overall electrochemical reaction of the system is given by the equation:

$$Li_xM_P + M_N \underset{discharge}{\overset{charge}{\rightleftharpoons}} M_p + Li_xM_N \quad (3)$$

The operating principle of Li-ion battery during charging and discharging is depicted in Fig. 1.2. The charge carriers move in opposite direction from each other during charging and discharging as shown in Fig. 1.2.

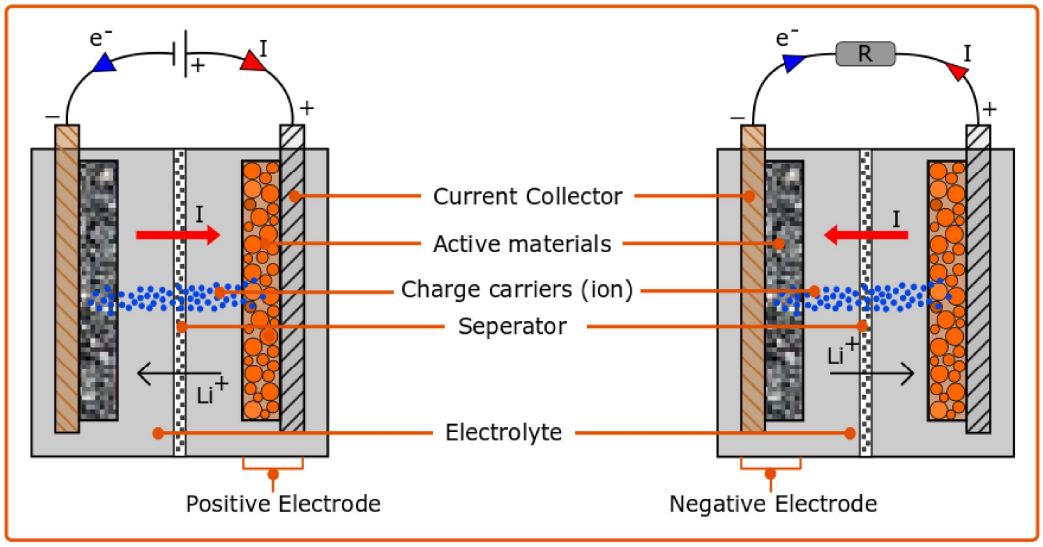

Fig. 1.2 Operating principle of Li-ion battery during charging (left) and discharging (right)

1.1.3. Positive electrode

The positive electrode is the electrode that has higher potential than the negative electrode. There exist numerous active materials for positive electrode. Table 2 highlights the characteristics of some of the commercially available materials with their advantage and drawbacks.

Typically, positive electrodes have 100-200 $mAhg^{-1}$ of specific capacity and 3-5V of average voltage vs Li/Li^+ as shown in Fig. 1.3.

Table 2 characteristics of positive electrode active materials [11]

Materials	Crystal structure	Mass capacity (theoretical/practical) (mAh/g)	Volumetric capacity (theoretical/practical) (mAh/cm^3)	Average potential vs Li^+/Li(V) [Voltage range]	Cost	Advantage	Drawback
NCA $\boldsymbol{LiNi_{0.8}Al_{0.05}Co_{0.15}O_2}$	Layered	279/200	1284/700	3.7V	Medium	High capacity and voltage with excellent performance	Resource limitation for Ni and Co
NMC 111 $\boldsymbol{LiNi_{1/3}Mn_{1/3}Co_{1/3}O_2}$	Layered	280/170	1333/600	3.7V	Medium	High operating voltage with moderate safety	Resource limitation for Ni and Co
LFP $\mathbf{LiFePO_4}$	Olivine	170/165	589	3.4V	Medium	Abundance of Fe, Safest, cycling capability, low toxicity	Low energy density and capacity
LMO $\mathbf{LiMn_2O_4}$	Spinel	148/120	596	4.1V	Low	Abundance of Mn, high operating voltage, moderate safety	Limited cycle life
LCO $\mathbf{LiCoO_2}$	Layered	274/148	1362/550	3.8V	High	High performance	High risk, limited availability of Co

The first material to be widely used as a positive electrode is the lithium cobalt oxide, $LiCoO_2$ (LCO). Unfortunately, Cobalt is a scarce resource which makes less economical to meet the demand. Moreover, LCO is unstable at higher operating temperature and releases oxygen that could easily react with organic electrolyte solvent leading to inflammation with high risk of explosion. Also, Co is toxic in nature. Thus, for these reasons, NMC is developed as a substitution to LCO. This material is moderate in cost, better thermal tolerance and higher specific capacity. Therefore, only Nickel-Manganese-Cobalt (NMC) material for the positive electrode is considered in this study.

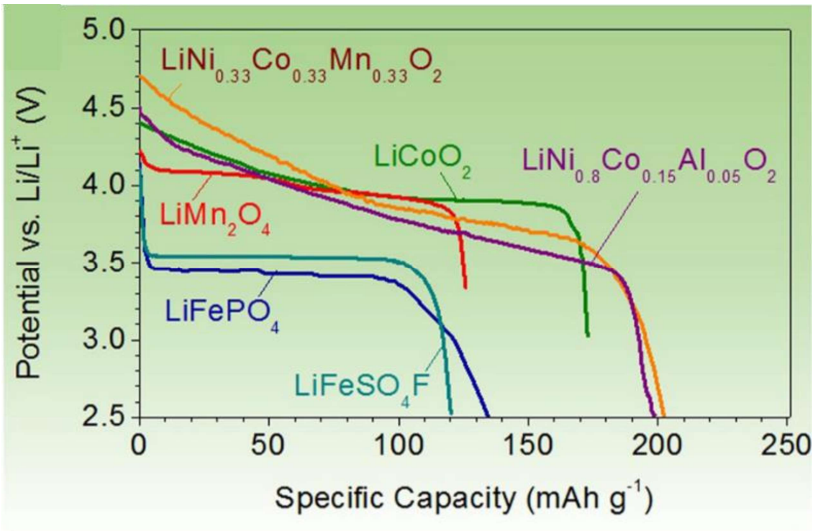

Fig. 1.3 Typical discharge profiles of various positive electrode active material [11]

The general electrochemical reaction for NMC positive electrode is given below:

$$LiNi_{\frac{1}{3}}Mn_{\frac{1}{3}}Co_{\frac{1}{3}}O_2 \underset{discharge}{\overset{charge}{\rightleftarrows}} xLi^+ + xe^- + Li_{1-x}Ni_{\frac{1}{3}}Mn_{\frac{1}{3}}Co_{\frac{1}{3}}O_5 \qquad (4)$$

The NMC material is a combination of one-third nickel, one-third manganese and one-third cobalt, but these ratios can vary from one manufacturer to another. The other combination of NMC material is NMC532, NMC622 and NMC811 representing the relative amounts of each metal in the electrode [12] [13]. NCM811 cells represent an important breakthrough due to the reduced use of cobalt, a scarce raw material, and therefore a significant step forward for the mass production of batteries worldwide currently [14].

1.1.4. Negative electrode

Negative electrode can be made out of different types of materials. Namely, Lithium metal oxide and those based on carbon and silicon as highlighted in Table 3. Each material has its own advantage and drawback.

Table 3 Characteristics of negative electrode active material [11]

Materials	**Graphite LiC_6**	**LTO $Li_4Ti_5O_{12}$**	**Si $LiSi_{22}$**
Crystal structure	Graphene planes	Spinel	Alloying material
Mass capacity (theoretical/practical) (mAh/g)	372/350	175/160	4200
Volumetric capacity (theoretical/practical) (mAh/ cm^{-3})	837	613	9786
Average potential in delithiation (V)	0.1	1.55	0.4
Lithiation potential vs Li^+/ Li(V)	0.07,0.10,0.19	1.55	0.4
Delithiation potential vs Li^+/ Li(V)	0.1,0.14,0.23	1.58	0.31,0.47
Voltage range (V)	1.5 – 0.01	2.0 – 1.0	1.2 – 0.01
Volume charge (%)	10	0.20	270
Cost	Medium	High	Low
Advantage	Abundant, long cycle life	Zero strain material with good cycle life	High capacity and abundant in nature
Drawback	Low energy density and inefficient due to SEI formation	High voltage, low capacity, gassing phenomena	Volume expansion and Li consummation for new SEI

Fig. 1.4 shows the intercalated crystal structure of different types of negative electrode and respective charge-discharge profiles at low charge/discharge rates including hysteresis [11]. The most common negative electrode in commercially available Li-ion batteries is the graphite owing to its abundancy and less cost. The important problem faced by the negative electrode is the formation of dendrites. This is during the charging process when the deposition of lithium ions forms a non-uniform layer. The dendrites can grow during cycling and puncture the separator leading to electrical short circuit.

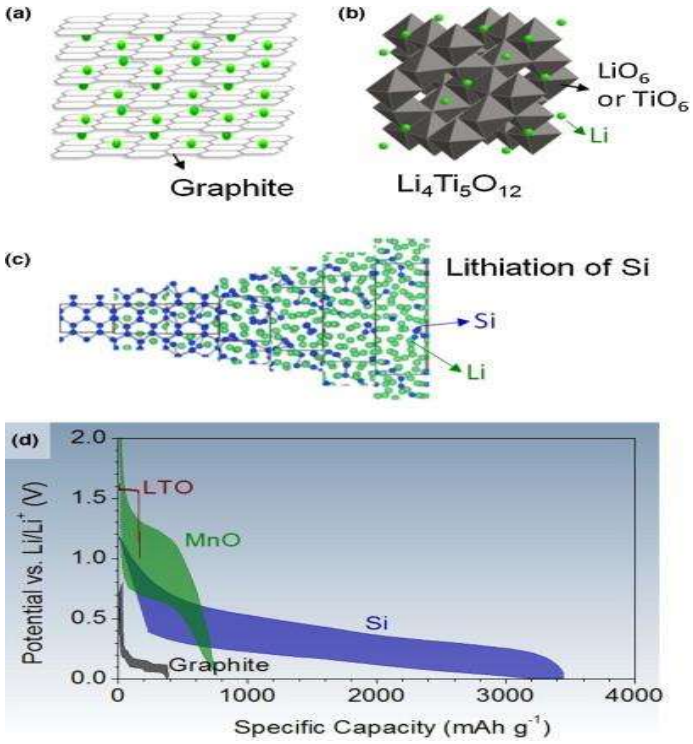

Fig. 1.4 Crystal structure (a) lithiated graphite (b) LTO and (c) Silicon during lithiation (d) charge-discharge profiles with voltage hysteresis for different materials[11].

However, the carbon-based negative electrode is less sensitive to the formation of dendrites when used as lithium intercalation materials. It has a low and flat operating voltage profile at about 0.3V V vs Li+/Li which makes it an excellent contender for negative electrode of lithium battery [15]. Since carbon is used under its crystalline form (graphite), it has a high capacity and stability to receive the Li^+ ions reversibly without altering its physical properties [16]. Graphite is an insertion material in which Li-ions come to lodge into to form intercalation. The structure of graphite allows a high reversibility because it is constituted of multilayered plane of graphene where the lithium ions penetrate right through and form a lithium/carbon intercalation compound $LixC_6$ as shown in Fig. 1.4.

The general electrochemical reaction of negative electrode involving graphite material is given below:

$$xLi^+ + xe^- + 6C \underset{discharge}{\overset{charge}{\rightleftharpoons}} Li_xC_6 \tag{5}$$

The Lithium Titanium dioxide (LTO) electrode is more susceptible for the formation of dendrites. But, high chemical and thermal stability make it a very good alternative for graphite

material. Moreover, it is a promising solution especially for EV application as it allows fast charging. Indeed, this material offers insertion of lithium at a superior electrochemical potential to the one with metallic lithium. Thus, allowing to accept higher current, contrary to the graphite material.

The electrochemical reaction of LTO negative electrode is given below:

$$xLi^+ + xe^- + Li_4Ti_5O_{12} \underset{discharge}{\overset{charge}{\rightleftarrows}} Li_{4+X}Ti_5O_{12} \quad (6)$$

1.1.5. Electrolyte

Electrolyte is a substance within the battery that allows the conduction of ions. Electrolytes can be found in several states such as liquid, solid and semi solid also known as gel electrolyte. The most common state of the electrolyte in commercial batteries is the liquid state. Practically, Li^+-ion does not flow through electrolyte. Instead, it transfers from one solvent molecule to another and reaches either positive or negative electrode based on the process. Therefore, only salts containing lithium ions dissolved in organic solvents can be used as electrolyte in Li-ion battery. As an example, for most common electrolyte is, lithium salt $LiPF_6$ dissolved in organic solvents mixture called ethylene and dimethyl-carbonate. However, this electrolyte has some drawbacks which are rather low ionic conductivity of the order of 10 $mS.cm^{-1}$ at room temperature) and strong in-flammability. The batteries used in this study has similar composition of electrolyte with additional components to increase the durability.

In the case of solid electrolyte used in polymer batteries, the lithium salts are incorporated on to polymer material [17] and after several sequential steps a film is obtained which is to be used directly as a separator. Solid electrolytes have low conductivity in room temperature and require heating for normal battery operation. Whereas, in recent studies this drawback has been addressed by the authors [18] and further improvements are in progress. The first solid electrolytes have been developed for negative electrode cells in lithium metal, in order to restrain the growth of dendrites. They now have also been used for lithium-ion cells. However, a difficulty exists at the solid graphite/electrolyte interface. In fact, the contact is less efficient compared to the liquid electrolyte which can infiltrate inside the pores of the graphite.

In the case of gel electrolytes used in solid-state batteries, they are obtained by dissolving a solid membrane in a solvent. Gel electrolytes provide better contact with the electrodes to

provide sufficient ionic conductivity at room temperature. The main advantage over liquid electrolyte is, it allows flexible packaging as in the case of pouch cells. The main set back of this type of electrolyte is the higher contact resistance than that of its counterpart.

1.1.6. Separator

Another important component in the battery is the separator. It is a monolayer or multi-layered porous polyethylene and polypropylene sheet electrically isolating both the electrodes. It allows ions to flow through them easily and repels the flow of electrons through them. The main properties to be possessed by the separator are listed below [19]:

- Good puncture strength to avoid penetration of electrode material or dendrites to prevent short circuit,
- Very low electronic conductivity.
- Very good wettability which allows the separator to soak with electrolyte for good ionic conductivity.
- Separators have to be chemically stable, i.e they should be inert to both strong reducing and strong oxidising conditions without any signs of degradation.
- Exhibit very good thermal stability without shrinking significantly.

Separators are divided into several types based on their physical and chemical characteristics. They can be molded, woven, nonwoven, microporous, bonded, papers, or laminates. In recent years, there has been a trend to develop solid and gelled electrolytes that combine the electrolyte and separator into a single component. In most batteries, the separators are either made of nonwoven fabrics or microporous polymeric films. Batteries that operate near ambient temperatures usually use separators fabricated from organic materials such as cellulosic papers, polymers, and other fabrics, as well as inorganic materials such as asbestos, glass wool, and SiO_2. In alkaline batteries, the separators used are either regenerated cellulose or microporous polymer films. In general, lithium batteries with organic electrolytes mostly use microporous films.

1.1.7. Current collectors

The current collector is responsible for transferring the electrons from the active material of the electrode to the external circuit. Aluminum is a good candidate for positive electrode. Since, it is very light and good electrical conductor. Also, it reacts with Li-ions at an electrode potential below 0.7V vs Li^+/ Li. Therefore, Copper is a very good choice for negative electrode and is a very good conductor of electricity. The oxidation of copper takes place above 3.2V vs Li^+/Li. Indeed, when cycling the graphite electrode potential is well below 3.2V vs Li+/Li and the positive electrode potential is above 0.7V vs. Li+/Li

1.1.8. Batteries for EV application

As the world is tackling climate change and air pollution and shifting towards green energy, the transportation industry is also replacing conventional energy such as petrol, diesel and gasoline by alternative energy to power their vehicles. Decreased emission, smoother rides and less fluctuation in fuel price is increasing the demand and gaining consumer interest to shift towards electric vehicles (EV's). According to Bloomberg report on global EV forecast, nearly 35 million EV's are expected to be on road by the end of 2035 as compared to 1 million by the end of 2018 [20].

EV's are classified into 3 main categories based on the extent of electricity used for propulsion. Battery electric vehicle (BEV's) are powered solely by electricity. Hybrid electric vehicles (HEV's) are powered by conventional fuel with a small energy storage device on-board and uses an electric motor for propulsion. Whereas, a plug-in hybrid electric vehicle (PHEV's) uses a large energy storage device alongside the conventional fuel and the energy in the storage device can be replenished. Usually, energy storage device for EV's are secondary batteries. Currently, majority of the EV's are being powered by Li-ion batteries owing to its higher energy and volumetric density. Due to recent technological advancement in the battery technology, other batteries such as solid-state or aluminum-ion are also in contender position for EV application. Despite, the technological advancement in Li-ion batteries, it possesses a variety of challenges such as high cost, longer recharging time, safety and construction of recharging infrastructure for any EV auto maker.

The operating cost of EV's relative to ICE is lower. Nevertheless, the high upfront price remains a hurdle for wide EV implementation. The EV's price is mainly dependent on the price of the battery and it needs to be reduced to make them affordable. In addition to cost, recharging time is also an obstacle for customer experience. Currently, EV's take hours to fully recharge and it works for overnight recharge for example. But it is inconvenient for driving over long distance. Recently, the upgrades in the charging infrastructure has allowed to reduce recharging time significantly. However, more efforts are required to meet the goal of recharging 80% △SOC in 20 minutes.

Safety is the critical factor in EV battery design as the battery failure can lead to undesirable consequences. Battery failure is mainly categorized in to two, namely internal and external. On one hand internal failure is due to dendrite growth, thermal runaway and separator damage. On the other hand, the external failure is due to accidents, over charge/ discharge. From an environmental point of view, the LFP battery are very friendly as they are cause minimal pollution to the environment since the materials are easily available. In contrast, NMC battery are less environmentally friendly, due to the mining of materials such as cobalt and magnesium. A possible solution for the later problem is to extract the materials from deep seabed that contains cobalt and other metals abundantly according to International Seabed Authority (ISA). Table 4 Summarizes the requirements for the battery mainly for EV application.

Table 4 Summary of requirements for EV battery [21]

Attributes	**Requirements**	**Chemistry**	
		LFP	**NMC**
Specific energy density	250 – 350 Wh/kg	No	Yes
Volumetric energy density	~750 Wh/L	No	Yes
Range	400 – 600 km	Yes	Yes
Fast Charge	80% △SOC in 20min	Yes	Yes
Life span	10 – 20 years	Yes	No
Performance	190 – 225 Wh/mile	Yes	Yes
Safety	rupture/fire/explosion	Yes	No
Environmental impact	Non toxic	Yes	No
Cost	~$130/kWh	Yes	No

1.2 Terminologies

This section introduces the main terminologies used all over this study in general.

1.2.1. C-rate

C-rate is one of the important factors as far as fast charge is considered. C-rate is a measure of the rate at which the battery is charged or discharged relative to its maximum initial capacity. Normally, C-rate defines the charge or discharge current in Amperes as a proportion of the initial capacity in Ah.

1.2.2. State of charge (SoC)

The State of charge (SoC) is an indication of the quantity of electricity or charge stored in the cell during charging. The SoC is determined as the ratio between the amount of capacity charged and the nominal capacity of the cell itself during charge.

$$SoC = \frac{Q_{charg}\ (t)}{Q_{charg\ \ initial}} * 100 \tag{7}$$

1.2.3. State of Discharge (SoD)

The State of charge (SoD) is an indication of the quantity of electricity or charge extracted from the cell during discharging. The SoD is determined as the ratio between the amount of capacity extracted and the nominal capacity of the cell itself during discharge.

$$SoD = \frac{Q_{discharge}(t)}{Q_{discharge\ initial}} * 100 \tag{8}$$

2. State of the art: Fast Charge

Fast charging for Li-ion battery is not very crucial for day to day use of electronic devices. However, for transportation sector it is of paramount importance. Li-ion batteries still have some serious drawbacks especially for fast charging protocols dedicated for EV application. Mainly, the drawbacks can be related for one part to surface phenomena occurring on the negative and positive electrodes and for another part to structural modifications (expansion-contraction, crystal disorder). In other words, internal degradations of active materials. Moreover, safety is also the main concern during the fast charging for this type of battery especially during high temperature elevation. In regards of fast charging process, the high temperature elevation is unavoidable. Therefore, reliable fast-charging protocols have to be developed. The following sections discusses various charging protocols developed by the researchers globally.

2.1 Constant current constant voltage technique

Constant current Constant Voltage (CC-CV) protocol [22] is the conventional charging technique widely used and recommended by manufacturers. It is also called as two stage charging method as depicted in Fig. 1.5. Under standard operating conditions, the amplitude of constant current and magnitude of maximum cell voltage is dependent on chemistry of the battery being used.

As an example, Fig. 1.5 depicts two stage charging method, in which, the first stage of the charging consists of applying constant current to the battery at a given C-rate until the upper cut-off voltage is reached. After the end of this stage, the battery is charged at constant voltage rate of V_{max} and the current is allowed to decay exponentially. The charging is presumed to be completed upon reaching I cut-off value ($I_{cellmin}$) value [23].

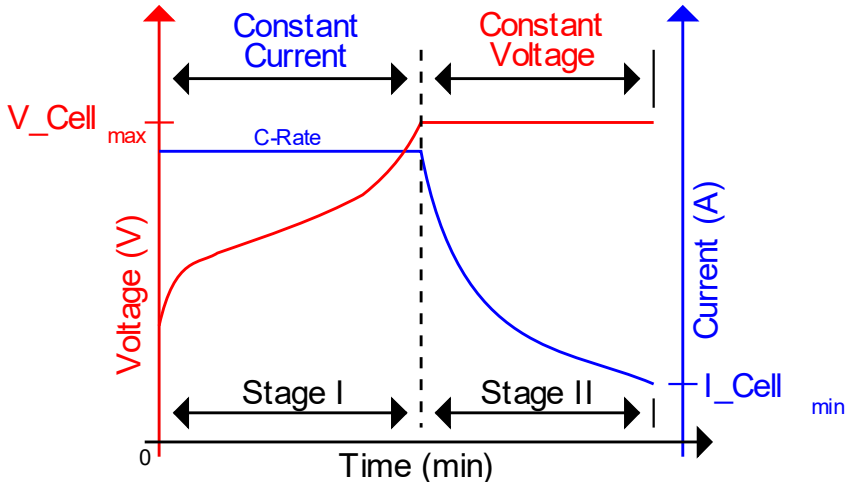

Fig. 1.5 Constant current constant voltage (CCCV) protocol (Blue: Current ; Red : Voltage)

Being simple, the main setback of this technique is the longer recharging time of nearly few hours since, the CV stage prolongs the charging as the current decays. To reduce the charging time, P.H.L. Notten et al. [24] proposed a higher charging rate in the stage 1 in their research and found that for cylindrical US18500 and Prismatic LP423048 with higher charging current, it was possible to recharge one-third of the rated capacity in 5 minutes without inducing any extra degradation. However, higher charging current in the stage 1 reduces charging efficiency due to irreversible heat dissipation known as joule heating. S. S. Zhang et al. [25], in their study on effect of charging protocol on cycle life concluded that, charging at higher C-rates accelerated capacity fade due to loss of Li^+ ions in association with lithium plating onto negative electrode.

P. Keil et al. [26] modified the standard CC-CV protocol by implementing a pulse current stage instead of Constant voltage and compared their results against CC-CV technique. This technique involves charging the battery using constant current at C/2 or higher C rates, Once the higher cut off voltage as prescribed by the manufactured is reached, the charging is continued by applying pulses of current. Typical values for minimum pulse and pause duration lies between 0.1s to 0.5s [27]. Implementing this protocol is simple and cost effective. However, this technique deteriorates the cycle life as charging pulses leads to higher voltage values exceeding the upper cut off voltage for a certain period.

Lopez et al. [1] observed that the total charging time is reduced quite significantly when the charging C-rate increases as shown in Fig. 1.6. For example, about 42% can be saved of charging time for a fast charge at 1.5C-rate compared to the nominal C-rate of C/2 to reach 90%

of charge. Nevertheless, their results show that the energy efficiency of the charging process decreases greatly when the charging C-rate rises, and their result mainly focus on the first stage of charging process which is the CC stage.

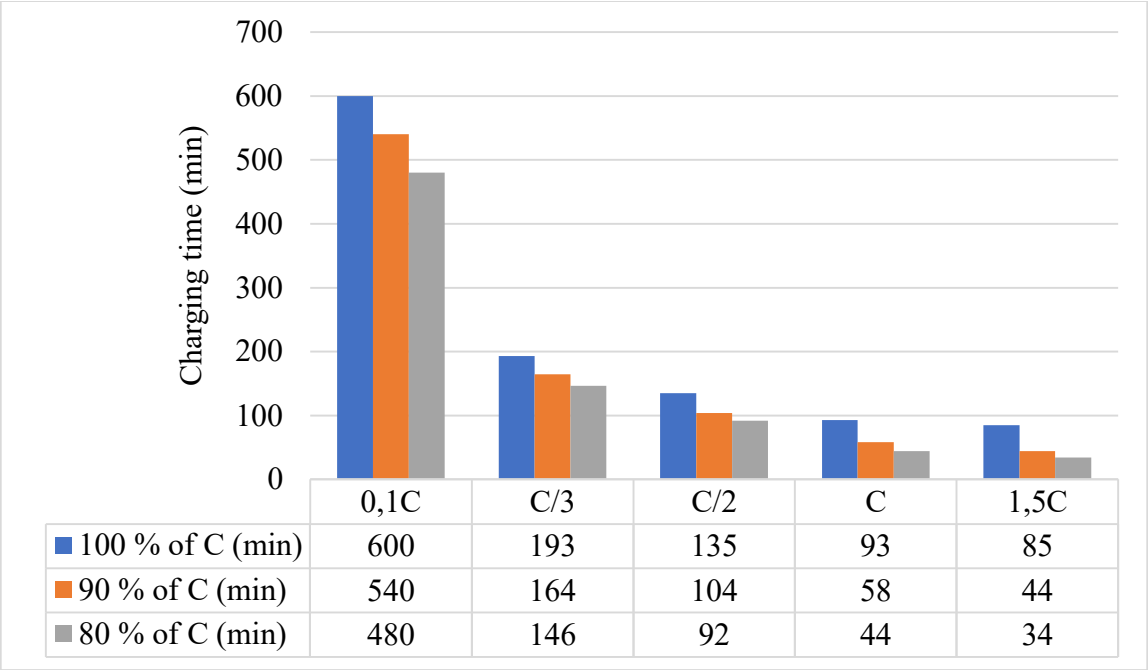

	0,1C	C/3	C/2	C	1,5C
100 % of C (min)	600	193	135	93	85
90 % of C (min)	540	164	104	58	44
80 % of C (min)	480	146	92	44	34

Fig. 1.6 Charging time (minutes) and battery discharged capacity (% C) when different charging rates (from 0.1C to 1.5C) are used in the constant current step: the constant voltage step finishes in each case when battery capacity reaches the desirable value [1]

2.2 Multistage constant current technique

Multistage constant current (MSCC) charging technique is based on multiple constant current stages as shown in Fig. 1.7. with a step wise descending current. The amplitude of current and number of stages depends on the various characteristics of the selected battery [23]. The MSCC is considered to be more advantageous than CC-CV technique because it does not contain CV stage. Therefore, it has drawn the attention of researchers globally. Apart from being simple, MSCC has better performance in terms of charging time and charging efficiency thereby preserving the life span.

Recently, L. Jiang et al [28] proposed a new five stage constant current charging using Taguchi orthogonal array method for optimization of current amplitude. The results show that,

with Taguchi optimization method for five stage constant current improved the charging efficiency by 2.8% and temperature rise is reduced by 2°C as compared with CC-CV technique.

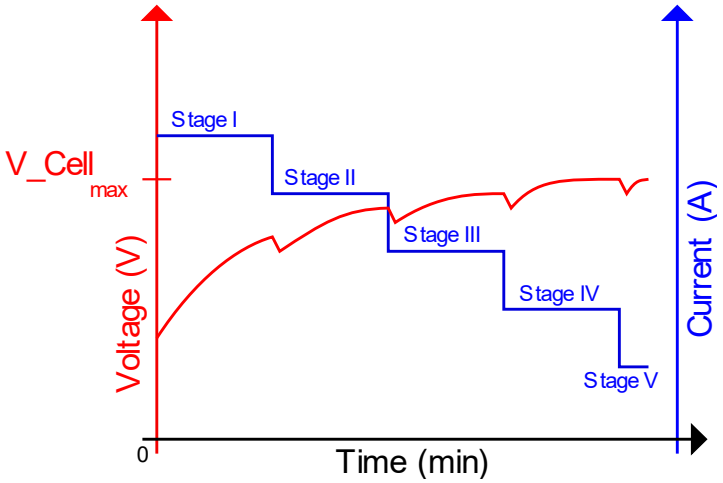

Fig. 1.7 Multistage Constant Current Constant Voltage (MSCCCV) technique

Wu et al. [29] proposed a Dynamic Programming (DP) algorithm to calculate the charging current based on the dynamic model of a first order equivalent circuit. The results show that, the proposed DP algorithm reduces the charging time by 7.66% as compared with CC-CV method. Similarly, the amplitude of current and duration of charging steps has to be estimated by either experimentally [24] by taking into account Internal Resistance (R_i) [30], temperature evolution or by mathematical modelling [31].

On the other hand, Huang et al. improve their fast charging strategies by evaluating and characterizing Li-ion battery [32]. Brief current of charging and discharging interrupts the charging process during constant current period to restrict the hysteresis effect. There's also a fast charging strategy of implying a multistage charging process during the constant current (CC) period [33] and constant voltage (CV) period [34] to reduce the charging time as shown in Fig. 1.8 and Fig. 1.9.

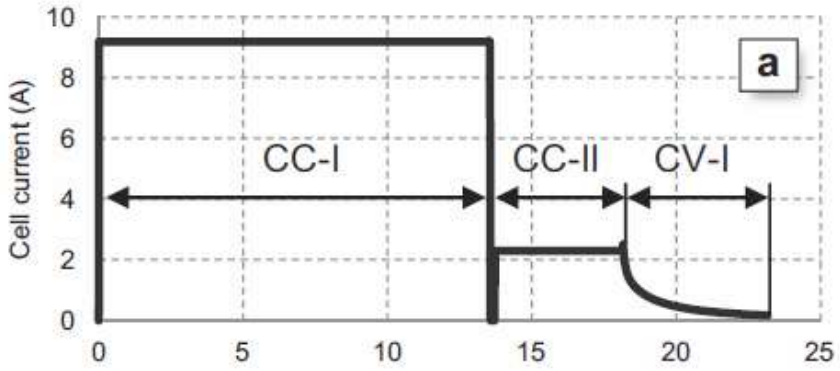

Fig. 1.8 Multistage fast charging strategy during constant current stage [33]

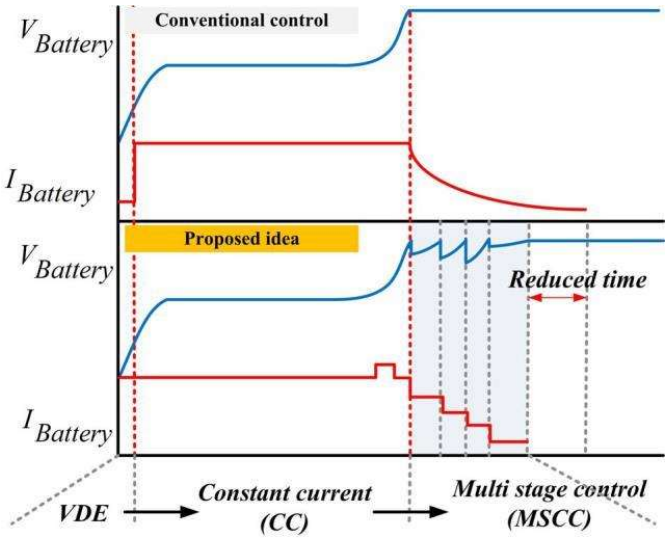

Fig. 1.9 Multistage fast charging strategy during constant voltage stage [34]

2.3 Constant current constant voltage with ohmic drop compensation technique

The "ohmic drop compensation" is a common technic use in electrochemistry, consisting to modify the applied voltage to the cell to compensate the ohmic drop. As well-know, in any electrochemical system, the cell voltage consists of interfacial terms ($V_{interface}$) and volumic ones($V_{volumic}$).

$$V = \sum V_{interface} + \sum V_{volumic} \quad (9)$$

$V_{interface}$ is the voltage between both electrode/electrolyte interfaces at open circuit voltage (OCV) and both overpotentials and given by:

$$\sum V_{interface} = OCV + \eta_{+} - \eta_{-} \quad (10)$$

$V_{volumic}$ is the ohmic drop induced by the charge transport in each volume of cell elements (current collectors, electrolyte, connections). This ohmic drop is proportional to the current applied and considering ohm's law:

$$\sum V_{volumic} \approx R_i * I \quad (11)$$

Where R_i is the internal resistance of the cell.

Then, the applied voltage to the cell is given by

$$V_{applied} = V_{cell} + R_i I \quad (12)$$

The use of Ohmic drop Compensation for fast charge was developed at LEPMI by the authors of [8]. Ohmic Drop Compensation (ODC) technique [8] consist of compensating the ohmic drop of the battery voltage due to the internal resistance R_i of the cell at the end of stage I by changing the upper cut off voltage limit as shown in the Fig. 1.10. In this method the ohmic-drop of the battery is compensated by changing the upper-bound voltage limit at the end of CC stage and this new upper bound voltage limit V'_{max} has to respect the maximum interfacial voltage value whatever the current rate (I), especially, at the end of the CC stage. In order to avoid the risk of side reactions in the case of overcompensation, a rate of compensation, α, is defined as a percentage of the internal resistance measured of the battery. In this condition, the new upper-bound limit voltage is given by Equation 13:

$$V'_{max} = V_{cell\,max} + \alpha * R_i * I \quad (13)$$

α being the compensation rate and $V_{cell\,max}$ is the upper-bound limit voltage from prescribed by the manufacturer.

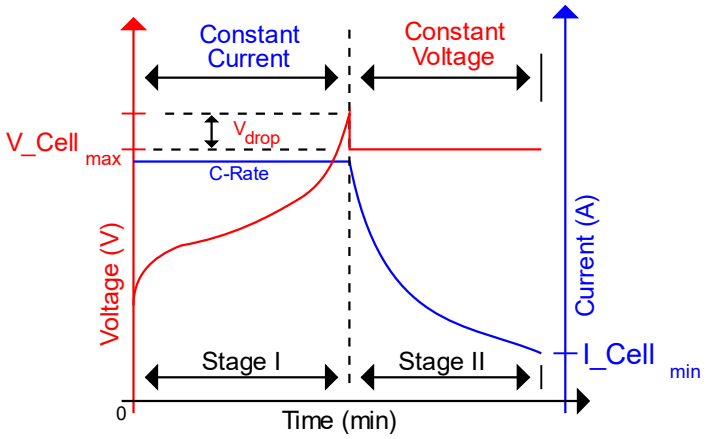

Fig. 1.10 CCCV technique with Ohmic Drop Compensation (ODC) technique [8]

The charging stage follows the conventional constant voltage, CV stage where the voltage is maintained at the upper-bound limit voltage from manufacturer, $V_{cell\ max}$. Although there is very less articles can be found on this technique.

Noh et al. [8] conducted their studies on ohmic drop compensation at the end of CC stage to investigate the impact of this technique on the life cycle in order to improve the charging time and found that, the rate of compensation, α (Equation (7) of [8]) does not have any impact at 6C rate on LTO/LFP battery. In contrary, for the same battery chemistry the total charging time seems to decrease quite linearly when the compensation rate rises at 11C-rate Fig. 1.11. Nevertheless, their study concluded with a 6C charge and 57% compensation, it takes 11minutes for C/LFP battery to reach of 95% SoC allowing 1500 cycles before reaching 80% of State of Health (SoH).

Lin et al. [36] proposed a charger with smooth control and built in external resistance compensator (BRC) to extend the stage I by 40% thereby reducing the overall charging time. The developed charger estimates the external resistance comprising of cable and connections dynamically to extend the CC stage resulting in shorter CV stage. The compensation is performed for a short delay as shown in Fig. 1.12. The results establish improvements in the charging time by means of external resistance compensation.

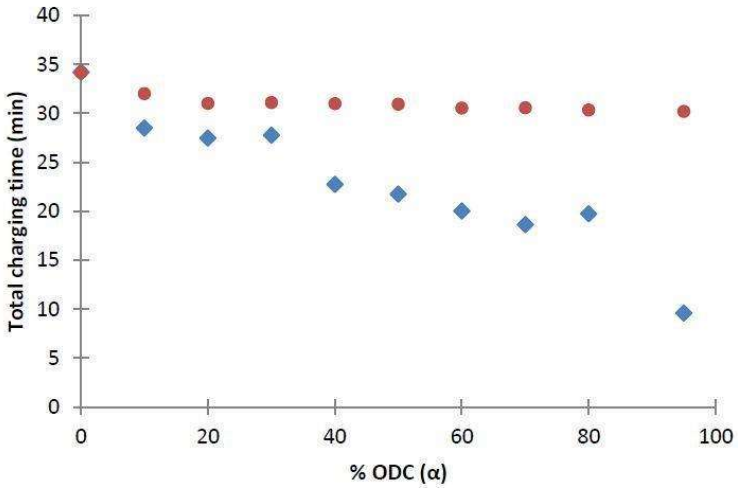

Fig. 1.11 Total charging time for different compensation rate (α) for LTO/LFP battery at 6Crate (red) and 11 C-rate (blue)

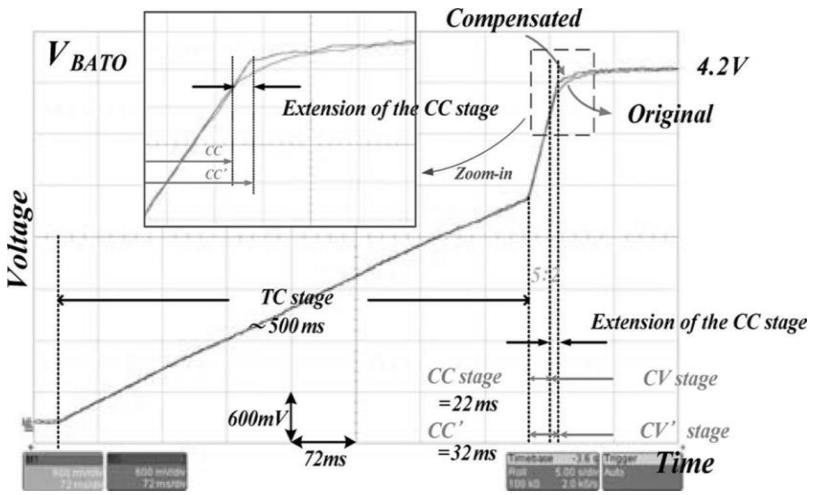

Fig. 1.12 Waveforms of the voltage with and without the BRC technique. The CC stage of the original design is extended to the CC' stage with the BRC design [36]

The ODC technique can also be applied to the battery during discharge [35]. The authors of [35] demonstrate the application of ODC technique for high current discharge.

2.4 Current based pulse charging technique

Pulse charging has shown a good overall performance, but the optimal configuration still challenges the researches globally as various parameters such as duty cycle [37], rate of intercalation [38] play a vital role in charging using pulse technique. Basically, Pulse charging consists of charging at constant current rate for a duration t_c with intermediate interruption of

current for certain period called relaxation period t_r. The sequence of the pulse can vary depending upon the pulse amplitude and duration as shown in Fig. 1.13.

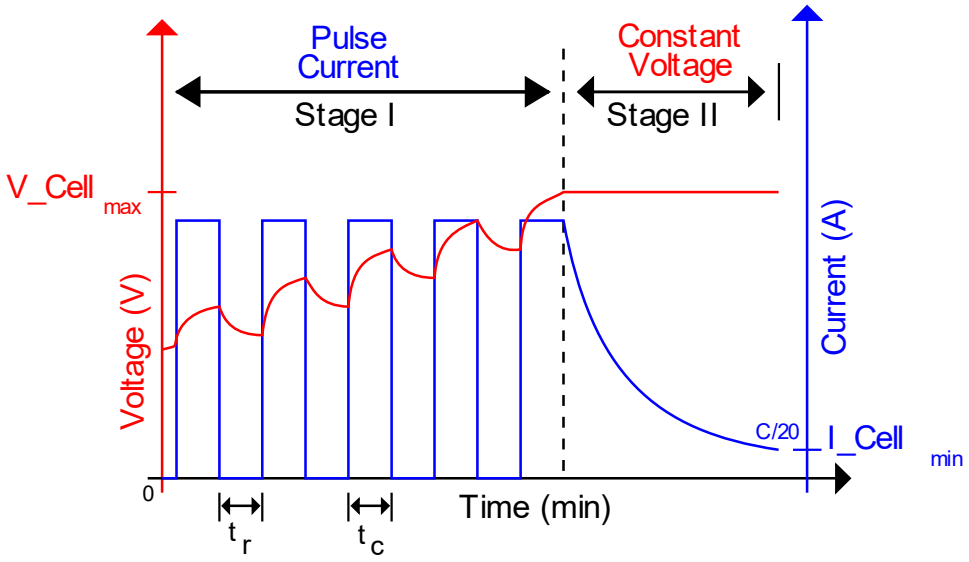

Fig. 1.13 Current pulse charging technique

The aim of this technique is to reduce the polarisation concentration thereby mitigating the lithium plating enabling better performance [39]. The pulse charging is based on constant current steps of short duration followed by relaxation periods. The sequences can vary depending on the pulse amplitude and duration, as well as on the relaxation time as shown in Fig. 1.14. This method is highly recommended for fast-charging purpose as the current imposed is really high. Pauses are required to reduce or prevent the metallic lithium formation. The metallic lithium formation can greatly interfere with the charging process according to Purushothaman et al [38]. However, their studies only focus on the empirical calculation and simulation without any real experiment implementation.

Recently, Savoye et al [40] conducted their studies on the impact of periodic current pulses of frequencies ranging from 200mHz to 100Hz on LFP batteries. Nevertheless, they found that the current pulse profiles, in comparison to constant current profiles on the basis of identical mean current was not advantageous on the cell performance. This is due to the high form factor F, which is the ratio of RMS current and the mean current. RMS is defined as the square root of the arithmetic mean square.

Globally, researchers have used various approaches to find the best parameters influencing the charging time and aging of the batteries. In [37] the authors have used Taguchi orthogonal

array approach to determine the factor and factor levels affecting the cycle life of Lithium-ion Polymer(LiPo) batteries. Whereas, in [41] the authors used numerical simulation to investigate the effect of pulse charging on LFP batteries. The results show that the relaxation duration of 25s helps to alleviate the capacity fade in comparison with CC-CV technique even when the intensity of current is as high as 3C. In a nutshell, pulse charging technique is completely dependent on the battery technology and it is a trade-off between charging time and capacity retention in practical application.

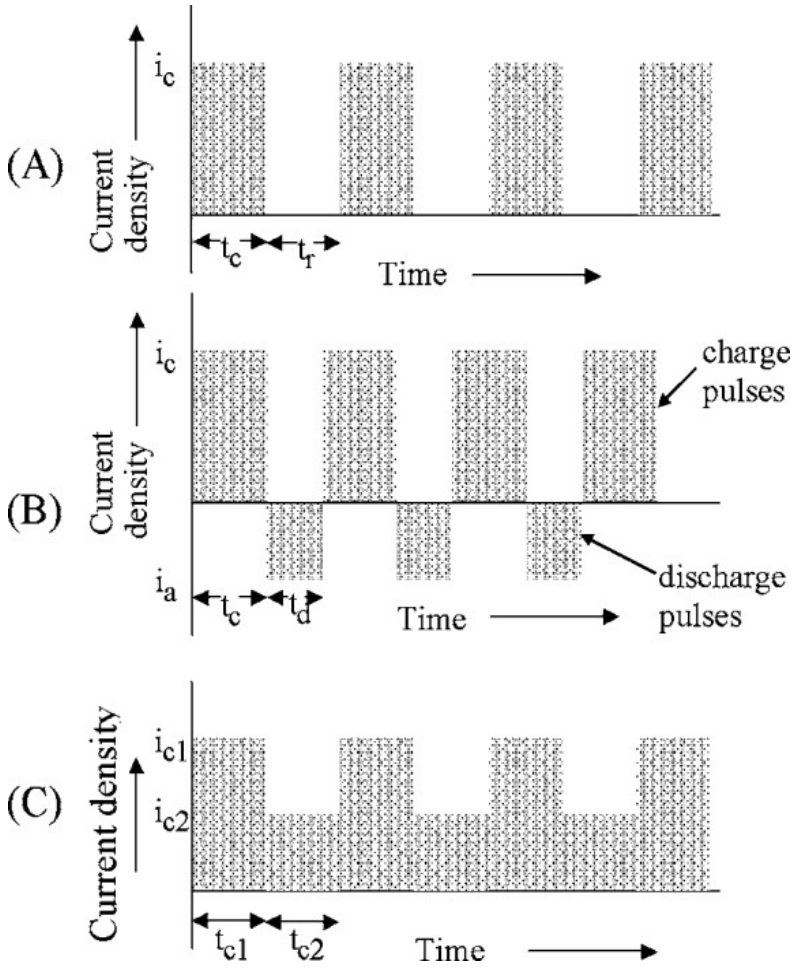

Fig. 1.14 Schematic of fast charging process of different pulse sequences. (A) Constant amplitude pulsed current interspersed with identical rest periods; (B) constant amplitude pulsed current interspersed with alternating constant amplitude discharge pulses; and (C) pulsed current consisting of a sequence of different amplitudes charge current density pulses [38]

2.5 Varying current technique

The varying current technique consists of dynamically changing the intensity of the charging current based on parameters obtained by numerical models and various assumptions on the parameters including State of Charge (SoC) [42], rate of intercalation of the Li-ion into the negative electrode and impedance of the cell. Recently, Cho et al. [43] demonstrated the impact of variable current technique on high power NCA based cells considering the SoC and internal resistance of the cell. This technique helped to maintain the power loss by reducing the temperature elevation of the battery.

With time, complex techniques can be used to improve the performance and reduce the charging time of Li-ion batteries. The recent advancement in the development of chargers, they can automatically modify the charging profiles by online calculation of Ri, SoC and State of Health (SoH). However, to achieve this, adding expensive complex control is required and increases the experimental resources.

2.6 Sinusoidal current charging technique

Sinusoidal ripple current (SRC) charging is a modified version of pulse charging technique, wherein, conventional square current pulse is replaced by frequency dependent sinusoidal current waveform to recharge the battery. This technique is intended to operate in smaller impedance region in accordance with the frequency so as to reduce the energy loss in the form of heat during charging. The authors of [44] and [45] demonstrated that a smaller charge transfer resistance resulted in better electrochemical reaction resulting in maximum energy transfer efficiency due to smaller ohmic resistance.

Chen et al. [46] used impedance analysis to explore the minimum impedance frequency and compared the SRC with square pulsed current and CC-CV technique ranging from 1Hz to 10kHz. Their results showed the SRC charging technique at lowest impedance frequency improved the charging time by 17% and reduced the temperature by 45.8% in comparison with CC-CV technique. Whereas, in comparison with square pulsed technique the charging time and rising temperature improved by 0.24% and 16.47% respectively. Hence, this method can reduce the charging time and energy loss significantly. Also, further improvements can be made to this technique by using empirical methodologies.

Ghassemi et al. [47] studied the effects of AC perturbation on degradation mechanism of LFP cells by superimposing sinusoidal AC on DC ranging from 0.1Hz to 1kHz. From the results, they concluded that the low frequency AC accelerates the degradation rate and was directly linked with Loss of Lithium inventory (LLI) and Loss of Active material (LAM) as a result of faradic reactions on longer time scales. Whereas, the high frequency AC has negligible ageing effects on the cells. This was due to reduced charge transfer resistance resulting in improved active material utilization.

2.7 Conclusion

Results from the numerous literatures reveal that optimum charging technique for Li-ion battery is complex and there exist no universal solution to reduce the charging time without accelerating the aging. The complex nature is due to the fact that, the Li-ion batteries are very much diverse in terms of chemistries and construction. So far, many researchers around the globe have contribute to the various techniques whether it is simple or complex but the influence of shape of the current waveform for given set of parameters is unexplored to date. Also, the impact of voltage control protocols on the cell performance is less explored. Therefore, the aim of this work is to experimentally investigate the impact of shape of the current wave and voltage control protocols on NMC based Li-ion battery and evaluate the performance.

3. State of the art: Ageing

3.1 Introduction

Since the commercialization of lithium-ion (Li-ion) batteries, significant improvements in energy density and power capability have made Li-ion batteries the preferred solution for low carbon mobility [48]. However, the change in behaviour of Li-ion batteries over a vehicle lifetime can have a significant detrimental effect on vehicle performance and lifetime [49]. Exploring the causes of battery ageing and developing mitigation strategies to avoid premature degradation is therefore of paramount importance. Li-ion batteries undergo complex electrochemical and mechanical degradation. This complexity is pronounced in electric vehicle

application, where highly demanding cycles of operation and varying environmental conditions lead to non-trivial interactions of ageing stress factors. This work presents the framework of various ageing phenomenon's occurring in Li-ion battery.

Understanding battery ageing is convoluted since many factors from environmental conditions to vehicle utilization interact to generate different ageing effects [2]. Battery degradation is accelerated with factors that include but are not limited to the frequency of cycling, large change in state of charge (SoC), large current magnitudes during both charge and discharge, high temperatures, and over voltage exposure. The resulting physical degradation can broadly manifest itself in two ways: capacity fade that affects the range of the vehicle and power fade, which is the increase in the internal resistance or impedance of the cell and limits the power capability of the system and decreases the efficiency of the vehicle.

Li-ion battery is mainly exposed to two types of ageing namely calendar ageing and cyclic ageing. The calendar ageing corresponds to the phenomena and the consequences of battery storages. On the contrary, cyclic ageing is associated with the impact of battery charge or discharge profiles.

An overview of various degradation methods is given in Fig. 1.15

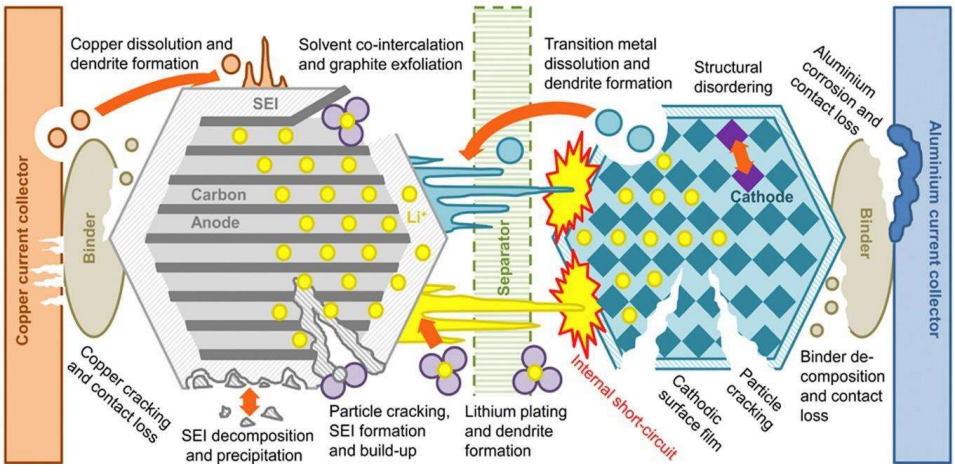

Fig. 1.15 Degradation mechanism inside Li-ion battery [50]

3.2 Calendar ageing

Calendar ageing is the irreversible ageing which is proportion to the lost capacity during a storage [51]. Self-discharge rate varies highly according to storage conditions. Hence, effects

occurring within the battery can be accelerated or slowed depending on the storage temperatures [52] and storage SoC [53]. Fig. 1.16 depicts the degradation associated with calendar ageing.

Indeed, each of these variables alter together the capacity and the internal resistance with respect to time nonlinearly. Studies evocate the more restrictive effect of high SOC and high temperature. Such results are just an interpretation from few experiences, and it remains to understand the complete effect of the combination of these two variables on the calendar ageing. For automotive application, calendar ageing corresponds to vehicle in parking mode. For example, when the vehicle is parked at airport for several weeks, then the battery is subjected to calendar ageing.

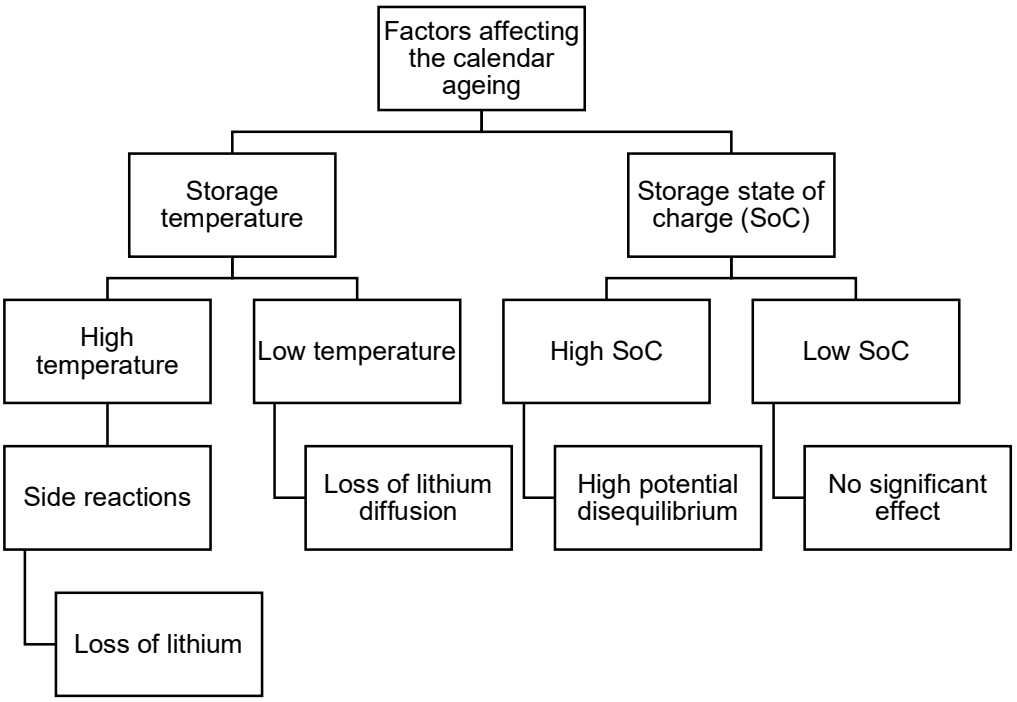

Fig. 1.16 Factors affecting the calendar ageing [54] [55]

3.3 Cyclic ageing

The cyclic ageing is due to the battery being subjected to charge and discharge cycles. The main accelerating factors of battery degradation are temperature, cycle number, SoC, current and voltage. The effects of these factors-based on literature are presented below using flow charts as shown in Fig. 1.17.

Typically, parasitic reactions lead to film formation while mechanical fatigue leads to structural degradation.

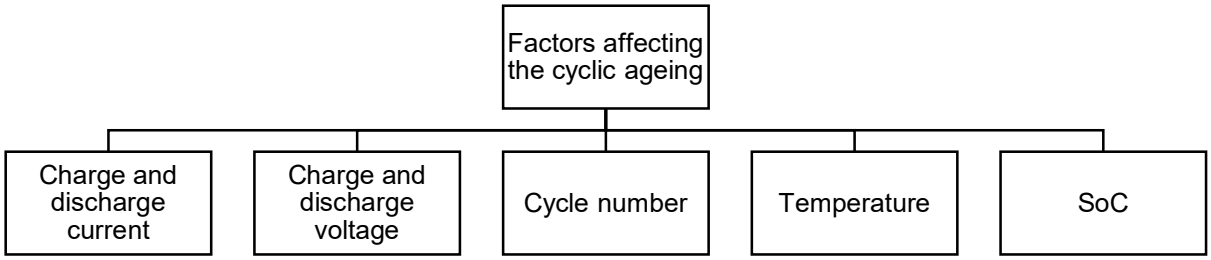

Fig. 1.17 Factors affecting the cyclic ageing [56]

The effects of high temperature are depicted in Fig. 1.18. The most notable cause of degradation attributed with elevated temperatures is electrolyte decomposition reactions at the negative electrode/electrolyte boundary which consume lithium ions—resulting in capacity fade—subsequently forming a solid electrolyte interphase (SEI) layer on the negative electrode surface. The SEI then acts as an impediment to ionic diffusion leading to power fade [57].

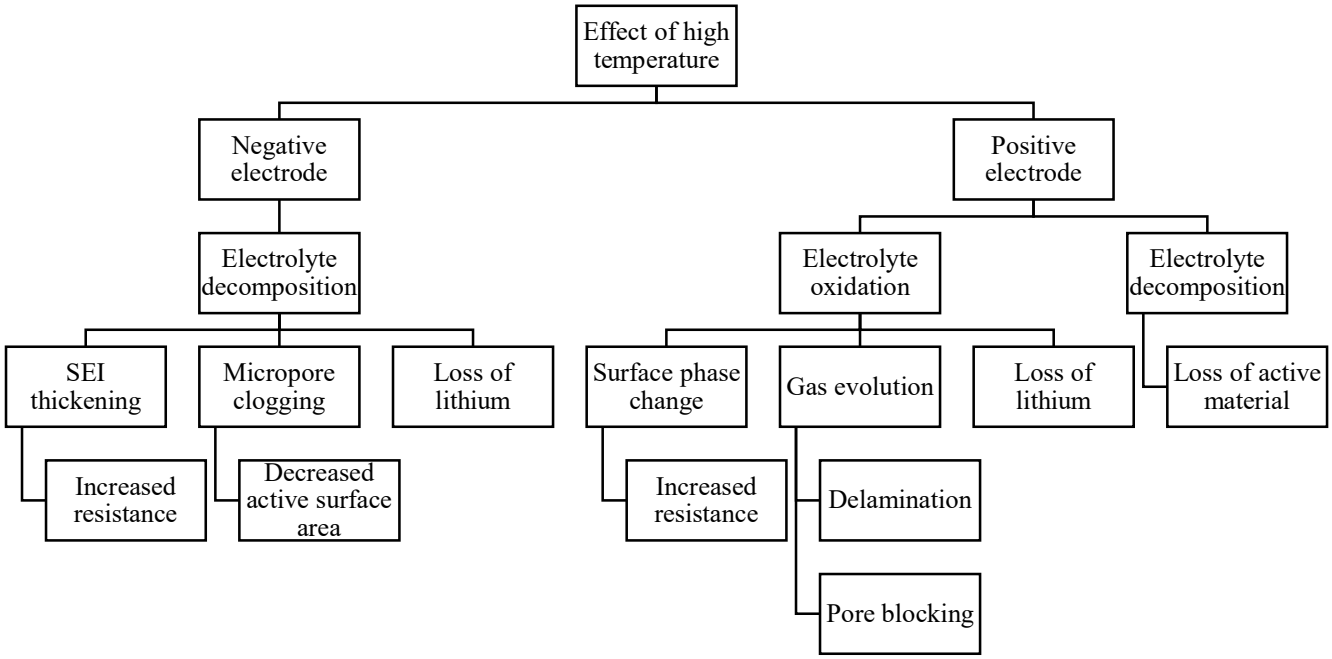

Fig. 1.18 Effect of high temperature on ageing [57]

At low temperatures lithium metal deposition is the principle degrader [57]. Lithium deposit takes place onto the electrode surface (deposition) when the proximity of the negative electrode reversible potential is close to that of the lithium deposition potential. Lithium plating

is exacerbated by conditions where Li intercalation kinetics are hindered. In addition to low operating temperatures as depicted in Fig. 1.19, heterogeneous current distribution and high charging rates also lead to Li plating.

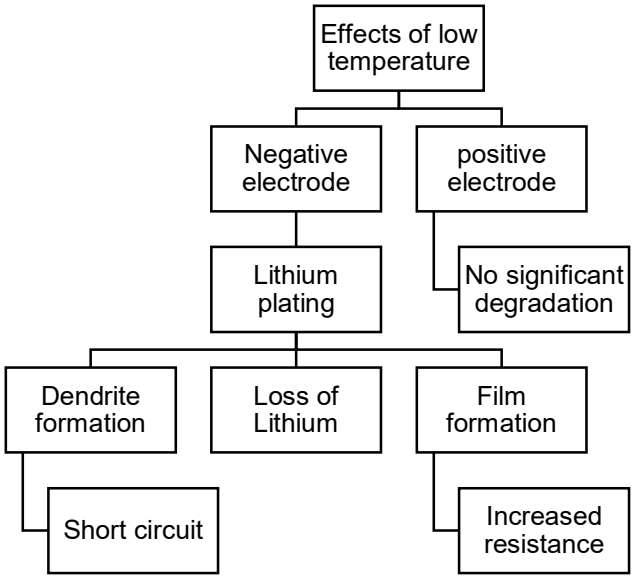

Fig. 1.19 Effect of low temperature on ageing [57]

Fig. 1.20 represents degradation attributed by large cycling currents [58].

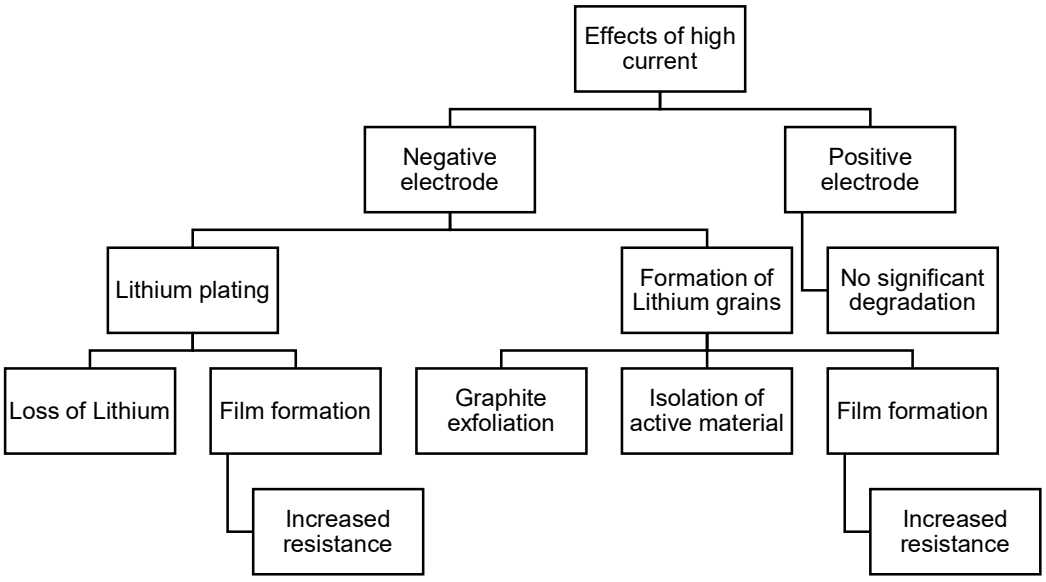

Fig. 1.20 Effect of high current on ageing [58].

Even under moderate conditions the battery is expected to degrade thorough the formation of SEI as time passes and mechanically as the battery is cycled. Fig. 1.21 highlights the expected degradation resulting from large amounts of cycling [59].

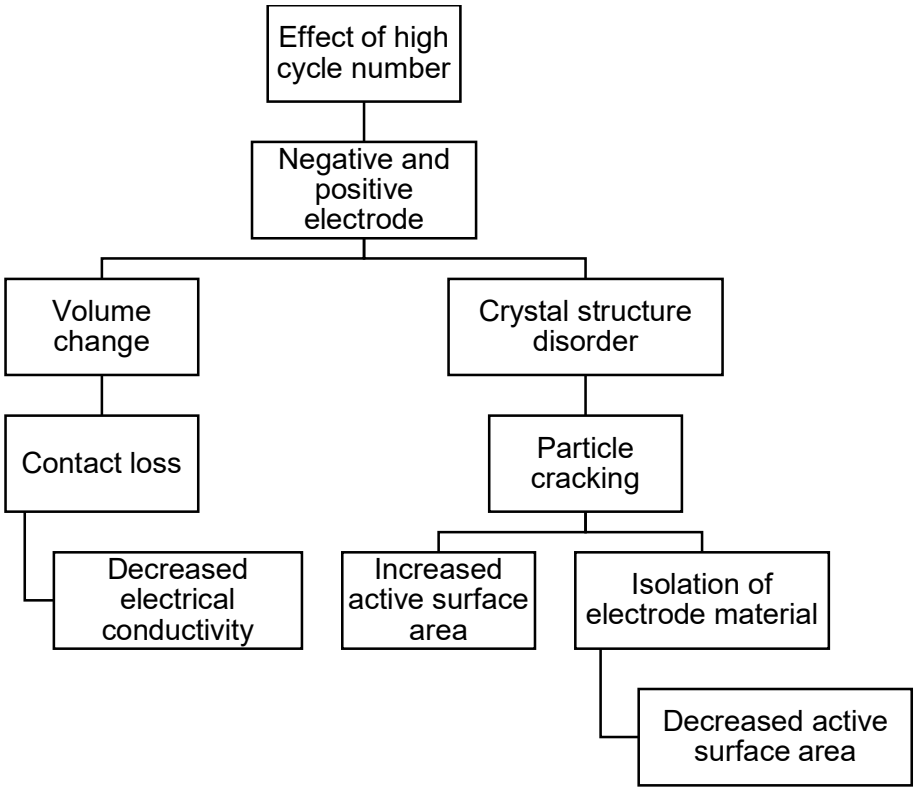

Fig. 1.21 Effect of cycle number on ageing [59]

An ageing study was performed by Fleury et al. [60] on the aged batteries as presented by Noh et al. [8]. The X-ray tomography and *post-mortem* analysis on C/LFP batteries revealed jelly roll deformations as shown in Fig. 1.22. and delamination of graphite electrode leading to the loss of active material due to fast charging using ODC method.

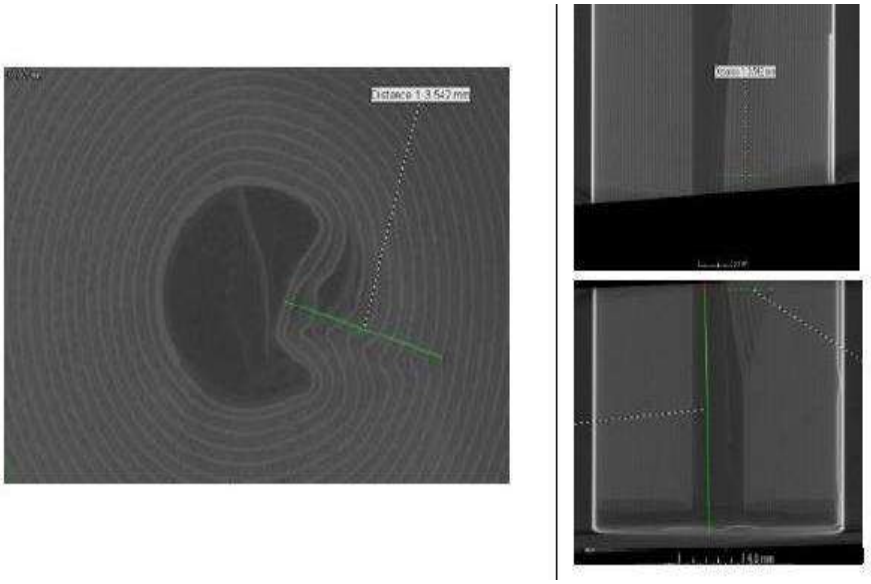

Fig. 1.22 X-Ray tomography of 6 C- high level ODC aged cell [60]

Whatever the routes are, the capacity or power fade of the battery primarily originated from high temperature elevation or/and high load of current and voltage. These degradations could also lead to the increase of the internal resistance of the battery.

3.4 Physio chemical analysis

An overview of individual steps in *post-mortem* analysis is given in Fig. 1.23. *Post-mortem* analysis is a destructive technique used to analyse the ageing mechanism by disassembling the cell completely. Therefore, before disassembly of the cells, non-destructive characterization methods such as incremental capacity analysis (ICA), Electrochemical impedance spectroscopy (EIS) are used to obtain ageing information. Although non-invasive electrochemical methods are powerful tools to get information on aging mechanisms, a direct observation of chemical changes is only possible by *post-mortem* analysis.

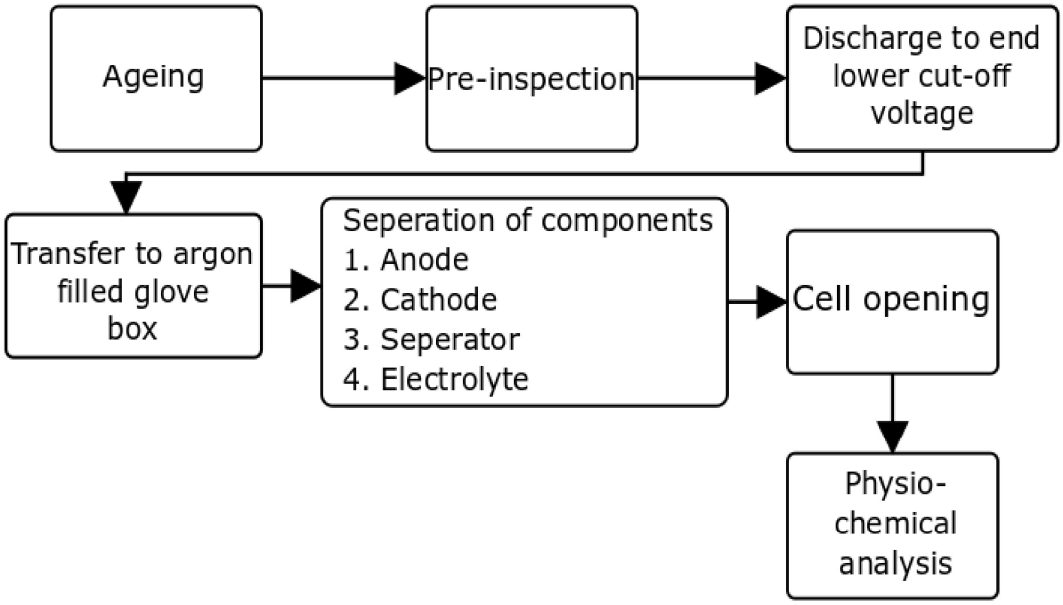

Fig. 1.23 Flow chart for disassembly of Li-ion cell and post-mortem analysis [61]

In the literature various physio-chemical characterization methods are described to find the evidence and possibilities for observing the specific degradation mechanisms. Fig. 1.24 [61] shows a scheme of the main cell components and corresponding available physio-chemical analysis methods to characterize them. Samples can originate from negative electrode, positive electrode, separator, current collector, or electrolyte, however, only a positive electrode is shown as an example in Fig. 1.24 to simplify matters. It can be seen from Fig. 1.24 that different parts of a solid sample can be distinguished: electrode surface, bulk, cross-sections, and different analysis methods can be assigned to them, respectively. The reasons for surface sensitivity of analysis methods are related to the physical nature of the involved types of radiation or particles. A simplified overview of physical/chemical principles (irradiation by and /or detection of electrons e-, electromagnetic radiation / photons hv, neutral particles, and ions) is shown in Fig. 1.25. These are briefly explained for each method in the Fig. 1.26.

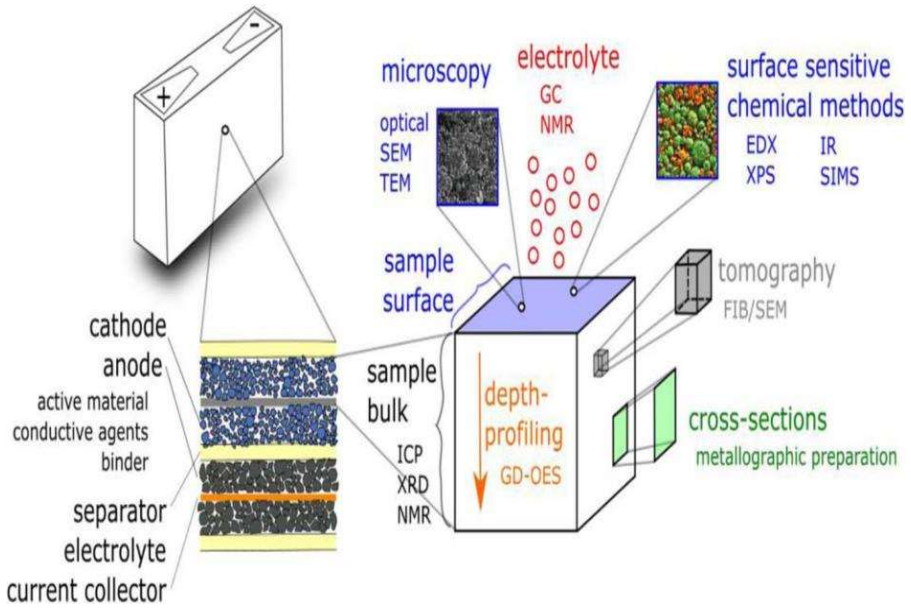

Fig. 1.24 Overview of inside components in a Li-ion battery and physio-chemical analysis methods [61]

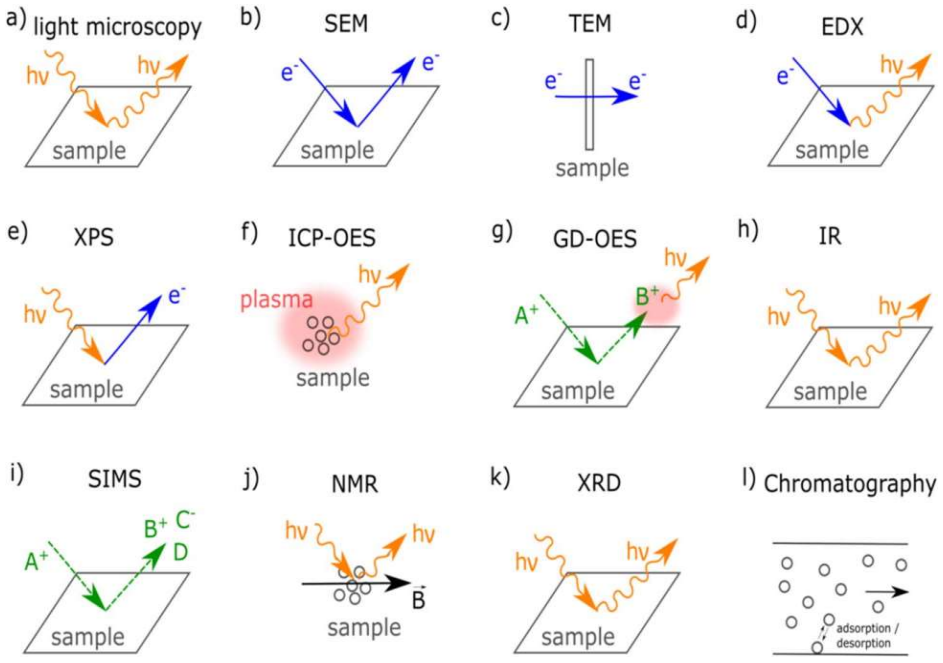

Fig. 1.25 a)-k) simplified schematics of detected particles in different analysis methods. Electromagnetic radiation hv corresponds to visible light in (a), (f), (g), X-rays in (d), (e), (k) and to radio waves in (j). In (b), the emitted electrons can be distinguished between backscattered electrons, Auges electrons, and secondary electrons. H) IR in reflectance mode. 1) Principle of separation of the components in a mixture in chromatography. The circles and the lines represent the sample molecules and the stationary phase, respectively [61].

Typical *physio-chemical* analysis methods for cell components and the aging mechanisms they revealed are discussed Fig. 1.26.

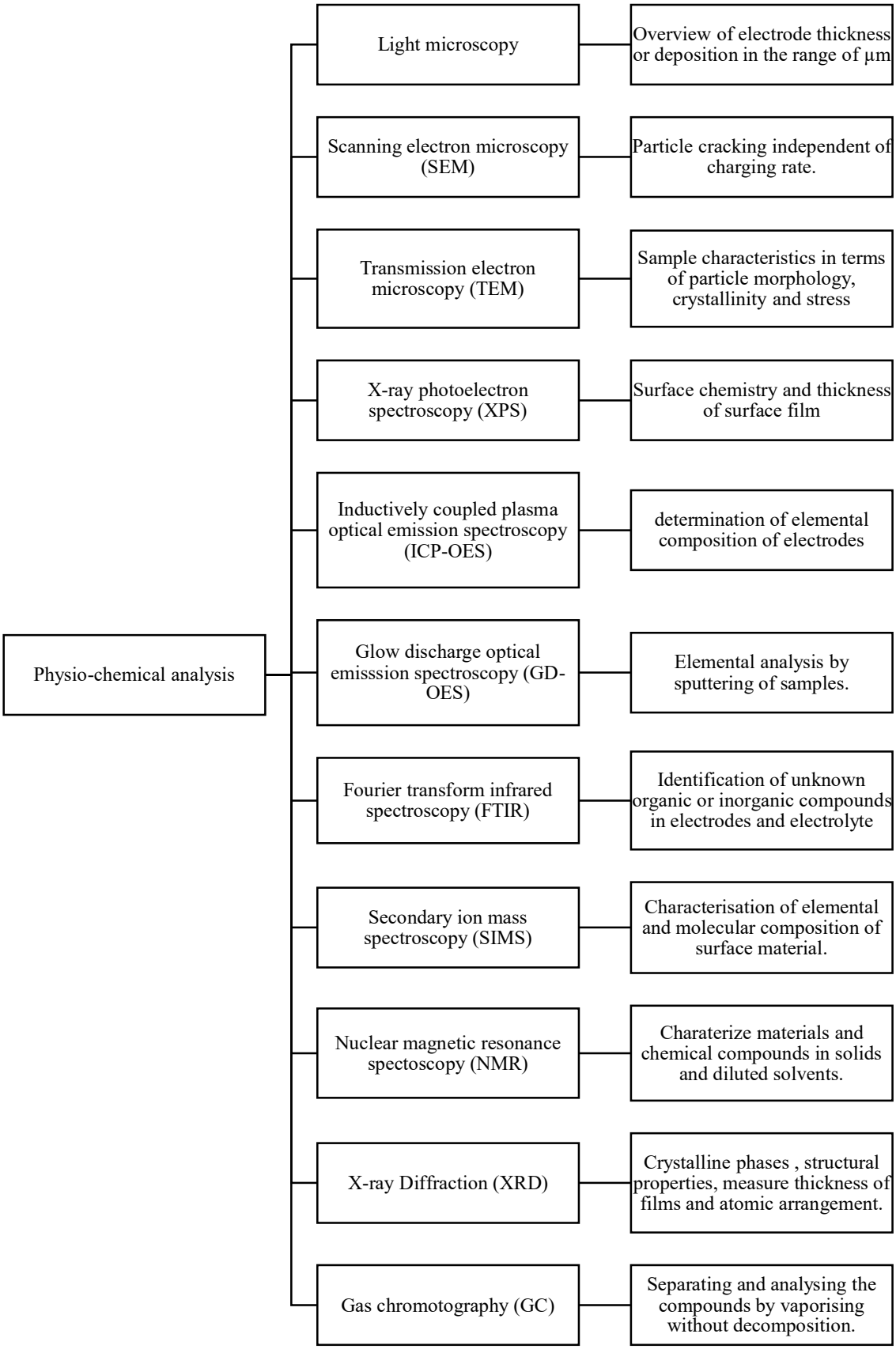

Fig. 1.26 Post-mortem analysis methods [61]

3.5 State of Health estimation

The state of health (SOH) of a battery is an indication of degradation of the battery. SoH estimation of Li-ion batteries as accurately as possible is major challenge which every automaker is solving currently. Indeed, it is important from the customers point of view to avail this information in order to timely replace the battery and reduce economic losses [62]. Also, it provides critical information about, life time, performance and allows better energy management. Extensive research on methods to estimate the battery SoH can be found in literatures. But, not all the methods can be implemented in real-time automotive application.

Fig. 1.27 illustrates the methods used to estimate SoH [63]. The SoH estimation methods can be divided into 3 categories, Experimental, model based and machine learning based methods. The latter methods are a combination of experimental and model-based methods.

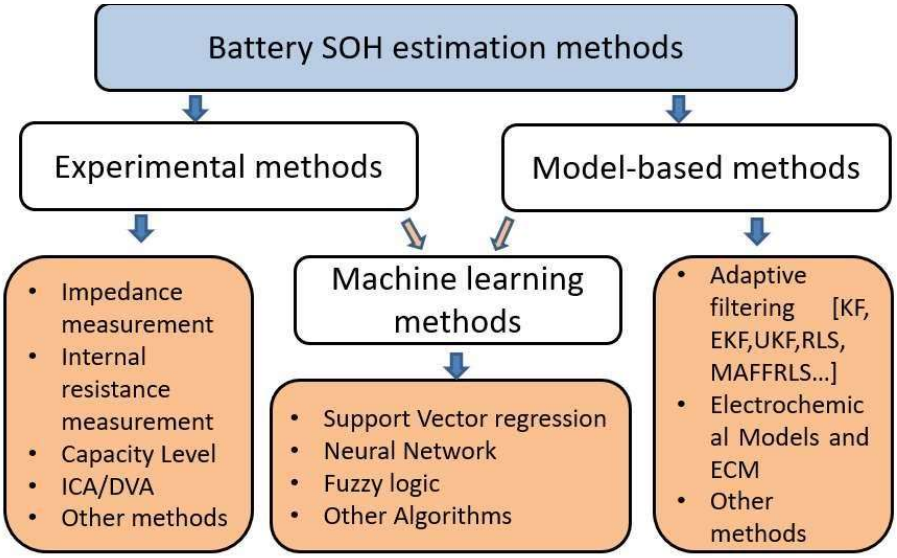

Fig. 1.27 SoH estimation methods[63]

In this thesis, the main thrust is given to experimental based SoH estimation methods. Namely, SoH and Incremental capacity analysis (ICA) is used as the prime methods.

For the SoH, there is two ways to calculate it. One based on the capacity and another based on resistance.

For, the capacity method the ratio between the actual discharge capacity and the initial discharge capacity of the cell is taken to estimate the SoH.

$$SOH = \frac{Q_{discharge\ actual}}{Q_{discharg\ \ initial}} * 100 \quad (14)$$

Where, $Q_{discharge\ actual}$ is the actual discharge capacity of the cell in nth cycle expressed as (mAh) and $Q_{discharg\ \ initial}$ is the initial discharge capacity of the cell when it is new expressed as (mAh).

For the resistance method, the ration between the actual resistance and the initial resistance of the cell is considered.

$$SOH = \frac{Ri_{initial}}{Ri_{\ actua}} * 100 \quad (15)$$

Where, Ri_{actual} is the actual resistance of the cell in nth cycle expressed as (mΩ) and $Ri_{\ initial}$ is the initial resistance of the cell when it is new expressed as (mΩ).

Whereas, for ICA method, SoH is estimated from the plot of ratio of differential capacity to differential voltage vs voltage of the cell. In detail the ICA methods are explained in the following chapters. In this thesis, SoH is mainly calculated using capacity.

3.6 Conclusion

Currently, Li-ion battery is the key player for energy storage applications. The wide deployment of Li-ion batteries for transportation sector especially in EV's and HEV's has led them to catch up with ICE's. This is due to Li-ion batteries, as they cater the needs of a more efficient and clean energy source. However, the major setback for EV's is the recharging time since its counterpart can refuel in minutes, whereas recharging of battery pack safely can take couple of hours. In recent years, many automobile manufacturers have come with various tailor-made fast charging strategies to cut down the recharging time.

As seen earlier, there exist many possibilities to perform fast charging of Li-ion batteries. Out of which, High C-rates, pulsating current, sinusoidal current, multistage charging protocol are highlighted. However, there is room for improvement in those protocols. Hence, this thesis will elaborate on different fast charging protocols in terms of charging time, temperature elevation and ageing mechanism. Further, in this manuscript the results will be highlighted.

In a real-time application, as previously presented factors influencing battery ageing interact to generate both capacity loss, resistance augmentation and loss of available power. Note that all factors are dependent on other external conditions as well. For electric vehicle application, temperature depends on climate, change in SoD depends on the driving cycle. Depending on successive accelerations or constant velocity, the battery temperature will not evolve the same way.

Chapter 2. Experimental setup

1. Experimental set up and characterization

1.1 Introduction

The aim of this section is to present different cells, instruments, methods and tests used during the study of fast charging on Li-ion battery. Cells with different electrochemical behavior of the same technology will be used for the latter purpose of the study and will be introduced in this section. The cells mentioned have their own advantages and inconvenience in the application. The terminologies used in this study is explained in Chapter 1. Besides that, a charging test bench developed during the study for fast charging of the cells will also be explained here. At last, some analysis methodologies for *post-mortem* study are described.

1.2 Lithium battery

Two different battery types were used in the experimental study. First, power optimised cell 18650-20R manufactured by Samsung SDI and secondly, energy optimised cell 18650-26M Manufactured by LG Chem. Both the batteries contain Nickel Manganese Cobalt Oxide (NMC) at the positive electrode and graphite as the negative electrode. The following section will describe more about their characteristics.

1.2.1. Power optimized cell, C/NMC

Power optimised cell designs are used for high power applications which uses smaller particles of active material on both positive electrode and negative electrode. The authors of [64] used a tear down approach to investigate the internal components and found that the positive electrode of power optimised cells possessed high porosities which was not the case in negative electrode. The resistance of individual components in the power optimised cells is reduced to be as low as possible. Due to these advantages, power optimised C/NMC cells was chosen to undergo fast charge process at high currents. The nominal voltage of the cell is about 3.6V under no-load condition. The operating temperature ranges between 0°C to 50°C and nominal capacity of the cell is 2Ah. The manufacturer claims that the battery can perform fast charging with 2C-rate using CCCV method. Table 5 recapitulates the specifications of the cell.

Table 5 Power optimised 18650C/NMC cell characteristics from Samsung

Characteristics	INR 18650 20R
Manufacturer	Samsung SDI
Type	Power
Rated capacity	2000 mAh
Nominal voltage	3.6 V
Standard charge	CCCV, 0.5C 4.2V C/20 Cut off
Rapid charge	CCCV, 2C 4.2V C/20 Cut off
Standard Discharge	0.2C, 2.5V cut off
Maximum continuous discharge current	22 A
Operating Temperature during charge	0 to 50°C
Chemistry	NMC

1.2.2. Energy optimized cell, C/NMC

Energy optimized cell designs are used for high energy demanding applications such as remote grid storage. The main difference is in the particle size of the active material which is bigger. Also, the resistance of the individual components is slightly high. This type of battery was selected in order to investigate the impact on the cell's electrochemical behavior and capacity retention as it undergoes fast charging at higher current. The nominal voltage of the cell is about 3.65V under no-load condition. The operating temperature ranges between 0°C to 45°C and nominal capacity of the cell is 2.6Ah. The manufacturer claims that the battery can perform fast charging with 1C-rate using CCCV method. More details regarding the specification if the cell is highlighted in Table 6.

Table 6 Energy optimized 18650 C/NMC characteristics from LG Chem

Characteristics	INR 18650 26M
Manufacturer	LG Chem
Type	Energy
Rated capacity	2600 mAh
Nominal voltage	3.65 V
Standard charge	CCCV, 0.5C 4.2V C/20 Cut off
Rapid charge	CCCV, 1C 4.2V C/20 Cut off
Standard Discharge	0.2C, 2.75 V Cut off
Maximum continuous discharge current	10 A
Operating Temperature during charge	0 to 45°C
Chemistry	NMC

1.3 Battery test bench

1.3.1. Commercial equipment

Two equipments are used during the study of fast charge protocols. The first being the VSP potentiostat coupled with a booster of 20A from Bio-Logic Science Instrument Company. This is controlled with the help of EC-lab Software that helps in defining the charging protocol and characterization of the cells. The second being the Cycler BCS-815 from Bio-Logic Science Instrument Company and another from Arbin Instruments. The BCS-815 cycler is controlled using BT-lab software and Arbin Instruments is controlled using Mits-Pro software that helps in cycling the cells. The battery is connected to the equipments using C-clamps. For the temperature measurements during the experiments, a Pt100 sensor is fixed on the outer surface of the cells. All the experiments were carried out in a controlled temperature environment using climatic chamber at 25°C. The illustration of the setup is as shown Fig. 2.1.

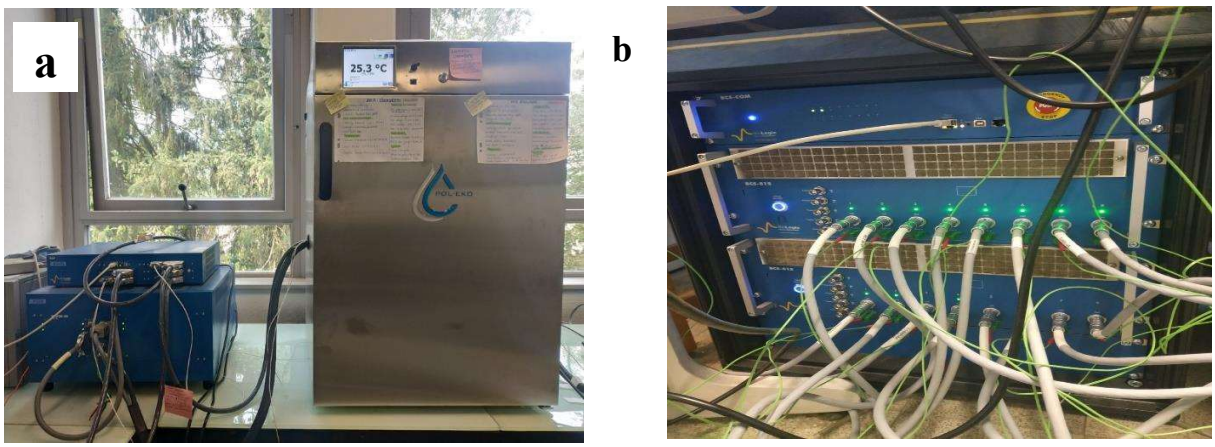

Fig. 2.1 (a) Biologic potentiostat with climatic chamber and (b) Biologic cycler for ageing study

1.3.2. Pulse charging test bench developed: High frequency current pulses

The biologic potentiostat explained in section 1.3.1 is incapable of applying current pulses greater than 1kHz frequency. Wherein, frequency is defined as the number of waveforms passing in unit time. In general frequency is the inverse of the time period expressed in Hertz

(Hz). 1Hz is defined as one cycle per second. Wherein, 1 cycle corresponds to sum of one crest and one trough.

$$Frequency = \frac{1}{t} Hz \tag{16}$$

Where, *t* is the time period of the wave comprising of one crest and one trough. Therefore, it is necessary to develop a fast charger that is capable of applying current pulses greater than 1kHz to be able to study the influence of high frequency square current pulses on the charging time and temperature increase on the cells. The test bench is made up of following components:

- A constant current square pulse block comprising of IRF540 N-type Mosfet to generate square pulses
- A constant voltage block comprising of linear voltage regulator LT
- An STM-32 microcontroller to drive the gate of the Mosfet and collect voltage and current data.

The designed charger is capable of generating square current pulse ranging from 1mHz to 10kHz. Fig. 2.2 shows the schematics of the pulse charger schematics.

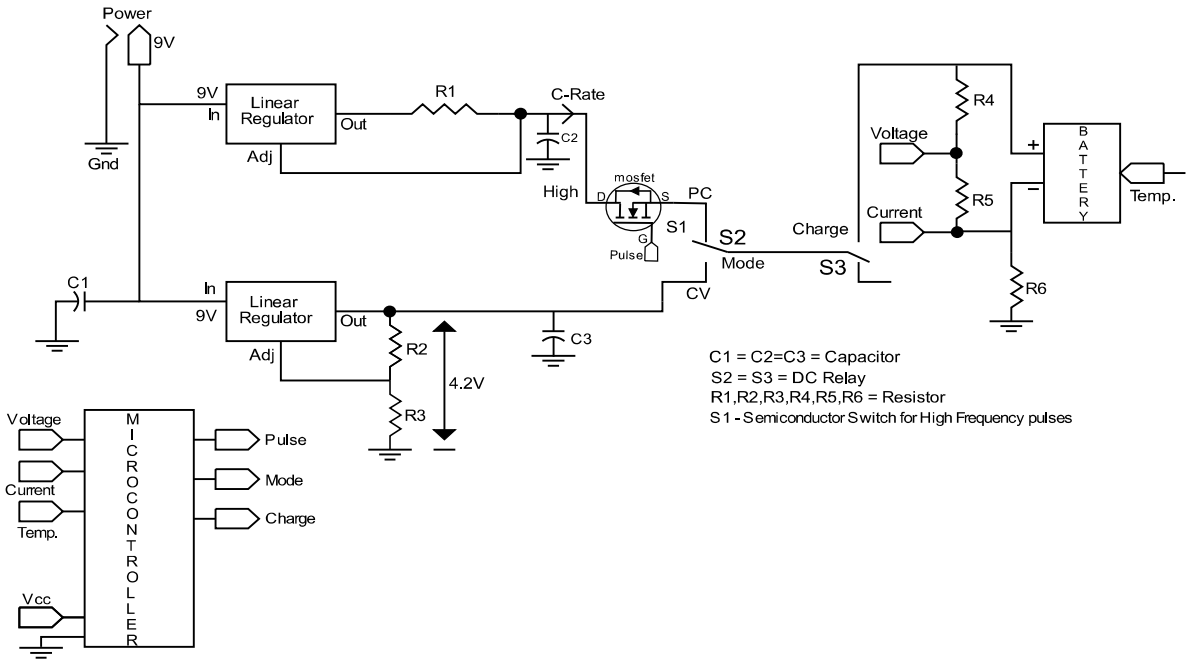

Fig. 2.2 Schematic diagram of the high frequency pulse charger

The designed schematics is not optimal since the objective is to carry out a feasibility study of high frequency current pulses. In this study, a high frequency current pulse is applied to the cell during stage 1 as explained in Chapter 1.2.4 in order to operate the cell at lowest resistance value to limit temperature increase caused by internal resistance. Through the results it is possible to estimate the impact of high frequency current pulse on cell temperature and charging time.

1.3.2.1 Pulsating block

The LT1083 acts as a linear current regulator with the help of series resistor that controls the current through the adjust pin. Once the constant current of required C-rate is obtained it is fed to the N-type Mosfet connected in series with the cell. The Mosfet converts the constant current into pulsating current that is to be applied to the cells. The series resistor value required to regulate the current is calculated using the formula below:

$$Duty\ Cycle\ (DT) = \frac{t_{On}}{t_{on} + t_{off}} * 100 \tag{17}$$

Where, t_{On} is the time ON time in seconds and t_{off} is the turn OFF time of the wave comprising of one crest and one trough

The maximum C-rate that can be applied is limited by the power supply used and it is 6A (2C-rate).

1.3.2.2 Constant voltage block

For the constant voltage block, another LT1083 is used which act as a linear voltage regulator with the help of two resistors connected between output pin, adjust pin and ground. The resistor placed between output pin and adjust pin causes a constant current to flow through the adjust pin to set the output voltage. The formula used to calculate the output voltage is given below:

$$V_{out} = 1.25 * \left(1 + \frac{R_2}{R_3}\right) volts \tag{18}$$

1.3.2.3 Measurement block

To monitor the charging process, a measurement block is required to measure the voltage of the cell and current flowing in the cell. The most common method to measure the voltage

with microcontroller is to use a voltage divider circuit. The voltage divider circuit divides the voltage of the cell proportional to the resistance connected across the less. The output voltage is then sent to STM32 microcontroller to retrieve the actual voltage of the cell.

Another vital parameter to be measured is the current through the cell. This is achieved by connecting a shunt resistor of 20mΩ, since current cannot be measured directly. The ideology behind this is to utilise ohm's law. The current flowing through the cell is made to flow through the shunt resistor, then by ohms law, voltage drop across the shunt resistor is proportional to current flowing through it. Since, the shunt resistor value is known and the voltage across it can be measured by the STM32 microcontroller, the current can be easily calculated.

1.3.2.4 Output current measurements

In order to determine the quality of the square current pulse, a preliminary study of the output current was carried out using Keysight oscilloscope connected across the 20mΩ shunt resistor. The output current from the charger at different frequencies is presented in Fig. 2.3.

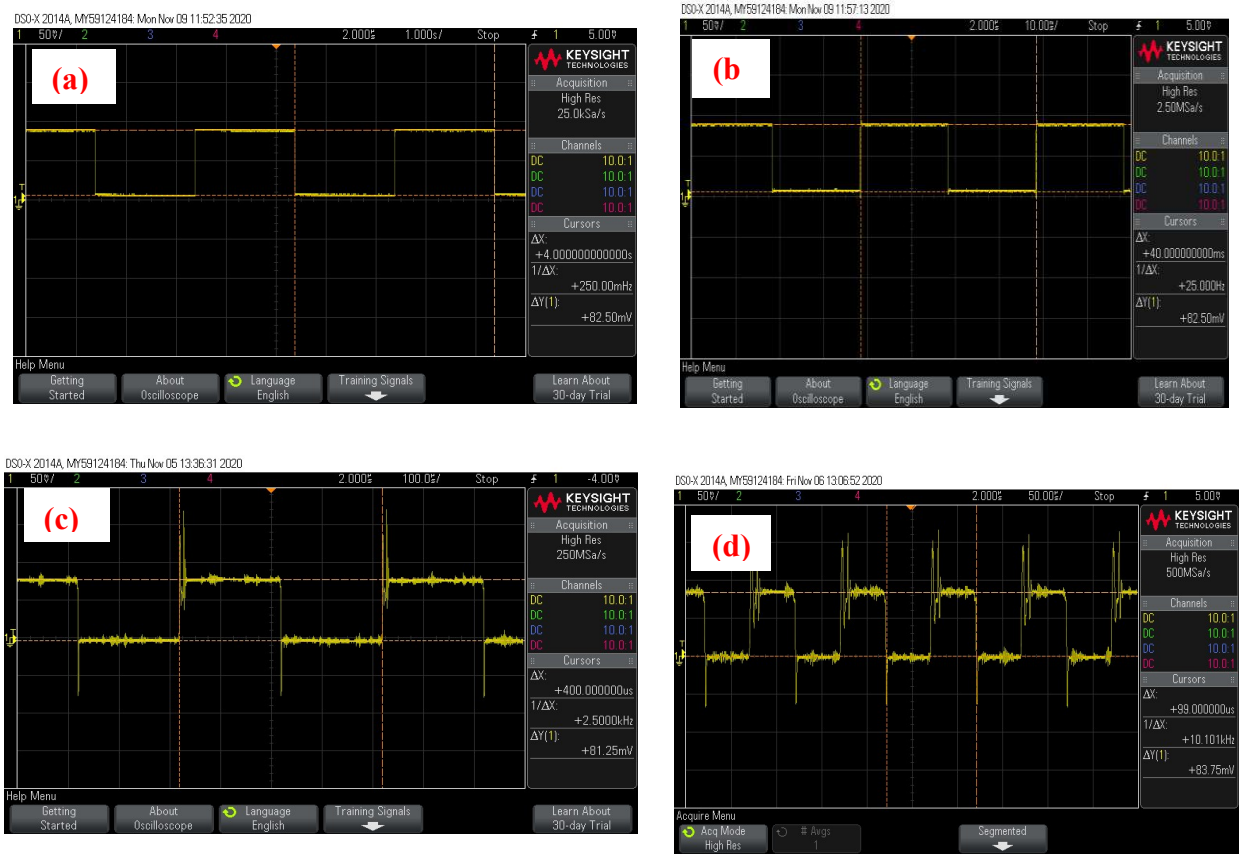

Fig. 2.3 Voltage drop across 20mΩ shunt resistor measured using Keysight oscilloscope for 4A with 50% duty cycle (2C equivalent of power cell) at (a) 250mHz (b) 25Hz (c) 2.5kHz and (d) 10kHz respectively

The output current is used to recharge the battery at different frequency ranging from 10mHz to 10kHz.

2. Cell characterization

2.1 Precondition

The main objective of this test is to remove any passivation to which the cell was subjected during manufacturing and stabilise the capacity. At first, the battery was full discharged using -C/5 C-rate constant current (CC) until the lower cut off voltage was reached. Next, the battery was fully charged up-to 4.2 V using CC-CV technique. The charging was terminated when the current dropped to C/20 in the CV stage. Following the charging, the cell is relaxed for 1 hour and the battery was discharged to lower cut off voltage using -C/5 discharge current. This procedure was conducted for 5 consecutive cycles. The battery is considered to be preconditioned, if capacity change between any two consecutive cycle is less than 2%. Table 7 summarizes the mean capacity value for the cells used. Fig. 2.4 depicts the voltage and current curves of the cells during their reference charge and discharge process. Fig. 2.5 illustrates the average discharge capacity for 5 consecutive cycles during preconditioning with their respective standard deviation for 4 power and energy cell used during this study. In Fig. 2.4,the reference charging process, rest period, reference discharging process is highlighted. Moreover, CC and CV stages are also outlined for each type of the battery. The power cell is normally charged until 100% SoC in about 124 minutes whereas, Energy cell takes 140 minutes. The evolution of curves for voltage and current for both the type of cell are very similar. This mainly due to the same nature of active materials in both the types for positive electrode. The duration of the CC stage for the power cell is more when compared to that of Energy cell. Contrariwise, the duration of CV stage is less for power cell than for energy cell. This phenomenon is related to the ohmic drop of the cells. As the energy cells have higher internal resistance, during CC stage they reach uppercut-off voltage fast when compared with power cell.

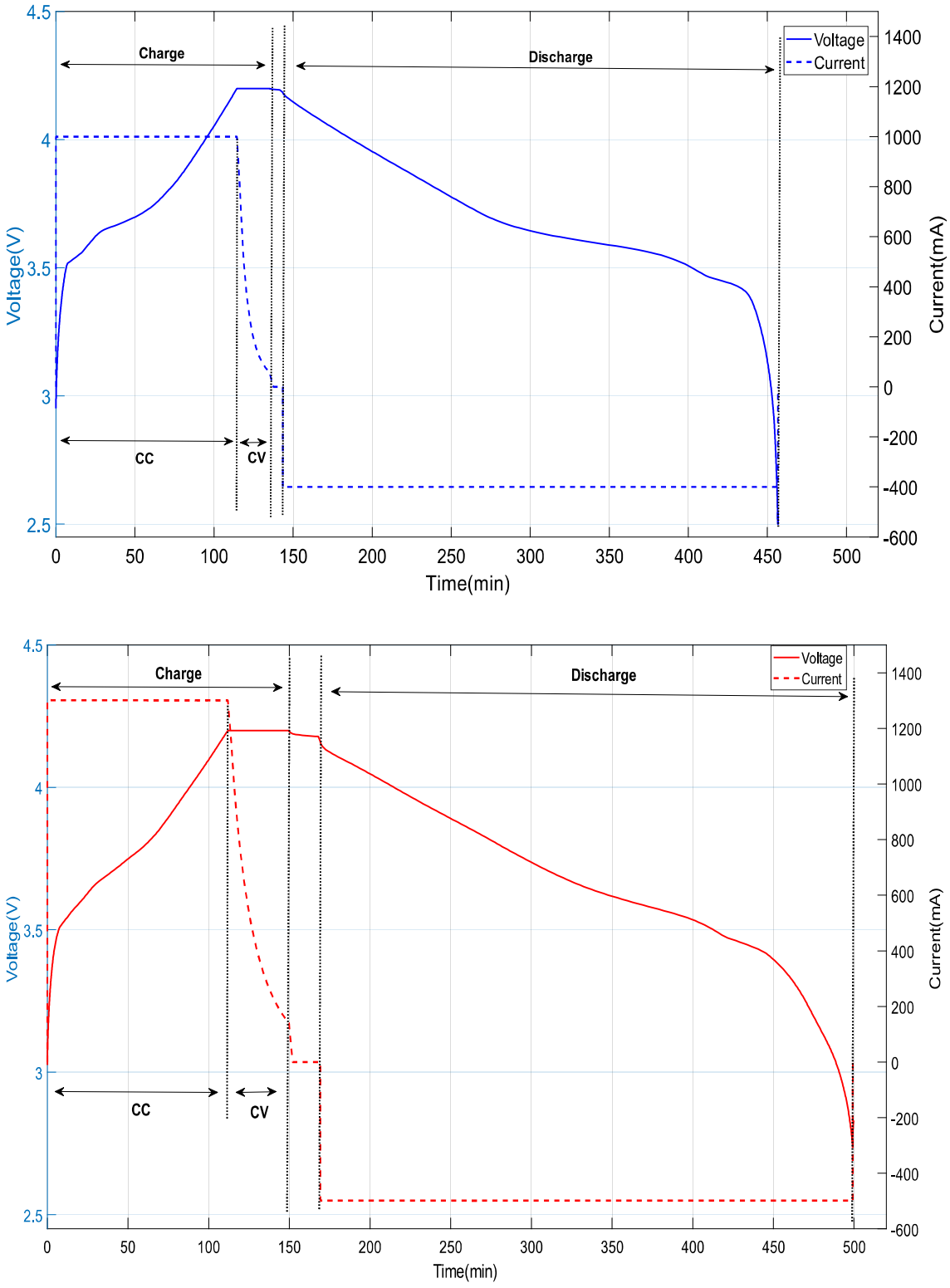

Fig. 2.4 Voltage and current curves at 25°C for C/NMC power (top) and energy (bottom) cell during the reference charging, relax period and reference discharging process

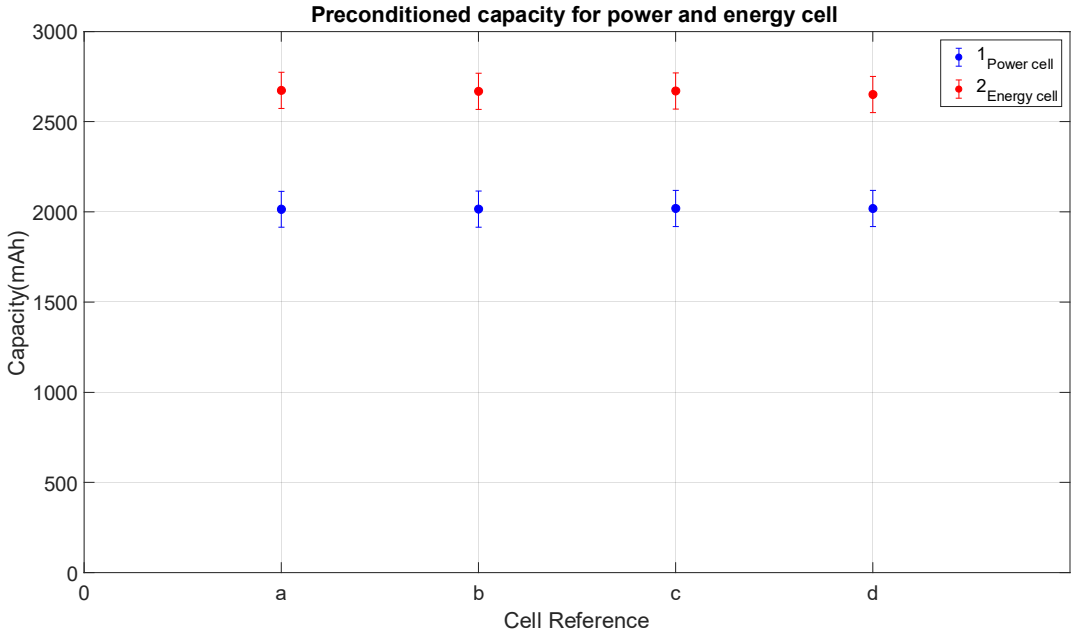

Fig. 2.5 Average discharge capacity at 25°C for power (blue) and energy (red) cells with standard deviation during preconditioning

2.2 Internal resistance estimation using current interrupt

Internal resistance (R_i) of the cell is defined as the opposition for the flow of current within the cell. The basic parameters which affect the R_i are the ohmic resistance and ionic resistance that are dependent on temperature [65]. The ohmic resistance comprises the resistance of the cell components such as negative electrode, positive electrode, current collectors and electrolyte. Whereas ionic resistance is the resistance offered mainly by electrolyte to the flow of ions. This polarisation effect is slow than the ohmic resistance therefore, the total effective resistance is mainly due to ohmic resistance.

The current interrupt technique (CI) present in the EC-lab software by BioLogic is used to estimate R_i. The R_i is determined at 50% SoC by applying a current pulse equivalent to C/5 C-rate for 10 to 20 impulsions at 0.04ms (approximately 25kHz). The average R_i is calculated using current-voltage relationship given by the two points on a charge curve.

$$R_i = \frac{V_1 \sim V_2}{I_1 \sim I_2}\ \Omega \tag{19}$$

The CI is a direct current method which is only suitable for estimating ohmic resistance.

Table 7 provides the overview of experimental characteristics of the cells with the reference used for the experiments in Chapter 3 and Chapter 4.

Table 7 Overview of the characteristics of the cells

	Reference	Capacity, Q (mAh)	Internal Resistance, R_i (mΩ)
INR 18650-20R	1a	2014	19 ± 1
	1b	2015	20 ± 1
	1c	2019	19 ± 1
	1d	2018	20 ± 1
INR 18650-26M	2a	2673	33 ± 1
	2b	2668	33 ± 1
	2c	2670	33 ± 1
	2d	2650	30 ± 1

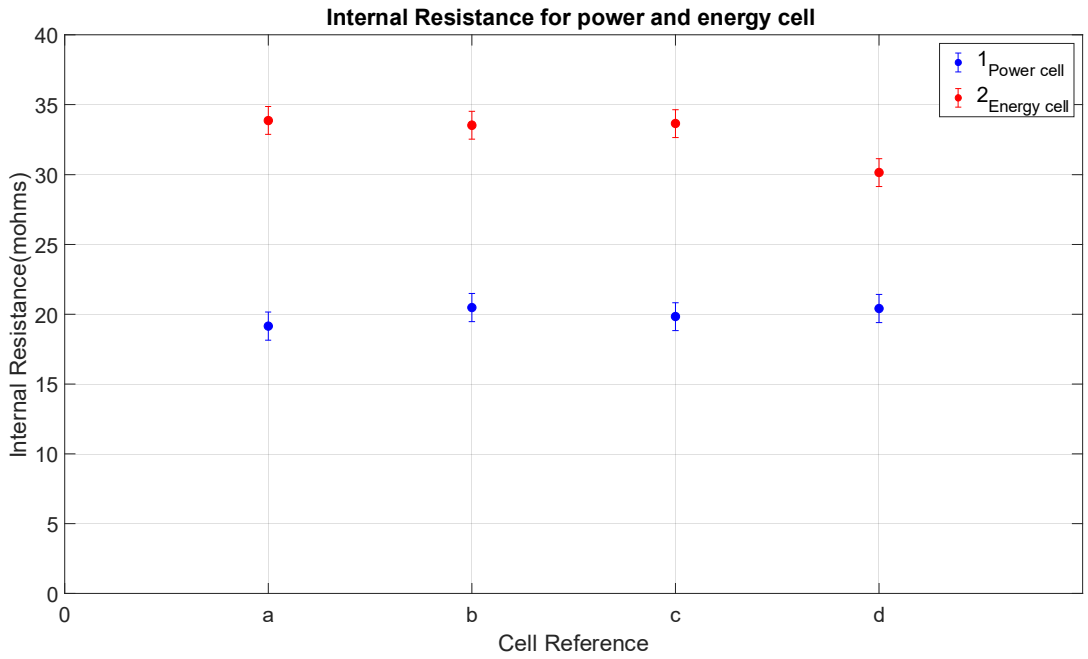

Fig. 2.6 Internal resistance in mohms at 25°C for power (blue) and energy (red) cells used in this study with respective standard deviation.

The experimental results in Fig. 2.7 shows internal resistance vs SoC curves in mΩ. As expected, the internal resistance has higher value at 0% and 5%SoC. It tends to decrease at 10% SoC and remains approximately at the same values until 100% SoC.

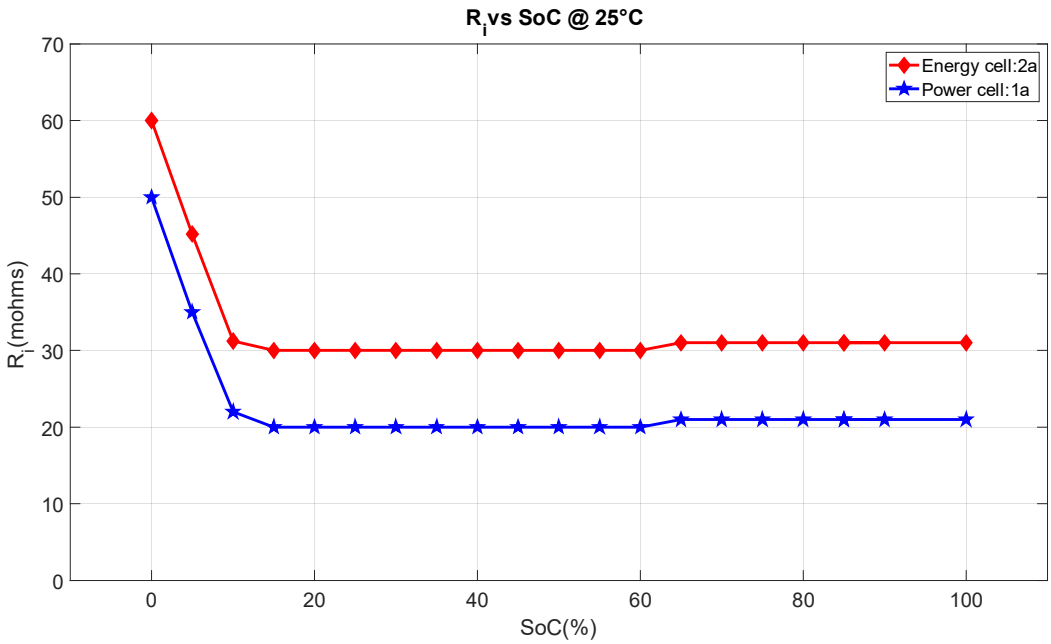

Fig. 2.7 Internal resistance in mohms for power (blue) and energy (red) cells at 25°C at different SoC

The power cell 1a, 1b and energy cell 2a, 2b are used for current control fast charging experiments. Whereas, the power cell 1c, 1d and energy cell 2c, 2d are used for voltage control fast charging experiments.

2.3 Electrochemical impedance spectroscopy (EIS)

Electrochemical impedance spectroscopy (EIS) is a complex non-invasive technique used in electrochemical research. EIS allows to understand the electrode kinetics, double layer capacitance and electron transfer resistance. This technique uses the time response of electrochemical behavior using low amplitude alternating current (AC) voltage over a range of frequencies to characterize the cell. The resulting real and imaginary components on a Nyquist plot gives information about the kinetic and mass transport properties of the cell as well as surface properties through double layer capacitance.

The Galvano electrochemical impedance spectroscopy (GEIS) present in the EC-lab software by BioLogic is used to estimate the impedance of the cell. The impedance is determined at 50% SoC by applying a sinusoidal ac current equivalent to C/5 C-rate from 10mHz to 10kHz with 8 points per decade. Fig. 2.8 presents the Nyquist plots at 50% SoC and 25°C ambient temperature for fresh power (blue) and energy (red) cells.

From Fig. 2.8, for both power and energy cells, it is clear that at lower frequencies, the impedance for the cell tends to increases and at higher frequencies the impedance of the cells decreases. To better explain these phenomena, we consider the electrical equivalent model of the cell comprising of a resistance, capacitance and inductance as shown in Fig. 2.9. Hence, the behavior of the cell at low frequency is capacitive coupled with resistive in nature and at high frequency it is inductive coupled with resistive in nature. Therefore, at low frequency, the impedance is mainly dependent on the reactance of the capacitor that is inversely proportional to the frequency and at high frequency, the impedance is mainly dependent on reactance of inductor which is directly proportional to the frequency.

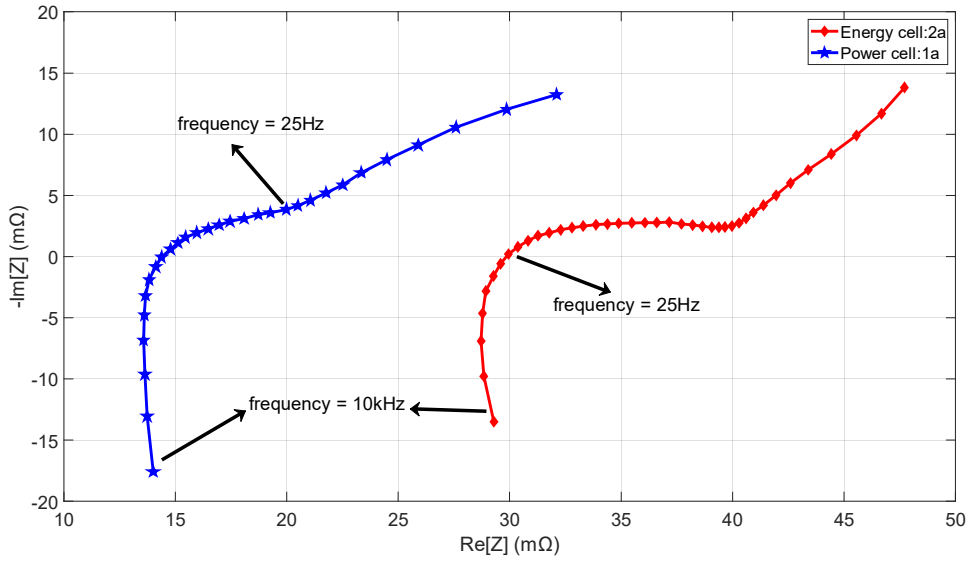

Fig. 2.8 AC impedance evolution at 50% SoC and at 25°C ambient temperature for new power (blue) and energy (red) cells

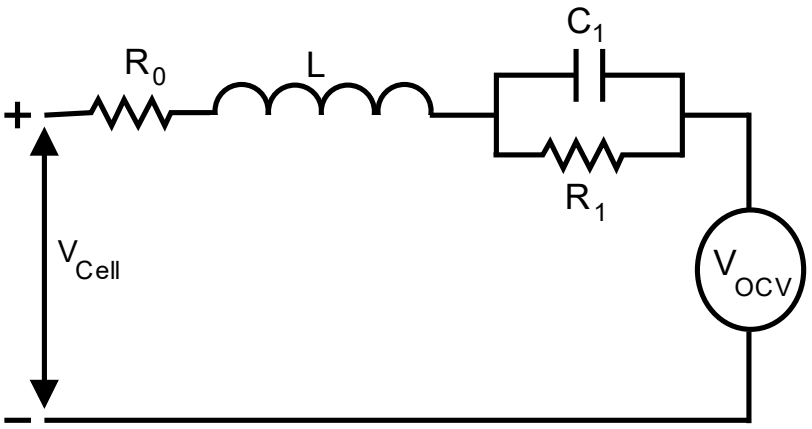

Fig. 2.9 Electrical equivalent circuit (EEC) model of the cell

2.4 Incremental capacity analysis

Incremental capacity analysis (ICA) is a an electrochemical technique providing information about the internal cell state using cell current and voltage measurements [66] [67]. The ICA depicts the incremental capacity change with respect to voltage step and is given by:

$$ICA_{cell}\left(\frac{Ah}{V}\right) = \frac{dQ_{cel}\ (Ah)}{dV_{cell}\ (V)} \tag{20}$$

Where Q_{cell}, is the capacity charge/discharge and V_{cell}, is the cell voltage during charge and discharge.

At first, the battery is discharged completely using C/5 constant current (CC) until the lower cut off voltage. Next, the battery is fully charged up-to 4.2 V using CC at C/20. Following the charging, after the rest of 1 hour, the battery was discharged to lower cut off voltage using -C/20 discharge current. Upon completion of the experiment the ICA curve is plotted using ICA equation vs voltage for the cells. Fig. 2.10 plots the ICA curve at 100% SoH for 1a and 2a cells at fresh states.

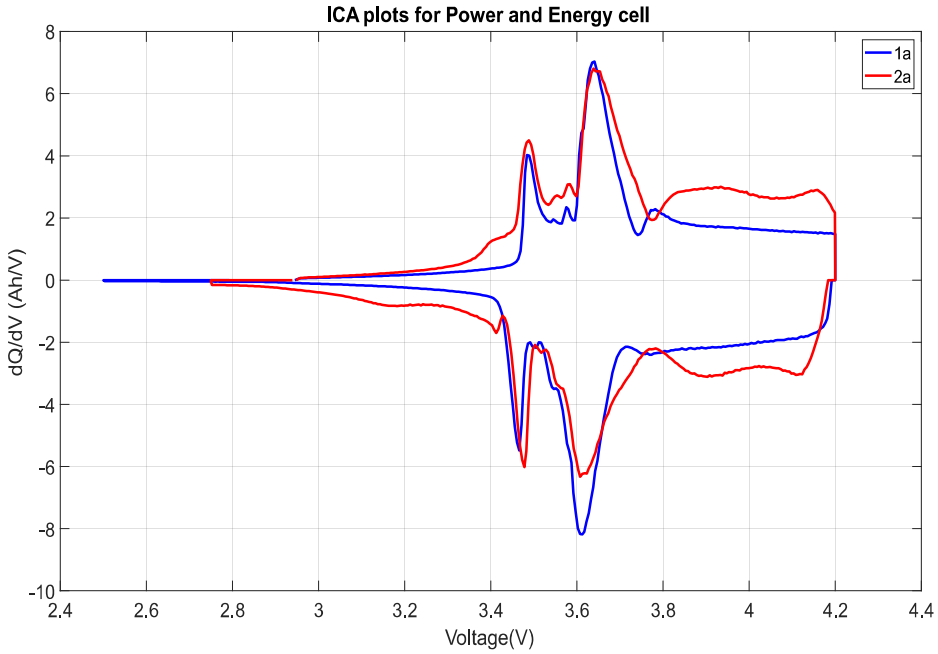

Fig. 2.10 incremental capacity analysis for power cell (blue) and energy cell (red)

2.5 Open circuit voltage (OCV)

The Open-Circuit Voltage (OCV) is a measure of the electromotive force (EMF) of the cell. This measure depends on the State of charge (SoC) of the cell. Moreover, the OCV will change because of the variation in internal resistance, capacity, hysteresis, and relaxation. In this work, the OCV is measured as the difference in voltage between the terminals of a cell when the circuit is open (no-load condition). The characteristic shape of the curve is given by the chemistry of the electrodes of the cell. In addition, the existing literatures shows that the OCV versus SoC changes with cell temperature.

The Open-circuit Voltage (OCV) is highly dependent on the operating condition, especially on the temperature. The goal of this test is to measure the OCV and plot OCV vs SoC characteristic for power and energy cells at 25˚C as shown in Fig. 2.11. The curve was obtained at a low current condition (C/100 C-rate)

At first, the battery is discharged completely using C/5 constant current (CC) until the lower cut off voltage. Next, the battery is fully charged up-to 4.2 V using CC at C/100. Following the charging, after the rest of 1 hour, the battery was discharged to lower cut off

voltage using C/100 discharge current. Upon completion of the experiment the OCV curve is plotted vs SoC as shown in Fig. 2.11 for 1a and 2a cells at fresh states.

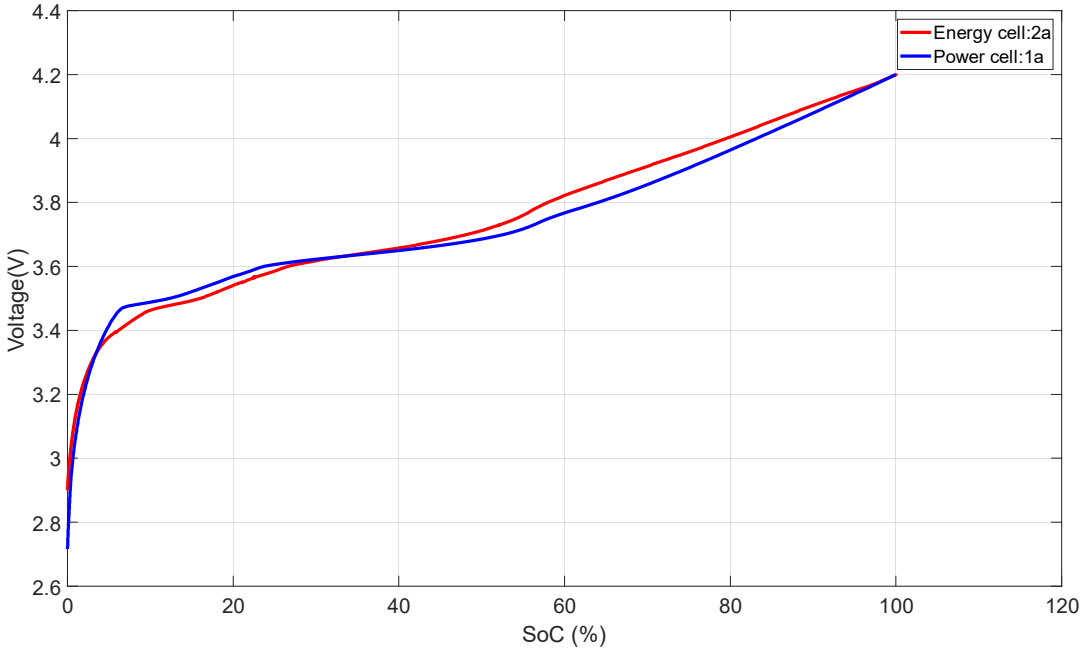

Fig. 2.11 OCV vs SoC characterization for power (blue) and energy (red) cells at 25°C for fresh cells

3. Post-mortem analysis methodology

3.1 X-ray tomography

The X-ray tomography scans were performed on the batteries using a NANOTOM 180S Phoenix (GE Technologie). The batteries were rotated 360° about their long axis whilst 1500 projections were captured with the focus tube operating at 120 kV and 130 µA. The sample and detector were positioned in projection magnification providing an effective pixel size of 24.42 µm for the high-resolution imaging.

3.2 Electrochemical characterization with coin cell

Finally, electrochemical tests were performed with coin half-cells consisting of graphite-based electrode and NMC-based electrode (Diameter=16 mm) harvested from the commercial cell and Celgard® 2400 separator (Diameter=18.5 mm) with a metal lithium electrode (16 mm) in 1:1:1 wt EC:DMC:EMC + 1M LiPF6 electrolyte. The capacity of lithium de/re-intercalation into both graphite and NMC electrodes recovered from aged cells is investigated with coin half-cells. Charge and discharge cycling were carried out at C/10 C-rate in order to know their own capacities and compare their performances to the full-cells ones.

Chapter 3. Current control technique

1. Introduction

Developing fast charging protocol is of paramount importance to draw the consumer interest for wider deployment of EV's. In this section, fast charging of Li-ion batteries is investigated for CCCV protocol with and without Ohmic Drop Compensation (ODC), square current pulse and triangular current pulse. For CCCV protocol, C-rates starting from 0.5C to 4C are investigated. Whereas for the current pulses, the range of frequencies investigated are 0.25 Hz to 10 kHz at 50% duty cycle and 80% duty cycle. In this chapter, the main importance is given to Triangular current pulse, wherein, the current is linearly varied with respect to time until peak current I_{pk} is reached. The rate at which the slope of the triangular pulse changes defines the frequency of the pulses. This chapter will put forth all the experimental results for comparison with respect to charging time and Δ temperature elevation. Mainly the discussion is pivoted around two axes. First being the evolution of charging time and temperature elevation for 100% SoC. Second being the target. As a reminder, the target for fast charging time and Δ temperature elevation to recharge 80% of SoC is 20 minutes and 25°C respectively. Towards the end of the chapter, comparisons between square current pulse and triangular current pulse is also put forth.

2. Fast charging technique : constant current constant voltage protocol

2.1 Constant current constant voltage technique

2.1.1. Presentation of protocol and full charge study

The most common method to recharge the lithium-ion batteries is through two-stage consecutive constant current-constant voltage which is also known as CCCV technique, as depicted in Fig. 1.5 of section 2.1 in Chapter 1. The current rate in the CC stage also known as stage 1 and predefined upper cut-off voltage in the CV stage also known as stage 2 solely depends on the lithium ion battery chemistry, wherein these parameters are specified by the battery manufacturer for safe operation. Initially, in the beginning of the charging, constant current at a given C-rate of 0.5C, 1C, 2C, 3C and 4C is passed through the battery until the upper cut-off voltage of 4.2V is reached. After the end of this stage, the battery is charged at

constant voltage of 4.2V and the charging current exponentially decays. The charging is presumed to be completed upon reaching a lower threshold value of 130 mA and 100mA for energy and power cells as shown in Fig. 3.1 for 0.5 C-rate and 4C-rate

It can be observed from Fig. 3.1 that with the increase in C-rate from 0.5C to 4C, the total charging time decreased from 136 min to 34 min for power cell and from 152 min to 85 min for energy cell. Indeed, at 4C-rate the CC stage is extremely short compared to one at 0.5C-rate. Namely, the CC stage lasts only about 22 seconds at 4C-rate against about 122 min at 0.5C-rate for energy cell. Whereas, for power cell, the CC stage lasts about 25min at 4C-rate against 120min at 0.5C-rate. This phenomenon is mainly related to the contribution of ohmic drop at higher currents. Which means that the cells are charging in the CV for most of the time especially at 4C-rate for energy cell.

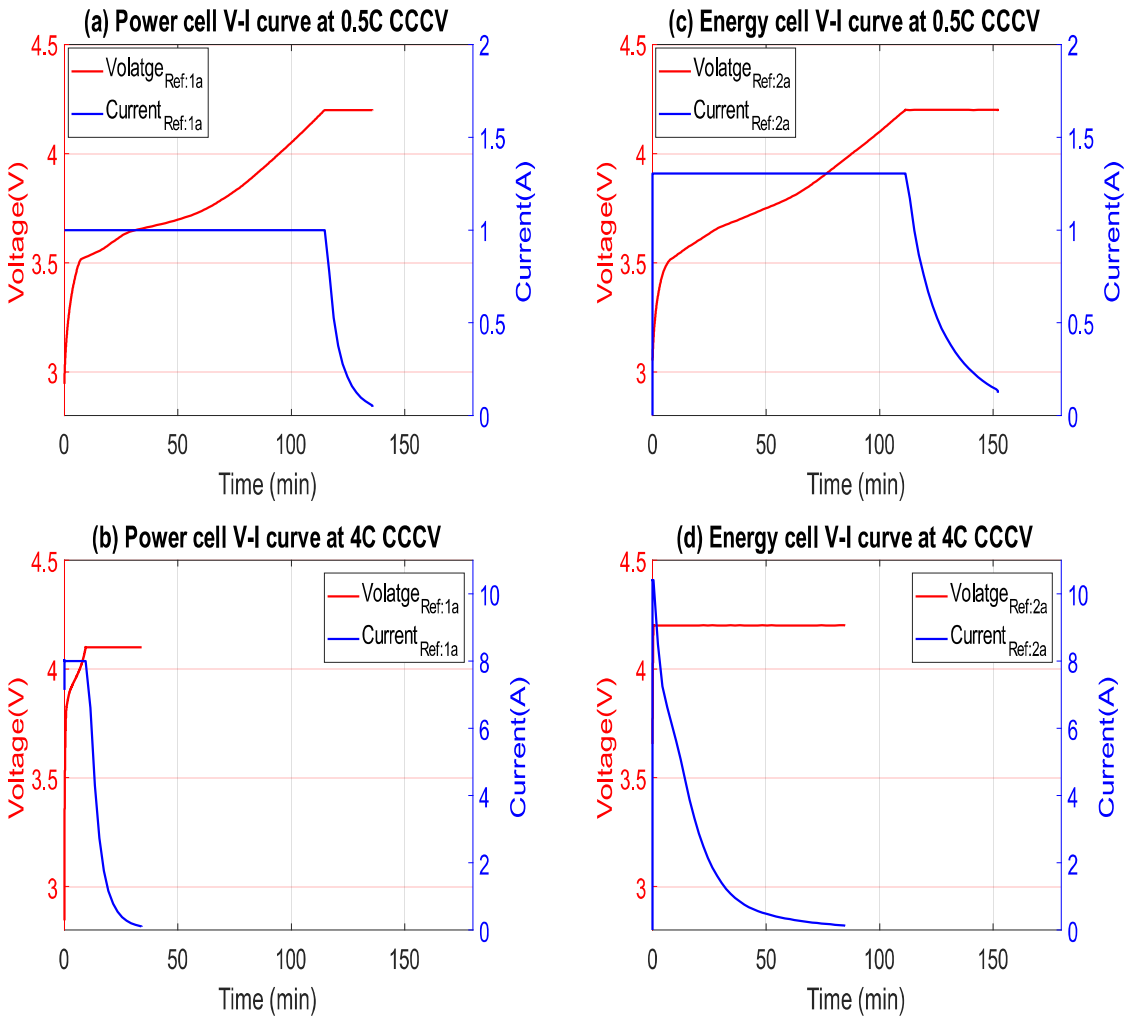

Fig. 3.1 Current in blue and cell voltage in red variation during charging using CCCV method at (a) 0.5C-rate for power cell (b)4C-rate for power (c) 0.5C-rate for energy cell and (d) 4C-rate for energy cell.

The experimental data values concerning CCCV protocol are gathered in Table 8.

Fig. 3.2 depicts the temperature difference between the surface and the ambient (Δ temperature $= T_{surf} - T_{ambient}$) in red and SoC in blue for the cells during CCCV charging at 0.5C-rate and 4C-rate. At 0.5C rate charging process, a very low temperature rise is observed for both power and energy cell. Whereas, at 4C-rate the surface temperature increases by 3 times in comparison with 0.5C-rate for both the types of cells. This is mainly due to the joule effect proportional to the square of current applied during CC-stage.

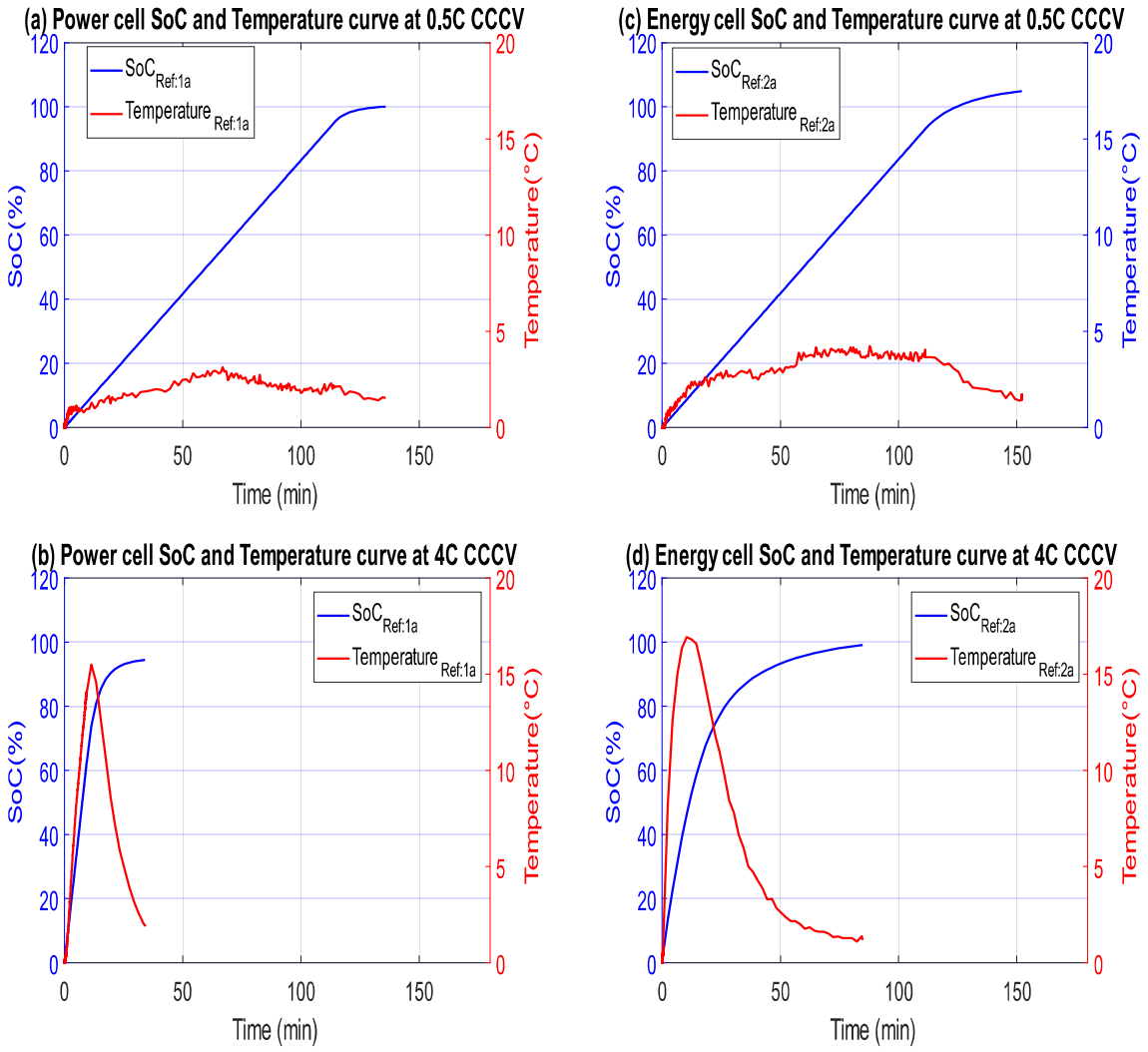

Fig. 3.2 SoC in blue and Δ Temperature in red variation during charging using CCCV method at (a) 0.5C-rate for power cell (b)4C-rate for power (c) 0.5C-rate for energy cell and (d) 4C-rate for energy cell.

2.1.2. Discussion in relation to target

Fig. 3.3 shows the time taken to recharge only 80% of Δ SoC from 0% SoC and elevation of surface to ambient temperature (Δ temperature) difference from 0.5C to 4C for Energy and Power cells using CCCV method.

From Fig. 3.3, it is clear that, to recharge 80% of Δ SoC, the charging time decays when the C-rate is increased. For the energy cell, the charging time reaches a lowest value at 3C-rate before increasing again.

The time taken to recharge 80% SoC at 4C-rate is approximately 17 minutes and 28 minutes for power and energy cells respectively. For the power cell, it is then possible to charge it in a duration lower than 20 minutes for a C-rate higher than 3C while it is never possible to reach the target with the energy cell. For energy cell, this is mainly because, at C-rate higher than 3C-rate, CV stage is more prevalent than CC stage and the cell charges only in CV.

Whatever the battery, the duration of CC stage is reducing while the duration of CV increases with the increase in C-rate. Indeed, for energy cell, at 3C-rate, the duration of CC stage reduces to 10 minutes while the CV stage is about 11 minutes. For the power cell, the CC stage at 4C-rate is 10 minutes against 7 minutes for the CV one.

This phenomenon is due to the contribution of internal resistance which is one third higher for energy cell. The ohmic drop contribution becomes more and more prominent at higher C-rates allowing the battery to reach the upper cut-off voltage in less time. This means that, at higher C-rate the battery charges in only CV stage.

For energy cell, the Δ temperature elevation until 3C-rate increases reaching a maximum value of 29°C and reduces for 4C-rate. This is due to the fact that, the charging is done in the CV stage during which the current exponentially decays. Whereas, for the power cell, the Δ temperature elevation is from 1°C to 15°C when the C-rate is changed from 0.5C to 4C principally due to the joule effect in proportion to the square of the applied current during CC stage. For the power cells, the temperature elevation is well within the temperature limit set by the manufacturer 45°C. For the energy cell, the temperature is exceeded at 3C where the cell reaches at surface temperature equal to 54°C.

Also, it is worth noting that, with these protocols it is difficult to reach the target of 80% SoC in 20 minutes with less than 25°C of temperature elevation for the energy cell while it is

possible to reach it for power cell. With the CCCV protocol a tradeoff between recharging time and temperature elevation is needed.

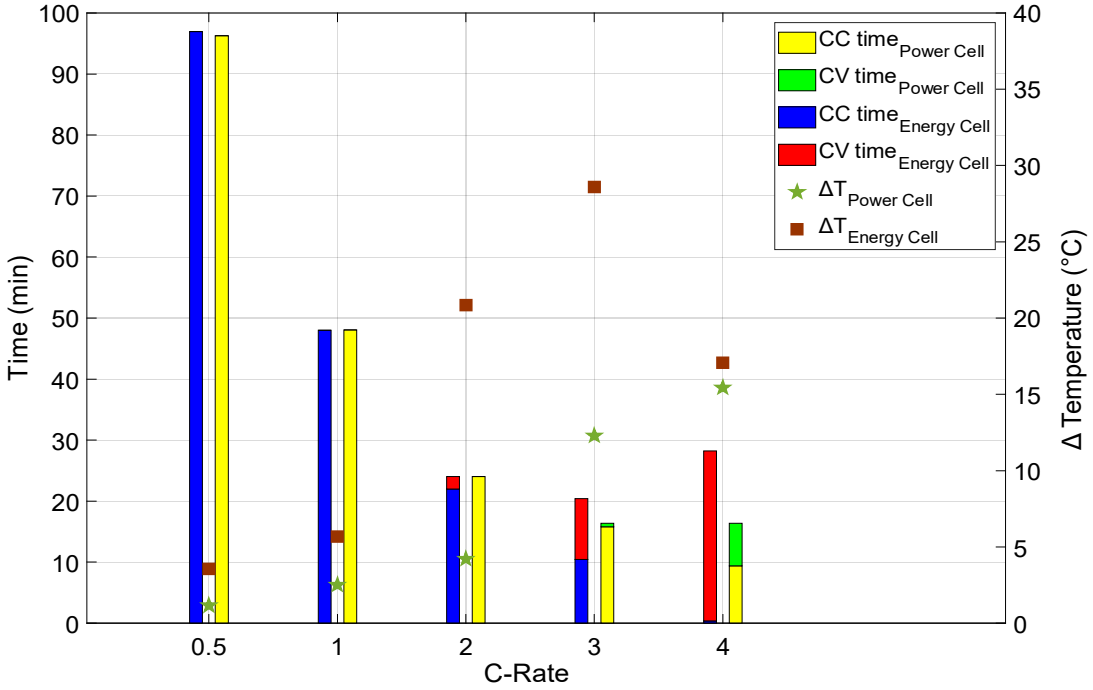

Fig. 3.3 Time taken to charge 80% SoC from 0% SoC and Δ Temperature from 0.5C to 4C-rate for energy and power cells

2.2 Constant current constant voltage with Ohmic Drop Compensation

2.2.1. Presentation of protocol and full charge study

ODC method also known as Ohmic Drop Compensation method consists in compensating the ohmic-drop caused by the internal resistance and contact resistance of the battery cell as explained in Fig. 1.10 in Chapter 1. Fig. 3.4 illustrates the V-I curves for energy cell with a constant current at 3C. Initially, constant current equivalent to 3C-rate is passed through the battery until the corrected cut-off voltage V'_{max} is reached (see equation 13 in section 2.3 of Chapter 1). As a reminder, the internal resistance (R_i) is approximately 20mΩ and 30mΩ for power and energy cells respectively with α of 100% being the compensation rate. Therefore,

the new upper cut-off voltage at 3C-rate is approximately 4.32V and 4.43V for power and energy cells respectively:

$$Power\ cell:\ V'_{max} = 4.2 + 1 * 20 * 10^{-3} * 6 = 4.32V \quad (21)$$

$$Energy\ cell:\ V'_{max} = 4.2 + 1 * 30 * 10^{-3} * 7.8 = 4.43V \quad (22)$$

Later, the charging is continued with a constant voltage phase of 4.2V until the current decays to C/20 (130 mA).

As example, the new upper cut-off voltage calculation for energy cell at 3C-rate is given below:

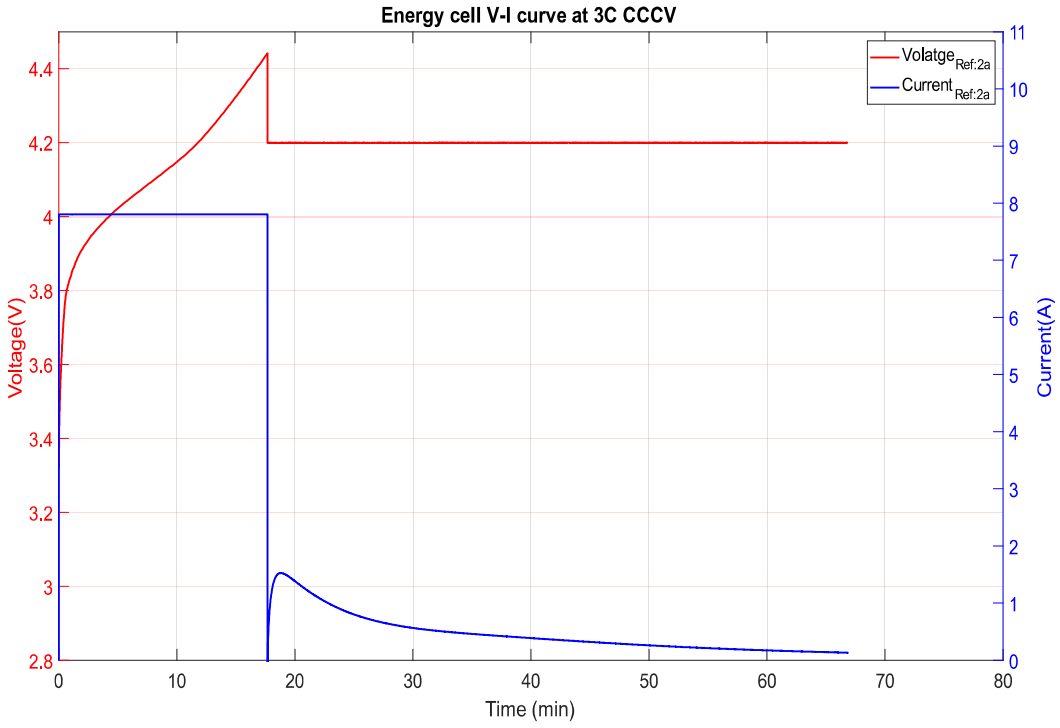

Fig. 3.4 3C-rate CC CV with ohmic drop compensation for Energy cell at 25°C ambient temperature

To go further, it can be observed from Fig. 3.5 that with the increase in C-rate from 0.5C to 3C, the total charging time decreased from 135 min to 34 min for power cell and from 155 min to 80 min for energy cell. As per equation 13, the contribution of ohmic drop is significantly less for both power and energy cell at 0.5C-rate as highlighted in (a) and (c) of Fig. 3.5. This means that at low currents the Ohmic drop compensation method has negligible effect on the charging time irrespective of the internal resistance of the cell. At 3C-rate, the ohmic drop plays

a significant role for both power and energy cell by shifting the upper cut-off voltage value during CC stage to a higher value as highlighted in (b) and (d) of Fig. 3.5.

Another aspect that is really interesting to point out is the impact of internal resistance on upper cut-off voltage value. According to Fig. 3.5, at 3C-rate, the ohmic drop of energy cell is greater than power cell. This means that, for ODC method internal resistance of the cell and charging C-rates plays a vital role and needs precise estimation of internal resistance.

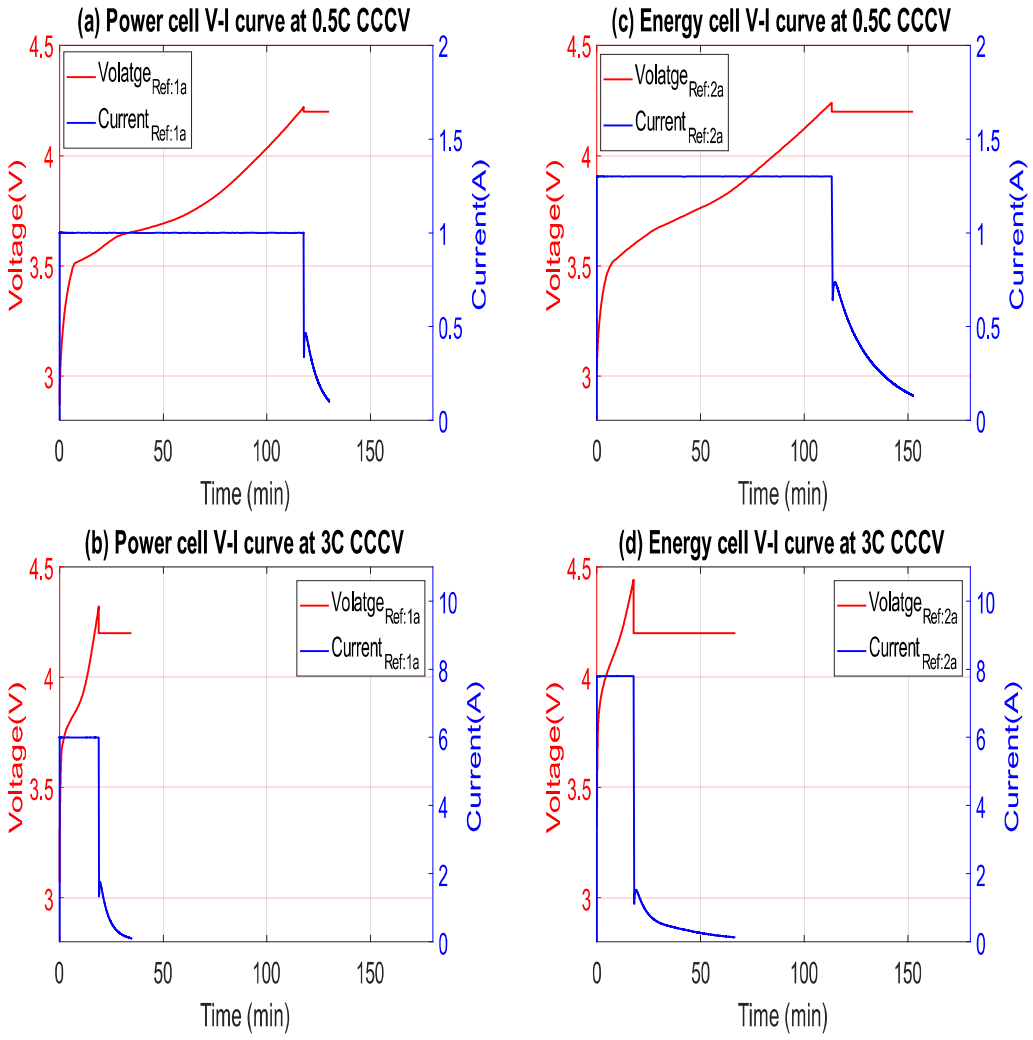

Fig. 3.5 Current in blue and cell voltage in red variation during charging using CCCV method with ODC at (a) 0.5C-rate for power cell (b)3C-rate for power (c) 0.5C-rate for energy cell and (d) 3C-rate for energy cell.

Fig. 3.6 depicts the Δ temperature in red and SoC in blue for the cells during CCCV with ODC charging at 0.5C-rate and 3C-rate. At 0.5C rate charging process, a very low temperature rise is observed for both power and energy cell. Whereas, at 3C-rate the surface temperature

increases by 3.5 times in comparison with 0.5C-rate for both the types of cells. This is mainly due to the joule effect. In this scenario the temperature elevation exceeds the target of 25°C beyond the ambient temperature.

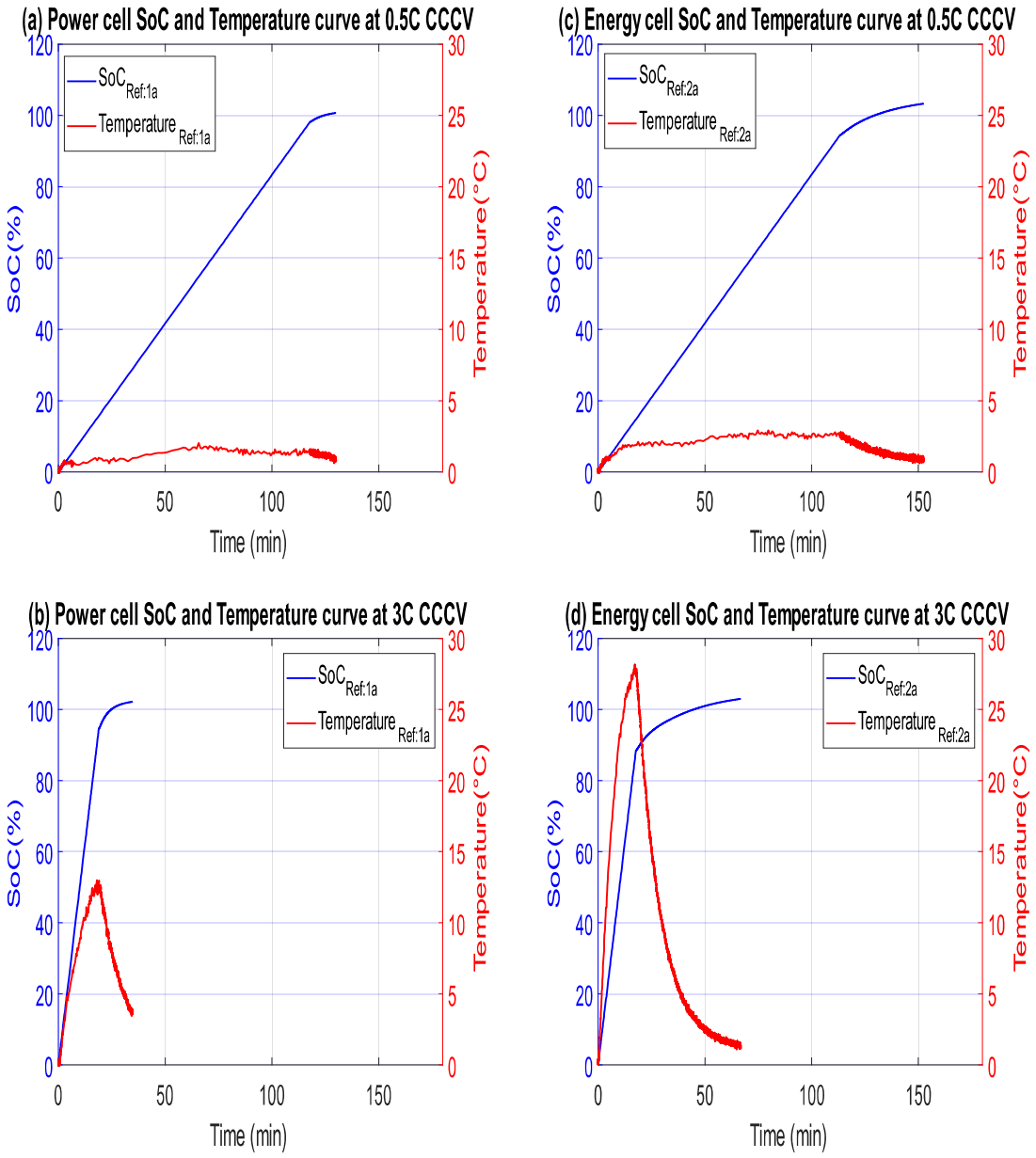

Fig. 3.6 SoC in blue and Δ Temperature in red variation during charging using CCCV method with ODC at (a) 0.5C-rate for power cell (b)3C-rate for power (c) 0.5C-rate for energy cell and (d) 3C-rate for energy cell.

2.2.2. Discussion in relation to target

Fig. 3.7 shows the time taken to recharge 80% SoC from 0% SoC and the Δ temperature increase ($T_{max} - T_{ambient}$) from 0.5C to 3C for power and energy cells with ODC using

CCCV method. It can be observed from Fig. 3.7. that with the increase in C-rate from 0.5C to 3C the charging time reduces by about 80 minutes.

It is clear that the charging time decays when the C-rate is increased to reach the duration target at 3C. Another interesting aspect is that for both power and energy cells, even at 3C-rate there is no CV stage. This means that, for CCCV with ODC, 80% SoC can be recharged from 0% SoC in only CC stage.

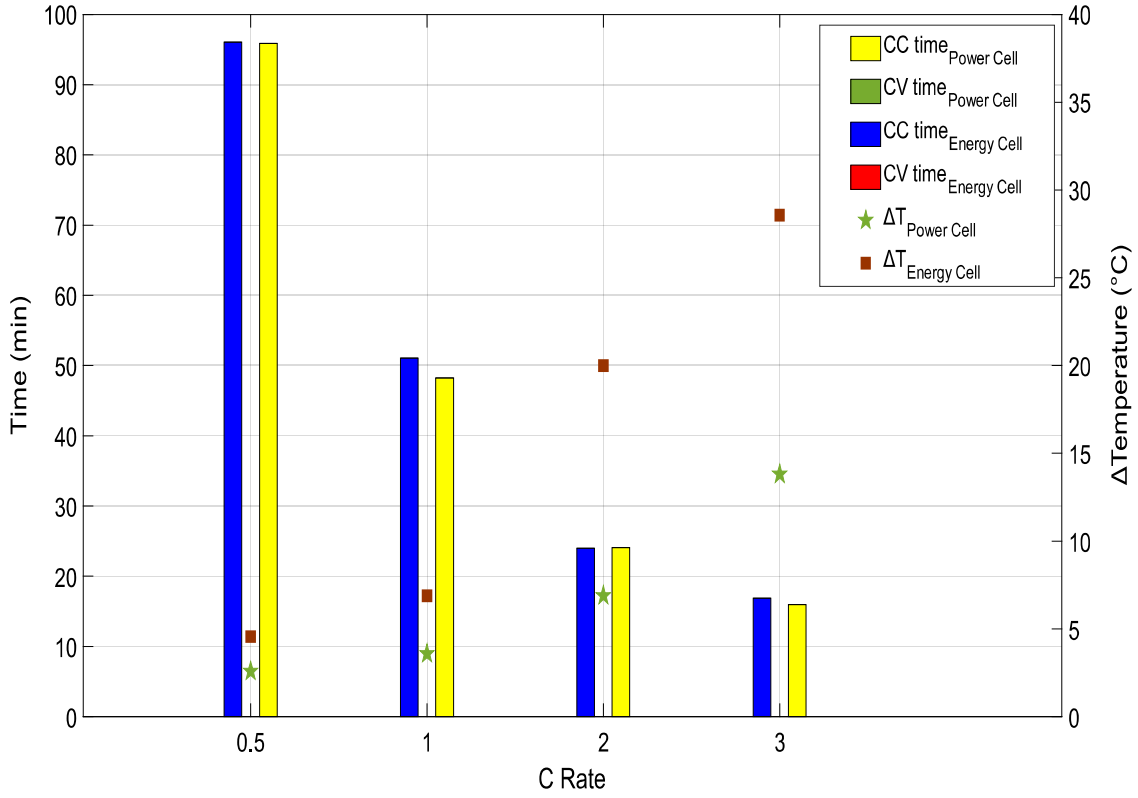

Fig. 3.7 Time taken to charge 80% SoC from 0% SoC and Δ Temperature from 0.5C to 3C-rate with ODC for energy and power cells

It is worth mentioning that, for energy cell, the temperature increases from 4.5°C to 28.51°C when the C-rate is changed from 0.5C to 3C with ODC. While, for the power cell, the temperature increases from 3°C to 13.81°C when the C-rate is changed from 0.5C to 3C with ODC. The increase in temperature with the increase in C-rate [68] in both energy and power cells is due to the joule effect during CC stage. As shown in Fig. 3.7, for energy cell at 3C-rate, the temperature increases rapidly and reaches its maximum value of 54°C and exceeds the temperature targeted. While for the power cell, the temperature is far behind 50°C limit. This temperature elevation for energy cell during fast charge with ODC could shorten the life time

of the battery by accelerating the ageing phenomena [8],[60]. The battery itself could be damaged or the high temperature degrades the battery components and may induce thermal runway.

2.3 Comparison of CCCV with and without ODC in relation to target

The Fig. 3.8a illustrates the voltage comparison between ODC and without ODC charging protocol at 3C-rate for energy cell. While Fig. 3.8b compares the evolution of SoC. From the Fig. 3.8a, the difference in upper cut off voltage can be clearly seen at the end of CC stage for energy cell at 3C-rate. Also, it is clearly evident that with the ODC, the duration of the CC stage can be increased and so, decreasing the duration of CV stage. Thanks to ODC, the duration of CC stage increases due to the increase in cut-off voltage value of the cells according to Equation 13. It is worth mentioning that for energy cell at 3C-rate, the charging time reduced by 4 minutes after implementing ODC technique as shown in Fig. 3.8b.

Fig. 3.9 shows the time taken to recharge 80% SoC from 0.5C to 3C-rate for power and energy cells with and without ODC using CCCV method.

It can be observed from Fig. 3.9, that at C-rates from 0.5C to 2C, there is no significant change in the recharging time from 0% SoC to 80% SoC for both energy cell and power cell. Whereas, for the energy cell at 3C rate, without ODC the recharging time increased by 4 minutes as compared to CCCV with ODC allowing to be well within the target time.

When C rate is increased from 0.5C to 3C for CCCV without ODC the recharge time for 80% SoC reduced by 80 minutes and 76 minutes for power and energy cells respectively. Whereas, for the CCCV with ODC, the recharging time reduced by 80 minutes for both power and energy cells.

Also, for CCCV without ODC, the temperature elevation is 11°C and 25°C for power and energy cells respectively when the C-rate is increased from 0.5C-rate to 3C-rate. Similar temperature elevation can be observed for CCCV with ODC when the C-rate is increased from 0.5C-rate to 3C-rate. Also, the temperature upsurge is quite high for energy cell at 3C-rate with ODC protocol. In fact, it surpasses the temperature limits set by the manufacturer by 8°C.

Even though we meet the target of 80% SoC using 3C-rate CCCV with ODC for both power and energy cells, this protocol is not recommendable because of the safety reasons and accelerated ageing of the cells owing cell over voltage and temperature increase.

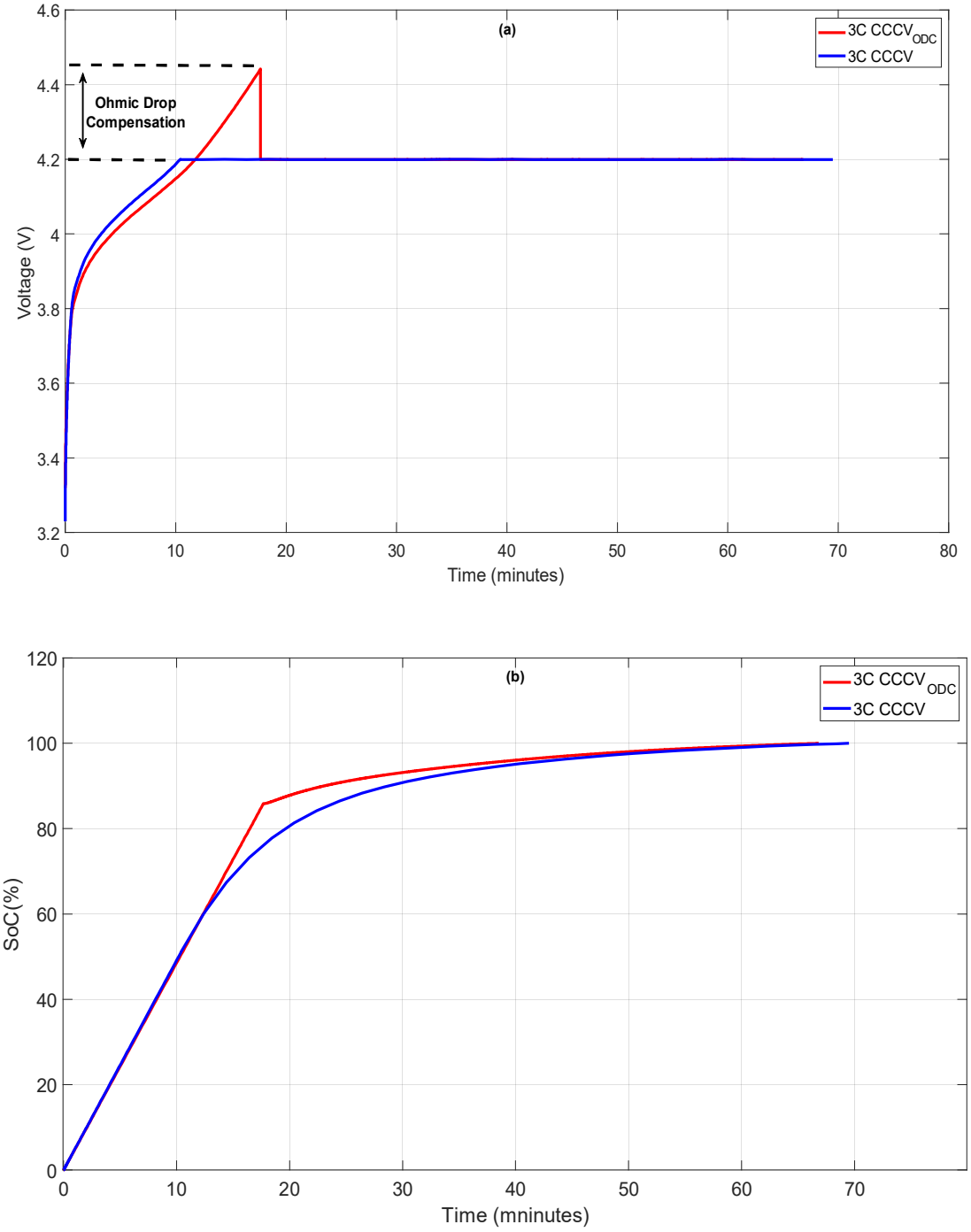

Fig. 3.8 (a)Voltage and (b) SoC comparison between CCCV with and without ODC at 3C-rate for energy cell

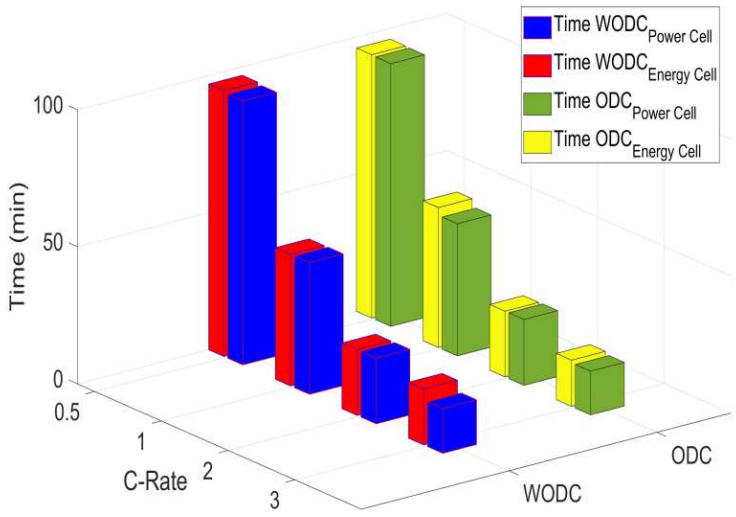

Fig. 3.9 Comparison of time taken to charge 80% SOC from 0% Soc at different C rates with ODC and without ODC for power and energy cell at 25°C ambient temperature.

Table 8 Summary results of all the experiments on CC CV technique

		Crate	Time for 80% SoC (mn)	CC time (mn)	CV time (mn)	Total time (mn)	Δ Temperature (°C)
Power	Without ODC	0.5	96.29	118.99	17.57	136.98	1.16
		1	48.08	56.23	23.25	79.48	2.51
		2	24.02	25.81	23.94	49.75	4.21
		3	16.36	15.81	25.09	40.9	12.29
		4	16.38	9.40	24.60	34	15.44
	ODC	0.5	95.89	119.95	16.37	136.32	2.58
		1	48.22	58.18	19.64	77.82	3.58
		2	24.05	29.55	17.48	47.03	6.89
		3	15.94	19.17	16.45	35.62	13.81
Energy	Without ODC	0.5	96.97	122.98	28.18	151.16	3.56
		1	48.02	48.95	52.78	101.73	5.68
		2	24.01	22.01	48.77	70.78	20.85
		3	20.42	10.42	59.08	69.5	28.59
		4	28.24	0.37	84.63	85	17.07
	ODC	0.5	96.07	103.63	103.63	143.15	4.56
		1	51.06	49.63	41.54	91.17	6.88
		2	23.98	25.47	25.58	51.05	19.99
		3	16.88	17.61	50.44	65.88	28.51

In conclusion, to meet the target of 80% SoC in less than 20minutes using CCCV protocol with and without ODC is possible only at higher C-rates resulting in operating the cells near the temperature threshold of 45°C and 50°C set by the manufacturer. In order to use these protocols a tradeoff between charging time, CC stage cut off voltage and temperature elevation is required.

3. Fast charge technique: Pulse charge method

Due to the inherent disadvantages of standard charging and rapid charging using CCCV protocol at higher C rates, there is a need to develop a charging method which is both simple and has less temperature impact on the battery. Hence, pulse charge methods are proposed during the CC stage or stage I to study the effects on the battery.

The developed pulse charger is not capable of delivering 3C-rate peak current due to the limitation in power supply. Therefore, in this section, to study the impact of frequency on pulse charging method, all the experiments were carried out with 2C-rate peak current only. Also, there was lack of time to improve the pulse charger.

3.1 Presentation of protocol: square current with rest pulse

Current pulse charging protocol involves carefully selected and controlled charge current pulses to charge the battery. The attributes and intensity of the pulses impacts the charging time, battery life and battery impedance. A constant current intensity for example 2C-rate is applied during the charging pulse (tc) followed by a rest period (tr) where no current is passing through the battery as shown in Fig. 3.10. The train of pulses is applied until the voltage reaches an upper cut-off voltage of $Vcell_{max}$ to complete stage I followed by Constant voltage stage also known as stage II at $Vcell_{max}$ until $Icell_{min}$ of 100mA and 130mA is reached for power and energy cell respectively.

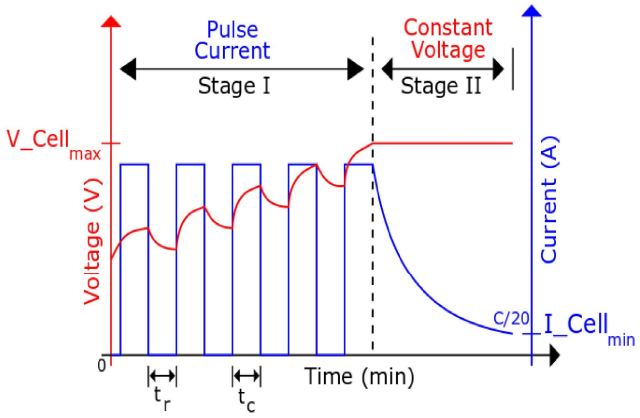

Fig. 3.10 square Current pulse charging technique

Table 9 summarizes the parameters used for the experiments to investigate the impact of square current with rest pulse in this section. Two duty cycles, 50% and 80% are used during the study. In each duty cycle, frequencies starting from 0.25Hz up to 10kHz are investigated. An amplitude of 2 C-rate is chosen for the peak current. Hence, for the square current with rest pulse, the mean current is defined as the average of current over stage I. Therefore, a 50% DT has 1C-rate mean current and 80% DT has 1.6C-rate of mean current in stage I.

Table 9 Summary of the parameters used to study the impact of square current with rest protocol

Duty Cycle (%)	I_{mean} (C-rate)	Frequency (Hz)	tc (s)	tr (s)
50	1	0.25	2	2
		2.5	$200 *10^{-3}$	$200*10^{-3}$
		25	$20*10^{-3}$	$20*10^{-3}$
		250	$2*10^{-3}$	$2*10^{-3}$
		2500	$0.2*10^{-3}$	$0.2*10^{-3}$
		5000	$0.1*10^{-3}$	$0.1*10^{-3}$
		10000	$50*10^{-6}$	$50*10^{-6}$
80	1.6	0.25	3.2	0.8
		2.5	$320*10^{-3}$	$80*10^{-3}$
		25	$32*10^{-3}$	$8*10^{-3}$
		250	$3.2*10^{-3}$	$0.8*10^{-3}$
		2500	$0.32*10^{-3}$	$0.08*10^{-3}$
		5000	$0.16*10^{-3}$	$0.04*10^{-3}$
		10000	$80*10^{-6}$	$20*10^{-6}$

3.1.1. Full charge study

Fig. 3.11 (a), (b), (c) depicts the experimental voltage, current, state of charge (SOC) and temperature curves for power cell with an on duration of 2s, rest period of 2s and duty cycle of 50%. The charging takes 79.61 minutes to charge from 0% SOC to 100% SOC with a change in temperature of only 4.08˚C beyond ambient temperature. Additionally, identical experiments were carried out at different frequencies and duty cycle as summarized in Table 10 .

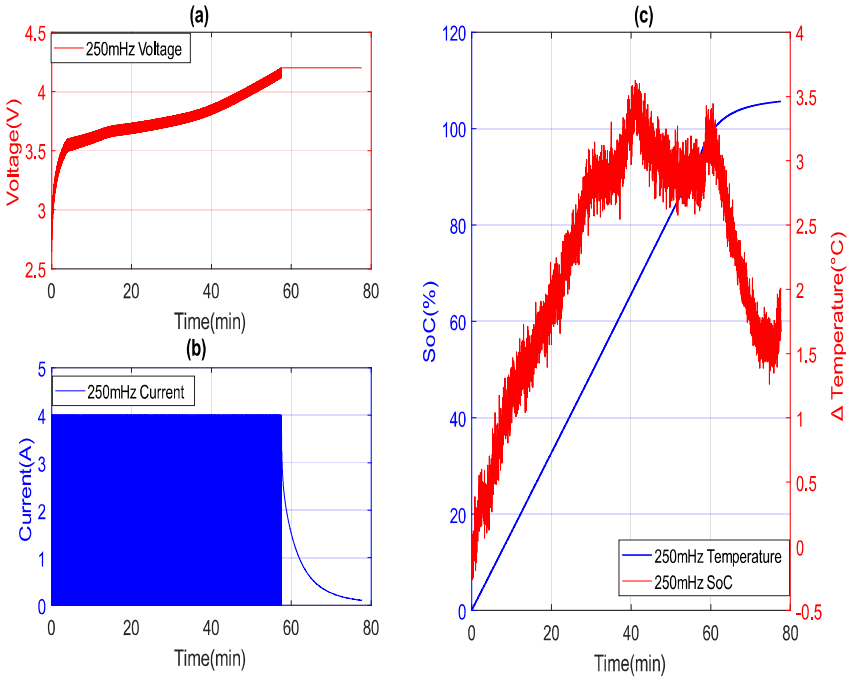

Fig. 3.11 (a) voltage, (b) current, (c) SoC and Δ temperature curves for power cell charging at 2C peak current with tc = 2s, tr = 2s and a duty cycle of 50% at 25°C ambient temperature

Fig. 3.12 compares the temperature elevation for frequencies ranging from 25mHz to 10kHz for both energy and power cells at 50% and 80% of duty cycle. For power and energy cells the surface temperature is reducing with the increase in frequency. When the frequency was increased from 250mHz to 10 kHz at 50% duty cycle and 80% duty cycle the surface temperature reduced by approximately 30%. As a reminder, from 2.5kHz to 10kHz, the high frequency pulse charger described in chapter.1 of section 1.3 is used.

3.1.2. Sensitivity analysis to the protocol parameters

Fig. 3.13 and Table 10 compares the time taken to recharge 80% SoC from 0% SoC at 50% and 80% Duty cycle for frequencies ranging from 250mHz to 10kHz for both energy and power

cells even though it is impossible to reach the time target in these conditions. As expected, there is no change in the total charging time with the increase in frequency of the current pulses at a given duty cycle. Whereas, if the duty cycle is increased by 37.5% i.e. from 50% to 80%, the total charging time reduces by approximately 37.5% for both power and energy cells. According to Table 10, for energy cell at 80% Duty cycle, the time taken to recharge from 0% up to 80%SoC includes both CV and CC stage, while it performs only along CC stage for 50% DT. This is due to the fact that the mean current is higher (1.6C-rate) which results in higher ohmic drop. As seen in the previous section, at higher C-rates without ODC the time required to reach upper-cut off voltage value is shorter and hence the CV stage comes into picture. Therefore, for square current pulse the charging time mainly depends on the C-rate and duty cycle of the current pulses.

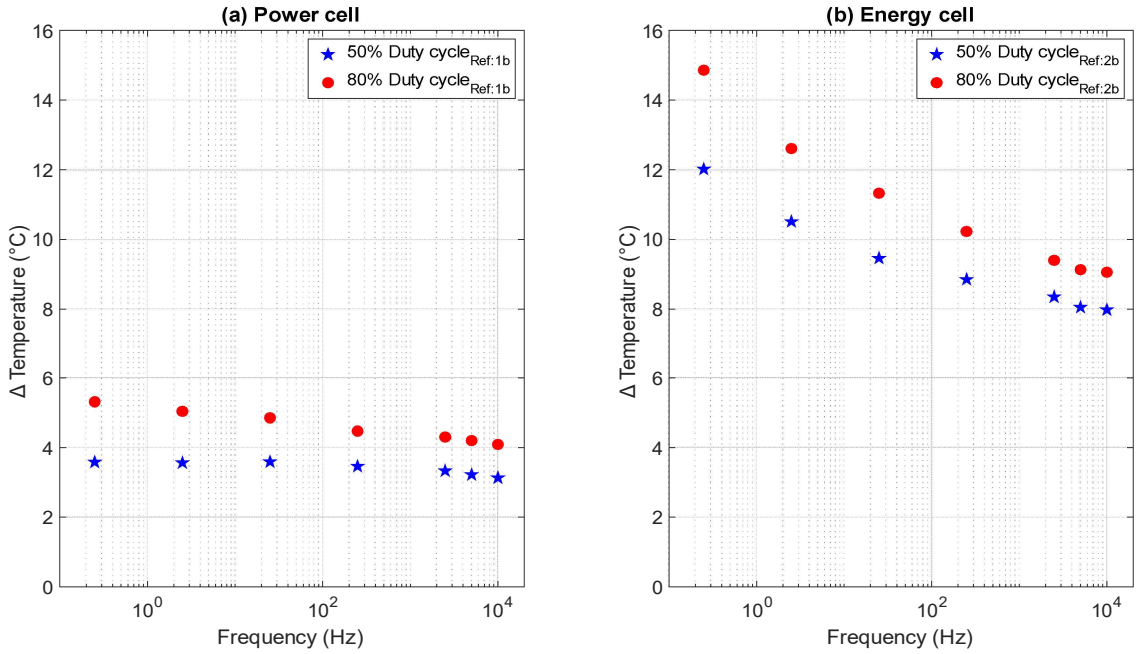

Fig. 3.12 Δ Temperature comparison for current pulse technique at 50% and 80% Duty cycle at different frequencies for energy and power cells

Another important aspect to be noted is the evolution of temperature with the increase in frequency. As shown Fig. 3.12, the Δ Temperature goes decreasing whatever the cell and DT when increasing the frequency. For example, from Table 10 and considering power cell at 80% duty cycle, when the frequency is increased by from 250mHz to 10kHz, the surface temperature reduced by approximately 1°C. Similarly, for energy cell the surface temperature reduced by 4°C and 5.5°C at 50% and 80% duty cycle respectively. Therefore, there exist a strong correlation between the frequency of the pulses and surface temperature. This later phenomenon

is due to the fact that, the impedance of the cell decreases with the increase in frequency and hence the temperature reduces due to lower joule effect. The impact of the frequency on the cell internal impedance is highlighted in fig. 2.8 in the chapter 2. In this case, it is not possible to reach the target in less than 20 minutes.

Table 10 Summary results of all the experiments on Square Current with rest pulse

	Duty Cycle	Frequency (Hz)	Time for 80% SoC (mn)	Pulse time (mn)	CV time (mn)	Total time (mn)	Δ Temperature (°C)
Power	50	0.25	49.08	59.49	20.12	79.61	3.58
		2.5	50.04	59.82	19.59	79.41	3.56
		25	48.23	57.68	20.04	77.72	3.59
		250	47.67	59.98	20.14	80.12	3.46
		2500	47.98	59.36	20.25	79.61	3.33
		5000	48.06	59.57	19.63	79.2	3.25
		10000	47.57	59.75	21.25	81.00	3.12
	80	0.25	30.45	35.32	19.32	54.64	5.31
		2.5	30.89	45.15	18.61	63.76	5.04
		25	30.26	35.61	19.09	54.70	4.85
		250	30.98	35.12	19.45	54.57	4.47
		2500	30.65	35.54	19.25	54.79	4.35
		5000	30.20	35.69	19.54	55.23	4.21
		10000	30.68	35.14	19.38	54.52	4.08
Energy	50	0.25	47.96	48.15	48.69	96.84	12.02
		2.5	48.06	48.77	52.36	101.13	10.51
		25	48.43	48.94	51.26	100.20	9.46
		250	47.86	48.36	50.98	99.34	8.85
		2500	48.23	48.72	50.54	99.26	8.35
		5000	48.65	48.93	50.58	99.51	8.05
		10000	48.36	49.02	50.23	99.25	7.98
	80	0.25	31.12	26.28	50.52	76.8	14.86
		2.5	31.73	26.85	50.92	77.77	12.61
		25	31.46	26.72	51.60	78.32	11.33
		250	31.87	26.57	51.56	78.13	10.23
		2500	31.65	26.64	51.57	78.21	9.40
		5000	31.98	26.76	51.69	78.45	9.13
		10000	31.21	26.87	51.82	78.69	9.09

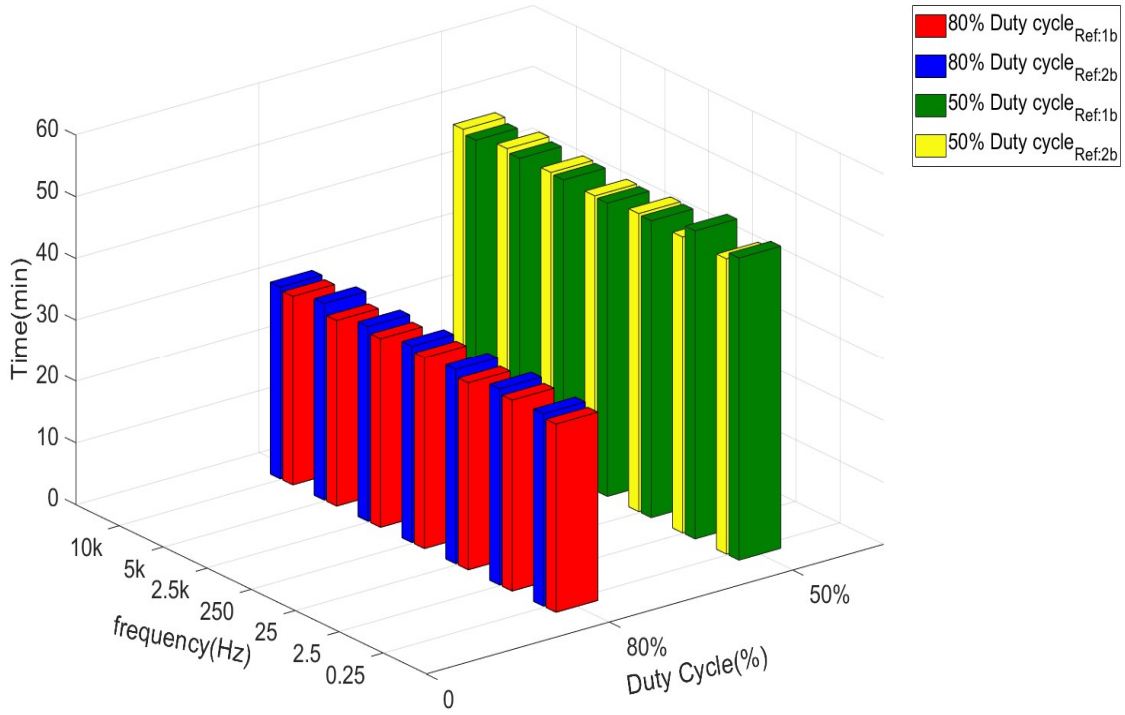

Fig. 3.13 Time taken to recharge 80% SOC from 0% SOC at 50% and 80% duty cycle for frequencies ranging from 0.25Hz to 2.5kHz for energy and power cell at 25°C ambient temperature

3.2 Presentation of protocol: square current with discharge pulse

Other pulsing charging methods proposed in the literature are square current with intermediate discharge pulse [69] [38]. This method has shown better performance in terms of cycle life when compared to the equivalent current CCCV protocol. The authors of [69] and [38] propose that the reason behind is that the short discharge pulse can increase the utilization of the active materials which could result in a higher discharging capacity and longer lifetime. Also, the authors of [70] demonstrate that the pulse charging with discharge pulses help in eliminating concentration polarization leading to increase in power transfer rate. Therefore, it is interesting to investigate the impact of square current with short discharge current pulse on charging time and temperature elevation.

In this protocol, constant amplitude pulse current (tc) is interspersed with alternating discharge pulses (td) instead of rest period as shown in Fig. 3.14. Table 11summarizes the parameters used for the experiments to investigate the impact of square current with discharge current pulse in this section. Two duty cycles, 50% and 80% is used during the study. In each

duty cycle, frequencies starting from 0.25Hz up to 250Hz is investigated. An amplitude of 2 C-rate is chosen for the peak charge current and -0.1 C-rate is chosen for peak discharge current. Hence, the mean current for 50% DT is 0.95C-rate and 80% DT is 1.52C-rate in stage I.

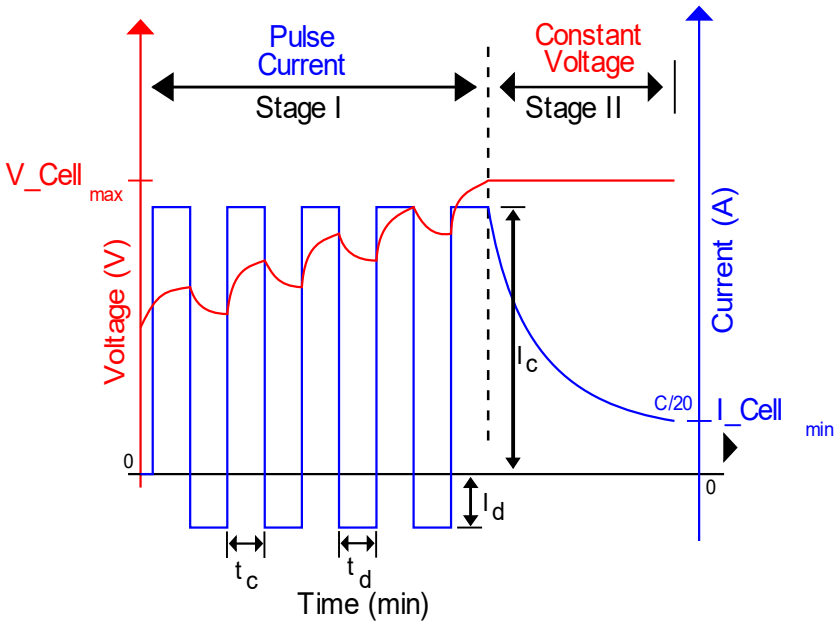

Fig. 3.14 Illustration of square current pulse with intermediate discharge pulses

Table 11 Summary of the parameters used to study the impact of square current with discharge pulse protocol

Duty Cycle (%)	$I_{peak\ charge}$ (C-rate)	$I_{peak\ discharge}$ (C-rate)	I_{mean} (C-rate)	Frequency (Hz)	tc (s)	tr (s)
50	2	-0.1	0.95	0.25	2	2
				2.5	$200*10^{-3}$	$200*10^{-3}$
				25	$20*10^{-3}$	$20*10^{-3}$
				250	$2*10^{-3}$	$2*10^{-3}$
80			1.52	0.25	3.2	0.8
				2.5	$320*10^{-3}$	$80*10^{-3}$
				25	$32*10^{-3}$	$8*10^{-3}$
				250	$3.2*10^{-3}$	$0.8*10^{-3}$

3.2.1. Full charge study

Experimental current pulse sequence of alternating charge at 2C for 2s and discharge pulse at -0.1C for 2s is shown schematically for power cell in Fig. 3.15. The evolution of voltage and current is shown in Fig. 3.15 (a) and (b) respectively. Whereas Fig. 3.15 (c) depicts the evolution of SoC and temperature elevation during charging. From Fig. 3.15, the time taken to recharge 100% SoC is approximately 81 minutes with a temperature elevation of about 5°C.

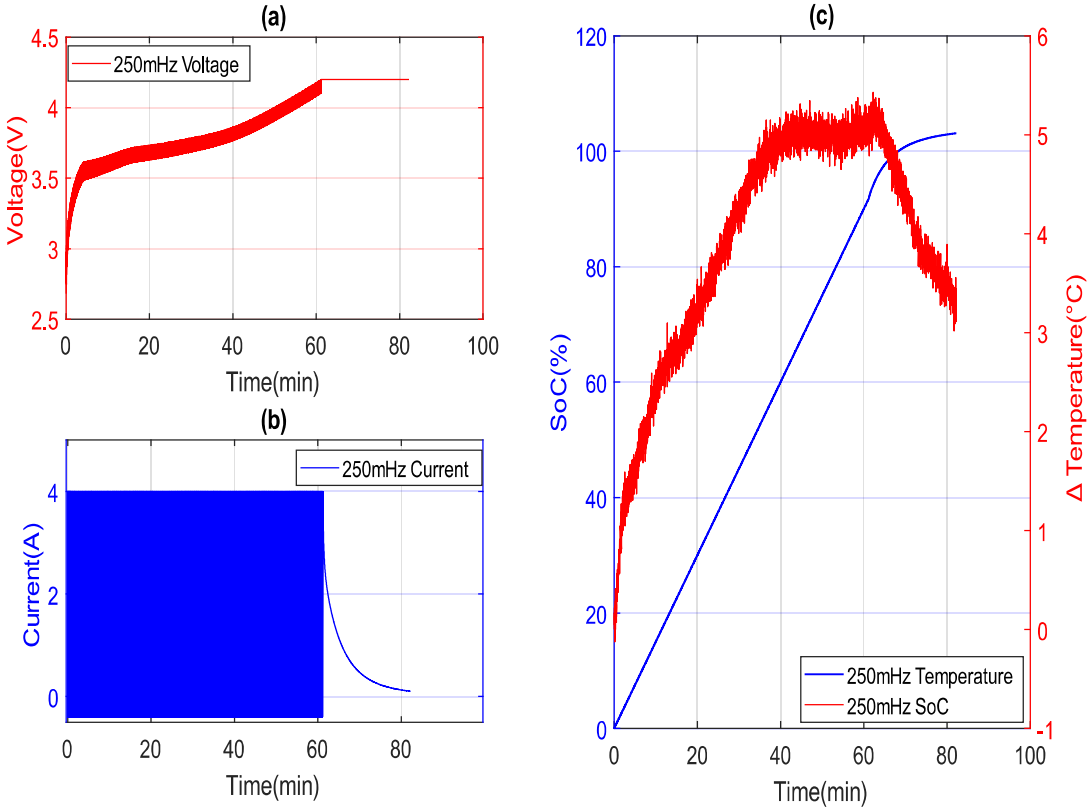

Fig. 3.15 (a) voltage, (b) current, (c) SoC and Δ temperature curves for power cell charging at 2C and -0.1C-rate current pulse with tc = 2s, td = 2s and a duty cycle of 50% at 25°C ambient temperature

From Table 12, for both power and energy cells no significant change in recharge time is observed for 100% SoC at a given DT irrespective of frequency. Although a small change in time is observed for energy cell at 50% DT. This is due to the artifact of experiments on the cells and equipment. As expected, the increase in DT leads to shorter recharge time due to the increase in mean C-rate of current.

3.2.2. Sensitivity analysis to protocol parameters

Fig. 3.16, allows comparing the time taken to recharge 80% of Δ SoC from 0% SoC at 50% and 80% Duty cycle for frequencies ranging from 250mHz to 2.5kHz for both power and energy cells. For power and energy cells, when the frequency is increased from 250mHz to 250 Hz at 50% and 80% DT, there is no significant change in the recharging time for 80% SoC.

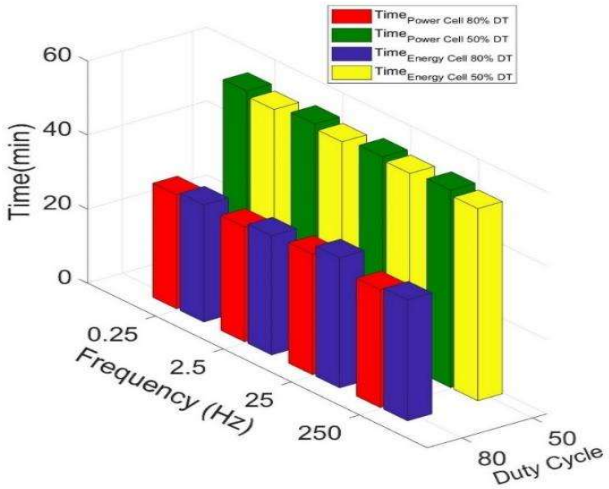

Fig. 3.16 Time taken to recharge 80% SOC from 0% SOC at 50% and 80% duty cycle for frequencies ranging from 250mHz to 250Hz for energy and power cell at 25°C ambient temperature

Fig. 3.17 compares the Δ temperature elevation for frequencies ranging from 250m Hz to 250 Hz for both energy and power cells at 50% and 80% duty cycle. From Fig. 3.17 and Table 12 it is worth noting that with the increase in frequency of the current pulse from 250mHz to 250Hz the elevation of temperature is reducing. considering power and energy cell, at 50% duty cycle, the temperature elevation is reduced by 1°C and 2.5°C respectively.

Whereas, the Δ temperature rise increases when the duty cycle is increased for the same set of frequency. Considering power cell at 250Hz, with the increase in duty cycle, the temperature rise is increased by approximately 1.5°C. This is due to the fact that, increase in duty cycle increases the mean current flowing through the battery resulting in higher temperature increase.

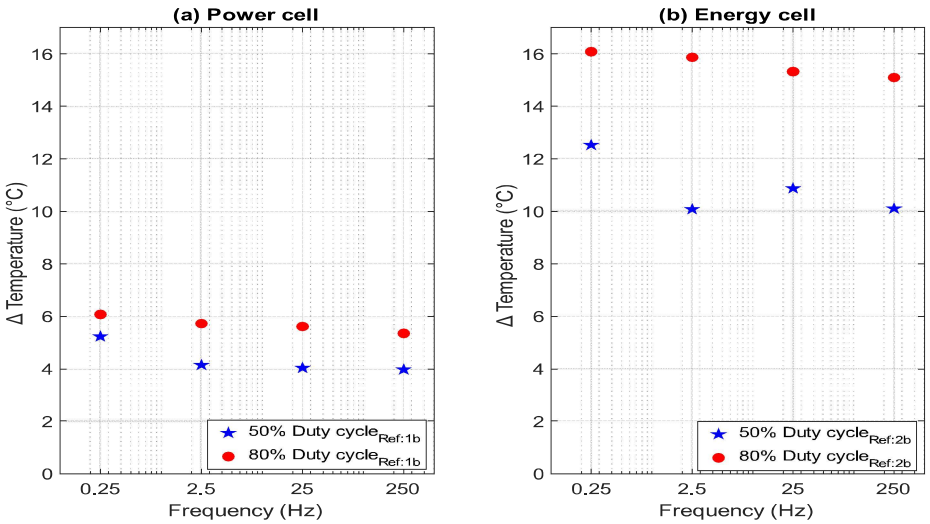

Fig. 3.17 Δ Temperature comparison for current with discharge pulse technique at 50% and 80% Duty cycle for frequencies ranging from 0.25Hz to 250Hz for energy and power cells

Table 12 Summary results of all the experiments on Square Current with discharge pulse

	Duty Cycle	Frequency (Hz)	Time for 80% SoC (min)	Pulse time (min)	CV time (min)	Total time (min)	Δ Temperature (°C)
Power	50	0.25	53.34	61.42	20.83	82.25	5.15
		2.5	53.37	61.69	19.37	81.06	4.16
		25	53.38	61.11	20.56	81.67	4.05
		250	53.26	60.27	19.58	79.85	3.98
	80	0.25	30.81	34.95	20.05	55	6.07
		2.5	30.96	34.62	20.46	55.08	5.73
		25	32.54	34.57	20.55	55.12	5.62
		250	31.86	34.21	20.29	54.5	5.36
Energy	50	0.25	51.92	46.92	55.63	102.55	12.53
		2.5	52.10	47.7	52.28	99.98	10.08
		25	52.44	47.16	54.19	101.35	10.88
		250	51.86	46.25	52.17	98.42	10.11
	80	0.25	31.61	25.95	53.75	79.7	16.07
		2.5	32.18	25.59	54.54	80.13	15.86
		25	35.14	24.45	55.08	80.53	15.32
		250	32.64	25.10	55.14	80.24	15.09

With the square current pulse using intermediate discharge pulse protocol it is difficult to reach the target time.

3.3 Presentation of protocol: Triangular current pulse

So far only square current pulse with variations in amplitude, frequency and DT is discussed in literature. Therefore, it is interesting to study the impact of triangular current pulse on cell performance in terms of recharging time and temperature elevation. Triangular current pulse protocol is a modified version of square current pulse protocol. Where in the current is linearly increased (dI/dt) and decreased (-dI/dt) with respect to time until a peak pre-set C-Rate is reached as shown in Fig. 3.18. In this protocol the slope of current determines the frequency of the current. The rate of change of current is constantly varied until upper cut-off voltage 4.2 V is reached. Later the charging is continued with classical CV stage until the current drops to C/20.

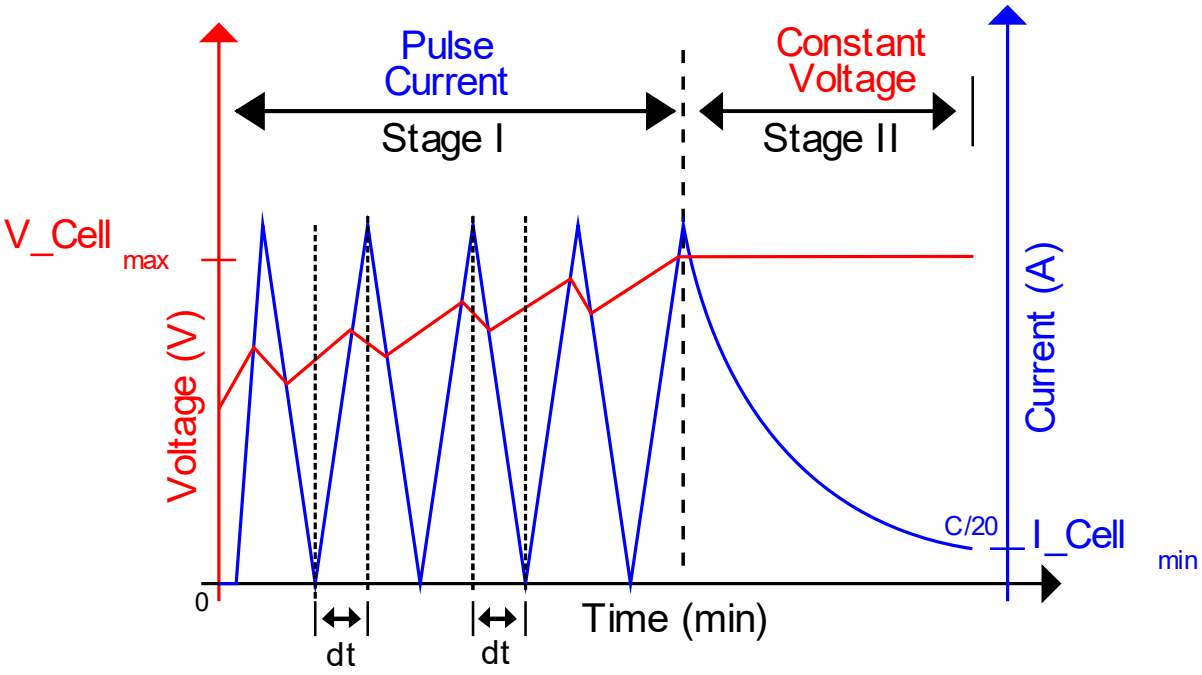

Fig. 3.18 Illustration of triangular current pulse

Table 13 summarizes the parameters used for the experiments to investigate the impact of Triangular current pulse in this section. Two frequencies, 250mHz and 500mHz are used during the study. This frequency is chosen due to the limitation of the potentiostat (BioLogic or Arbin or developed pulse charger). For each frequency, with and without ODC is investigated. A full ohmic drop compensation is considered in this section. An amplitude of 2 C-rate and 4C-rate is chosen for the peak current. Hence, the mean current in all the experiments are 1C-rate and 2C-rate respectively in stage I.

Table 13 Summary of the parameters used to study the impact of triangular current pulse protocol

Protocol	Frequency (Hz)	dt (s)	$I_{peak\ charge}$ (C-rate)	dI/dt (C-rate/s)	I_{mean} (C-rate)
Without ODC	$250 * 10^{-3}$	2	2	1	1
	$500 * 10^{-3}$	1		2	
ODC	$250 * 10^{-3}$	2		1	
	$500 * 10^{-3}$	1		2	

3.3.1. Full charge study

Fig. 3.19 illustrates the voltage and current evolution for complete charging. While Fig. 3.20 is the snippet of voltage and current curves for energy cell charging with a frequency of 250mHz at 20minutes. In this condition, the current pulse and CV stages last respectively 42 and 58 minutes for a total charging time of 100 minutes.

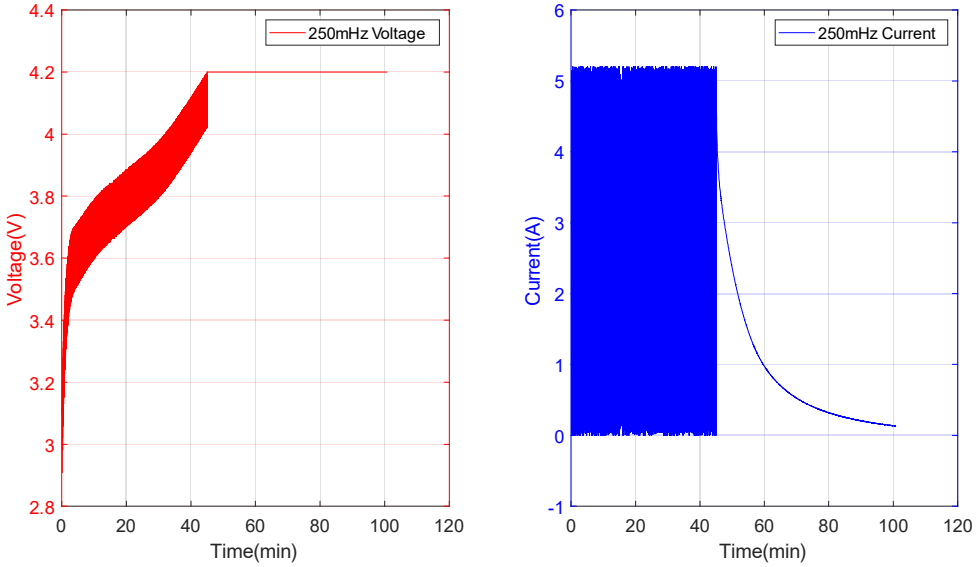

Fig. 3.19 voltage in red and current in blue for energy cell charging at 2C-rate triangular pulse with dI/dt =2.6A/s and a frequency of 250mHz at 25°C ambient temperature

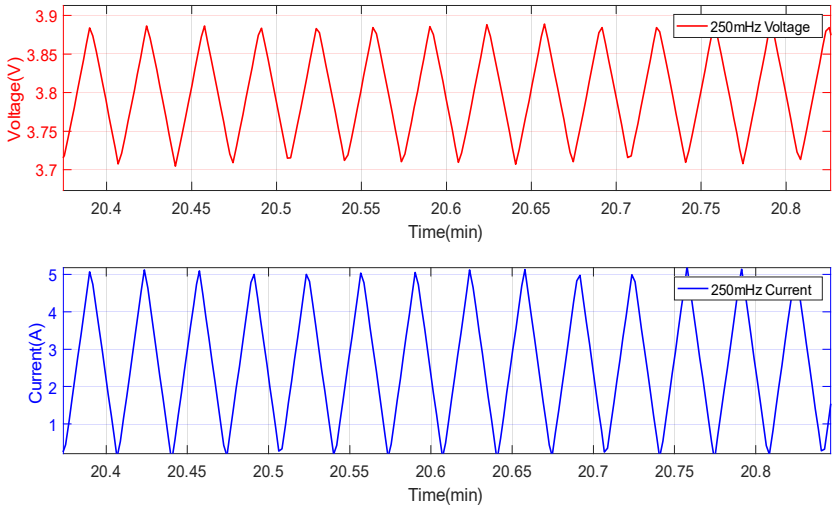

Fig. 3.20 Snippet of voltage in red and current in blue at 20 minutes for energy cell charging at 2C triangular pulse with dI/dt =2.6A/s and a frequency of 250mHz at 25°C ambient temperature

Table 14 summarize all the results for triangular current pulse method with and without ODC. Without Ohmic Drop Compensation, the influence of the parameters for the triangular pulses are very similar to the one observed with the square pulses.

Ohmic Drop compensation allows increasing the pulse current stage. From the *Table 14*, for power cell, at 250mHz, at 1C-rate mean current, the ODC increased approximately 2 minutes of the pulse charging time yielding 4% increase in SoC with a temperature elevation of 1°C. For, energy cell, at 250mHz, at 1C-rate mean current, the ODC increased the charging time by 10 minutes yielding 17% more SoC with a temperature elevation of only 1.25°C.

At 2C-rate mean current (4C-rate peak current), for power cell, at 250mHz, the ODC increased the pulse charging time by 4 minutes resulting in an increase of SoC by approximately 14% with a temperature elevation of only 0.85°C. Whereas, for energy cell, at 250mHz, the ODC increased the pulse charging time by 10 minutes resulting in an increase of SoC by approximately 34% without any temperature elevation. Between 250mHz and 500mHz no significant change is observed as these frequencies are very close together (i.e. the impedance being almost the same).

3.3.2. Sensitivity analysis to protocol parameters

To go further, Fig. 3.21 compares the time taken to recharge 80% of Δ SoC from 0% SoC at 1C-rate (2C-rate peak current), and 2C-rate mean current (4C-rate peak current) with and without ODC from energy (a) and power (b) cell at 25°C ambient temperature. From

Fig. 3.21 and *Table 14*, it is clear that increasing the peak C-rate or mean C-rate during charging by a factor 2 reduces the time taken to recharge 80% SoC by approximately 50% as expected for both energy and power cell irrespective of the applied frequency and with or without ODC. Also, it is worth mentioning that for power cell, even at 2C-rate mean current irrespective of ODC, there is no Stage II or CV stage according to Fig. 3.21. But for energy cell, without ODC, to recharge 80% SoC it is impossible without stage II or CV stage. By using ODC method the CV stage can be eliminated to recharge 80% of SoC.

Hence, even with ODC, at 2C-rate mean current (4C-rate peak current) it is difficult to meet the target of 80% SoC in 20 minutes. Increasing the peak C-rate with ODC could be a possible solution. Nevertheless, doing so, the cell will be subjected to over voltage condition for longer duration leading to damage of the cell.

Table 14 Summary results of all the experiments on current pulse with discharge technique

	Mean C-rate		Frequency (Hz)	Time for 80% SoC (min)	Stage I time (min)	Qc at the end of stage I (mAh)	Δ Temperature (°C)
Power	1	Without ODC	0.25	49.75	56.38	1877.66	2.95
			0.5	49.32	56.23	1874.33	3.29
		ODC	0.25	48.16	58.64	1954.66	3.99
			0.5	48.21	58.72	1957.33	3.48
	2	Without ODC	0.25	24.05	24.46	1630.66	11.36
			0.5	23.96	24.58	1638.66	10.16
		ODC	0.25	24.11	28.74	1916.26	12.21
			0.5	24.09	28.69	1912.98	12.17
Energy	1	Without ODC	0.25	49.19	41.70	1807.32	8.23
			0.5	49.25	41.44	1795.73	7.96
		ODC	0.25	48.01	51.91	2249.43	9.48
			0.5	48.09	51.64	2237.73	8.80
	2	Without ODC	0.25	23.13	14.44	1251.46	21.12
			0.5	23.08	14.19	1229.28	21.19
		ODC	0.25	23.89	24.9	2158.32	20.06
			0.5	23.42	25.10	2175.34	19.87

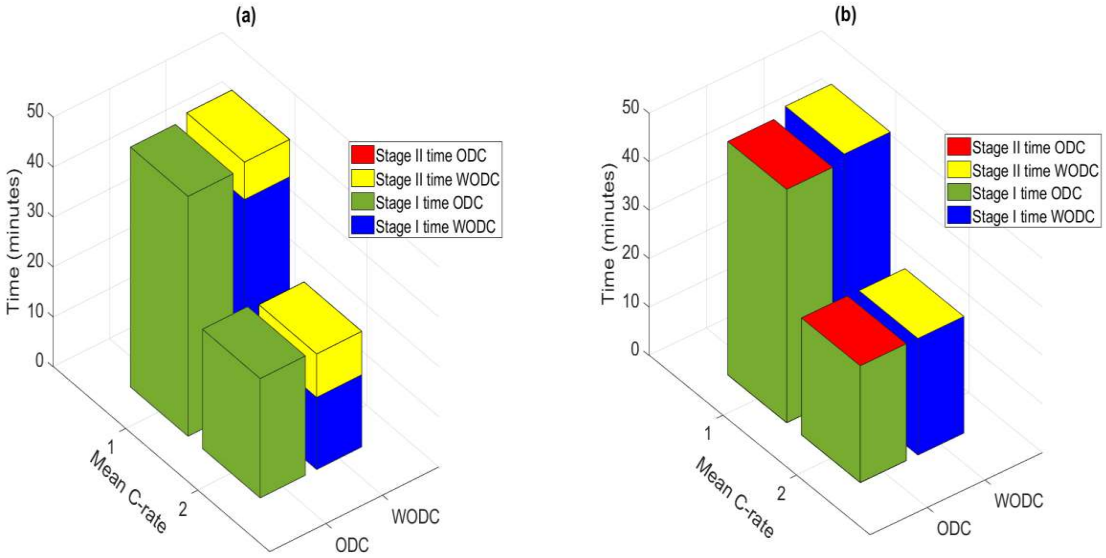

Fig. 3.21 Comparison of time taken to charge 80% SOC from 0% Soc at different mean C rates with ODC and without ODC for energy (a) and power (b) cell at 25°C ambient temperature

4. Discussion of current based protocol

This section compares CCCV, square and triangular protocols discussed so far in previous section, with respect to charging time and temperature rise. Fig. 3.22 illustrates the comparison between voltage and current curves for square and triangular current pulse charging at 250mHz, 2C-rate peak current.

Fig. 3.23 compares the voltage, current, SoC and temperature evolutions for energy cell at an average of 1C-rate and 2C-rate for CCCV and square current pulse. From the Fig. 3.23 it is clear that irrespective of the protocol, the total recharging time remains same relative to the mean current applied for energy cell and the same holds good for power cell as well. Also, from Fig. 3.23, for 1C-rate mean current, the Δ temperature elevation for the square current pulse protocol at 500mHz, 50% DT is approximately 7°C. For 2C-rate mean current, the temperature elevation between CCCV and Square current pulse protocol at 500mHz, 50% DT is approximately 7°C higher than the one for between CCCV.

Table 15 summarize the experimental data for CCCV, square and triangular current pulse technique at 250mHz and 500mHz with and without ODC for power and energy optimized cells. In order to investigate the effect of shape of the waveform and frequency of pulses on the cells for recharging time and temperature, two different mean C-rates (1C-rate and 2C-rate) are tested.

According to Table 15, for power and energy optimized cells, the frequency and shape of the waveform has no significant effect on the time take to recharge 80% SoC in comparison with the mean C-rate. Moreover, the total charging also remains approximately same for square and triangular pulse current with and without ODC. The duration of the stage I i.e pulse stage increases by using ODC technique coupled with square or triangular current pulse. This is mainly due to the ohmic drop contribution and it is explained in detail in previous section.

From Table 15, at 2C-rate mean current, the time taken to recharge 80% SoC is close to the target time for both power and energy cells even though we are well within the target temperature elevation. This indicates that to meet the target time a C-rate higher than 2C-rate is necessary for both power and energy cells.

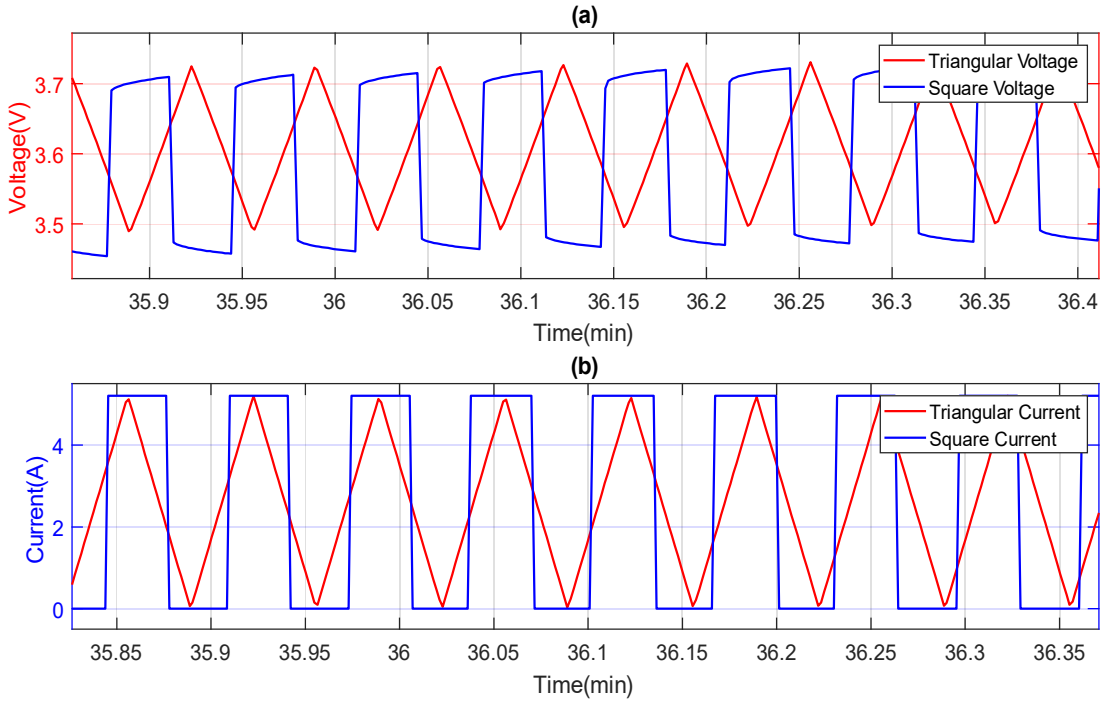

Fig. 3.22 (a) Comparison of Voltage curves for Square in blue and Triangular in red. (b) Comparison of current curves for Square in blue and Triangular in red for Energy cell at 2C, 250mHz peak current and 50% DT

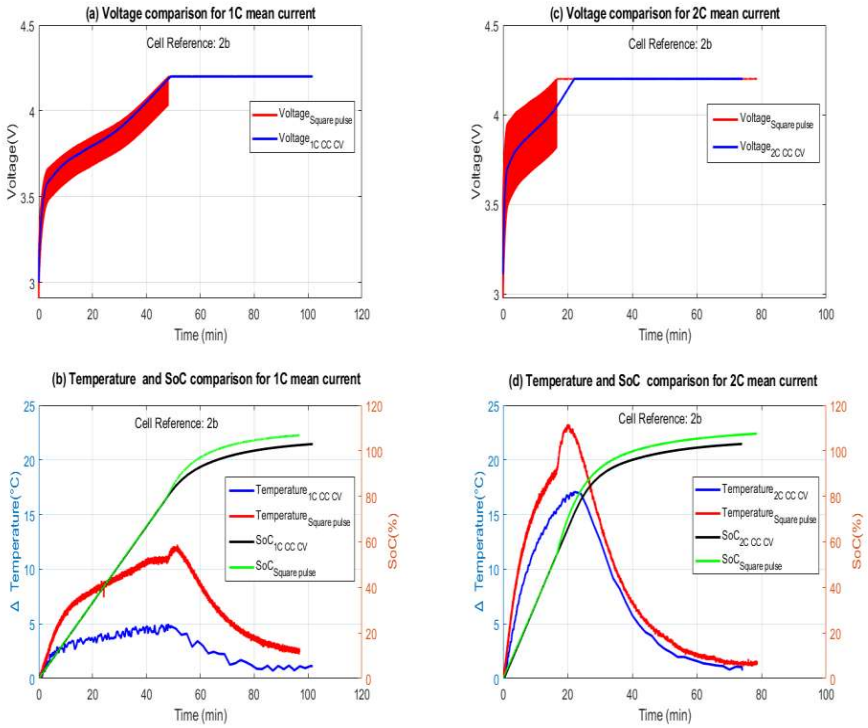

Fig. 3.23 (a)voltage (V) comparison between 1C CC-CV and 1C mean square current pulse without ODC at 500mHz for energy cell (b) Temperature (°C) and SoC (%) comparison between 1C CC-CV and 1C mean square current pulse without ODC at 500mHz and 50% DT for energy cell (c) voltage (V) comparison between 2C CC-CV and 2C mean square current pulse without ODC at 500mHz and 50% DT for energy cell (d) Temperature (°C) and SoC (%) comparison between 2C CC-CV and 2C mean square current pulse without ODC at 500mHz and 50% DT for energy cell

As shown in Table 15, even though the charging time is similar, difference in temperature between square and triangular current based charging can be observed. Whatever the C-rate, the Δ Temperature is always higher with square current pulses than with triangular one. For example, considering the energy cell charged with ODC at 0.25Hz, 1C-rate mean, the Δ Temperature with triangular current pulse approximately is 21% (i.e 2.54°C) less than the square current pulse.

This difference in temperature for similar recharging times can be comprehended with the help of Root Mean Square (RMS) currents.

$$I_{rms_{triangular}} = {I_{pk}}/{\sqrt{3}} \tag{23}$$

$$I_{rms\ \ square} = {I_{pk}}/{\sqrt{2}} \tag{24}$$

By equating the equation 16 and 17, the $I_{rms\_triangular}$ is equal to 0.816 times the I_{rms_Square} as given in equation 18

$$I_{rms_{triangular}} = {\sqrt{2}}/{\sqrt{3}} * I_{rms_{square}} \quad (25)$$

Hence, as a result of low value of RMS current for triangular wave the elevation of temperature is lower than that of Square wave due to less joule effect.

The RMS current which is the square root of arithmetic mean of the squares of current that is the actual mean DC equivalent current flowing through the battery for Triangular and Square wave given by equations 17 and 18.

These latter results show that in order to achieve the target of 80% SoC in 20 minutes, investigations must be made using a high C-rate. In our particular case, the ideal C-rate to achieve the target is a mean 3C-rate. However, care must be taken with respect to temperature elevation when working at mean 3C-rate current.

With the protocols discussed so far, to have a mean 3C-rate, the peak C-rate required is 6C-rate. By implying 6C-rate of current to the cell, the maximum cut-off voltage reaches faster and the charging continues only in CV stage due to the internal resistance. Also keeping in mind, the safety aspect, we did not procced ahead with higher C-rate.

Table 15 comparison of charging time and Δ Temperature between Square and Triangular current based pulse charging

		Wave form Shape	Frequency (Hz)	Time for 80% SoC (min)	Pulse time (min)	CV time (min)	Total time (min)	Δ Temperature (°C)
Power	Without ODC	1C CC CV	-	48.08	56.23	23.25	79.48	2.51
		Square	0.25	49.08	59.49	20.12	79.61	4.08
			0.5	49.23	58.83	20.54	79.37	3.98
		Triangular	0.25	49.75	56.38	21.23	77.61	2.95
			0.5	49.32	56.23	20.98	77.21	3.29
	ODC	1C CC CV		48.22	58.18	19.64	77.82	3.58
		Square	0.25	48.36	59.73	19.72	79.45	4.71
			0.5	48.24	60.12	19.64	79.76	3.92
		Triangular	0.25	48.16	58.64	19.89	78.53	3.99
			0.5	48.21	58.72	19.36	78.08	3.48
	Without ODC	2C CC CV	-	24.02	25.81	23.94	49.75	4.21
		Square	0.25	24.08	24.39	21.25	45.64	11.25
			0.5	24.12	24.46	21.19	45.65	11.36
		Triangular	0.25	24.05	24.58	21.45	46.03	10.16
			0.5	23.96	24.69	21.39	46.08	10.08
	ODC	2C CC CV	-	24.05	29.55	17.48	47.03	6.89
		Square	0.25	24.12	29.90	16.58	46.48	9.85
			0.5	24.06	29.97	17.02	46.99	10.06
		Triangular	0.25	24.11	28.74	15.57	44.31	12.21
			0.5	24.09	28.69	15.68	44.37	12.17
Energy	Without ODC	1C CC CV	-	48.02	48.95	52.78	101.73	5.68
		Square	0.25	49.08	41.76	48.36	90.12	12.53
			0.5	49.12	41.28	48.03	89.31	12.08
		Triangular	0.25	49.19	41.70	48.25	89.95	8.23
			0.5	49.25	41.44	48.16	89.60	7.96
	ODC	1C CC CV	-	51.06	49.63	41.54	91.17	6.88
		Square	0.25	47.96	48.15	48.69	96.84	12.0
			0.5	48.05	48.36	49.06	97.42	11.96
		Triangular	0.25	48.01	51.91	48.72	100.63	9.48
			0.5	48.09	51.64	49.12	100.76	8.80
	Without ODC	2C CC CV	-	24.01	22.01	48.77	70.78	20.85
		Square	0.25	22.86	14.16	60.94	75.10	23.88
			0.5	22.92	14.26	61.02	75.28	24.06
		Triangular	0.25	23.13	14.44	61.34	75.78	21.12
			0.5	23.08	14.19	61.09	75.28	21.19
	ODC	2C CC CV	-	23.98	25.47	25.58	51.05	19.99
		Square	0.25	26.58	23.21	66.19	89.4	21.35
			0.5	26.53	23.14	66.13	89.27	21.42
		Triangular	0.25	23.89	24.9	57.98	82.88	20.06
			0.5	23.42	25.10	58.06	83.16	19.87

5. Conclusion

Several experiments were conducted on power and energy optimized NMC based 18650 cells to study the impact in terms of shape of the waveform and temperature rise of fast charging. The square and triangular current pulse methods was compared with the classical CCCV protocol alongside with studying the impact of frequency on square current pulses. Even though square and triangular pulse current have similar charging times in the pulse charging stage, a considerable difference in temperature increase can be observed.

The thermal behavior for all the charging methods is studied parallelly. It turns out that, the temperature increase was in accordance with the C-rate. This temperature increase could be minimized by incorporating triangular pulses. Irrespective of the shape of the waveform, the CV stage is inevitable and thus prolongs the charging process resulting in longer recharging time. It is now of interest to study the impact of shape of the waveform on cell parameters in terms of ageing. Also, it is important to find an alternative technique that reduces recharging time below 20minutes without accelerating the ageing. Therefore, in Chapter 4, a protocol based on the voltage control will be investigated.

Chapter 4. Voltage control technique

1. Introduction

Fast charging of the batteries has become a key issue in the automotive world. With the rapid growth in adaptation to EV, the optimum protocol to recharge the battery in shorter time remains a mystery. Therefore, in this chapter, fast charging of the NMC based lithium batteries is investigated with respect voltage-based protocols. All the characteristics of the batteries used in this chapter can be found in section 1.2 of Chapter 2. This chapter will put forward the technique and results for fast charging protocols based on voltage control in terms of charging time, and temperature rise beyond ambient temperature to be compare to the time and temperature targets. In this Chapter, from the industrial aspect linked with IBIS project, the protocol starts from 10% SoC mainly for two reasons:

- The internal resistance of the cell at 0% SoC is greater than twice as that of 10% SoC (see Fig. 2.7 of Chapter 2 section 2.2)
- Also, in real time vehicle application, the battery is neither discharged to 0% SoC nor charged until 100% in a case of a fast charge.

To reiterate, CCCV with Ohmic Drop Compensation (ODC) consists in compensating the ohmic drop of the cell due to the internal resistance ($R_{internal}$) at the end of stage I by changing the upper cut off voltage limit. This protocol was used for fast charging of the LFP cells by Noh et al. [8]. In this method the ohmic drop of the battery is compensated by charging the battery to a higher upper-bound voltage limit at the end of CC stage. The upper bound voltage limit $V_{max}{}'$ is calculated according to equation 1 considering the high frequency internal resistance of the cell. As example, for a 3C-rate, the upper bound voltage is, thus, given by:

$$V'_{max} = V_{cell\,max} + R_{internal} * I_{3C-ra} \tag{26}$$

Where, $V_{cell\,max}$ is the upper-bound limit voltage in V prescribed by the manufacturer, $R_{internal}$ is the high frequency internal resistance in Ω, and I_{3C-ra} is defined by:

$$I_{3C-rate} = \frac{Q_{nominal}}{1/3 * 1h} \tag{27}$$

$Q_{nominal}$ being the nominal capacity of the cell in Ah.

As in our case, a target recharge time of 20 minutes in mandatory for EV application, a minimal C-rate of 3C is required that correspond to a time of one third (1/3).

The charging stage follows the conventional constant voltage, CV stage where the voltage is maintained at the upper-bound limit voltage from manufacturer, $V_{cell\ max}$.

2. Proposed techniques

This section discusses influence of voltage-based protocol on C/NMC battery. In particular, 2 protocols are tested so far and results are established in terms of charging time and temperature increase. Comparison of the effectiveness of the fast charging with voltage control and current control for the cells are also set forth. The idea of this protocol is to compensate the ohmic drop to determine the voltage profile applied to the cells.

2.1 Presentation of protocols

The proposed techniques consist of applying a given cell voltage profile in order to obtain a mean current of 3C-rate that allows to recharge 80% of the capacity of the battery in a duration lower than 20 minutes. The cell voltage profile can be estimated by considering the ohmic drop compensation and the open circuit potential (OCV) of cell, thanks to:

$$V_{3C} = V_{OCV(SoC)} + (R_{internal} * I_{3C-ra}) \quad (28)$$

Where,

$V_{ocv(SoC)}$ is the open circuit voltage as a function of SoC in V.

$R_{internal}$ is the internal resistance of the cell in mΩ.

$I_{3C-rate}$ is required current in Amps to recharge the cell

So, the corresponding applied cell voltage profile can be obtained by reconstructing the OCV curve by considering the ohmic drop contribution.

Since it is impossible to set a continuous cell voltage profile, we propose to discretize it by setting a constant step voltage. Furthermore, based on the limits of each step, the proposed protocol is divided into two sub-protocols. The first, called as Voltage Step with Time Limit (VSTL) consist in applying a specific step voltage for a given duration before proceeding to the next step. The second protocol is known as Voltage Step with Current Limit (VSCL) consist in applying a step voltage until the current reach a given current limit before proceeding to the next step. This voltage profiles are applied until the manufacturer's voltage cut-off is reached.

Upon reaching the manufacturer's cut-off voltage, the charging continues with a specific stepped pulse voltage.

So, irrespective of the type of the cells, the charge protocol is divided into different steps:

- at first, the cells are charged to 10% of Δ SoC using 0.5C-rate constant current and allowed to rest for 25 minutes to reach open circuit voltage (OCV).
- Secondly, specific voltage steps protocol starts from the open circuit voltage at 10% SoC of the battery and reaches the upper cut off voltage as prescribed by the manufacturer. The amplitude of voltage at each step is calculated using Equation 25.
- Finally, voltage pulses commence and the charging terminates after reaching 90% actual SoC.

In the next sections, two algorithms are proposed to set the specific voltage profile considering either a duration for the step voltage or a current limit as explained in following sections.

2.1.1. Voltage step with time as limit (VSTL)

VSTL profile is proposed by increasing the cell voltage step by step considering the time as a limiting condition at each step as shown in Fig. 4.1 (left). For every step *i,* the applied cell voltage $[V(SoC_i)_S]$ is given by equation 4.

$$V(SoC_i)_S = V_{pOCV}(SoC_i) + (R_{internal} * I_{3C-rate}) \quad (29)$$

This cell voltage is applied during the duration **"Δt"**

Since, the terminating condition for every step is time, the capacity at the end of each step can be estimated. Based on the calculated capacity, the corresponding pOCV is deduced at the end of step, and the ohmic drop contribution is added to calculate the next step voltage $[V(SoC_{i+1})_S]$.

To obtain the next step voltage $V(SoC_{i+1})_S$, SoC_{i+1} is calculated at the end of the step i:

$$SoC_{i+1} = SoC_i + \frac{\bar{I}_i \Delta t}{Q_{nominal}} \quad (30)$$

considering the average current $\bar{I}_i$ by using:

$$\bar{I}_i = \frac{\int_{t_i}^{t_i+\Delta t} Idt}{\Delta t} \tag{31}$$

To obtain the next step voltage:

$$V(SoC_{i+1})_S = V_{pOCV}(SoC_{i+1}) + (R_{internal} * I_{3C-rate}) \tag{32}$$

Note that, the duration of each step, Δt, can be symmetric or asymmetric.

Table 16 highlights the parameters used to charge the cells with VSTL protocol. As stated in Chapter 3, to meet the target of 80% of Δ SoC in 20 minutes, a mean of 3C-rate is maintained by carefully selecting the parameter ***"n"*** of Equation 25. The step time was varied from 5 seconds to 90 seconds based on the voltage step and capacity charge. In addition, after reaching the maximum cut off voltage prescribed by the manufacturer, the charging continues with constant step voltage pulses. The reason behind this is to avoid any side reactions causing due to higher cell voltage and to mitigate the Li plating thereby decelerating the ageing. The charge time is 0.8 seconds and rest time is 0.2 seconds that constitute a DT of 80%. The experiment is terminated based on the total capacity estimated by the equipment.

Parameter	Range of investigation
t_{step} (seconds)	5 → 90
Number of steps (N)	6 → 90
t_c (seconds)	0.8
t_r (seconds)	0.2
DT (%)	80
V_{init} (V)	3.7 → 3.9
V_{final} (V)	4.2 → 4.31
Ambient temperature (°C)	25

Table 16 Overview of the parameters used in the VSTL experiments

2.1.2. Voltage step with current as limit (VSCL)

Second protocol, VSCL is proposed by increasing the cell voltage step by step considering a current limit during each step. VSCL profile is shown in Fig. 4.1 (right). Namely, the step

voltage profile is configured to maintain a mean of 3C-rate current throughout in order to meet the target of 80% of Δ SoC in 20 minutes

During the step i, the applied cell voltage, $[V(SoC_i)_S]$ is calculated as previously thanks to equation 4 until the current limit is reached.

When the current limit is reached, the next step voltage $[V(SoC_{i+1})_S]$, is calculated by considering the equation 7 where SoC_{i+1} is calculated using

$$SoC_{i+1} = SoC_i + \frac{\bar{I}_i * \Delta t_i}{Q_{nominal}} \tag{33}$$

Where, Δt_i is the duration of the step time,i, and $\bar{I}_i$ is the average current which is calculated using:

$$\bar{I}_i = \frac{\int_{t_i}^{t_i + \Delta t_i} Idt}{\Delta t_i} \tag{34}$$

In order to have the mean 3C-rate current, the current limit is varied from 4C-rate to 2C-rate.

To reiterate both the methods VSTL (left) and VSCL (right) are illustrated in Fig. 4.1

Table 17 highlights the parameters used to charge the cells with VSCL protocol;

Table 17 Overview of the parameters used in the VSCL experiments

Parameter	Range of investigation
I_{limit} (A)	5 → 8
Number of steps (N)	7 → 10
t_c (seconds)	0.8
t_r (seconds)	0.2
DT (%)	80
V_{init} (V)	3.7 → 3.9
V_{final} (V)	4.2 → 4.31
Ambient temperature (°C)	25

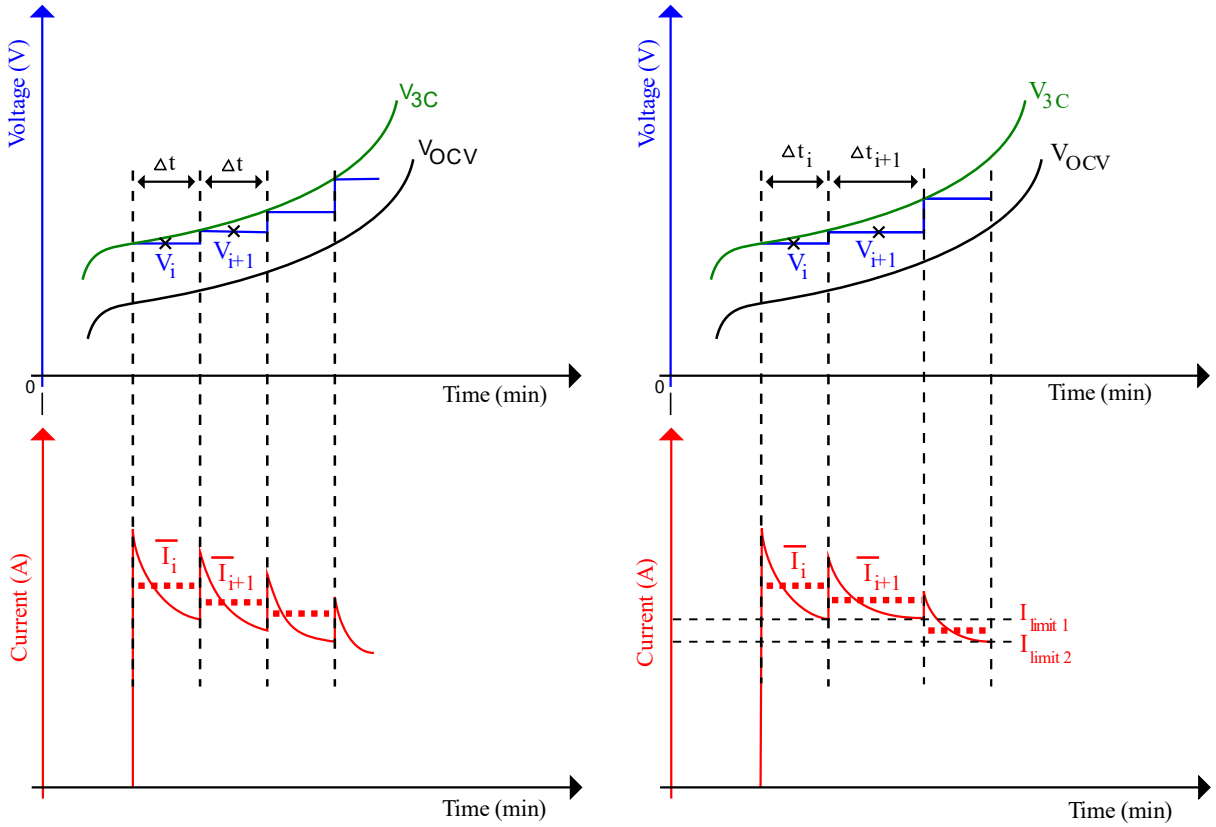

Fig. 4.1 Proposed voltage step with time limit (left) and voltage step with current limit (right) protocol

2.1.3. Pulsed voltage step

Irrespective to both previous voltage steps methods, after reaching the maximum cut off voltage prescribed by the manufacturer, the charging continues with a specific voltage pulsed step. Application of pulsed voltage step is beneficial to the cell especially at higher SoCs as it avoids any side reactions arising due to overvoltage and mitigate the Li plating which is one of the major degradation mechanisms for graphite electrode [4]. The literature [31] highlights that pulsing the potential of the electrode enables the control of equivalent diffusion layer thickness and limits the concentration of overpotentials.

Basically, stepped voltage pulse charging consists of applying a voltage step amplitude calculated using the previously equation 2 for a duration of t_c with intermediate interruption for a duration of t_r called relaxation period as shown in Fig. 4.2 .

For VSTL protocol (Fig. 4.2, left), the voltage pulses are applied during the same Δt duration considering the equation 10:

$$V(SoC_j)_P = V_{pocv}(SoC_j) + (R_{internal} * I_{3C-rate}) \quad (35)$$

To obtain the next pulsed voltage step $V(SoC_{j+1})_P$, SoC_{j+1} is calculated at the end of the step i:

$$SoC_{j+1} = SoC_j + \frac{\bar{I}_j \Delta t}{Q_{nominal}} \quad (36)$$

considering the average current $\bar{I}_i$ by using:

$$\bar{I}_j = \frac{\sum_k \left(\int_{t_k}^{t_k + t_c} I \, dt + \int_{t_k + t_c}^{(t_k + t_c) + t_r} 0 \, dt \right)}{\Delta t} \quad (37)$$

To obtain the next step voltage:

$$V(SoC_{i+1})_P = V_{pocv}(SoC_{i+1}) + (R_{internal} * I_{3C-ra} \quad) \quad (38)$$

Similarly, for VSCL (Fig 4.2, right), the pulsed voltage is applied until the I_{Limit} is reached during t_c duration and the average current is calculated using equation 14:

$$\bar{I}_j = \frac{\sum_k \left(\int_{t_k}^{t_k + t_c} I \, dt + \int_{t_k + t_c}^{(t_k + t_c) + t_r} 0 \, dt \right)}{\Delta t_i} \quad (39)$$

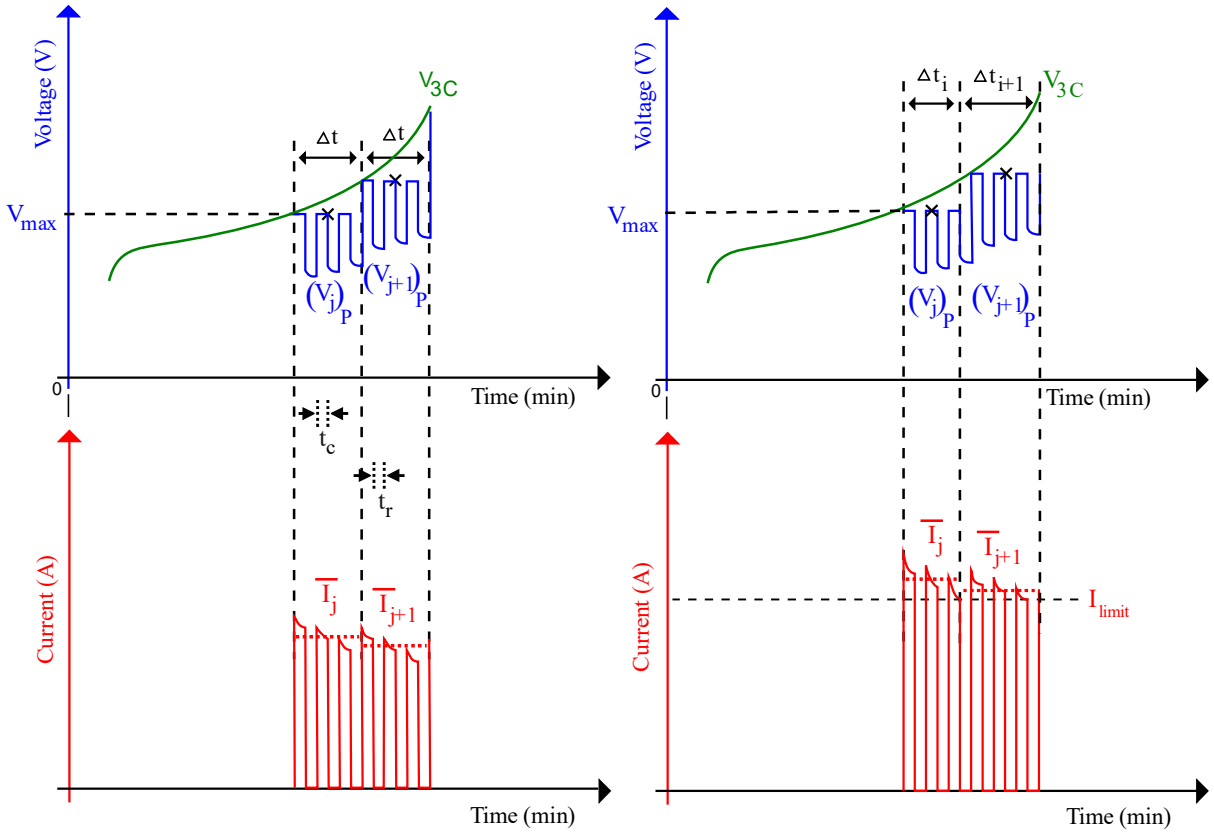

Fig. 4.2 Pulsed voltage steps for VSTL (left) and VSCL (right) protocols

2.2 Results and Discussion

In this section, the results obtained for VSTL and VSCL protocols is evaluated regarding the recharging duration and thermal behavior. As a reminder, the difference between VSTL and VSCL lies in the terminating condition for every step. i.e for VSTL time is the limit for every step and for VSCL current is the limit for every step. All the test parameters are given beforehand.

2.2.1. Voltage step with time as limit

Fig. 4.3 shows the cell voltage, current, Δ temperature elevation and SoC evolution during VSTL protocol at first iteration. In this iteration, an incremental voltage step is applied to charge from 10% SoC to 90% SoC by keeping a constant step time for both power and energy cell as shown in Fig. 4.3. As explained earlier, after reaching a maximum cut off voltage prescribed by the manufacturer, the charging resumes with a pulsating step voltage with charge time is 0.8

seconds and rest time is 0.2 seconds. In total, this protocol contained 90 steps with a constant step time of 8 seconds constituting a total recharging time of 12 minutes as shown in Fig. 4.3.

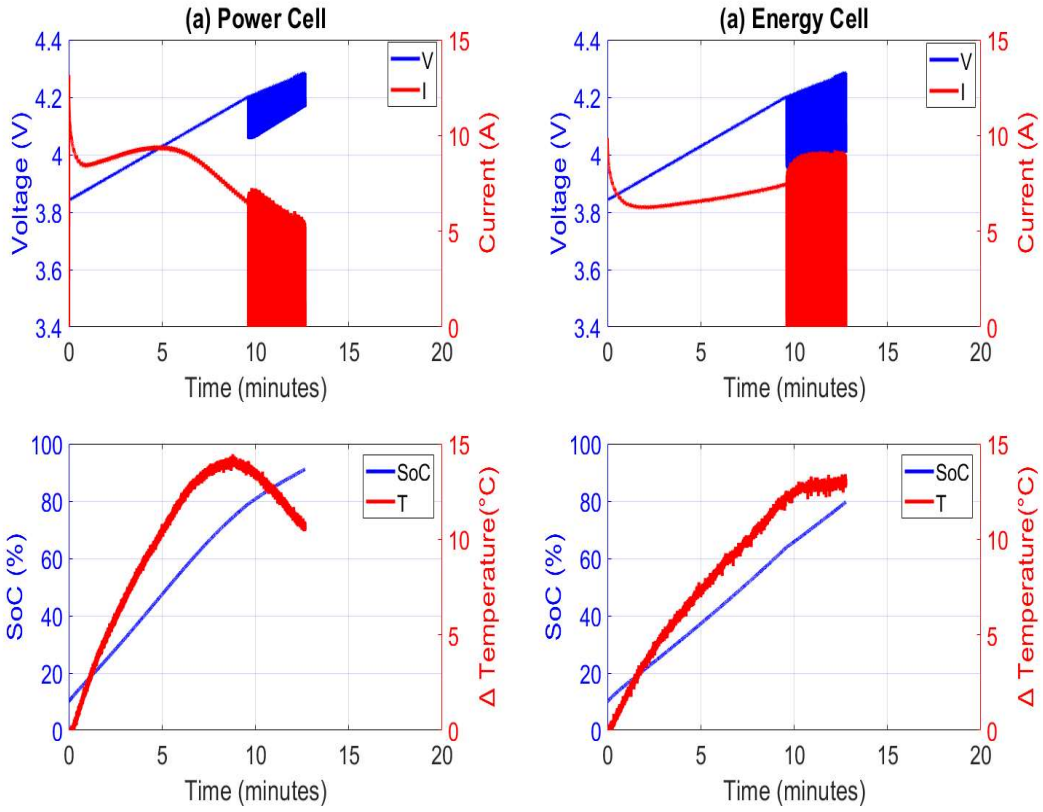

Fig. 4.3 voltage, current, Δ Temperature and SoC curves for (a) Power cell and (b) Energy cell using voltage step with time as step limit at first iteration at 25°C ambient temperature

Table 18 gives the summary of results for VSTL method at first iteration. From Fig. 4.3 and Table 18, as configured, the power cells take 12 minutes to be charged from 10% SoC to 90% SoC with a temperature elevation of approximately 15°C. For energy cell, in 12 minutes, the Δ SoC is only 70% with a temperature elevation of approximately 13°C. It is worth noting that it this experiment, the temperature elevation does not go beyond the manufacturer limits of 50°C and 45°C for power and energy cells respectively.

Table 18 summary results of voltage step with time as step limit at first iteration

	Δ Temperature (°C)	Total time (minutes)	Step time (seconds)	No. of steps
Power cell	14.86	12	8	90
Energy cell	13.26	12	8	90

From this first experiment, it is clear that, VSTL method can be applied to cells to meet the targets without exceeding the temperature limit set by the manufacturer. However, in this protocol, the cells are subjected to higher voltages after reaching 80% SoC, notably 4.3V approximately at the end of charge. This could induce loss of lithium inventory due to SEI growth [71]. Moreover, at high cell voltage electrolyte can degrade forming gas bubbles [72]. This later phenomenon could lead to loss of active material (LAM) i.e modification of electrode's materials resulting in electrode particle cracking or graphite exfoliation or structural disordering and hence there is need a to improve this protocol so as not to exceed the maximum cut-off voltage. Moreover, for the energy cell, the target of 80% of Δ SoC is not reached.

Therefore, the objective is to decrease the voltage at the end of the charge while reaching 80% of Δ SoC. Hence, by trial and error method, an adapted protocol is obtained at the end of 12^{th} iteration which has a reduced number of steps and varying time limit as shown in Fig. 4.4. Fig. 4.4 depicts the experimental voltage, current, temperature elevation and SoC curves for power and energy cells using voltage step with time as limit. For power cell (a) it takes 18.9 minutes to charge from 10% SoC to 90% Soc with a Temperature elevation of 13.03 °C. Whereas for Energy cell (b) it takes 23.93 minutes to charge from 10% SoC to 90% SoC with a Temperature elevation of 13.34°C. Table 19 gives the summary of results for voltage step with time as step limit.

It can be observed from Fig. 4.4. (a) and (b) for both power and energy cells, the current at each step reaches a peak value at the start of each step and decays exponentially towards the end of each step. The current exponentially decays towards the end of each step as the constant cell voltage converges toward the OCV when the cell is charge at a constant voltage

Another aspect that is interesting to point out is that, for both power and energy cell at higher SoC, it is difficult to maintain a mean of 3 C-rate due to the slow diffusion process of Li into the graphite particle [69]. This problem can be circumvented by applying higher voltages to overcome the internal resistance increase.

Another differentiating factor between power and energy cell is the number of steps between them. To meet the target, the power cell has 6 voltage steps. In contrary, the energy cells have 80 voltage steps. This is mainly because of the considerable higher internal resistance of the energy cell in comparison with power cell.

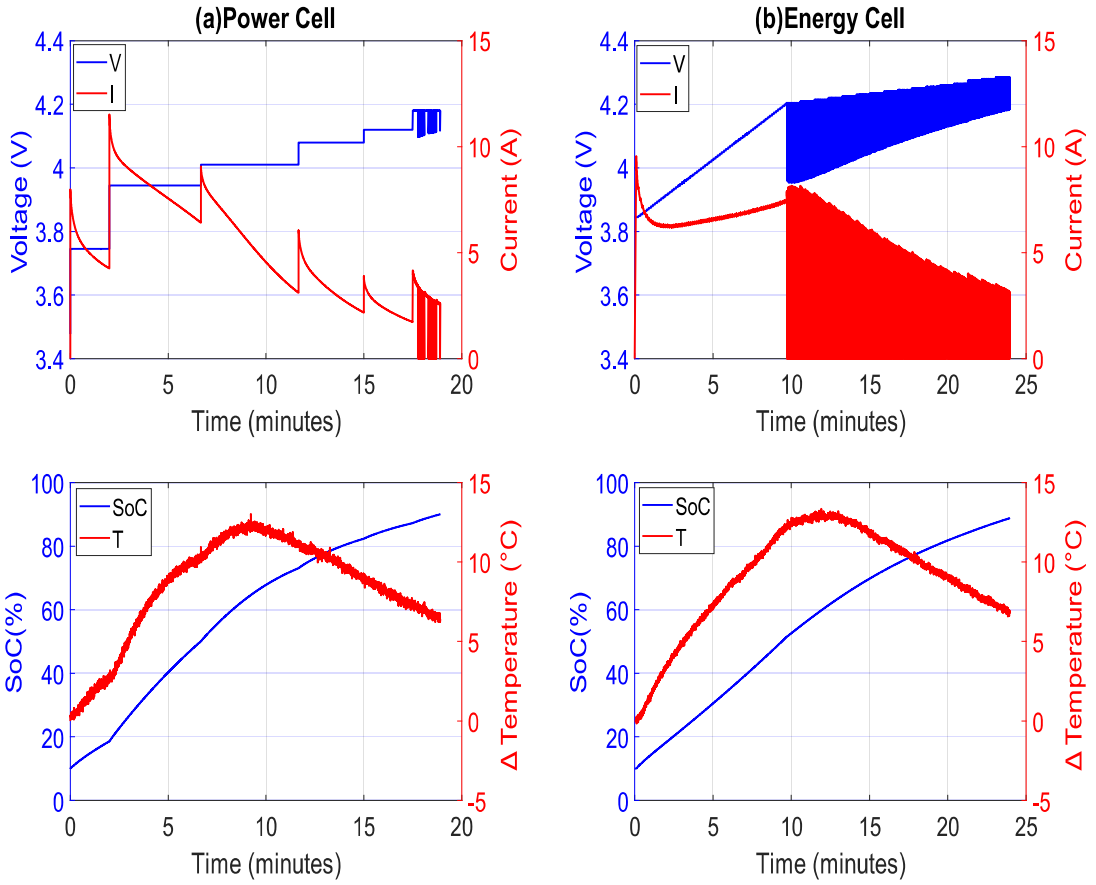

Fig. 4.4 voltage, current Δ Temperature and SoC curves for (a) Power cell and (b) Energy cell using voltage step with time as step limit at 25°C ambient temperature

Table 19 summary results of voltage step with time as step limit at 12th iteration

	Δ Temperature (°C)	Total time (min)	No. of steps
Power cell	13.03	18.9	6
Energy cell	13.34	23.93	80

Comparing Fig. 4.3 and Fig. 4.4. the number of steps is reduced by 84 and 10 for power and energy cells respectively. Also, for power cell, the maximum cell voltage reached is 4.2V thereby respecting manufacturer limits. Whereas, for energy cell, the maximum cell voltage reached was 4.3V exceeding the value prescribed by the manufacturer.

2.2.2. Voltage step with current as limit

Based on the experience from VSTL, the current limit for each step was chosen to vary from 4C-rate to 2C-rate to have a mean of 3C-rate during the experiment. Therefore, in this protocol, there is no iteration and we could meet the target at first time itself.

Fig. 4.5 depicts the experimental voltage, current, temperature elevation and SoC curves for power and energy cells using voltage step with current as step limit. For power cell (a) it takes 11.6 minutes to charge from 10% SoC to 90% Soc with a temperature elevation of 14.16 °C. It takes 19.3 minutes to charge from 10% SoC to 90% SoC with a Temperature elevation of 18.63°C for energy cell (b). Table 20 gives the summary of results for voltage step with current as step limit.

It can be observed from Fig. 4.5 (a) and (b) for both power and energy cells, that the current at each step reaches a peak value at the start of each step and decays exponentially towards the end of each step similar to VSTL protocol.

Another interesting aspect, for both power and energy cell at higher SoC, it is possible to maintain a mean of 3 C-rate, thanks to the step limit of the protocol with VSCL protocol. With VSCL, to meet the target, the power cell is charged with only 8 voltage steps. While, the protocol is done with 10 voltage steps for the energy cell. Upon close observation, the end voltage of energy cell is 4.31V whereas the end voltage of power cell is 4.2V. This is again because of the internal resistance of the energy cell that is one third higher than that of power cell in comparison.

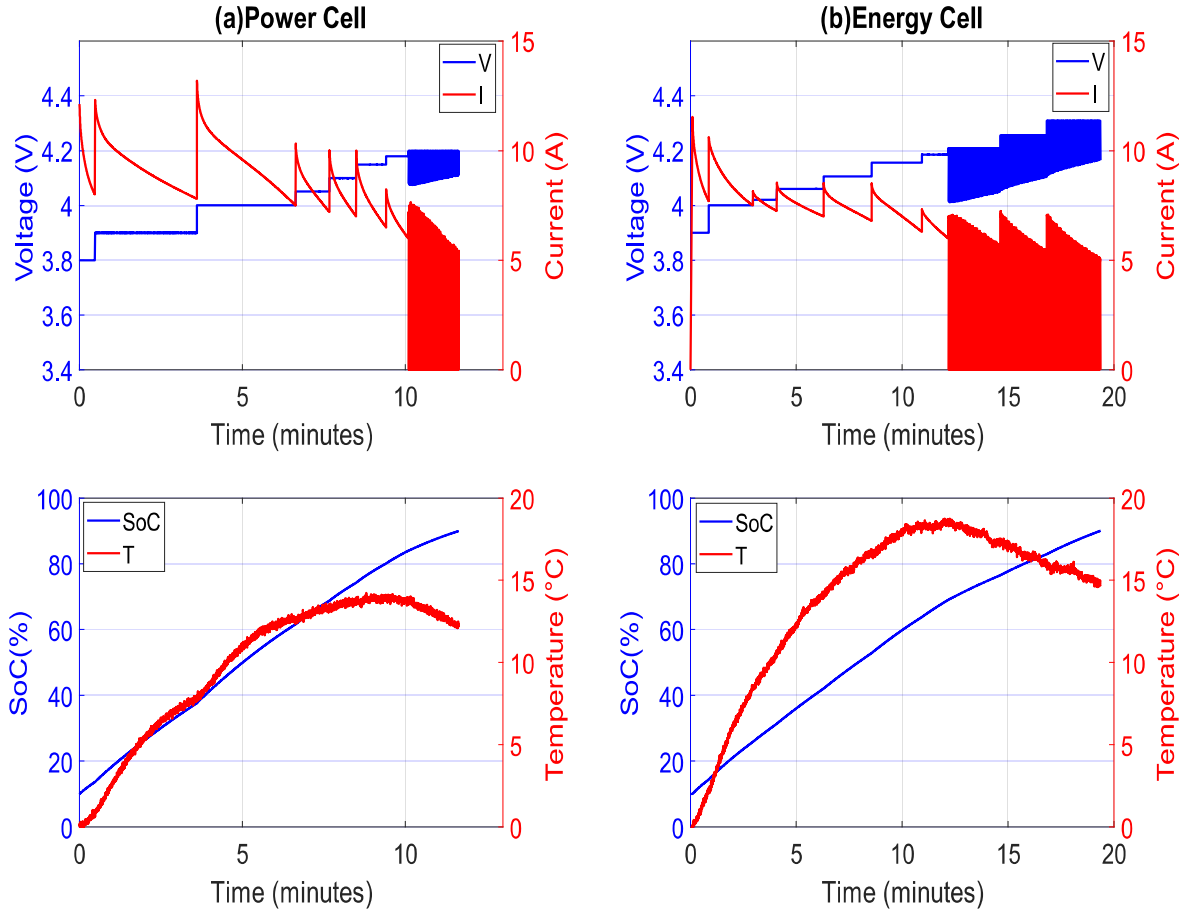

Fig. 4.5 voltage, current Δ temperature and SoC curves for (a) Power cell and (b) Energy cell using voltage step with current as step limit at 25°C ambient temperature

From Table 20 and Fig. 4.5, the difference between recharging time for power and energy cell is approximately 8 minutes. Also, the Δ temperature elevation of energy cell is 4°C higher than that of power cell. The main reason for this phenomenon is the internal resistance as mentioned above. Higher internal resistance leads to large potential drop of the cell and temperature elevation due to joule effect. The contribution of higher voltage drop has a direct impact on value of voltage step. As seen earlier, if the value of voltage step becomes closer to OCV values Li intercalation is slower and hence take more time.

Table 20 summary results of voltage step with current as step limit

	Δ Temperature (°C)	Total time (min)	No. of steps
Power cell	14.16	11.6	8
Energy cell	18.63	19.3	10

3. Comparison of protocols

3.1 Comparison between VSTL and VSCL

This section compares the VSTL and VSCL protocols discussed in the previous section. Fig. 4.6 illustrates the voltage comparison between VSTL and VSCL protocol for power cell. From Fig. 4.6, it is worth mentioning that, the VSTL protocol takes more time and requires higher number of steps to meet the target of 20 minutes.

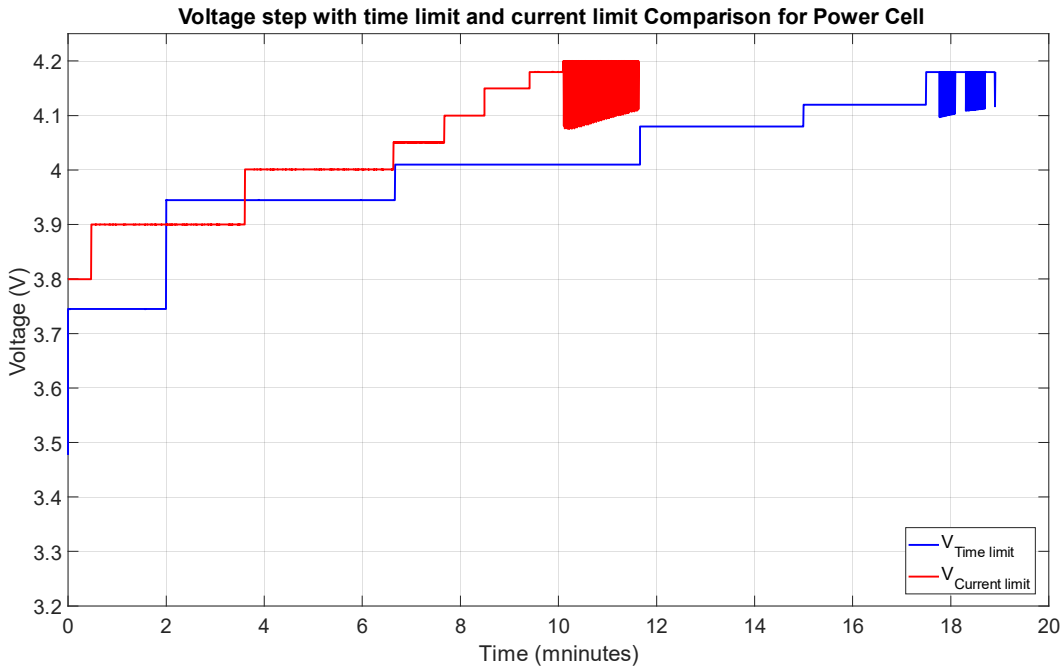

Fig. 4.6 Voltage comparison for VSTL (Blue Curve) and VSCL (Red Curve) protocol for power cell (reference 1c)

Table 21 compares both the voltage protocol with respect to charging time and temperature elevation for energy and power cells.

From Table 21, for both energy and power cell, the VSTL protocol takes longer duration to recharge 80% of Δ SoC when compared to VSCL. In VSCL protocol, as soon as the pre-set current limit is reached in a voltage step, it will automatically shift to the higher voltage thus increasing the C-rate. Therefore, throughout the protocol the current is always maintained at 3C-rate leading to faster recharge.

As a general rule for step voltage, at the beginning of the step, higher the difference between applied voltage and open circuit voltage (OCV), higher is the initial peak charge current. During the step, the decay of the current depends on the difference between the applied voltage and the OCV which increase due to the charge with the SoC. The smaller the difference, the higher is the decay. Due to which, it is difficult to maintain higher C-rates with VSTL protocol and it requires a greater number of voltage steps to maintain higher C-rate.

From Table 21, the Δ temperature increase for both energy and power cell is higher in VSCL protocol than VSTL protocol. This temperature increase is mainly because of the joule effect of the cells which is dominant at higher C-rates.

Table 21 comparison of VSTL and VSCL protocols to charge Δ SoC of 80% from 10% SoC

		VSTL	VSCL
Power cell	Δ Temperature (°C)	13.03	14.16
	Total time (min)	18.9	11.6
Energy cell	Δ Temperature (°C)	13.34	18.63
	Total time (min)	23.93	19.3

3.2 Comparison between VSCL and constant current with ODC

Fig. 4.7 compares the cell voltage, current, Δ SoC and Δ temperature evolution during charging process using VSCL and 3C CC with ODC for power cell at 25°C ambient temperature. To study the impact of VSCL on recharging time and Δ temperature elevation in comparison with CC protocol, the best C-rate is 3C-rate as the target of 80% Δ SoC can be meet without exceeding much the manufacturer temperature limit and upper cut-off voltage values.

In both the protocols, initially the cell is charged cell to 10% SoC using 0.5C constant current and allowed to rest for 25 minutes to reach open circuit voltage (OCV) and then cells are charged with respective protocols. It can be observed from Fig. 4.7 (a) that, in both the protocols the charging is terminated at the same voltage. From Table 22, for power cell, the charging time with 3C CC protocol is approximately 15 minutes and with VSCL is approximately 12 minutes. This is mainly due to the mean C-rate of the VSCL protocol. Even

though the protocol was designed with 3C-rate values, the cell response was higher than 3C-rate.

The more obvious difference between the protocols is the ohmic drop compensation between 3C CC with ODC and VSCL protocol. The VSCL compensates the ohmic drop of the cell at every step voltage that is a function of SoC, unlike 3C CC which compensates only after reaching the manufacturer charge cut-off voltage irrespective of SoC.

From Fig. 4.7 (b), the current response of the VSCL protocol is decreasing in nature. Meanwhile, the 3C CC with ODC has a constant profile. This particular characteristic response of Current for VSCL is the most probably the reason where both the protocol differs and it makes more consistent in terms of Δ SoC charged and temperature increase.

From Fig. 4.7(c), it is worth noting that the high mean C-rate of VSCL, leads to faster recharging and also small higher temperature elevation as shown Fig. 4.7(d). This response of higher C-rate for the mean current of power cell is quite interesting.

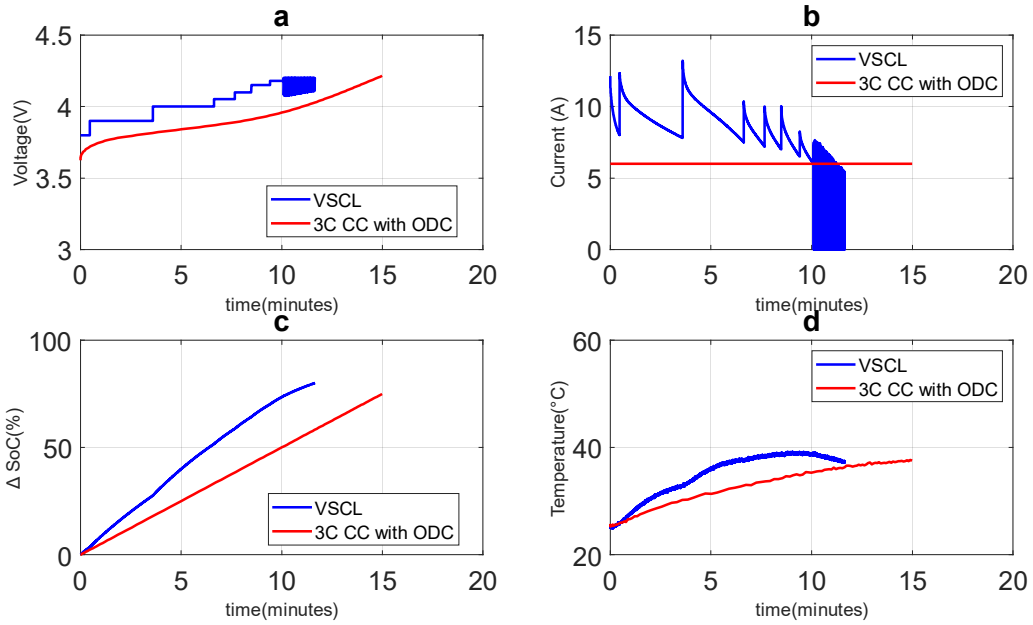

Fig. 4.7 Comparison of voltage (a), current(b), Δ SoC (c) and Temperature(d) curves for power cell (reference 1c) using voltage step with current as step limit (blue) and 3C CC with ODC (red) at 25°C ambient temperature

Fig. 4.8 shows the comparison for the cell voltage, current, Δ SoC and temperature evolution during charging process using VSCL and 3C CC with ODC for energy cell.

In both the protocols, initially the cell is charged cell to 10% SoC using 0.5C constant current and allowed to rest for 25 minutes to reach open circuit voltage (OCV) and then cells are charged with respective protocols. It can be observed from Fig. 4.8(a) that, in both the protocols the charging is terminated at the same voltage. From Table 22, for energy cell, the charging time with 3C CC protocol is 15 minutes and with VSCL is approximately 19 minutes. This latter difference is due to the voltage pulse stages at the end of the charge once the cell voltage has reached the manufacturer cut-off voltage i.e 4.2V.At the end of the charge voltage pulses are introduced mainly to limit the Li plating occurring at higher SoC and C-rate.

From Fig. 4.8 (c), it is worth noting that until 60% of Δ SoC, irrespective of the protocols the SoC profile remains quite similar. Also, from Fig. 4.8 (d), it is interesting to point out that, the temperature of the cell charged using 3C CC with ODC crosses 55°C which is 10°C higher than the 45°C temperature limit given by the manufacturer according to section 1.2 of Chapter 2. In contrary, the temperature elevation with VSCL is only 42°C and hence adhering to the limits prescribed by the manufacturer.

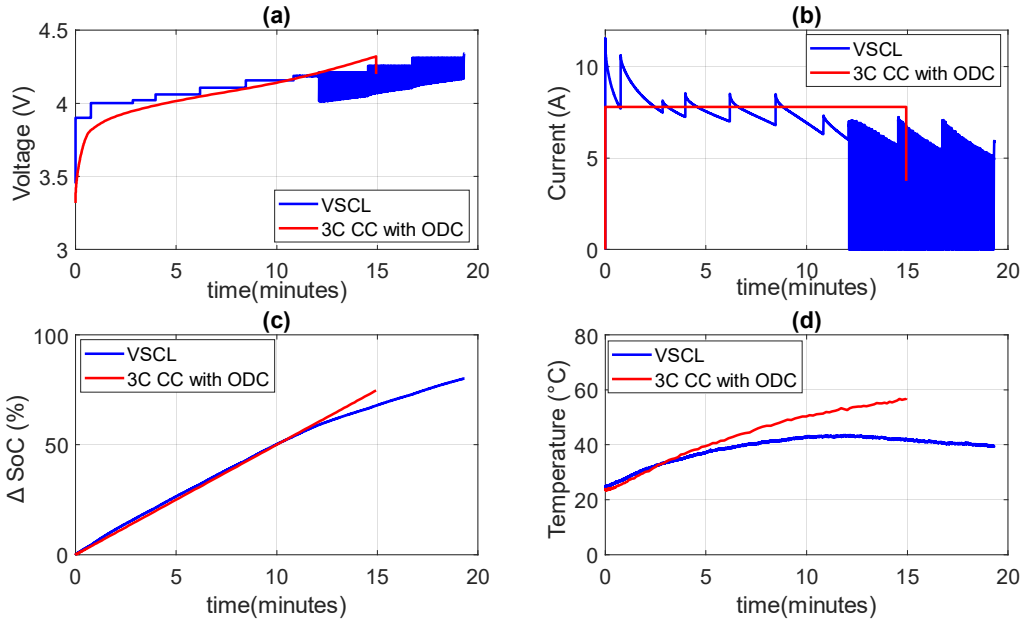

Fig. 4.8 Comparison of voltage (a), current(b), Δ SoC (c) and Temperature(d) curves for energy cell (reference 2c) using voltage step with current as step limit (blue) and 3C CC with ODC (red) at 25°C ambient temperature

For power cell the time taken to recharge with VSCL protocol is 25% lesser than that of 3C CC with ODC for the same temperature elevation. This is mainly because of the less internal resistance of the power cell, due to which the contribution of ohmic drop is less.

For energy cell, the VSCL protocol is a better option for fast charging as it is able to reach the target time (i.e. <20 minutes) with the temperature increase below the limits prescribed by the manufacturer even at higher C rates. This is mainly due to the exponential decay of the current at the end of each voltage steps. Hence, this result is quite an accomplishment considering the impact on temperature and charging time which is suitable for EV application.

Table 22 Comparison of VSCL and 3C CC with ODC protocols to charge Δ SoC of 80% from 10% SoC

		VSCL	3C CC with ODC
Power cell	Δ Temperature (°C)	14.16	14.23
	Total time (min)	12	15
	End voltage (V)	4.22	4.22
	Mean C-rate	~ 3	3
Energy cell	Δ Temperature (°C)	18.63	30.36
	Total time (min)	19	15
	End voltage (V)	4.3	4.3
	Mean C-rate	~ 3	3

4. Conclusion

Experiments were performed on 2 energy and power cells to study the impact of voltage-controlled protocols for fast charging. The VSTL, VSCL and 3C CC with ODC was compared at mean 3 C-rates. Charging the battery with VSCL protocol from 10% SoC to 90% SoC is a promising solution.

The thermal behavior for both protocols is studied. It turns out that the VSCL protocol is more suitable to recharge the cells with higher C-rates as it is possible to stay within the temperature limits prescribed by the manufacturer without compromising the recharging time. For 3C CC with ODC protocol the temperature exceeds the manufacturer temperature limit. This temperature issue can be minimized by reducing the C-rate. However, reducing the C-rate could prolong the charging process resulting in longer recharging time.

The VSCL protocol is employed on energy and power cell. The total charging time can be improved significantly when using VSCL protocol on energy cell as it considers the internal resistance when applying voltage steps. However, the VSCL has very little effect at mean 3 C-rate for power cell in terms of temperature increase because this type of cell has low internal resistance. It seems that the VSCL is more efficient for the energy cells having higher internal resistance and operating at high C-rates.

Chapter 5. Ageing study: Part-I

1. Introduction

In Chapter 3, the square and triangular current pulse was investigated for charge time and temperature elevation in comparison with classical CCCV protocol at high C-rates. The triangular current pulse has similar charging times in comparison with Classical CCCV protocol and square current pulse. Only, considerable difference in temperature elevation can be observed. This is mainly due to the lower rms value of triangular current pulse than the square current pulse.

In Chapter 4, voltage step with current limit (VSCL) was investigated for fast charge of NMC-graphite cells optimized for energy and power. This protocol is performed by applying a ascending voltage step. The transition from lower voltage to higher voltage occurs when the exponentially decaying current reaches pre-set current value allowing to maintain required average current of 3C-rate throughout the protocol.

Regarding ageing due to protocols as mentioned earlier, loss of lithium inventory (LLI) may be induced by SEI growth or electrolyte/binder decomposition. These both degradation mechanisms are accelerated at high cell voltage and temperature. The second cause of capacity fade is the modification of the electrode's materials which results from the electrode particle cracking graphite exfoliation, structural disordering as well as loss of electric contact of the electrode when increasing the current load. The latter cause is the loss of active material (LAM). Moreover, at high voltage or high temperature, electrolyte could also form gas bubbles due to degradation inside the cell [57]. Ageing mechanism were discussed in the chapter 1.

Whatever the route for the capacity fade discussed in Chapter1, loss of lithium inventory (LLI) or loss of active materials (LAM) can be due to either the cell voltage or the temperature elevation during fast charge. Thereby, the aim of this chapter is to investigate the impact of various protocols on NMC-graphite cells ageing.

2. Cyclic ageing

To study the impact of various protocols on cell life time, an ageing study is carried out. The characteristics of energy and power optimized NMC-graphite cells from LG Chem and Samsung used in this study is highlighted in section 1.2 of Chapter 2.

As shown in Fig. 5.1, the cyclic ageing commences with initial Characterization of fresh NMC-graphite cells for power and energy optimized to assess cell-to-cell variations in order to choose most similar cells. This is followed by Reference Performance Tests (RPTs), which establishes the baseline for performance parameters. Cycle life tests are then initiated with respective protocols. At the end of every 50 charge/discharge cycles again RPTs are performed and SoH is evaluated. If the SoH is less than 80% then the cycling is stopped.

The RPTs include capacity measurement, Internal resistance estimation and Incremental Capacity Analysis (ICA) test at the end of every 50 cycles. A brief explanation of all these tests are reiterated below:

- Capacity measurement:

  The capacity of the cells was estimated as an average of discharge capacity over three cycles. Each cycle comprised a standard constant current constant voltage (CC-CV) charging until 100% SOC (C/2 rate charging to 4.2V, constant voltage charging at 4.2V until the current dropped below C/20), and CC discharging at -C/5 rate until 2.5 V (≈ 0% SOC) for power optimized cell and 2.75V for energy optimized cell. Between each charge and discharge there was a rest time of 1 hour to allow the cells to reach equilibrium state.

- Internal resistance estimation:

  To estimate the internal resistance, the cell was charged to 50% SoC at C/2 rate followed by a rest of 30minutes. Later, R_i is estimated by applying a current pulse equivalent to 0.2C-rate for 10 to 20 impulsions at 0.04ms (approximately 25kHz).

- ICA:

  The C/20 rate charging/discharging test with a one-hour rest time was performed to obtain estimate the incremental capacity. The sample rate of the measurement was 5mV, and $\Delta Q/\Delta V$ vs. voltage is plotted to perform ICA.

- SoH estimation from measurements:

  To evaluate the aging of the cell, the SoH of batteries during cycling experiments has been estimated in different ways:

During cycling at each cycle, the SoH_C is estimated, based on the capacity charged at each charge step, using the following equation

$$SOH_C = \frac{Q\ charged\ at\ each\ cycle}{Q\ charge\ initial} \tag{40}$$

During the RPTs procedure, the SoH_D is estimated in term of loss of capacity evolution as following (measure at -C/5):

$$SOH_D = \frac{Q\ discharged\ at \frac{C}{5} during\ the\ RPT}{Q\ discharge\ initial} \tag{41}$$

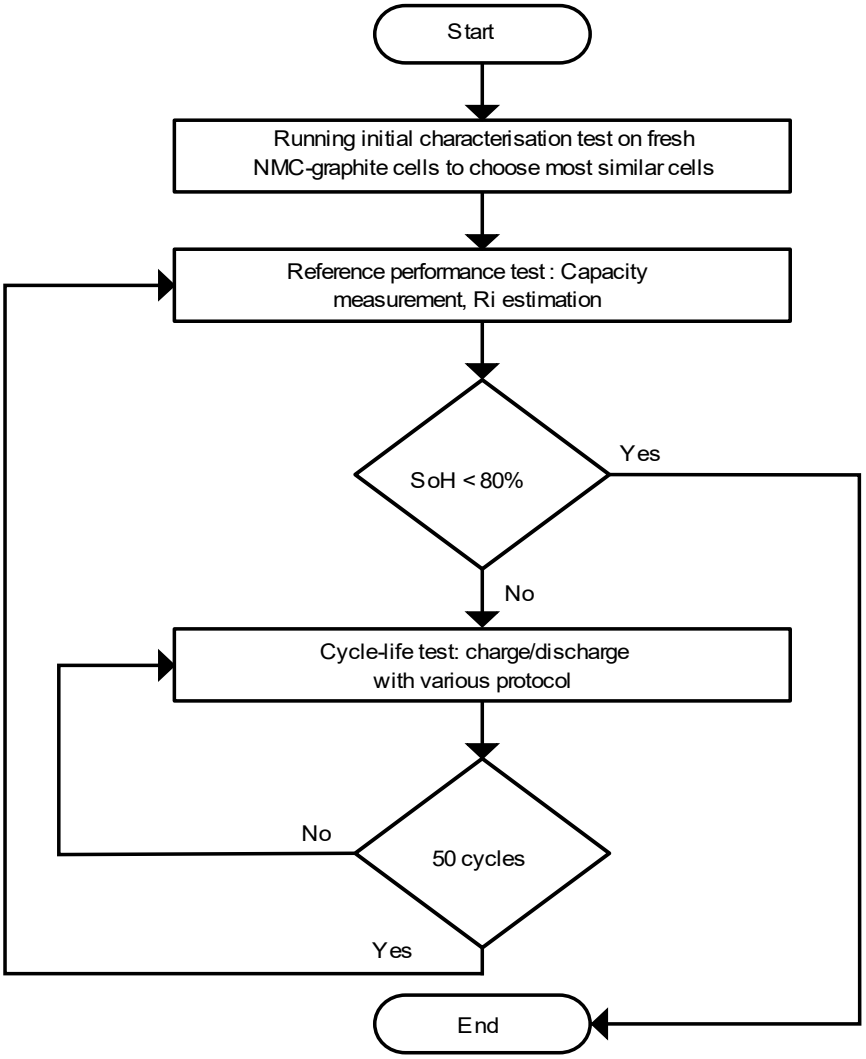

Fig. 5.1 Flow chart of experimental test procedure

Table 23 provides the overview of experimental characteristics of the cells with the reference used for the experiments in following sections. provides the characteristics for 13 cells out of which 8 are energy optimised from LG Chem and 5 are power optimised from Samsung SDI. Along with these 13 Cells, another set of 13 cells of energy and power optimised cells were cycled with respective protocols to verify the repeatability of results. Therefore, in total 26 cells of NMC-graphite were cycled with different charge protocols.

Table 23 Overview of cell characteristics used in following section

	Reference	Capacity, Q (mAh)	Internal Resistance, R_i (mΩ)	Protocol
Power Cell	1e	2014	18 ± 1	1C CC CV
	1f	2015	18± 1	Square CP 1C mean
	1g	2019	16 ± 1	Triangular CP 1C mean
	1k	2017	15 ± 1	VSCL
	1l	2015	16 ± 1	3C CC with ODC
Energy Cell	2e	2673	26± 1	1C CC CV
	2f	2668	29 ± 1	Square CP 1C mean
	2g	2670	26 ± 1	Triangular CP 1C mean
	2h	2650	25 ± 1	2C CC CV
	2i	2680	30± 1	Square CP 2C mean
	2j	2631	32± 1	Triangular CP 2C mean
	2k	2645	32± 1	VSCL
	2l	2658	31± 1	3C CC with ODC

2.1 Current based protocols

This section highlights the ageing results of power and energy optimized NMC-graphite cells cycled with current based protocol. Towards the end of this section the results obtained from SoH, internal resistance estimation and ICA are also discussed for the same cells.

2.1.1. Ageing

All the main experimental parameters used for cycling of power and energy cells using current control method is summarized in Table 24. Three charging methods at 2 different peak C-rates are compared. For both power and energy cells, the reference charging method is CCCV protocol with 1C-rate and 2C-rate in stage I. whereas for square and triangular current pulse protocol the peak current is 2C-rate and 4C-rate that corresponds to a mean of 1C-rate and 2C-rate during Stage I. The stage I is terminated upon reaching the cut-off voltage of 4.2V. Also, for square and triangular current pulse the operating frequency and duty cycle is 500mHz and 50% respectively. It is worth mentioning that the CV step is always performed at 4.2V until a cut-off current of C/20 rate is reached irrespective of the charging protocol. After each charging process, the battery is discharged at a constant current of -C/5 C-rate until the lower-bound cut-off voltage of 2.5V for power and 2.75V for energy cell is reached. When this cut-off voltage is reached, the discharging process is terminated. The relaxation time between charges/discharges is set at 1 hour to allow the cell to reach equilibrium state. The cycle-life test for all the experiments is carried out 25°C ambient temperature inside climatic chamber. The main thrust in this study is given to analyze the impact of shape of the waveform on the performance of the power and energy cells.

Fig. 5.2 compares the evolution of the percentage of capacity charge during the current and CV stages (ΔSoC) and charging time during stage I and stage II. ΔSoC are defined as follows:

$$\Delta SOC_I = \frac{Q\ stage\ I}{Q\ charge\ initial}\ and\ \Delta SOC_{II} = \frac{Q\ stage\ II}{Q\ charge\ initial} \quad (42)$$

Where $Q\ stage\ I$ and $stage\ II$ are the capacities charged during the stage I and II respectively and $Q\ charge\ initial$ the initial capacity of the cell.

In addition, Fig. 5.2 compares total SoH_C during cycling based on the charge (e) and the total charging time (e) for power cells cycled with classical 1C-rate CCCV, square CP and triangular CP with 1C-rate mean current.

Similarly, Fig. 5.3 show the same results for energy cells cycled with classical 1C-rate CCCV, square CP and triangular CP with 1C-rate mean current. Also, the same experiments at a mean C-rate of 2C are presented in Fig. 5.4 for comparison of energy cell.

Table 24 summary of experimental parameters used during cyclic ageing study for current based protocol

Protocol	CCCV	Square CP	Triangular CP
Cell reference	1e, 2e,2h	1f,2f,2i	1g,2g,2j
Peak C-rate	1 & 2	2 & 4	2 & 4
Mean C-rate	1 & 2	1 & 2	1 & 2
tc (seconds)	-	1	1
tr (seconds)	-	1	1
Frequency (mHz)	-	500	500
Duty cycle (%)	-	50	50
Stage I cut of voltage (V)	4.2	4.2	4.2
Stage II cut off current (C-rate)	C/20	C/20	C/20
Rest time (hours)	1	1	1
Discharge C-rate	-C/5	-C/5	-C/5
Discharge cut off voltage (V)	2.5V (Power cell) 2.75V (Energy cell	2.5V (Power cell) 2.75V (Energy cell	2.5V (Power cell) 2.75V (Energy cell

In general, irrespective of the type of the cell and mean C-rate, with the increase in cycle number the Δ SoC (a) and charging time (b) evolution during Stage I is decreasing. Whereas the Δ SoC (c) and charging time (d) evolution during Stage II is increasing. This behavior is mainly due to the increase in the internal resistance of the cell irrespective of the protocol. As stated earlier, the terminating condition for Stage I is cut off voltage of 4.2V. The increase in internal resistance results in higher ohmic drop at the same C-rate leading to shorter Stage I time and therefore less capacity charge during stage I. Conversely, the stage II time increases due to which the capacity charge during Stage II increases.

The effect of Stage I time and Stage II time can be seen on total charging time and SoH estimated at each cycle. With the increase in cycle number the SoH_C (e) decreases as expected while, the total charging time (d) increases irrespective of the protocol. This is mainly due to the increase in constant voltage (CV) phase or Stage II time.

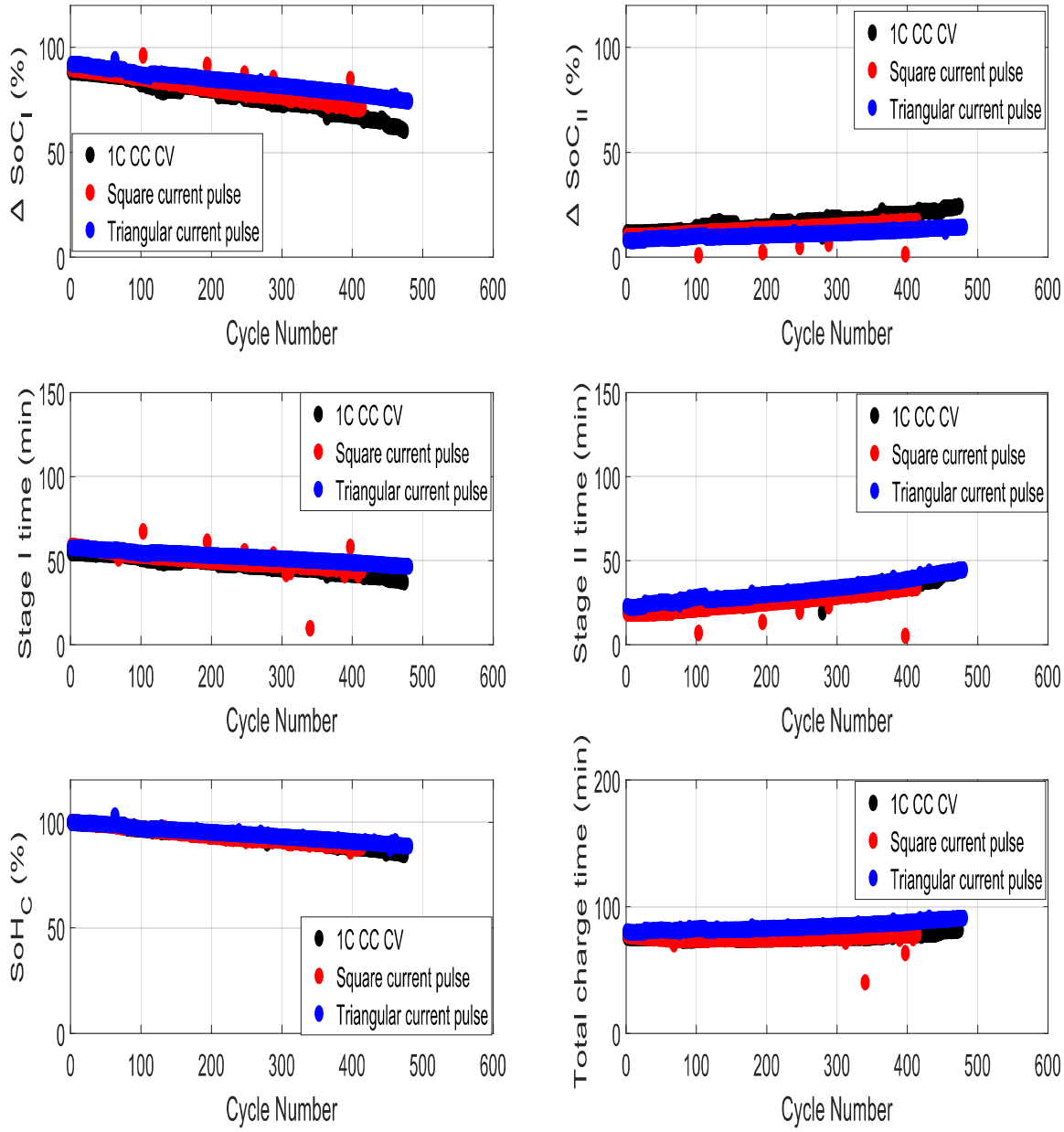

Fig. 5.2 Cycle-life test; Comparison of evolution of (a) Δ SoC (%) during stage I (b) stage I time (c) ΔSoC (%) during stage II (d) stage II time (minutes) (e) SoH (%) (f) total charge time (minutes) for power cells cycled with 1C-rate CCCV (black; Reference: 1e), square current pulse (Red; Reference: 1f) with 1C-rate mean current and Triangular current pulse (blue; Reference: 1g) with 1C-rate mean current

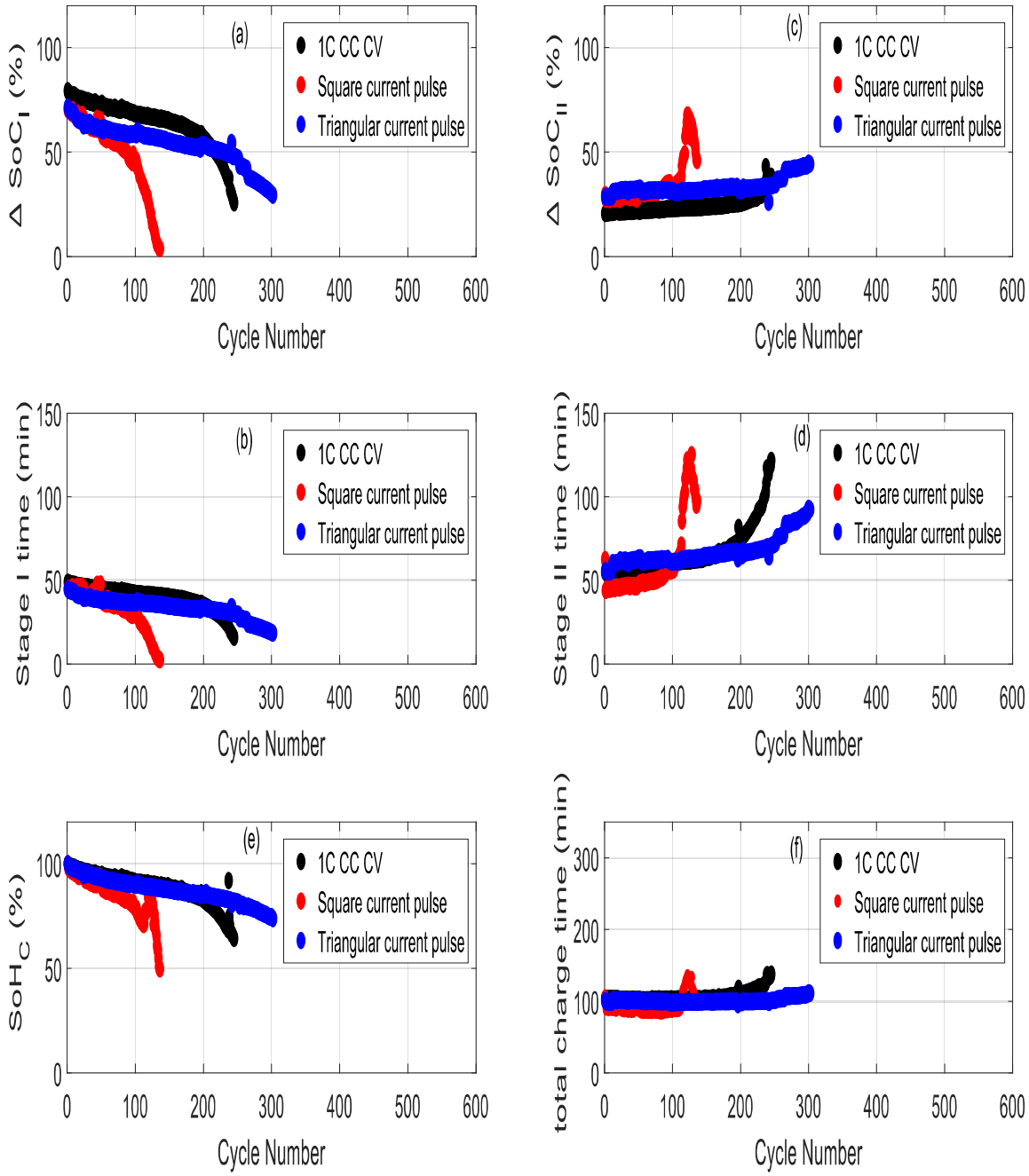

Fig. 5.3 Cycle-life test; Comparison of evolution of (a) Δ SoC (%) during stage I (b) stage I time (c) Δ SoC (%) during stage II (d) stage II time (minutes) (e) SoH (%) (f) total charge time (minutes) for energy cells cycled with 1C-rate CCCV (black; Reference: 2e), square current pulse (Red; Reference: 2f) with 1C-rate mean current and Triangular current pulse (blue; Reference: 2g) with 1C-rate mean current

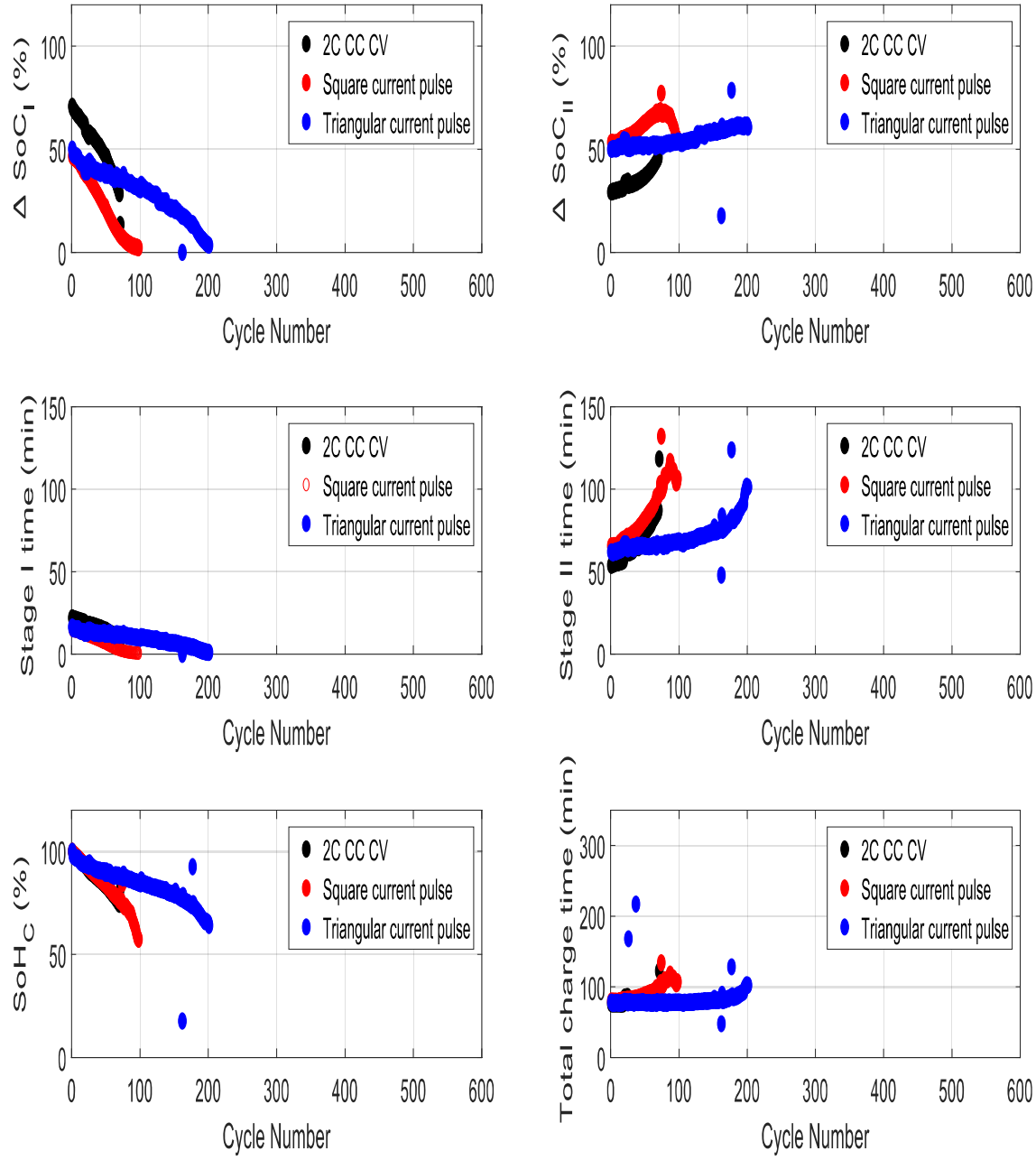

Fig. 5.4 Cycle-life test; Comparison of evolution of (a) Δ SoC (%) during stage I (b) stage I time (c) Δ SoC (%) during stage II (d) stage II time (minutes) (e) SoH (%) (f) total charge time (minutes) for energy cells cycled with 2C-rate CCCV (black; Reference: 2h), square current pulse (Red; Reference: 2i) with 2C-rate mean current and Triangular current pulse (blue; Reference: 2j) with 2C-rate mean current at 25C ambient temperature

More precisely, for power cells, it is worth noting that, the aging during cycling (SoH_C in Fig 5.2 e) is quite similar whatever the protocol used, suggesting a low impact of the different protocols on the cell ageing. These cells perform about 500 cycles without reaching the EoL criterion of 80%. The only difference is the slightly larger decrease in the amount of charge during stage I for the CP square and CC-CV protocols compared to triangular one.

Due to lack of time and unavailability of channels in Biologic cycler, the experiments were stopped at the end of 500 Cycles before reaching the end of life (EOL) criteria for power cells cycled with 1C CCCV, square CP and triangular CP.

For the energy-typed cells, it is notable to observe that the SoH_C of the cell reach 80% for a lower number of cycles than for the power-typed cells: between 100 and 250 cycles at 1C mean protocols and between 50 to 150 cycles at 2C mean protocol. On the other hand, it is interesting to highlight the slower aging with the protocol involving triangular pulses whether at 1C or 2C mean current. Furthermore, for the cell cycled with square CP (red curves) the total SoH_C (Refer Fig. 5.3 e) after 125th cycle tends to increase, reach a maximum and then decreases rapidly. This later phenomenon is mainly due to metallic lithium deposition on the negative electrode during charging.

In order to highlight this aspect, Fig. 5.5 compares the evolution of current and temperature elevation for square CP with 1C-rate mean current during stage II (CV stage). After 126th cycle the current during stage II slightly increases to form a plateau rather than exponentially decreasing. In the current plateau region, the temperature also starts to increase and reaches a maximum value. Notably, this temperature elevation is higher than that of maximum temperature that the cell experiences during cycling. On close observation, the temperature during the stage II for 1st cycle exponentially decreases and the maximum is reached at the end of stage I. Whereas, after 126th cycle, the temperature increases unexpectedly for a small increase in the current during stage II.

The unexpected temperature elevation behavior is similar to the internal short circuit as observed by some authors [73], [74], [75]. One possible root cause for this internal short circuit may be due to the Li plating resulting in temperature elevation and immediate capacity fade as observed in literature [76], [19], [70] ,[71]. Lithium plating appears when metallic lithium is electrochemically deposited onto a surface of negative electrode [79]. This Lithium plating is

reversible in nature. Overall this degradation is an effect of coupling between multiple root causes such as Li plating and SEI growth due to high C-rate cycling [80].

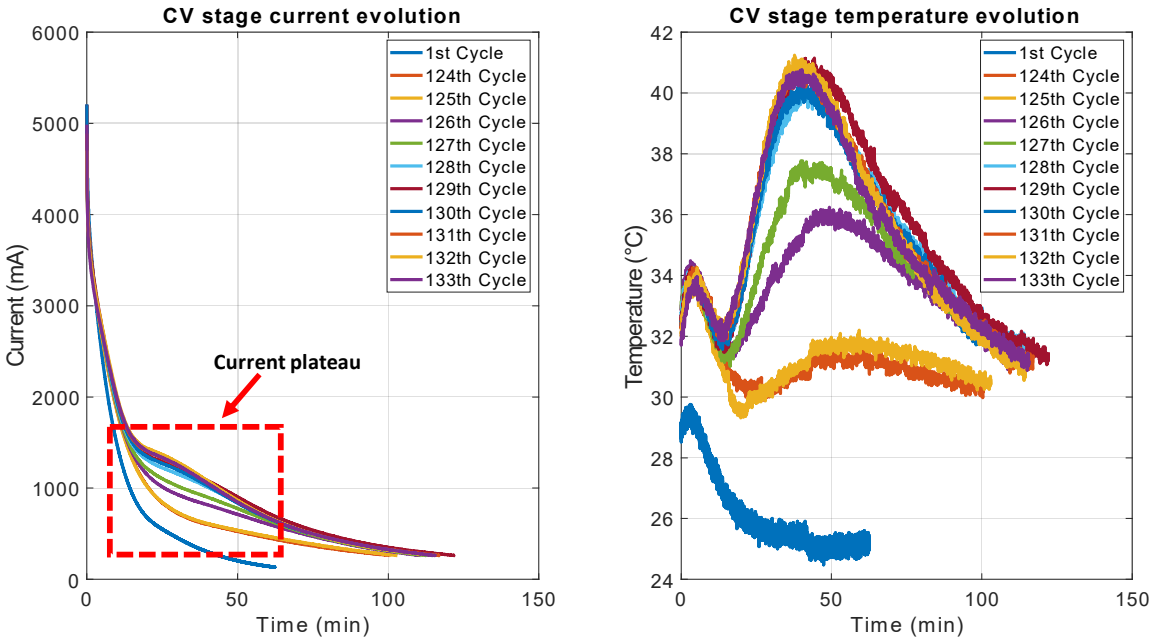

Fig. 5.5 Comparison of evolution of current (left) and temperature elevation (right) during stage II for energy cells cycled with square current pulse (Reference: 2f) with 1C-rate mean current at 25C ambient temperature.

2.1.1. SoH estimation

The Reference Performance Test (RPT) is done at regular intervals of 50 cycles for all the cells on which aging study was employed. The RPT is done to study the impact of charging protocols on the life time of the cells. The experimental procedure is given beforehand.

Fig. 5.6 compares the evolution of SoH_D (estimated from discharge at -C/5 left) and internal resistance vs SoH_D (right) for power and energy cells cycled at 1C-rate and 2C-rate CCCV, Square CP and Triangular CP. In general, the SoH of the cells are decreasing with respect to cycle number as expected. Also, the internal resistance of the cells is increasing when the SoH is decreasing.

The SoH_D of the power cells shows a really slow diminution of its capacity as expected. The cell cycled with square CP with 1C-rate mean current (2C-rate peak) shows a deviation from the reference method of 1C CCCV protocol. This result is in agreement with the authors

of [40] and [81]. In terms of resistance, no notable difference in its evolution is observed whatever the protocol for power cell with a low increase during cycling.

For the Energy cell, as already emphasized above, aging is rapid regardless of the protocol used in comparison with power cell. For energy-typed cells, the loss of capacity is accompanied by an increase in resistance essentially after 80% of SoH. It is nevertheless important to note that at an "identical" mean current, the triangular pulse method saves aging. This result highlights the likely effect of shape of the current waveform on the cell ageing.

Energy cell cycled with square CP with 1C-rate mean current (2C-rate peak) shows a sharp capacity fade right after 100 cycles. Whereas, the cell cycled with triangular CP with 1C-rate mean current (2C-rate peak) follows the reference method of 1C CCCV protocol until 200 cycles. After wards the cell cycled with reference protocol of 1C CCCV deviates from the triangular CP with sharp capacity fade. The total capacity fade for the cell cycled with 1C CCCV is 41% at the end of 150 cycles. For the cell cycled with square and triangular CP, the total capacity fade becomes 82% at the end of 250 cycles and 30% at the end of 300 cycles respectively. Another noticeable aspect is that, the ageing of the cells accelerates after a capacity fade of 20%. The charge protocol has a strong impact on the internal resistance of energy cell (Ri) which increases sharply for the cell cycled with square CP for a SoH below 90%, indicating a fast degradation of the cell. Whereas for cell cycled with triangular CP and 1C CC CV, there is moderate increase of the Ri only after 80% SoH.

Another surprising aspect is that the SoH evolution at 1C-rate CCCV is not so far from the one at mean 2C-rate Triangular CP. Indeed, this result is an achievement when comparing with other protocols which degrades more significantly the battery.

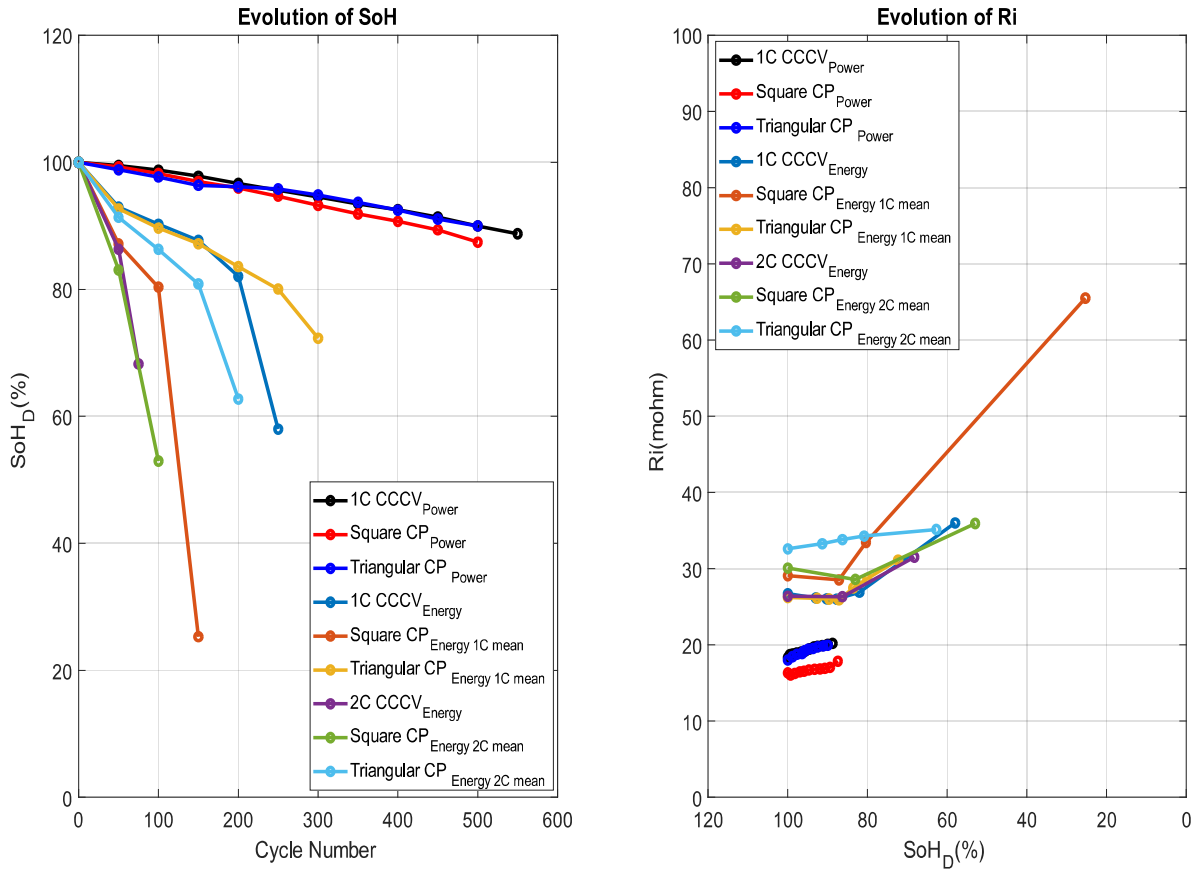

Fig. 5.6 Cycle-life test; Comparison of evolution of SoH (%) (left) and internal resistance vs SoH (right) for power cells cycled with 1C-rate CCCV (black; Reference: 1e), square current pulse (Red; Reference: 1f) with 1C-rate mean current and triangular current pulse (blue; Reference: 1g) with 1C-rate mean current; 1C-rate CCCV (Navy blue; Reference: 2e), square current pulse (orange; Reference: 2f) with 1C-rate mean current and triangular current pulse (yellow; Reference: 2g) with 1C-rate mean current for energy cells; 2C-rate CCCV (purple; Reference: 2h), square current pulse (Green; Reference: 2i) with 1C-rate mean current and triangular current pulse (cyan; Reference: 2j) with 2C-rate mean current at 25°C ambient temperature

2.1.2. ICA analysis

Incremental capacity curves are presented in this section for the cells cycled with CCCV, square CP and triangular CP protocols. The ICA curves are plotted at regular intervals of 50 cycles for all the cells on which aging study was employed. The ICA is carried out to extract the information with regards to degradation modes due to the impact of various charging protocols on the life time of the cells. The experimental procedure is given beforehand.

In general, two distinct peaks A and B referring to electrodes and phase transition in electrode materials is identified for investigation. As a rule of thumb, the shift of the peaks along x-axis indicates the change in internal resistance of the cell and the change in the intensity of the peaks relates mainly to loss of active material (LAM) [82] and loss of lithium (LLI) in positive or negative electrode.

Fig. 5.7 shows the IC curves for power and energy cells cycled with 1C-rate and 2C-rate CCCV (left), square CP (middle) and triangular CP (right) at 25°C ambient temperature over 500 cycles recorded every 50 cycles intermittently. Two peaks namely A and B is of much interest in this study. Since it is difficult to observe the change in the intensity of peaks in Fig. 5.7, Fig. 5.8 is plotted to compare only the intensities of peak A and B for the same cells.

Power	1C-rate mean	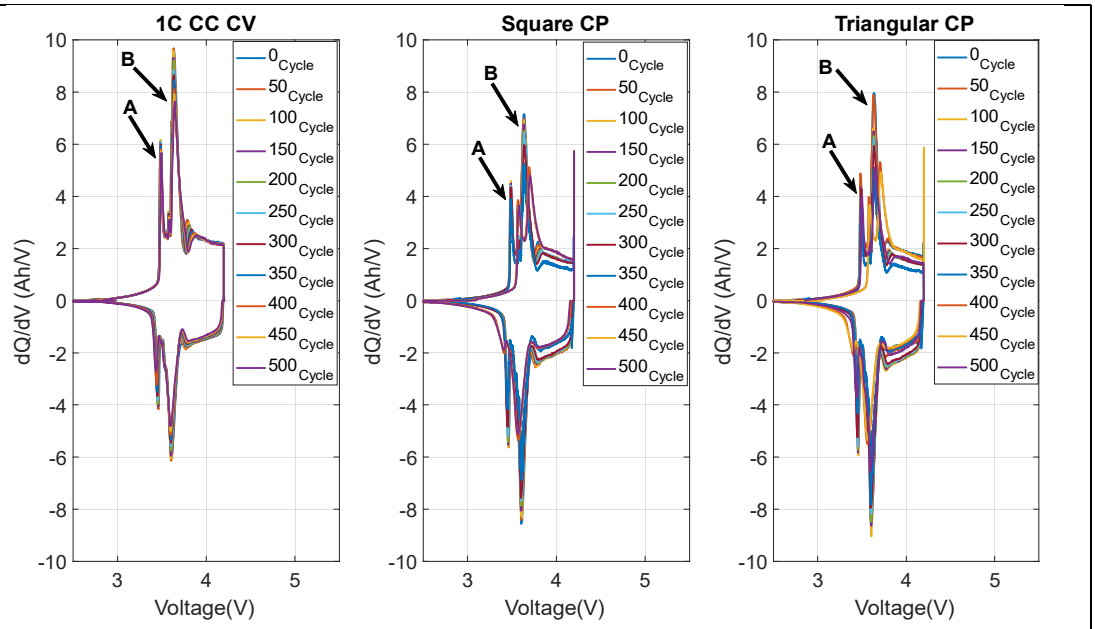
Energy	1C-rate mean	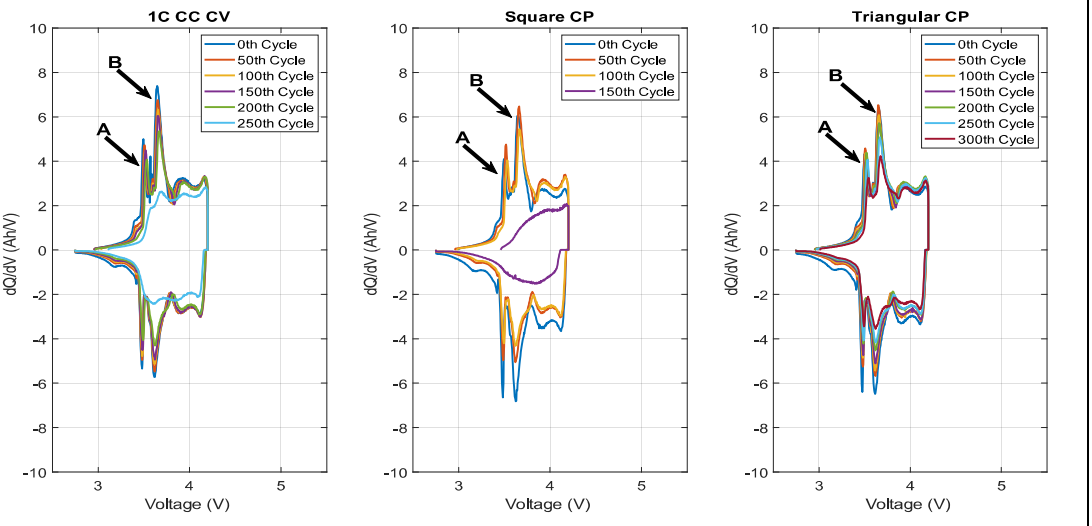
	2C-rate mean	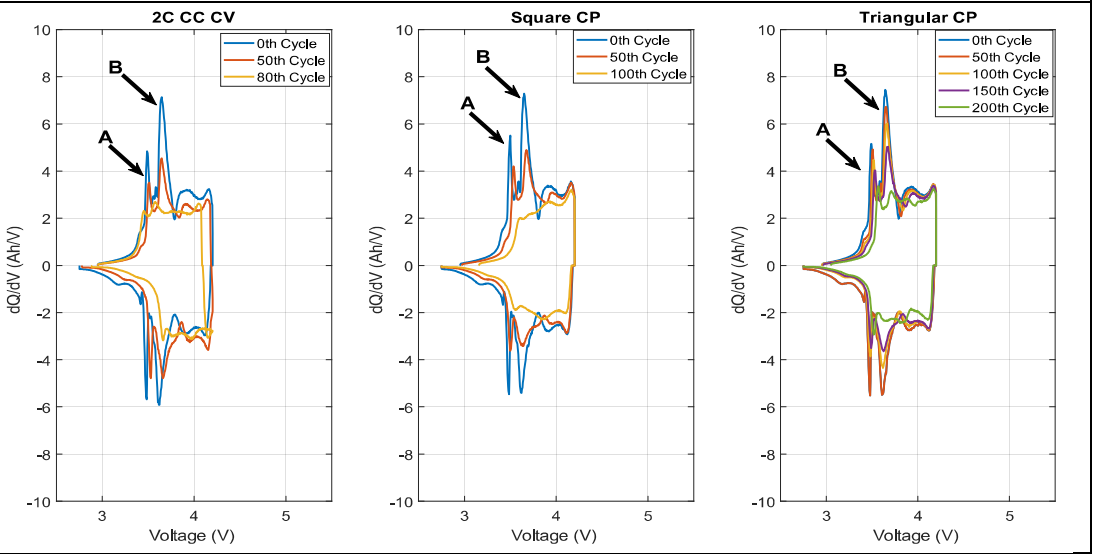

Fig. 5.7 ICA curves for power and energy cells cycled with 1C-rate and 2C-rate CCCV, Square CP and Triangular CP at 25°C ambient temperature.

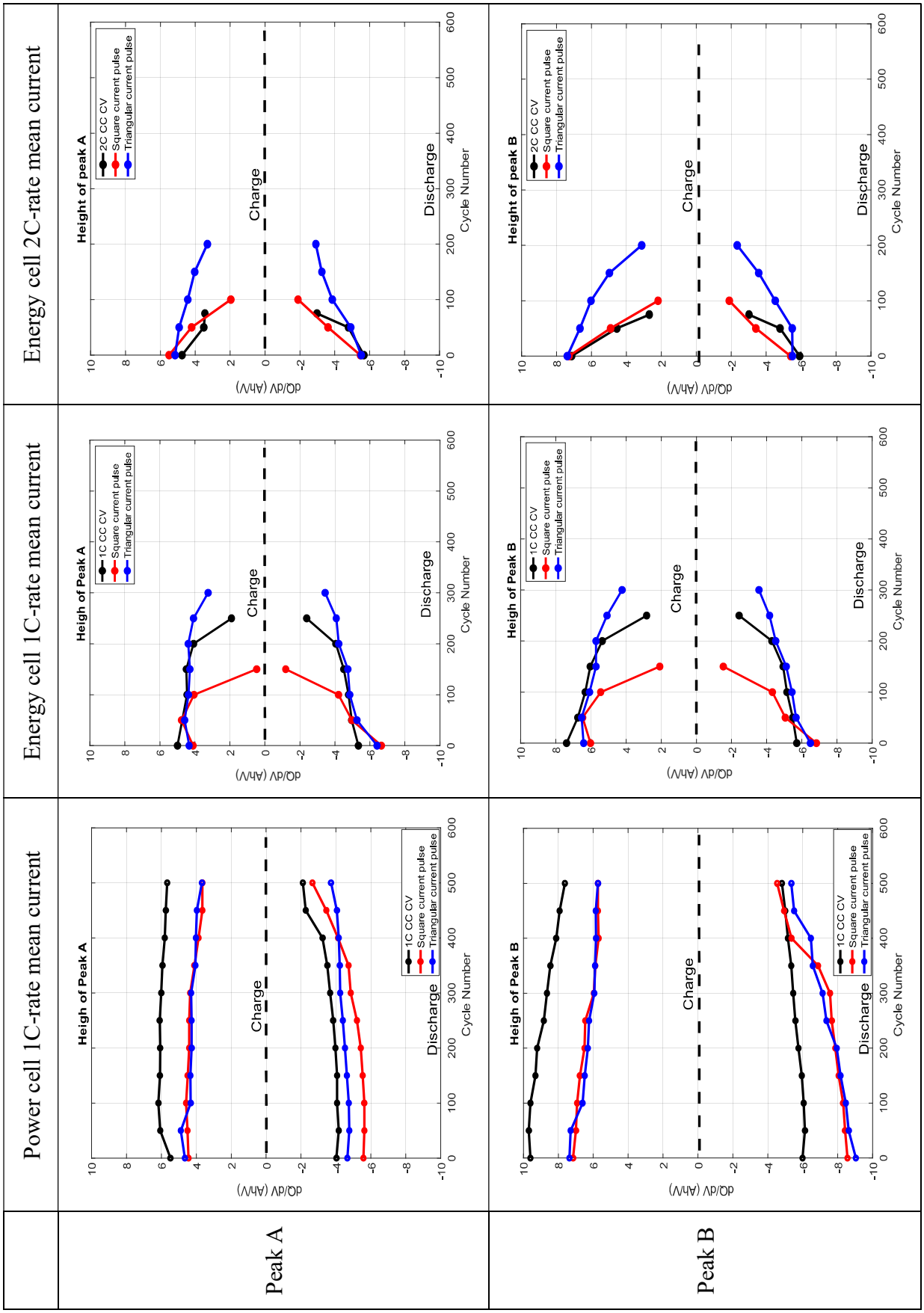

Fig. 5.8 comparison of peak A height (left) and peak B height (right)

From Fig. 5.7 irrespective of power or energy cells and charge protocols, the peaks shift towards higher potential with the increase in cycle number. This shift towards higher voltage is correlated to the increase in ohmic drop of the cells as they age [66], [83].

For power cell, from Fig. 5.8, both the peaks A and B show really slow diminution of intensity in the peaks which indicate lower LAM and lower LLI. The reason being the robustness of these cells which is designed for 2C fast charge and a maximal discharge of 22A.

For energy cell, the most obvious variation with increase in cycle number is the diminution of intensity of the peaks. Especially for cell cycled with Square CP irrespective of mean C-rate, the peaks A and B completely vanishes from the IC curves at the end of 150 cycles indicating a greater LAM and LLI. This is mainly because the degradation of the cells accelerates between 100 and 150 cycles. For the cell cycled with 1C CCCV, after 200 cycles, the intensities of both the peaks A and B reduces significantly. this indicates that the degradation accelerates between 200 and 250 cycles. Whereas, for the cell cycled with triangular CP, the diminution of the intensities of both the peaks is slow. This highlights that, the triangular CP induces less impact on the cells performance and helps preserve the active material and lithium inventory.

Upon closely investigating the evolution of peak A during the early cycles, we observe a slight increase before starting to reduce (Refer Fig. 5.8; power Cell peak A height comparison). The same behavior is observed by authors of [84], [85], [86] and [87]during cycling. The reason for this increase in capacity seems to be originating from the negative electrode as explained by the authors of [84]. The authors used a combination of non-destructive diagnostic methods in a full cell and post-mortem analysis in a coin cell. From the ICA analysis and *post-mortem* of the cells, the authors found that the, negative electrode d-space enlarges and separates the negative electrode layer structure, facilitating the Li+ diffusion, hence increasing the battery capacity.

Based on the ICA results obtained, a strong correlation can be made between intensity of the peaks and SoH.

The peaks A and B seems to be a good indicator of the cell ageing since a correlation may be found between their intensity and SoH.

2.2 Voltage based protocols

This section highlights the ageing results of power and energy optimized NMC-graphite cells cycled with voltage-based protocol. Towards the end of this section the results obtained from SoH, Ri estimation and ICA are also discussed for the same cells.

2.2.1. Ageing

All the main experimental parameters used for cycling of power and energy cells using voltage control method is summarized in Table 25. Two charging methods, voltage step with current limit (VSCL) and 3C-rate with ODC are compared against each other for power and energy cells. The reference charging method is 3C-rate CC with ODC protocol. Whereas for VSCL protocol, the current limit is 3C-rate. In both the protocols, initially the cell is charged to 10% SoC using 0.5C constant current and allowed to rest for 25 minutes to reach open circuit voltage (OCV) and then cells are charged with respective protocols. To reiterate, for VSCL, after reaching the manufacturer maximum cut-off voltage (4.2V) with stepped voltage, the charging continues with voltage pulses. The charging is terminated at the same voltage (i.e. 4.21 for power cell and 4.31V for energy) for both the protocols. After each charging process, the battery is discharged at a constant current of -C/5 C-rate until the lower-bound cut-off voltage of 2.5V for power and 2.75V for energy cell is reached. When this cut-off voltage is reached, the discharging process is terminated. The relaxation time between charges/discharges is set at 1 hour to allow the cell to reach equilibrium state. The cycle-life test for all the experiments is carried out 25°C ambient temperature inside climatic chamber. The main thrust in this study is given to analyze the impact of voltage step protocol in comparison with the mean C-rate using CC protocol on the performance of the power and energy cells.

Fig. 5.9 and Fig. 5.10 compares the evolution of total Δ SoC (left) and total charging time (right) for power and energy cells cycled with VSCL (Blue plot; cell reference: 1k and 2k) and 3C CC with ODC (red plot; cell reference: 1l and 2l) respectively. Whereas, Fig. 5.11 and Fig. 5.12 compares the Δ temperature elevation of the cells during cycling for power and energy cells cycled with VSCL and 3C CC with ODC at 25°C ambient temperature respectively. Since both the cells are not fully charge with the implemented protocols, to compare the two protocols, Equivalent full cycle (EFC) is used. EFC is defined as the ratio of sum of the charge and

discharge capacity during charging to twice the nominal capacity. Δ SoC is defined as the ratio of total capacities during charge (includes initial 10% charge, charge with voltage step and charge during voltage pulse) to maximum initial capacity obtained after preconditioning.

Table 25 summary of experimental parameters used during cyclic ageing study for voltage-based protocol

Protocol	3C CC with ODC	VSCL
Peak C-rate	3	-
Mean C-rate	3	>3 (3C current limit)
Initial SoC (%)	10	10
tc (seconds)	-	1
tr (seconds)	-	1
Frequency (mHz)	-	500
Duty cycle (%)	-	50
cut of voltage (V)	4.21V (Power cell) 4.31V (Energy cell)	4.21V (Power cell) 4.31V (Energy cell)
Rest time (hours)	1	1
Discharge C-rate	-C/5	-C/5
Discharge cut off voltage (V)	2.5V (Power cell) 2.75V (Energy cell	2.5V (Power cell) 2.75V (Energy cell

In general, as expected, with the increase in EFC, the total Δ SoC (left) and total charging time decreases (right) irrespective of the protocol for both power and energy cells.

This is mainly due to the increase in internal resistance of the cell irrespective of the protocol. Since, the terminating condition for both the protocol is cut off voltage of 4.21V and 4.31V for power and energy, the increase in internal resistance results in higher ohmic drop leading to shorter charge time and therefore less capacity charged. Another noticeable point here is that the slope of the SOH curve for the cells cycled with VSCL and 3C CC with ODC is very similar. This suggests that the capacity fade of both the protocols is identical.

For the energy cells cycled with VSCL and 3C CC with ODC lasts only 70 cycles before drastically losing capacity. Also, the capacity fade is identical between these two protocols.

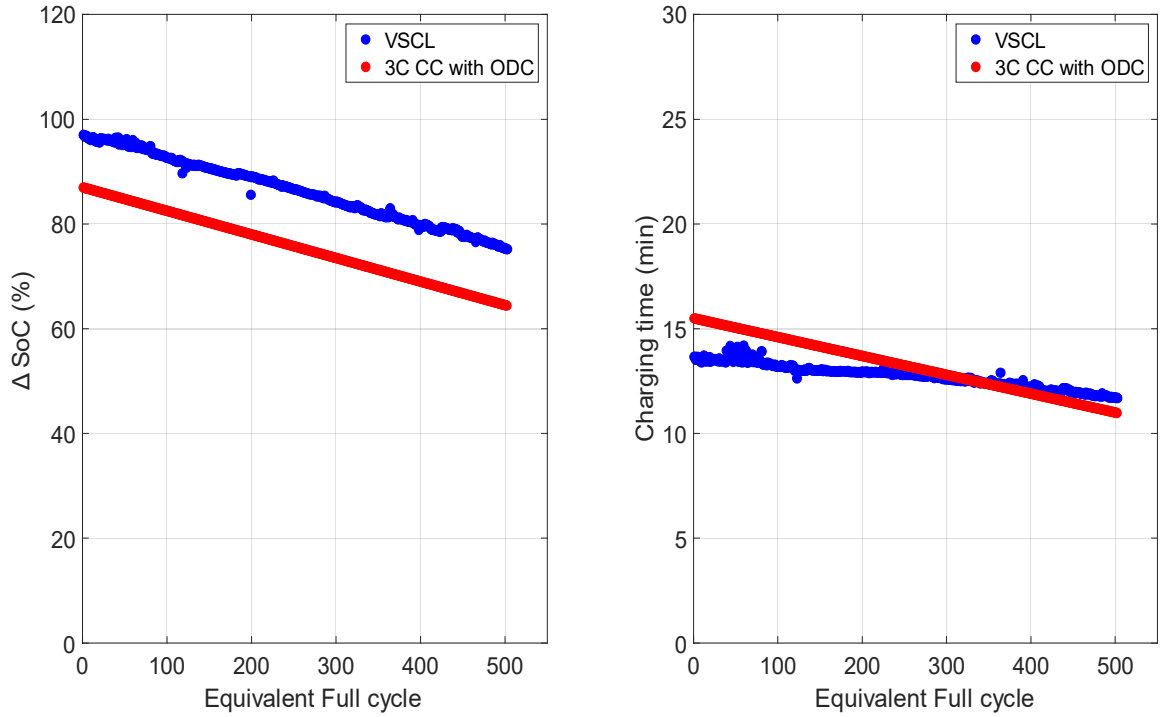

Fig. 5.9 Cycle-life test; Comparison of evolution of (a) Δ SoC (%) (left) total charge time (minutes) (right) for power cell cycled with VSCL (blue; Reference: 1k), 3C CC with ODC (red; Reference: 1l) at 25°C ambient temperature

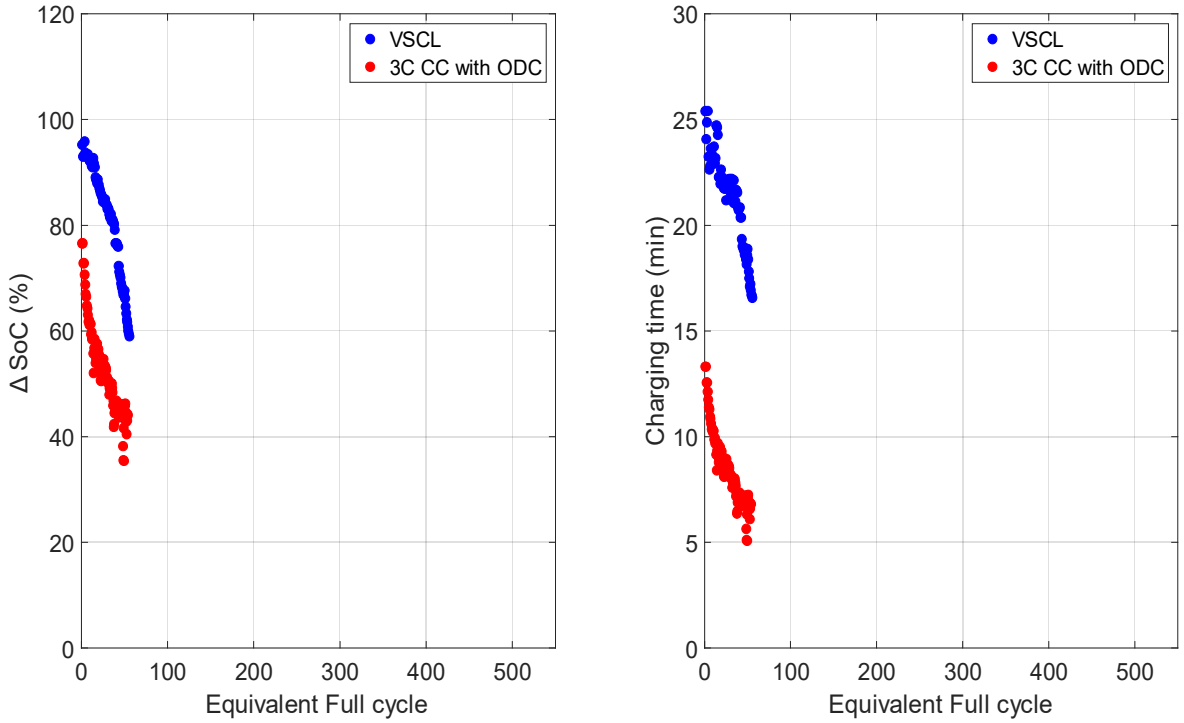

Fig. 5.10 Cycle-life test; Comparison of evolution of (left) Δ SoC (%) (right) total charge time (minutes) for energy cell cycled with VSCL (blue; Reference: 2k), 3C CC with ODC (red; Reference: 2l) at 25°C ambient temperature

Fig. 5.11 and Fig. 5.12 compares the Δ temperature elevation of the power and energy cells during cycling with VSCL and 3C CC with ODC at 25°C ambient temperature. From Fig. 5.11, for power cell, the temperature difference between VSCL and 3C CC with ODC is approximately 6°C. The high temperature elevation for VSCL is mainly because of 4C-rate mean current in VSCL observed for a current limit of 3C-rate. It is worth noting that during cycling, the temperature remains approximately constant.

For energy cell, the temperature difference between VSCL and 3C CC with ODC is approximately 5°C (Fig. 5.12). The lower Δ temperature elevation for the VSCL protocol is related to the longer charging time (Fig. 5.10).

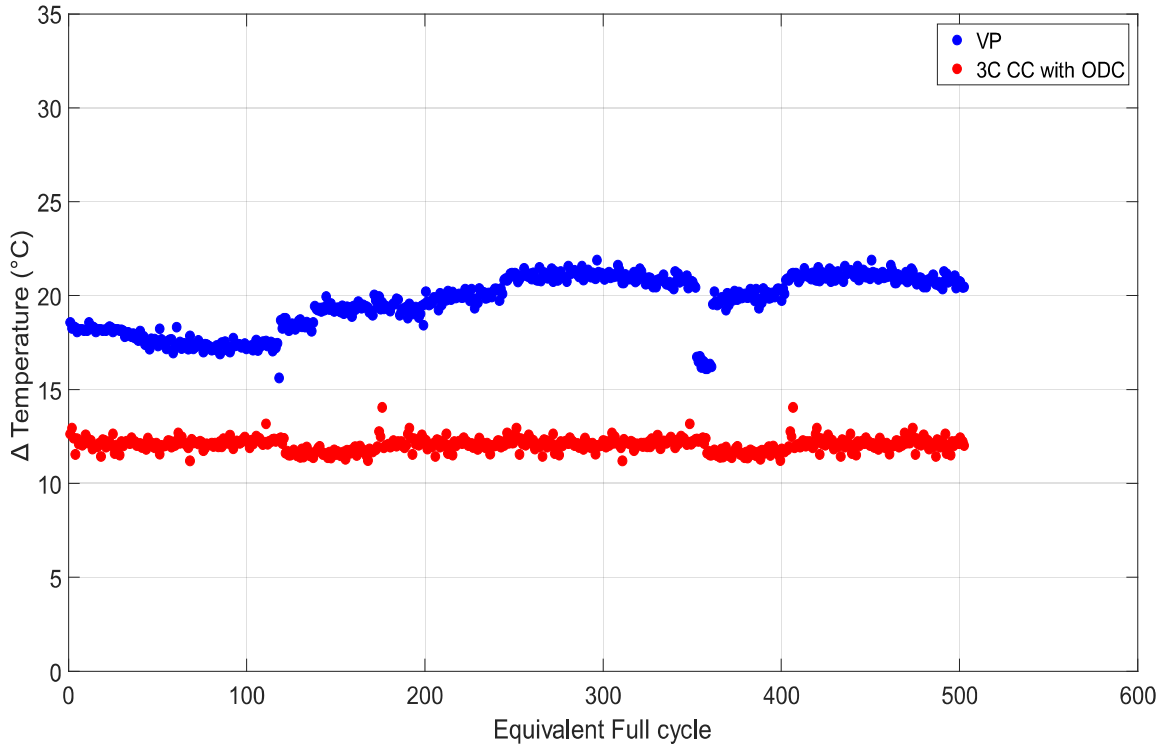

Fig. 5.11 Cycle-life test; Comparison of temperature elevation for power cell cycled with VSCL (blue; Reference: 1k), 3C CC with ODC (red; Reference: 1l) at 25°C ambient temperature

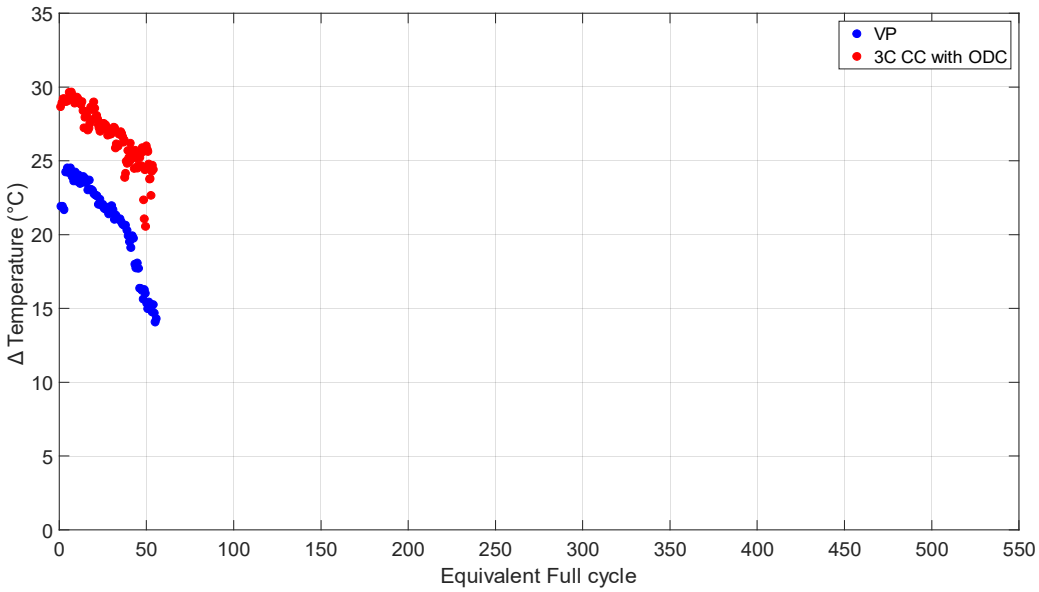

Fig. 5.12 Cycle-life test; Comparison of temperature elevation for energy cell cycled with VSCL (blue; Reference: 2k), 3C CC with ODC (red; Reference: 2l) at 25°C ambient temperature

2.2.2. SoH estimation

The reference performance test (RPT) is done at regular intervals of 50 cycles for all the cells on which aging study was employed. The RPT is done to study the impact of charging protocols on the life time of the cells. The experimental procedure is given beforehand.

Fig. 5.13 compares the evolution of SoH_D (left) and internal resistance vs SoH_D (right) for power and energy cells cycled with VSCL (blue; Reference: 1k;2k) and 3C CC with ODC (red; Reference: 1l ;2l) at 25°C ambient temperature. For power cell, theSoH_D shows a really slow diminution versus cycle number. The cells show identical capacity fade. This suggests that the VSCL has no significant impact on the life span of the cells. In fact, with VSCL, for same aging as reference protocol ageing, fast recharging can be achieved without further accelerating the degradation. At the end of 550 cycles both the cells have lost approximately 15% of capacity.

The SoH_D of the energy cells shows a really identical diminution of its capacity as expected. This suggests that the VSCL has no significant impact of the life span of these cells. In fact, with VSCL, for similar aging as reference protocol ageing, fast recharging can be achieved without further accelerating the degradation. At the end of 100 cycles both the cells have lost approximately 20% of capacity.

Regarding the evolution of internal resistance for all the cells, the Ri tends to increase with the decrease in SoH_D as shown in Fig. 5.13 (right). For power cell, similar internal resistance increase is observed regardless the charge protocol. On contrary, for energy cell, cycled with 3C CC with ODC undergoes a sharp increase of its internal resistance while it is more moderate for the VSCL protocol. At the EOL criteria the internal resistance of the cell cycled with 3C CC with ODC is approximately 65% higher than the cell cycled with VSCL. This suggests that the VSCL has less impact on the internal resistance of the cell and thereby helps to preserve the lifespan.

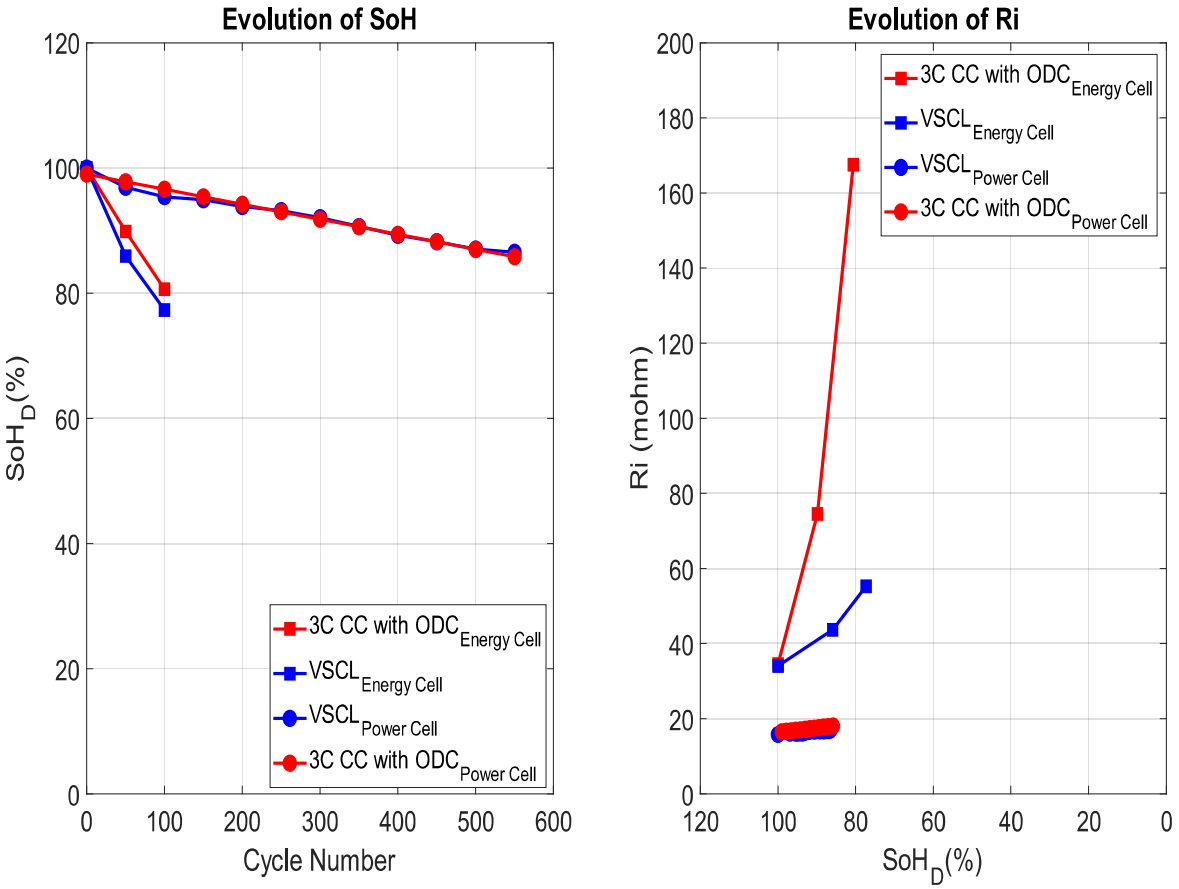

Fig. 5.13 Cycle-life test; Comparison of evolution of SoH (%) (left) and internal resistance vs SoH (right) for power(●)and energy (■)cells cycled with VSCL (blue; Reference: 1k;2k) and 3C CC with ODC (red; Reference: 1l;2l) at 25°C ambient temperature

2.2.3. ICA estimation

The ICA is carried out to extract the information with regards to degradation modes due to the impact of various charging protocols on the life time of the cells. The experimental procedure is given beforehand.

Fig. 5.14 shows the ICA curves for both power and energy cells cycled with VSCL (left), and 3C CC with ODC (right) at 25°C ambient temperature recorded every 50 cycles intermittently.

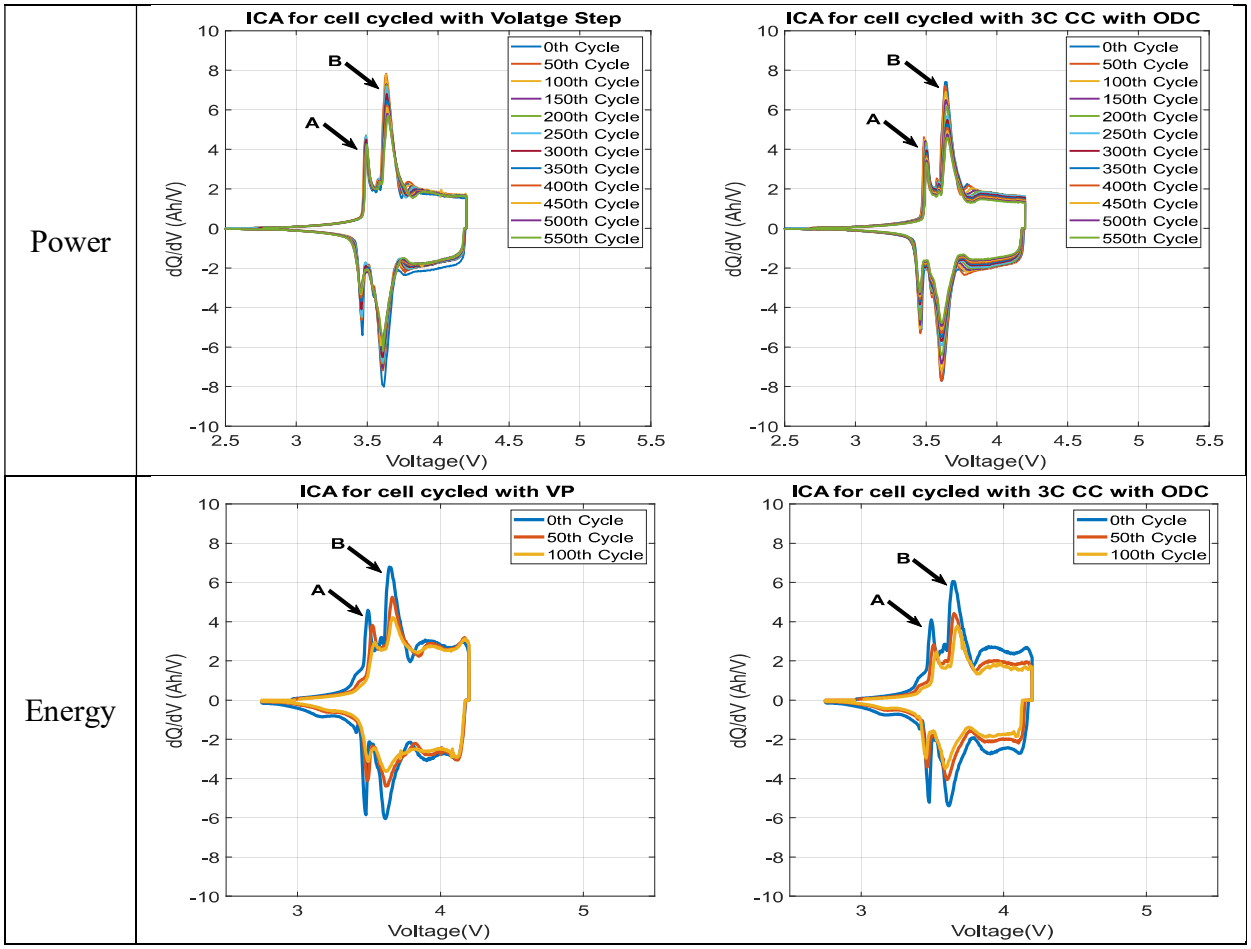

Fig. 5.14 IC curves for power(top) and energy (bottom) cells cycled with VSCL (left; Reference: 1k;2k), and 3C CC with ODC (right; Reference: 1l;2l) at 25°C ambient temperature

From Fig. 5.14, irrespective of the charge protocol and type of cell, the peaks shift towards higher potential with the increase in cycle number. This shift towards higher voltage is corelated to the increase in ohmic drop of the cells as they age.

From Fig. 5.15, the most obvious variation with increase in cycle number is the diminution of intensity of the peaks irrespective of the protocol. The power cells show really slow diminution of intensity in the peaks which indicate lower LAM and lower LLI. The reason being the robustness of these cells.

Upon close examination, the slopes of both the peaks A and B, for the cell cycled with 3C CC with ODC is similar to the slopes of the cell cycled with VSCL.

From Fig. 5.15, VSCL does not accelerate the ageing as compared to 3C CC with ODC for power and energy cells. But rather, it helps to preserve the life span of the cells. These results, highlights that the VSCL is not detrimental to the cells compared to 3C CC with ODC.

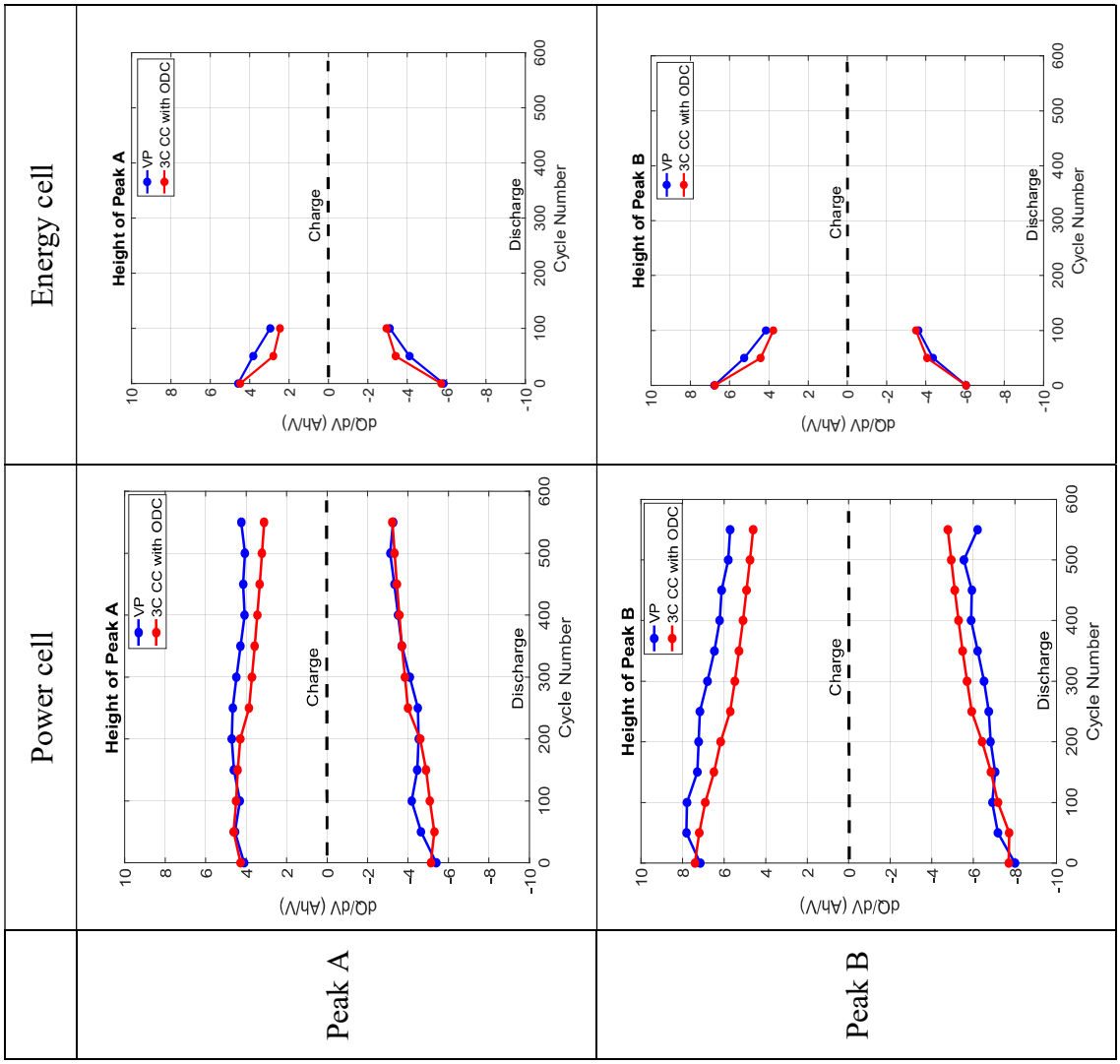

Fig. 5.15 Comparison of A peak height (left) and B peak height (right) for power (bottom) and energy (top)cells cycled with VSCL 1C-rate CCCV (Reference: 1k;2k), and 3C CC with ODC (Reference: 1l;2l) at 25°C ambient temperature

3. Reproducibility of results

One of the important parts during this ageing study is to investigate the reproducibility of the experimental results employing new fast charging protocol and to validate the same. This is carried out to eliminate the dependence of the fast charging protocol only to one cell. Namely, some of the reasons for the deviation in SoH curves maybe due to the variation during construction of the cells or variation in contact resistance while connecting to the cyclers or variation in internal resistance of the cell or small variation between the channels of the cycler.

Therefore, in this section, the ageing results due to various charging protocols as discussed in earlier sections are compared. This section is divided into mainly 2 parts dedicated to current based protocols as discussed in section 2. and voltage-based protocols in section 3 of this Chapter. In general, the reproducibility of the results is tested using 2 cells for each charging protocol coming from the same manufacturer. Due to the lack of time and unavailability of channels on the equipment, it is difficult to perform a real reproducibility study with statistically adequate number of cells.

3.1 Current based protocol

In this section, the reproducibility of the experimental results for the cells cycled 1C-rate CCCV, 2C-rate CCCV, square CP and triangular CP with 1C-rate and 2C-rate mean current is discussed. The experimental procedure and protocols are given beforehand in section 2. To quickly investigate the reproducibility, only the SoH_D at regular intervals of 50cycles is compared.

Fig. 5.16 compares the evolution of average SoH_D for power cells cycled with 1C-rate CCCV (black), square current pulse (Red) and triangular current pulse (blue) with 1C-rate mean current at 25°C ambient temperature along with standard deviation. Whereas, Fig. 5.17 compares the evolution of average SoH_D for energy cells cycled with CCCV (black), square CP (red) and triangular CP (blue) with 1C-rate and 2C-rate mean current at 25°C ambient temperature along with standard deviation.

For power cell, in total 6 cells were used to investigate the reproducibility. Out of which 2 cells was used for 1C CCCV, 2 cells for square CP, and 2 cells for triangular CP with 1C-rate

mean current. In all the experiments the overall standard deviation in SoH_D is found not to exceed 3% as shown in Fig. 5.16. The cells employing square CP tends to age more than the cells employed with 1C CCCV and triangular CP. Thus, the triangular CP can have less impact on cell ageing and it is not confined to only one cell in particular.

For energy optimised cell, in total 12 cells were used to investigate the reproducibility. Out of which 2 cells was used for 1C CCCV, 2 cells for square CP, and 2 cells for triangular CP with 1C-rate mean current and similarly for 2C-rate mean current. The overall standard deviation in SoH_D is found not to exceed 3% for all the cells except for the cell cycled using square CP at 1C-rate mean current as shown in Fig. 5.17. one reason for this big deviation may be due to the uncertainty during manufacturing. From Fig. 5.17, irrespective of the mean C-rate, the cells employing square CP tends to age more than the cells employed with CCCV and triangular CP.

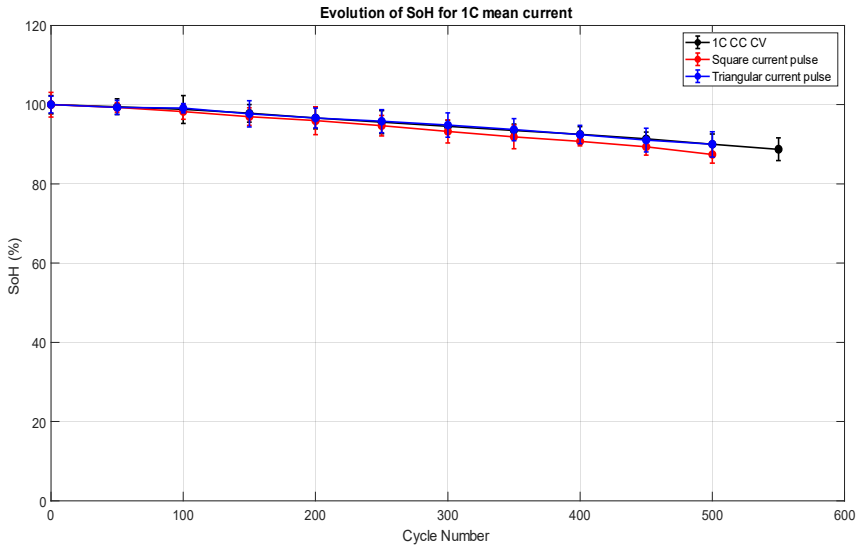

Fig. 5.16 Average SoH for power cells cycled with 1C CCCV (black), square CP (red) and triangular CP (blue) with standard deviation during ageing at 25°C

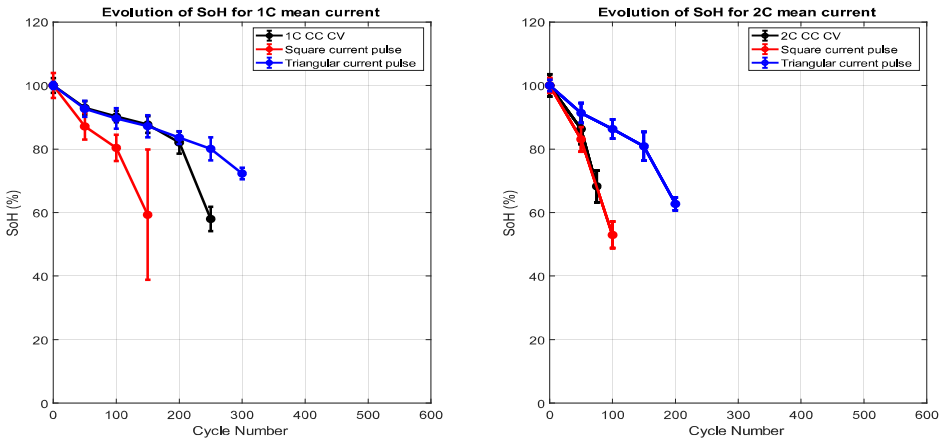

Fig. 5.17 Average SoH for energy cells cycled with CCCV (black), square CP (red) and triangular CP (blue)with 1C-rate mean current (left) and 2C-rate mean current (right) with standard deviation during ageing at 25°C

3.2 Voltage based protocol

Fig. 5.18 compares the evolution of average SoH_D for power cells cycled with VSCL (blue) and 3C CC with ODC (red) at 25°C ambient temperature along with standard deviation. For power optimised cell, in total 4 cells were used to investigate the reproducibility. Out of which 2 cells was used for VSCL, 2 cells for 3C-rate CC with ODC. In all the experiments the overall standard deviation in SoH is found not to exceed 2% as shown in Fig. 5.18.Indeed, the slopes of the cells employing cycled with VSCL and 3C CC with ODC are very similar exhibiting slow diminution of capacity fade. Thus, the VSCL can recharge the in shorter time and at the same time can have less impact on cell ageing in comparison to 3C CC with ODC.

Similar to power cells, Fig. 5.19 compares the evolution of average SoH_D for energy cells cycled with VSCL (blue) and 3C CC with ODC (red) at 25°C ambient temperature along with standard deviation. For energy optimised cell, in total 4 cells were used to investigate the reproducibility. Out of which 2 cells was used for VSCL, 2 cells for 3C-rate CC with ODC. In all the experiments the overall standard deviation in SoH is found not to exceed 2% as shown in Fig. 5.19. Again, the slopes of the cells employing cycled with VSCL and 3C CC with ODC are very similar demonstrating that VSCL is an effective protocol even for energy cell.

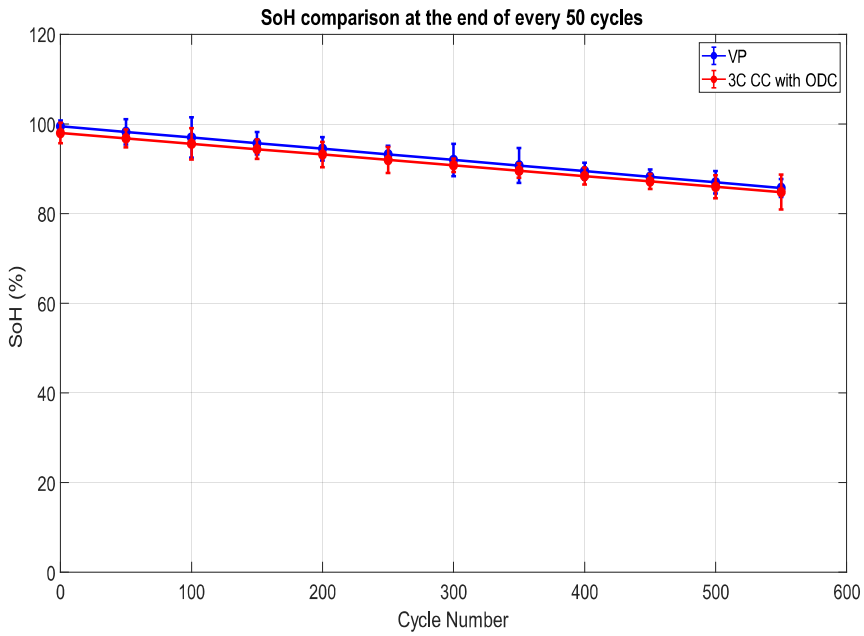

Fig. 5.18 Average SoH for power cells cycled with VSCL (blue) and 3C CC with ODC (red) with standard deviation during ageing at 25°C

Fig. 5.19 Average SoH for energy cells cycled with VSCL (blue) and 3C CC with ODC (red) with standard deviation during ageing at 25°C

4. Conclusion

Experiments were performed on energy and power cells to study the impact of current and voltage-controlled protocols on ageing of the cells. *Table 26* gives the overview of SoH_D and total number of cycles for the cells. For the current controlled protocol, from the results, Triangular CP is very effective protocol to recharge NMC based cells. As this protocol does not accelerate the aging for this Li-ion cell.

For voltage-controlled protocol, the VSCL was compared with 3C-rate CC with ODC at mean 3 C-rates between 10% SoC to 90% SoC. From the results we can conclude that employing VSCL is beneficial for the cell in terms of ageing.

Nevertheless, it will be interesting to investigate the impact of triangular CP for other chemistries as well before drawing a general conclusion.

Table 26 summary of SoH of all the cycled cells.

	Reference	Protocol	SoH (%)	No. Of cycles
Power Cell	1e	1C CC CV	85	600
	1f	Square CP 1C mean	85	500
	1g	Triangular CP 1C mean	85	500
	1k	VSCL	85	550
	1l	3C CC with ODC	85	550
Energy Cell	2e	1C CC CV	60	250
	2f	Square CP 1C mean	40	150
	2g	Triangular CP 1C mean	78	300
	2h	2C CC CV	65	100
	2i	Square CP 2C mean	55	70
	2j	Triangular CP 2C mean	60	200
	2k	VSCL	80	100
	2l	3C CC with ODC	80	100

Chapter 6. Ageing Study: Part-II

1. Introduction

In chapter 5, the ageing results of various fast charging protocols is discussed for power and energy cell. Hence, in this chapter we will discuss the results relating to the diagnosis of the ageing mechanisms for energy cell. Energy cells are very much interesting because, they have degraded significantly and can give more insights about the degradation when compared to that of power cell. So only results on Energy are reported in this chapter. The cells are first analysis using tomography X ray in order to observe the internal deformation and the state of security of the cell. After, the cell is dismantled at 0% of SOC in glove box and the recovered electrodes are characterized by half-coin cell versus lithium.

2. X-ray Tomography of cells

It was demonstrated that, when fast charging protocols are employed on the cells, the surface temperature increases and the cells experience temperature gradients internally. For example, the surface temperature of the cells cycled with 3C-rate CC with ODC reaches 55°C (See Chapter 4). At the same time, the cell voltage reaches highest at the end of charge exceeding cut-off voltage value prescribed by the manufacturer. Regarding the capacity fade mechanism, these both effects may induce internal degradations resulting in a more or less rapid loss of capacity according to the chosen charging protocol. To go further in the ageing investigation and in the internal modification of the battery materials, X-Ray tomography has been performed on the energy cells.

Fig. 6.1 illustrates the longitudinal cross section of fresh energy cell highlighting various components as seen in X-ray tomography. The solid white line as seen in the image is the outer steel casing of the cell. Current Interrupt Device (CID) can be seen in the highlighted region near the positive terminal contact. The CID is an irreversible protective pressure valve, when triggered due to increase in the internal pressure, disconnects the electrical contact between the positive terminal and electrode inside the cell [88]. Also, we can see the jelly roll comprising, negative electrode, positive electrode and separator. The empty space in the center of the image is the space of the mandrel on which the jelly roll was constructed. Before sealing the cell, the mandrel is removed.

Fig. 6.2 illustrates the cross-sectional view of X-ray tomography of energy cell cycled with 1C-rate CCCV, Square CP and triangular CP with 1C-rate mean current, 3C CC with ODC and

VSCL protocol. These cross-sectional snaps are taken from the analysis zone highlighted in Fig. 6.1. From Fig. 6.2, In general for energy cell cycled with 1C CCCV, Square CP with 1C-rate mean current and 3C CC with ODC, we can notice the deformation of jelly roll into the middle of the cell due to the absence of mandrel there. This is possible only due to the excess of pressure. So, this kind of deformations reveals an increase of the internal pressure during ageing. Comparing the current control protocols, we see that the cell aged with Square CP deforms much than 1C CCV and triangular CP. The cell aged with later protocol exhibits very less deformation. It is important to mention that no deformation is observed for the cell aged with triangular CP in reference to fresh cell.

Whereas, comparing the VSCL and 3C CC with ODC, we can see that the later protocol leads a pronounced default in its jelly roll halfway from the positive terminal., while the former protocol, has very less deformation in comparison to fresh cell.

The deformation of the jelly roll may be related to the formation of high-pressure gas. The formation of gas conceivably comes from the side reactions of the electrolyte or electrolyte additive components at high voltage and high temperature. The fast ageing of the cell cycled with 3C CC with ODC seems to be related to the concomitant effect of cell voltage higher than 4.2V during charging and temperature higher than 55°C. Such gas emission has been already reported in the literature [89], [90].

For other energy and power cells, the X-ray topography was not possible due to lack of time and unavailability of the equipment. In near future it is interesting to perform tomography for other cells as well.

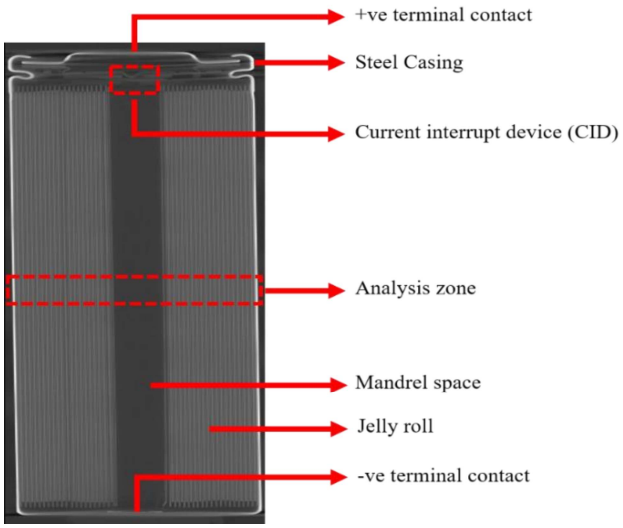

Fig. 6.1 longitudinal cross section of the fresh energy cell showing various parts.

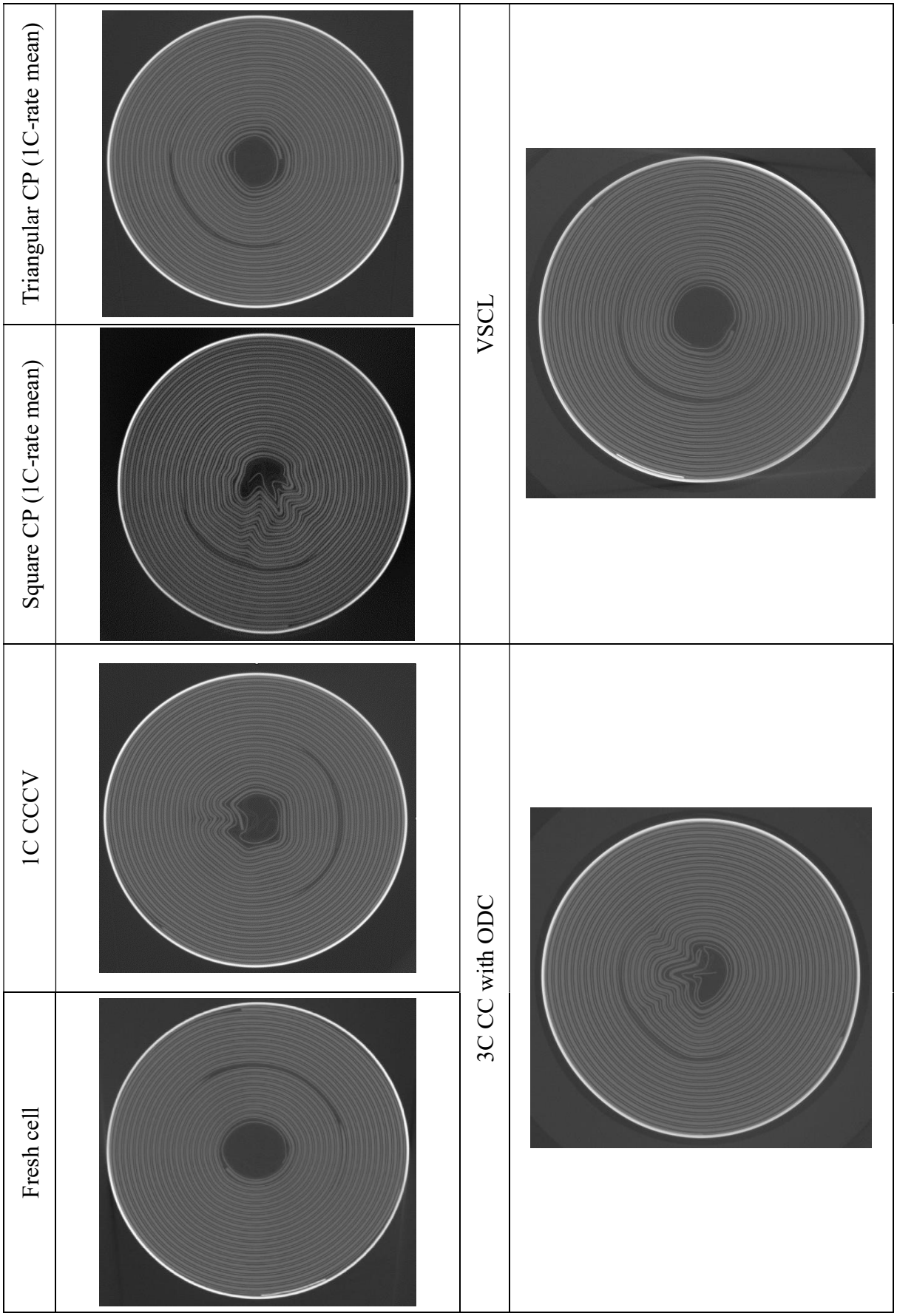

Fig. 6.2 X-ray Tomography of energy cells cycled with various charging protocols alongside with fresh cell

3. Characterization of Aged electrodes

3.1 Coin cell construction

To understand the impact of charging protocols on the evolution of the performance of a cell, it is interesting to study each recovered electrode from cell individually against a Lithium counter electrode. The electrochemical characterization of electrodes is done by constructing two half cells in CR2032 coin cell format consisting of a positive or negative electrode facing the metallic lithium. Note that, to construct the coin cells, fresh energy cell fully discharged (i.e. under 0% SoC) is dismantled in an argon-controlled atmosphere inside the glove box. Also, before construction of the coin cells, the coating must be removed on one of the two sides of the disassembled electrodes from cells using NMP solution. Next, 14 mm diameter discs are cut, washed in DMC and dried under vacuum before assembling into coin cells facing a metallic lithium electrode as shown in Fig. 6.3.

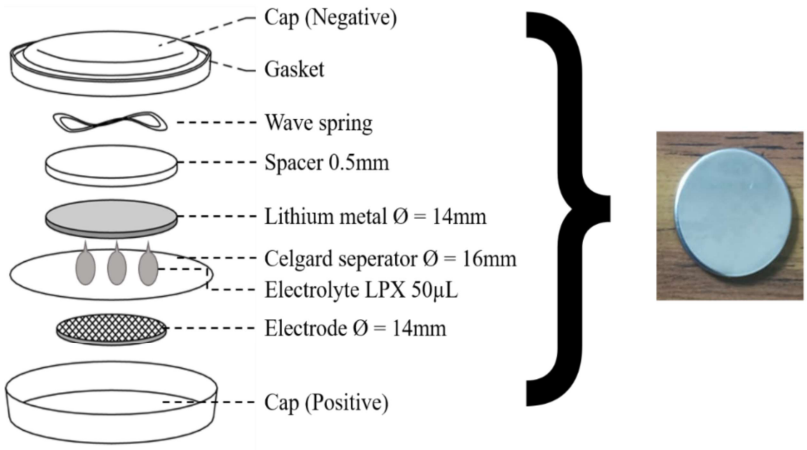

Fig. 6.3 Various components in a coin cell [91]

The electrolyte used during the construction of coin cells consists of LiPF6 (1mol/L) salt dissolved in the solvents such as Ethylene Carbonate, Ethyl Methyl Carbonate and Dimethyl Carbonate (EC/EMC/DMC 1:1:1 by mass). This electrolyte is generally called as LPX and has a composition close to that of electrolytes used in commercial cells, which is why it has been chosen here[92].

3.2 Characterization method

Prior characterization of electrodes, it is important to complete the delithiation of negative electrode and lithiation of positive electrode so as to reach the maximum limits of electrode materials. In addition, from this the residual capacity can be measured. This residual capacity corresponds to the capacity remaining in the electrode after complete discharge before dismantling of the complete cell.

The coins cells are characterized at a constant C/10 C-rate between 3V vs Li/Li^+ to 4.3V vs Li/Li^+ for positive electrode coin cell and between 10mV vs Li/Li^+ to 1.5V vs Li/Li^+ for negative electrode coin cells. The evolution of Open Circuit Potential (OCP) of the electrodes at the Beginning of Life (BOL) is normalized for the full cell and is illustrated in Fig. 6.4 (a). After having the OCP's of the electrode, the negative electrode OCP is repositioned in such a way that the final point of OCP's of both the electrode coincide at the same point. Hence, we can see the shift of OCP of negative electrode towards the negative X-axis in Fig. 6.4 (b). Now, experimental OCV of the full cell is introduced into the graph and is highlighted by solid black line in Fig. 6.4 (c). This fitting procedure follows the principle as done by Maxime Montaru [93].

Three input parameters, C_{Pos}, C_{Neg} and OFS are considered to fit the experimental OCV curve from positive and negative OCP's between V_{max} and V_{min} of the full cell OCV. To built the cell OCV signal, the offset parameter (OFS) is therefore introduced to shift the negative electrode OCP to the left as shown in Fig. 6.4 (d). The OCP curves are shrunk until the OCV curve obtained by subtracting the positive to the negative electrode OCP's matches the experimental OCV curve.

The offset parameter (OFS) is related to the non-lithiated capacity fraction of the positive electrode and lithiated capacity fraction of the negative electrode [93]. Any variation in C_{Pos} and C_{Neg}, of OCP's are related to LAM of respective electrodes while fitting the curves.
Hence, the percentage of LAM can be obtained by C_{pos}, and C_{Neg}. The LAM is calculated as follows:

$$LAM_{PE\ or\ NE}(\%) = \frac{\max\left(C_{BOL_{pos\ or\ neg}}\right) - \max\left(C_{nth\ cycle_{pos\ or\ neg}}\right)}{\max\left(C_{BOL_{pos\ or\ neg}}\right)} * 100 \qquad (43)$$

Extracting the information related to LLI is more tricky because the developed model from [93] takes into account the calendar ageing where the LLI can be calculated easily. Since, we are under cyclic ageing determining LLI from the developed model [93] required further development.

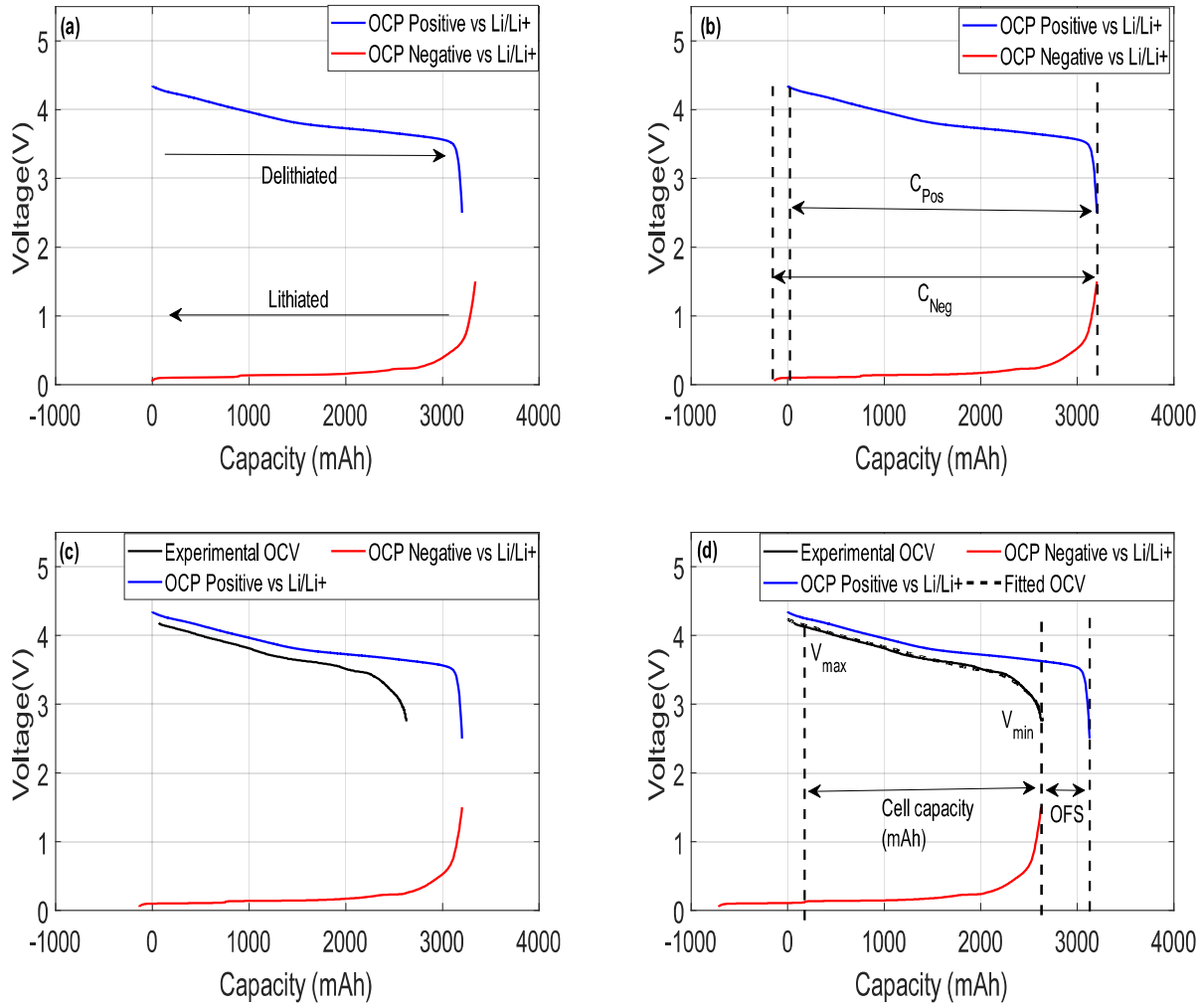

Fig. 6.4 OCV model procedure for eneryg cell (a) OCP's of electrodes vs lithium content, (b) initialisation of OCP's to start at same position vs lithium content, (c) OCP's of electrode and full cell experimental OCV vs capacity (d) OCP's of electrode, full cell experimental OCV and fitted OCV vs capacity

3.3 Charging protocol discussion

Based on the fitting procedure described in the previous section and thank to the Equation 21, the percentage LAM for energy cell can be obtained and is given in and Fig. 6.5

The LAM in the negative electrode (LAM_{NE}) can occur as a result of particle cracking or electronic contact loss between particles of the active electrode material or between the active

material and the current collector. The lithium trapped inside the isolated graphite particles can no longer be cycled, leading to a decrease in the cell's capacity As a result, less active material is available at the negative electrode to intercalate Lithium, which is manifested in a shrinkage of the OCP of the negative electrode versus capacity. More LAM_{NE} means that the current density on the remaining material is increased during cycling, which could in turn lead to accelerated aging of the electrode and in the worst case, to lithium plating on the surface if the charging rates exceed the rates of lithium diffusion into graphite.

The LAM in the positive electrode (LAM_{PE}) is analogous to LAM_{NE}. It is a result of electronic contact loss to positive electrode material.

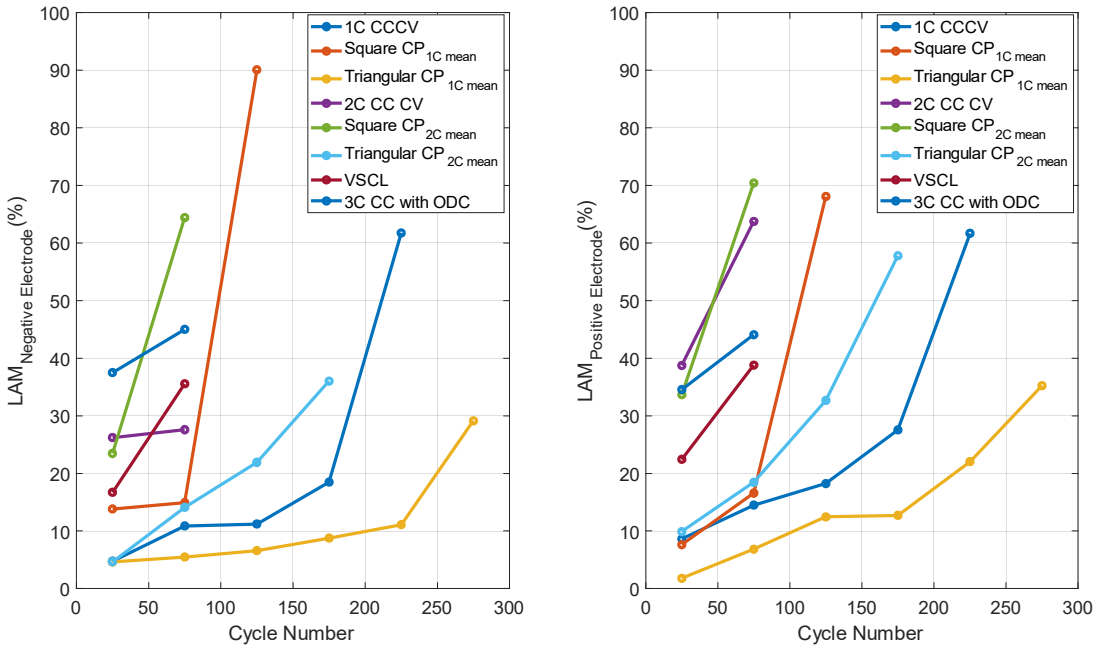

Fig. 6.5 LAM evolution for negative electrode (left) and positive electrode (right) between the RPT's for energy cell cycled with various protocol during ageing

From, Fig. 6.5, we can observe that the LAM of negative electrode of the cell cycled with square CP with mean 1C-rate has the highest predicted value and this explains the low SoH of the cell at the end of 150th cycle. The LAM of negative electrode for the cell cycled with 3C CC with ODC is quite higher when compared to cell cycled with VSCL protocol. The same holds good for the positive electrode LAM.

All these results are predicted, thanks to fitting method from [93] and hence need validation by post-mortem analysis of the cell.

4. Conclusion

The development of fast charging method for lithium batteries remains a key point of their deployment. Saving the charging time can be damaging to the life of the battery. Indeed, fast charging with square CP and 3C CC with ODC induces accelerated capacity fade due to degradation mechanisms at high cell voltage and temperature. The formation of gas due to degradation of electrolyte induces pressure on the jelly-roll leading to deformation has been observed using X-ray tomography and internal visual inspection.

Electrochemical analysis using coin cells show both active materials degradation and loss of lithium inventory to be root cause for capacity fade, which may be related to the high temperature and cell voltage. Moreover, SEI decomposition and growth can be also involved. Nonetheless, with VSCL we can achieve the target recharging time without accelerating the ageing in comparison to the conventional protocol.

General Conclusion

General Conclusion

This thesis is a part of the industrial IBIS project concerning the development of smart storage systems for vehicle or stationary application. In particular, the objective of this thesis consists of evaluating fast charging protocols for Li-ion battery with current control and voltage control techniques in relation to the architecture of the new modular pack. To achieve this objective, it is essential to evaluate the protocols with regards to target recharge time of 20 minutes for 80% of Δ SoC and Δ temperature elevation less than 25°C to limit the degradation of the cell.

For this purpose, first, a through literature survey was carried out concerning different charging protocols. In this regard, there are several fast charging protocols. All the protocols discussed in the literature have their own advantage and drawback. Later in this thesis, various techniques are employed to characterize the cells. Two different C/NMC cells are used in particular, power optimised 18650-20R from Samsung SDI and energy optimised 18650-26M from LG Chem. Each type of the battery has similar characteristics with notable difference in the internal resistance. The energy cell has an internal resistance of one third higher than the power cell. As shown, in this work, the fast charging can be done by either controlling the current or voltage.

Influence of current control protocol on battery performance

Several experiments were conducted to study the impact in terms of shape of the waveform and temperature rise of fast charging based on current control. The square and triangular current pulse methods was compared with the classical CCCV protocol alongside with studying the impact of frequency on square current pulses. Even though square and triangular pulse current have similar charging times in the pulse charging stage, a considerable difference in temperature increase can be observed.

The thermal behavior for all the charging methods is studied parallelly. The temperature increase was in accordance with the C-rate. This temperature increase could be minimized by incorporating triangular pulses. Irrespective of the shape of the waveform, the CV stage is inevitable and thus prolongs the charging process resulting in longer recharging time

The ageing study with square, triangular current pulse and CCCV methods reveal that the triangular CP exhibits better performance in comparison with CCCV and square CP at a given mean C-rate. From X-ray tomography and ageing model, the square CP is detrimental as it leads

to formation of gas due degradation of electrolyte (side reaction) and LAM in both the electrodes.

Influence of voltage control protocol on battery performance

The Voltage Step with Current Limit (VSCL) protocol is employed on energy and power cell. The total charging time can be improved significantly when using this protocol on energy or power cell as it considers the internal resistance when applying voltage steps. However, the VSCL has very little effect at mean 3 C-rate for power cell in terms of temperature increase because this type of cell has low internal resistance. It seems that the VSCL is also efficient for the energy cells even if these cells have higher internal resistance.

The thermal behavior for both protocols was also studied and the VSCL protocol is more suitable to recharge the cells with higher C-rates as it is possible to stay within the temperature limits prescribed by the manufacturer without compromising the recharging time. The VSCL was compared with 3C-rate CC with ODC protocol and with later the temperature exceeds the manufacturer temperature limit.

The ageing study of these two-protocol revealed identical capacity fade. But the X-ray tomography on the energy cells cycled with VSCL and 3C-rate CC with ODC revealed that the 3C-rate CC with ODC has significant impact on the electrode structure due to the formation of high-pressure gas.

Then it seems that, the VSCL protocol developed in this work paved the way to new fast charge protocol.

Future perspectives

The VSCL fast charging protocol can be implemented on the IBIS architecture without accelerating the ageing. This method will replace or to diminish other fast-charging methods but in contrary, it is very good complementary and alternative for the existing fast charging methods to be used in the automotive sector principally. However, this thesis is just the beginning regarding the potential of voltage control during charge protocol. Indeed, up until now, this method has just been studied on a single cell and a lot of information can be acquired from that alone. In perspective, it would be interesting to further this study more deeply in the several following directions:

- Exploring other types of lithium-ion battery technologies: study of this protocol with LFP or other NMC ratio stoichiometry.
- Further evaluation of VSCL method on a battery-pack: This protocol is able to charge easily one cell, but the charge of the battery pack could be more challenging due to the association of the cells in series and parallel configuration.
- To optimise VSCL protocol by considering other parameters such as entropy and impedance.
- To combine VSCL protocol with triangular voltage pulse into one charging protocol at the end of charge and further studies for a better understanding of this method at harsh weather condition (i.e. winter weather, summer weather)
- To optimise the ageing characterisation for implementing LLI.

References

[1] J. Lopez, M. Gonzalez, J. C. Viera, and C. Blanco, “Fast-charge in lithium-ion batteries for portable applications,” in *INTELEC 2004. 26th Annual International Telecommunications Energy Conference*, 2004, pp. 19–24, doi: 10.1109/INTLEC.2004.1401439.

[2] J. Vetter *et al.*, “Ageing mechanisms in lithium-ion batteries,” *J. Power Sources*, vol. 147, no. 1, pp. 269–281, 2005, doi: https://doi.org/10.1016/j.jpowsour.2005.01.006.

[3] G. Patry, A. Romagny, S. Martinet, and D. Froelich, “Cost modeling of lithium-ion battery cells for automotive applications,” *Energy Sci. Eng.*, vol. 3, Oct. 2014, doi: 10.1002/ese3.47.

[4] Z. Z. and Y. T. Chunlei Jiang, Xing Meng, Yongping Zheng, Jiaxiao Yan, “High-Performance Potassium-Ion-Based Full Battery Enabled by an Ionic-Drill Strategy,” *Chinese Chem. Soc.*, vol. 3, no. 9, pp. 85–94, 2021.

[5] J. Barker, M. Y. Saidi, and J. L. Swoyer, “A Sodium-Ion Cell Based on the Fluorophosphate Compound {NaVPO}[sub 4]F,” *Electrochem. Solid-State Lett.*, vol. 6, no. 1, p. A1, 2003, doi: 10.1149/1.1523691.

[6] K. M. Abraham, “How Comparable Are Sodium-Ion Batteries to Lithium-Ion Counterparts?,” *ACS Energy Lett.*, vol. 5, no. 11, pp. 3544–3547, Nov. 2020, doi: 10.1021/acsenergylett.0c02181.

[7] A. El Kharbachi, O. Zavorotynska, M. Latroche, F. Cuevas, V. Yartys, and M. Fichtner, “Exploits, advances and challenges benefiting beyond Li-ion battery technologies,” *J. Alloys Compd.*, vol. 817, p. 153261, 2020, doi: https://doi.org/10.1016/j.jallcom.2019.153261.

[8] M. H. Noh, P. X. Thivel, C. Lefrou, and Y. Bultel, “Fast-charging of lithium iron phosphate battery with ohmic-drop compensation method,” *J. Energy Storage*, vol. 8, pp. 160–167, 2016, doi: https://doi.org/10.1016/j.est.2016.10.005.

[9] John S Newman; Karen E Thomas-Alyea, *Electrochemical systems*. 2004.

[10] L. Ménard, G. Fontes, and S. Astier, “Dynamic energy model of a lithium battery,” *Math. Comput. Simul.*, vol. 81, pp. 327–339, Oct. 2010, doi: 10.1016/j.matcom.2010.07.026.

[11] N. Nitta, F. Wu, J. T. Lee, and G. Yushin, “Li-ion battery materials: present and future,” *Mater. Today*, vol. 18, no. 5, pp. 252–264, 2015, doi: https://doi.org/10.1016/j.mattod.2014.10.040.

[12] R. Jung, M. Metzger, F. Maglia, C. Stinner, and H. A. Gasteiger, “Oxygen Release and Its Effect on the Cycling Stability of Cathode Ma,” *J. Electrochem. Soc.*, vol. 164, no. 7, pp. A1361--A1377, 2017, doi: 10.1149/2.0021707jes.

[13] E. Commission, J. R. Centre, L. Boon-Brett, N. Lebedeva, and F. Di Persio, *Lithium ion battery value chain and related opportunities for Europe*. Publications Office, 2018.

[14] S.-T. Myung *et al.*, “Nickel-Rich Layered Cathode Materials for Automotive Lithium-Ion Batteries: Achievements and Perspectives,” *ACS Energy Lett.*, vol. 2, pp. 196–223, 2016, doi: 10.1021/acsenergylett.6b00594.

[15] E. D. concepts Aux and Applications, *Electrochimie: Des concepts aux applications*, 4th ed. 2011.

[16] A. Manthiram, “Materials Challenges and Opportunities of Lithium Ion Batteries,” *J. Phys. Chem. Lett.*, vol. 2, no. 3, pp. 176–184, Feb. 2011, doi: 10.1021/jz1015422.

[17] Q. Zhao, S. Stalin, C.-Z. Zhao, and L. A. Archer, “Designing solid-state electrolytes for safe, energy-dense batteries,” *Nat. Rev. Mater.*, vol. 5, no. 3, pp. 229–252, 2020, doi: 10.1038/s41578-019-0165-5.

[18] X. Ji *et al.*, “Efficient room-temperature solid-state lithium ion conductors enabled by mixed-graft block copolymer architectures,” *Giant*, vol. 3, p. 100027, 2020, doi: https://doi.org/10.1016/j.giant.2020.100027.

[19] P. Arora and Z. (John) Zhang, “Battery Separators,” *Chem. Rev.*, vol. 104, no. 10, pp. 4419–4462, Oct. 2004, doi: 10.1021/cr020738u.

[20] M. Hussain, M. M. Beg, M. Alam, and S. Laskar, “Big Data Analytics Platforms for Electric Vehicle Integration in Transport Oriented Smart Cities: Computing Platforms for Platforms for Electric Vehicle Integration in Smart Cities,” *Int. J. Digit. Crime Forensics*, vol. 11, pp. 23–42, Jul. 2019, doi: 10.4018/IJDCF.2019070102.

[21] J. Deng, C. Bae, A. Denlinger, and T. Miller, “Electric Vehicles Batteries: Requirements and Challenges,” *Joule*, vol. 4, no. 3, pp. 511–515, 2020, doi:

https://doi.org/10.1016/j.joule.2020.01.013.

[22] S. S. Zhang, K. Xu, and T. R. Jow, “Study of the charging process of a LiCoO2-based Li-ion battery,” *J. Power Sources*, vol. 160, no. 2, pp. 1349–1354, 2006, doi: https://doi.org/10.1016/j.jpowsour.2006.02.087.

[23] D. Anseán, V. García Fernández, M. Gonzalez, J. Viera, J. C. Antón, and C. Blanco, *Efficient fast-charging strategies for Li-ion batteries*. 2015.

[24] P. H. L. Notten, J. H. G. O. het Veld, and J. R. G. van Beek, “Boostcharging Li-ion batteries: A challenging new charging concept,” *J. Power Sources*, vol. 145, no. 1, pp. 89–94, 2005, doi: https://doi.org/10.1016/j.jpowsour.2004.12.038.

[25] S. S. Zhang, “The effect of the charging protocol on the cycle life of a Li-ion battery,” *J. Power Sources*, vol. 161, no. 2, pp. 1385–1391, 2006, doi: https://doi.org/10.1016/j.jpowsour.2006.06.040.

[26] P. Keil and A. Jossen, “Charging protocols for lithium-ion batteries and their impact on cycle life—An experimental study with different 18650 high-power cells,” *J. Energy Storage*, vol. 6, pp. 125–141, 2016, doi: https://doi.org/10.1016/j.est.2016.02.005.

[27] G. Pistoia, *Battery operated devices and systems: from portable elctronics to industrial products*. London, 2009.

[28] L. Jiang *et al.*, “Optimization of multi-stage constant current charging pattern based on Taguchi method for Li-Ion battery,” *Appl. Energy*, vol. 259, p. 114148, 2020, doi: https://doi.org/10.1016/j.apenergy.2019.114148.

[29] X. W. and W. S. and J. Du, “Multi-Objective Optimal Charging Method for Lithium-Ion Batteries,” *Energies*, vol. 10, pp. 1–18, 2017, [Online]. Available: https://ideas.repec.org/a/gam/jeners/v10y2017i9p1271-d109928.html.

[30] W. Liu, X. Sun, H. Wu, Z. He, and G. Yang, “A multistage current charging method for Li-ion battery bank considering balance of internal consumption and charging speed,” 2016, pp. 1401–1406, doi: 10.1109/IPEMC.2016.7512495.

[31] T. T. Vo, W. Shen, and A. Kapoor, “Experimental comparison of charging algorithms for a lithium-ion battery,” in *2012 10th International Power Energy Conference (IPEC)*, 2012, pp. 207–212, doi: 10.1109/ASSCC.2012.6523265.

[32] S.-J. Huang, B.-G. Huang, and F.-S. Pai, “Fast Charge Strategy Based on the Characterization and Evaluation of LiFePO4 Batteries,” *IEEE Trans. Power Electron.*, vol. 28, pp. 1555–1562, 2013, doi: 10.1109/TPEL.2012.2209184.

[33] D. Anseán, M. González, J. C. Viera, V. M. García, C. Blanco, and M. Valledor, “Fast charging technique for high power lithium iron phosphate batteries: A cycle life analysis,” *J. Power Sources*, vol. 239, pp. 9–15, 2013, doi: https://doi.org/10.1016/j.jpowsour.2013.03.044.

[34] Y.-D. Lee and S.-Y. Park, “Rapid charging strategy in the constant voltage mode for a high power Li-Ion battery,” *2013 IEEE Energy Convers. Congr. Expo.*, pp. 4725–4731, 2013.

[35] L. Christine, D. Céline, T. Pierre-Xavier, and M. T. Nicolas, “Procédé de diagnostic d’une batterie et procédé de contrôle associé,” B04482 FR-RT2021002, 2022.

[36] C. Lin, C. Hsieh, and K. Chen, “A Li-Ion Battery Charger With Smooth Control Circuit and Built-In Resistance Compensator for Achieving Stable and Fast Charging,” *IEEE Trans. Circuits Syst. I Regul. Pap.*, vol. 57, no. 2, pp. 506–517, 2010, doi: 10.1109/TCSI.2009.2023830.

[37] J. M. Amanor-Boadu, A. Guiseppi-Elie, and E. Sánchez-Sinencio, “The Impact of Pulse Charging Parameters on the Life Cycle of Lithium-Ion Polymer Batteries,” *Energies*, vol. 11, no. 8, 2018, doi: 10.3390/en11082162.

[38] B. Purushothaman and U. Landau, “Rapid Charging of Lithium-Ion Batteries Using Pulsed Currents,” *J. Electrochem. Soc.*, vol. 153, pp. A533–A542, Mar. 2006, doi: 10.1149/1.2161580.

[39] Yi-Hwa Liu, Jen-Hao Teng, and Yu-Chung Lin, “Search for an optimal rapid charging pattern for lithium-ion batteries using ant colony system algorithm,” *IEEE Trans. Ind. Electron.*, vol. 52, no. 5, pp. 1328–1336, Oct. 2005, doi: 10.1109/TIE.2005.855670.

[40] F. Savoye, P. Venet, M. Millet, and J. Groot, “Impact of Periodic Current Pulses on Li-Ion Battery Performance,” *IEEE Trans. Ind. Electron.*, vol. 59, no. 9, pp. 3481–3488, 2012, doi: 10.1109/TIE.2011.2172172.

[41] H. Lv, X. Huang, and Y. Liu, “Analysis on pulse charging–discharging strategies for

improving capacity retention rates of lithium-ion batteries," *Ionics (Kiel).*, vol. 26, no. 4, pp. 1749–1770, 2020, doi: 10.1007/s11581-019-03404-8.

[42] Z. Guo, B. Y. Liaw, X. Qiu, L. Gao, and C. Zhang, "Optimal charging method for lithium ion batteries using a universal voltage protocol accommodating aging," *J. Power Sources*, vol. 274, pp. 957–964, 2015, doi: https://doi.org/10.1016/j.jpowsour.2014.10.185.

[43] I. Cho, P.-Y. Lee, and J. Kim, "Analysis of the Effect of the Variable Charging Current Control Method on Cycle Life of Li-ion Batteries," 2019.

[44] R. M. Spotnitz, "AC impedance simulation for lithium-ion cells," in *Fifteenth Annual Battery Conference on Applications and Advances (Cat. No.00TH8490)*, Jan. 2000, pp. 121–126, doi: 10.1109/BCAA.2000.838391.

[45] D. Qu, "The ac impedance studies for porous MnO $_{2}$ cathode by means of modified transmission line model," *J. Power Sources*, vol. 102, no. 1, pp. 270–276, Jan. 2001, doi: 10.1016/S0378-7753(01)00810-2.

[46] L. Chen, S. Wu, D. Shieh, and T. Chen, "Sinusoidal-Ripple-Current Charging Strategy and Optimal Charging Frequency Study for Li-Ion Batteries," *IEEE Trans. Ind. Electron.*, vol. 60, no. 1, pp. 88–97, 2013, doi: 10.1109/TIE.2012.2186106.

[47] A. Ghassemi, P. Chakraborty Banerjee, A. F. Hollenkamp, Z. Zhang, and B. Bahrani, "Effects of alternating current on Li-ion battery performance: Monitoring degradative processes with in-situ characterization techniques," *Appl. Energy*, vol. 284, p. 116192, 2021, doi: https://doi.org/10.1016/j.apenergy.2020.116192.

[48] J. M. Tarascon and M. Armand, "Issues and Challenges Facing Rechargeable Lithium Batteries," *Nature*, vol. 414, pp. 359–367, Dec. 2001, doi: 10.1038/35104644.

[49] K. Uddin, A. Picarelli, C. Lyness, N. Taylor, and J. Marco, "An Acausal Li-Ion Battery Pack Model for Automotive Applications," *Energies*, vol. 7, pp. 5675–5700, Sep. 2014, doi: 10.3390/en7095675.

[50] C. R. Birkl, M. R. Roberts, E. McTurk, P. G. Bruce, and D. A. Howey, "Degradation diagnostics for lithium ion cells," *J. Power Sources*, vol. 341, pp. 373–386, 2017, doi: https://doi.org/10.1016/j.jpowsour.2016.12.011.

[51] A. Barré, B. Deguilhem, S. Grolleau, M. Gérard, F. Suard, and D. Riu, “A review on lithium-ion battery ageing mechanisms and estimations for automotive applications,” *J. Power Sources*, vol. 241, pp. 680–689, Nov. 2013, doi: 10.1016/j.jpowsour.2013.05.040.

[52] I. Bloom *et al.*, “An accelerated calendar and cycle life study of Li-ion cells,” *J. Power Sources*, vol. 101, pp. 238–247, Oct. 2001, doi: 10.1016/S0378-7753(01)00783-2.

[53] J. Belt, V. Utgikar, and I. Bloom, “Calendar and PHEV cycle life aging of high-energy, lithium-ion cells containing blended spinel and layered-oxide cathodes,” *J. Power Sources - J POWER SOURCES*, vol. 196, pp. 10213–10221, Dec. 2011, doi: 10.1016/j.jpowsour.2011.08.067.

[54] M. Maures, Y. Zhang, C. Martin, J.-Y. Delétage, J.-M. Vinassa, and O. Briat, “Impact of temperature on calendar ageing of Lithium-ion battery using incremental capacity analysis,” *Microelectron. Reliab.*, vol. 100–101, p. 113364, 2019, doi: https://doi.org/10.1016/j.microrel.2019.06.056.

[55] P. Keil *et al.*, “Calendar Aging of Lithium-Ion Batteries,” *J. Electrochem. Soc.*, vol. 163, no. 9, pp. A1872--A1880, 2016, doi: 10.1149/2.0411609jes.

[56] X. Han *et al.*, “A review on the key issues of the lithium ion battery degradation among the whole life cycle,” *eTransportation*, vol. 1, p. 100005, 2019, doi: https://doi.org/10.1016/j.etran.2019.100005.

[57] M. Broussely, S. Herreyre, P. Biensan, P. Kasztejna, K. Nechev, and S. RJ, “Aging mechanism in Li ion cells and calendar life predictions,” *J. Power Sources*, vol. 97–98, pp. 13–21, 2001, doi: 10.1016/S0378-7753(01)00722-4.

[58] H. Gabrisch, J. D. Wilcox, and M. M. Doeff, “TEM study of fracturing in spherical and plate-like $LiFePO_4$ particles,” *Electrochem. Solid-State Lett.*, vol. 11, pp. A25–A29, Jan. 2008, doi: 10.1149/1.2826746.

[59] S. Bourlot, P. Blanchard, and S. Robert, “Investigation of aging mechanisms of high power Li-ion cells used for hybrid electric vehicles,” *Lancet*, vol. 196, pp. 6841–6846, Aug. 2011, doi: 10.1016/j.jpowsour.2010.09.103.

[60] X. Fleury, M. H. Noh, S. Geniès, P. X. Thivel, C. Lefrou, and Y. Bultel, “Fast-charging of Lithium Iron Phosphate battery with ohmic-drop compensation method: Ageing

study," *J. Energy Storage*, vol. 16, pp. 21–36, 2018, doi: https://doi.org/10.1016/j.est.2017.12.015.

[61] T. Waldmann *et al.*, "Review—Post-Mortem Analysis of Aged Lithium-Ion Batteries: Disassembly Methodology and Physico-Chemical Analysis Techniques," *J. Electrochem. Soc.*, vol. 163, pp. A2149–A2164, Jan. 2016, doi: 10.1149/2.1211609jes.

[62] C. Zhu, B. Zheng, Z. He, M. Gao, C. Sun, and Z. Bao, "State of Health Estimation of Lithium-Ion Battery Using Time Convolution Memory Neural Network," *Mob. Inf. Syst.*, vol. 2021, p. 4826409, 2021, doi: 10.1155/2021/4826409.

[63] N. Noura, L. Boulon, and S. Jemeï, "A Review of Battery State of Health Estimation Methods: Hybrid Electric Vehicle Challenges," *World Electr. Veh. J.*, vol. 11, no. 4, 2020, doi: 10.3390/wevj11040066.

[64] M. J. Lain, J. Brandon, and E. Kendrick, "Design Strategies for High Power vs. High Energy Lithium Ion Cells," *Batteries*, vol. 5, no. 4, 2019, doi: 10.3390/batteries5040064.

[65] B. ~V. Ratnakumar, M. ~C. Smart, L. ~D. Whitcanack, and R. ~C. Ewell, "The impedance characteristics of Mars Exploration Rover Li-ion batteries," *J. Power Sources*, vol. 159, no. 2, pp. 1428–1439, Jan. 2006, doi: 10.1016/j.jpowsour.2005.11.085.

[66] E. Riviere, A. Sari, P. Venet, F. Meniere, and Y. Bultel, "Innovative Incremental Capacity Analysis Implementation for C/LiFePO4 Cell State-of-Health Estimation in Electrical Vehicles," *Batteries*, vol. 5, p. 37, Apr. 2019, doi: 10.3390/batteries5020037.

[67] M. Dubarry *et al.*, "Identifying battery aging mechanisms in large format Li ion cells," *J. Power Sources*, vol. 196, no. 7, pp. 3420–3425, 2011, doi: https://doi.org/10.1016/j.jpowsour.2010.07.029.

[68] G. Liu, M. Ouyang, L. Lu, L. Jianqiu, and X. Han, "Analysis of the heat generation of lithium-ion battery during charging and discharging considering different influencing factors," *J. Therm. Anal. Calorim.*, vol. 116, 2014, doi: 10.1007/s10973-013-3599-9.

[69] X. Huang *et al.*, "A Review of Pulsed Current Technique for Lithium-ion Batteries," *Energies*, vol. 13, p. 2458, May 2020, doi: 10.3390/en13102458.

[70] J. Li, E. Murphy, J. Winnick, and P. A. Kohl, "The effects of pulse charging on cycling

characteristics of commercial lithium-ion batteries," *J. Power Sources*, vol. 102, no. 1–2, pp. 302–309, 2001, doi: 10.1016/s0378-7753(01)00820-5.

[71] J. Edge *et al.*, "Lithium Ion Battery Degradation: What you need to know," *Phys. Chem. Chem. Phys.*, vol. 23, 2021, doi: 10.1039/D1CP00359C.

[72] N. Laszczynski, S. Solchenbach, H. A. Gasteiger, and B. L. Lucht, "Understanding Electrolyte Decomposition of Graphite/{NCM}811 Cells at Elevated Operating Voltage," *J. Electrochem. Soc.*, vol. 166, no. 10, pp. A1853--A1859, 2019, doi: 10.1149/2.0571910jes.

[73] G. Zhang, X. Wei, X. Tang, J. Zhu, S. Chen, and H. Dai, "Internal short circuit mechanisms, experimental approaches and detection methods of lithium-ion batteries for electric vehicles: A review," *Renew. Sustain. Energy Rev.*, vol. 141, p. 110790, 2021, doi: https://doi.org/10.1016/j.rser.2021.110790.

[74] S. Huang *et al.*, "Understanding Li-Ion Cell Internal Short Circuit and Thermal Runaway through Small, Slow and In Situ Sensing Nail Penetration," *J. Electrochem. Soc.*, vol. 167, no. 9, p. 90526, Jan. 2020, doi: 10.1149/1945-7111/ab8878.

[75] S. Kim *et al.*, "Simulation Study on Internal Short Circuits in a Li-Ion Battery Depending on the Sizes, Quantities, and Locations of Li Dendrites," *Front. Mater.*, vol. 9, 2022, doi: 10.3389/fmats.2022.850610.

[76] C. von Lüders *et al.*, "Lithium plating in lithium-ion batteries investigated by voltage relaxation and in situ neutron diffraction," *J. Power Sources*, vol. 342, pp. 17–23, Feb. 2017, doi: 10.1016/j.jpowsour.2016.12.032.

[77] T. Waldmann, B. I. Hogg, and M. Wohlfahrt-Mehrens, "Li plating as unwanted side reaction in commercial Li-ion cells – A review," *Journal of Power Sources*, vol. 384. Elsevier B.V., pp. 107–124, Apr. 30, 2018, doi: 10.1016/j.jpowsour.2018.02.063.

[78] U. R. Koleti, T. Q. Dinh, and J. Marco, "A new on-line method for lithium plating detection in lithium-ion batteries," *J. Power Sources*, vol. 451, p. 227798, 2020, doi: https://doi.org/10.1016/j.jpowsour.2020.227798.

[79] U. Janakiraman, T. R. Garrick, and M. E. Fortier, "Review-Lithium Plating Detection Methods in Li-Ion Batteries," *J. Electrochem. Soc.*, vol. 167, no. 16, p. 160552, Dec.

2020, doi: 10.1149/1945-7111/abd3b8.

[80] M. C. Smart and B. V Ratnakumar, “Effects of Electrolyte Composition on Lithium Plating in Lithium-Ion Cells,” *J. Electrochem. Soc.*, vol. 158, no. 4, pp. A379--A389, Feb. 2011, doi: 10.1149/1.3544439.

[81] M. Uno and K. Tanaka, “Influence of High-Frequency Charge–Discharge Cycling Induced by Cell Voltage Equalizers on the Life Performance of Lithium-Ion Cells,” *IEEE Trans. Veh. Technol.*, vol. 60, no. 4, pp. 1505–1515, 2011, doi: 10.1109/TVT.2011.2127500.

[82] A. Krupp, E. Ferg, F. Schuldt, K. Derendorf, and C. Agert, “Incremental Capacity Analysis as a State of Health Estimation Method for Lithium-Ion Battery Modules with Series-Connected Cells,” *Batteries*, vol. 7, no. 1. 2021, doi: 10.3390/batteries7010002.

[83] G. Seo *et al.*, “Rapid determination of lithium-ion battery degradation: High C-rate LAM and calculated limiting LLI,” *J. Energy Chem.*, vol. 67, pp. 663–671, 2022, doi: https://doi.org/10.1016/j.jechem.2021.11.009.

[84] J. Guo, Y. Li, J. Meng, K. Pedersen, L. Gurevich, and D.-I. Stroe, “Understanding the mechanism of capacity increase during early cycling of commercial NMC/graphite lithium-ion batteries,” *J. Energy Chem.*, vol. 74, pp. 34–44, 2022, doi: https://doi.org/10.1016/j.jechem.2022.07.005.

[85] B. Gyenes, D. A. Stevens, V. L. Chevrier, and J. R. Dahn, “Understanding Anomalous Behavior in Coulombic Efficiency Measurements on Li-Ion Batteries,” *J. Electrochem. Soc.*, vol. 162, no. 3, pp. A278--A283, 2014, doi: 10.1149/2.0191503jes.

[86] M. Dubarry, C. Truchot, and B. Y. Liaw, “Synthesize battery degradation modes via a diagnostic and prognostic model,” *J. Power Sources*, vol. 219, pp. 204–216, 2012, doi: https://doi.org/10.1016/j.jpowsour.2012.07.016.

[87] M. Lewerenz, J. Münnix, J. Schmalstieg, S. Käbitz, M. Knips, and D. U. Sauer, “Systematic aging of commercial LiFePO4|Graphite cylindrical cells including a theory explaining rise of capacity during aging,” *J. Power Sources*, vol. 345, pp. 254–263, 2017, doi: https://doi.org/10.1016/j.jpowsour.2017.01.133.

[88] B. Xu, L. Kong, G. Wen, and M. Pecht, “Protection Devices in Commercial 18650

Lithium-Ion Batteries," *IEEE Access*, vol. 9, pp. 66687–66695, 2021, doi: 10.1109/ACCESS.2021.3075972.

[89] G. Nagasubramanian, "Comparison of the thermal and electrochemical properties of LiPF 6 and LiN(SO 2C 2F 5) 2 salts in organic electrolytes," *J. Power Sources - J POWER SOURCES*, vol. 119, pp. 811–814, 2003, doi: 10.1016/S0378-7753(03)00246-5.

[90] B. S. J. Garche, C. Dyer, P. Moseley, Z. Ogumi, D. Rand, *Encyclopedia of Electrochemical Power Sources*, 1st ed. ELSEVIER, 2009.

[91] J. J. Wu and W. R. Bennett, "Fundamental investigation of Si anode in Li-Ion cells," in *2012 IEEE Energytech*, 2012, pp. 1–5, doi: 10.1109/EnergyTech.2012.6304667.

[92] P. Kuntz, "Evolution du comportement scuritaire de batterie lithium-ion pendant leur vieillissement," Université Grenoble Alpes, 2020.

[93] M. Montaru, S. Fiette, J.-L. Koné, and Y. Bultel, "Calendar ageing model of Li-ion battery combining physics-based and empirical approaches," *J. Energy Storage*, vol. 51, p. 104544, 2022, doi: https://doi.org/10.1016/j.est.2022.104544.